



Deformation and Phase Transformation Processes in Polycrystalline NiTi and NiTiHf High Temperature Shape Memory Alloys

Othmane Benafan
Glenn Research Center, Cleveland, Ohio

NASA STI Program . . . in Profile

Since its founding, NASA has been dedicated to the advancement of aeronautics and space science. The NASA Scientific and Technical Information (STI) program plays a key part in helping NASA maintain this important role.

The NASA STI Program operates under the auspices of the Agency Chief Information Officer. It collects, organizes, provides for archiving, and disseminates NASA's STI. The NASA STI program provides access to the NASA Aeronautics and Space Database and its public interface, the NASA Technical Reports Server, thus providing one of the largest collections of aeronautical and space science STI in the world. Results are published in both non-NASA channels and by NASA in the NASA STI Report Series, which includes the following report types:

- **TECHNICAL PUBLICATION.** Reports of completed research or a major significant phase of research that present the results of NASA programs and include extensive data or theoretical analysis. Includes compilations of significant scientific and technical data and information deemed to be of continuing reference value. NASA counterpart of peer-reviewed formal professional papers but has less stringent limitations on manuscript length and extent of graphic presentations.
- **TECHNICAL MEMORANDUM.** Scientific and technical findings that are preliminary or of specialized interest, e.g., quick release reports, working papers, and bibliographies that contain minimal annotation. Does not contain extensive analysis.
- **CONTRACTOR REPORT.** Scientific and technical findings by NASA-sponsored contractors and grantees.

- **CONFERENCE PUBLICATION.** Collected papers from scientific and technical conferences, symposia, seminars, or other meetings sponsored or cosponsored by NASA.
- **SPECIAL PUBLICATION.** Scientific, technical, or historical information from NASA programs, projects, and missions, often concerned with subjects having substantial public interest.
- **TECHNICAL TRANSLATION.** English-language translations of foreign scientific and technical material pertinent to NASA's mission.

Specialized services also include creating custom thesauri, building customized databases, organizing and publishing research results.

For more information about the NASA STI program, see the following:

- Access the NASA STI program home page at <http://www.sti.nasa.gov>
- E-mail your question to help@sti.nasa.gov
- Fax your question to the NASA STI Information Desk at 443-757-5803
- Phone the NASA STI Information Desk at 443-757-5802
- Write to:
STI Information Desk
NASA Center for AeroSpace Information
7115 Standard Drive
Hanover, MD 21076-1320



Deformation and Phase Transformation Processes in Polycrystalline NiTi and NiTiHf High Temperature Shape Memory Alloys

Othmane Benafan
Glenn Research Center, Cleveland, Ohio

National Aeronautics and
Space Administration

Glenn Research Center
Cleveland, Ohio 44135

Acknowledgments

I would like to express my sincere gratitude to: Prof. Raj Vaidyanathan: for his technical advice and support, and for the opportunity to join his research group. Prof. Ali Gordon, Prof. Jan Gou, Prof. Aravinda Kar and Prof. Helge Heinrich: for serving on my thesis committee and for valuable teachings throughout my time at UCF. Dr. Santo Padula II, Dr. Ronald Noebe, Dr. Anita Garg, Darrell Gaydosh, Glen Bigelow at NASA Glenn Research Center for supporting this research and for numerous fruitful discussions that helped shape this work. I am also thankful to Dr. Michael Nathal for given me the opportunity to join the SMA research group at NASA GRC. Dr. Don Brown, Dr. Bjørn Clausen, Dr. Sven Vogel, Thomas Sisneros, Matt Reiche and Leilani Conradson at Los Alamos National Laboratory: for their time and help with the neutron diffraction measurements and analysis. My office-mates and my friends Doug Nicholson, Dr. Shipeng Qiu, Dr. Mahadevan Manjeri and Matthew Fox: for their endearing friendship. Cynthia Harle, Angelina Feliciano, Karen Glidewell and Kari Stiles at the Advanced Materials Processing and Analysis Center (AMPAC): for their administrative support and help in all sorts of paperwork. This work was supported by funding from the NASA Fundamental Aeronautics Program, Supersonics Project including (Grant No. NNX08AB51A). This work has also benefited from the use of: (1) The Lujan Neutron Scattering Center at LANSCE, which is funded by the Office of Basic Energy Sciences DOE. LANL is operated by Los Alamos National Security LLC under DOE Contract No. DE-AC52-06NA25396. (2) The Spallation Neutron Source at Oak Ridge National Laboratory, which is funded by the Division of Scientific User Facilities, Office of Basic Energy Sciences, U.S. Department of Energy under Contract DE-AC05- 00OR22725 with UT-Battelle, LLC.

Trade names and trademarks are used in this report for identification only. Their usage does not constitute an official endorsement, either expressed or implied, by the National Aeronautics and Space Administration.

This work was sponsored by the Fundamental Aeronautics Program at the NASA Glenn Research Center.

Level of Review: This material has been technically reviewed by technical management.

Available from

NASA Center for Aerospace Information
7115 Standard Drive
Hanover, MD 21076-1320

National Technical Information Service
5301 Shawnee Road
Alexandria, VA 22312

Available electronically at <http://www.sti.nasa.gov>

Preface

This research results presented herein constitute a dissertation prepared by Othmane Benafan under the direction of Professor Raj Vaidyanathan for the degree of Doctor of Philosophy in the Department of Mechanical, Materials and Aerospace Engineering, in the College of Engineering and Computer Science at the University of Central Florida.

Contents

Preface	iii
Abstract	1
Nomenclature	2
Chapter 1.—Motivation and Organization.....	3
1.1 Motivation.....	3
1.2 Organization.....	4
Chapter 2.—Introduction	5
2.1 Introduction to Shape Memory Alloys.....	5
2.1.1 Shape Memory Effect	5
2.1.2 Superelasticity	6
2.1.3 Design With Shape Memory Alloys	7
2.2 Introduction to Neutron Diffraction.....	8
2.2.1 Neutron Diffraction at Los Alamos National Laboratory	8
2.2.2 Neutron Data Analysis	10
Chapter 3.—Temperature Dependent Deformation of B2 Austenite in a NiTi Shape Memory Alloy	13
3.1 Introduction.....	13
3.2 Experimental Techniques.....	15
3.2.1 Material	15
3.2.2 Neutron Diffraction Experiments.....	15
3.2.3 Transmission Electron Microscopy.....	16
3.2.4 Neutron Diffraction Data Analysis	16
3.3 Self-Consistent Polycrystalline Deformation Model	16
3.4 Experimental and Modeling Results	17
3.4.1 Macroscopic Stress-Strain Response for Ni _{49.9} Ti _{50.1}	17
3.4.2 Modeling Results	24
3.4.3 Thermal Recovery of the Isothermally Deformed Samples.....	27
3.5 Discussion.....	30
3.5.1 Macroscopic Stress-Strain Behavior.....	30
3.5.2 Microstructural and Micromechanical Evolution	31
3.5.3 B2 Deformation Map	32
3.5.4 Strain Partitioning	34
3.6 Conclusions.....	34
Chapter 4.—Role of B19' Martensite Deformation on the Stability of Niti Two-Way Shape Memory Effect	37
4.1 Introduction.....	37
4.2 Experimental Techniques.....	39
4.3 Results and Discussion	39
4.3.1 B19' Martensite Deformation.....	39
4.3.2 TWSME Characterization.....	45
4.4 Summary	48
Chapter 5.—Thermomechanical Cycling Of A Niti Shape Memory Alloy Investigated Using Neutron Diffraction	51
5.1 Introduction.....	51
5.2 Material and Experimental Procedures	52
5.2.1 Material	52
5.2.2 Ex situ Testing	52
5.2.3 In situ Neutron Diffraction Measurements	52

5.2.4	Ex situ Neutron Diffraction Measurements	53
5.1.1	Neutron Diffraction Data Analysis	53
5.3	Experimental Results and Discussion	53
5.3.1	Ex situ Macroscopic Behavior	53
5.3.2	In Situ Neutron Diffraction Results	57
5.3.3	Ex situ Neutron Diffraction Results	67
5.4	Conclusions.....	69
Chapter 6.—	In Situ Neutron Diffraction Study of Shape Setting Niti Shape Memory Alloy	71
6.1	Introduction.....	71
6.2	Material and Experimental Procedures	72
6.2.1	Material	72
6.2.2	Test Procedures	72
6.2.3	Neutron Diffraction Data Analysis	73
6.3	Results.....	74
6.3.1	Pre-Straining before Shape Setting	74
6.3.2	Shape Setting	75
6.3.3	Second Shape Set	82
6.3.4	Pre- and Post-Shape Set Shape Memory Behavior	83
6.4	Discussion.....	86
6.5	Conclusions.....	88
Chapter 7.—	Microstructural Response During Isothermal and Isobaric Loading of a Precipitation Strengthened Ni-29.7Ti-20Hf High-Temperature Shape Memory Alloy	89
7.1	Introduction.....	89
7.2	Experimental Methods	90
7.2.1	Sample Preparation	90
7.2.2	Experimental Setup and Test Procedures.....	90
7.3	Results.....	92
7.3.1	Stress-Free Structure of the Ni-29.7Ti-20Hf Alloy	92
7.3.2	Isothermal Loading in Martensite	92
7.3.3	Isobaric Strain-Temperature Behavior	96
7.4	Discussion.....	99
7.4.1	Initial Ni-29.7Ti-20Hf Microstructure	99
7.4.2	Isothermal Response	100
7.4.3	Isobaric Response	101
7.5	Conclusions.....	103
Chapter 8.—	Design of a Multiaxial Loading Capability on an Engineering Neutron Diffractometer	105
8.1	Introduction.....	105
8.2	Engineering Materials Diffractometer—VULCAN.....	106
8.3	Design Requirements	106
8.4	Grip Components.....	106
8.5	Heat Transfer and Torsional Analyses.....	110
8.5.1	Heat Transfer Analysis.....	110
8.1.1	Torsional Analysis	113
8.6	Preliminary VULCAN Diffraction Spectra	115
8.7	Concluding Remarks.....	117
Chapter 9.—	Conclusions	119
Appendix A.—	Grip Design Machine Drawings.....	121
References.....		133

List of Tables

Table 3.1.—Experimental test conditions (temperature and strain) under which neutron data were acquired in SMARTS and HIPPO for specimens 1-5. The ‘x’ indicates conditions where neutron data were obtained.....	16
Table 3.2.—Elastoplastic self-consistent (EPSC) model inputs for austenitic Ni _{49.9} Ti _{50.1}	17
Table 3.3.—Approximate partitioning of strains during the isothermal deformation of Ni _{49.9} Ti _{50.1}	28
Table 5.1.—Experimental test conditions for 13 specimens tested ex situ and/or in situ as indicated by the ‘x’	52
Table 6.1.—Calculated intergranular stress mismatch between {100} _A and {111} _A austenite reflections during constrained heating and cooling. The macroscopic stress differences are also shown for comparison	79
Table 6.2.—Load-biased and stress-free shape memory behavior for NiTi in the as-received and shape-set conditions	84
Table 8.1.—Properties of INCONEL 718 used in the analyses.....	107
Table 8.2.—Properties of binary NiTi used in the analyses	111
Table 8.3.—Geometric parameters and fluid properties used in the analyses	112

List of Figures

Figure 2.1.—Stress-strain-temperature response of a typical NiTi shape memory alloy. (0→1) Austenite transformation to self-accommodated martensite, (1→2) reorientation and detwinning region, (2→3) nonlinear unloading and finally (3→0) transformation to the austenite phase after heating with the concomitant strain recovery.	6
Figure 2.2.—Thermally induced phase transformation curve showing transformation specific properties.....	7
Figure 2.3.—Superelastic effect showing strain recovery at a constant temperature.	7
Figure 2.4.—Cutaway schematic of SMARTS diffractometer showing the beam path, sample environment and detector arrangements [13]. (Reproduced with permission from LANL).	9
Figure 2.5.—Schematic of the SMARTS diffractometer experimental setup showing the incident and diffracted beams. The perpendicular and parallel lattice planes are shown.....	9
Figure 2.6.—Schematic of HIPPO showing the beam path, sample environment and the arrangement of detector tubes in panels arranged on rings of constant diffraction angle [14]. (Reproduced with permission from LANL.)	10
Figure 2.7.—Example of GSAS Rietveld refinement for NiTi. The measured data are indicated by cross-marks and the calculated profile is indicated by the solid line. The tick-marks below the profile pattern indicate the reflections. The lower curve is the difference between the measurement and refinement.....	11
Figure 3.1.—Tensile stress-strain response during in situ neutron diffraction experiments of Ni _{49.9} Ti _{50.1} at four different temperatures above A_f . The stress relaxations are due to the 30 min holding periods necessary for neutron data acquisition.	18
Figure 3.2.—Monotonic tensile data for Ni _{49.9} Ti _{50.1} as a function of temperature. (a) Stress-strain curves for samples tested ex situ and (b) stress values at various strain levels as a function of temperature, obtained by taking vertical slices through the stress-strain curves at selected strains.....	19
Figure 3.3.—Normalized neutron diffraction spectra acquired at incremental strains up to 18 percent while holding constant temperature at (a) 165 °C, (b) 230 °C, (c) 290 °C and (d)	

320 °C. These reflections are from lattice planes perpendicular to the loading axis. Subscripts “ _A ” and “ _M ” denote austenite and martensite, respectively.	20
Figure 3.4.—Stress-induced martensite phase fractions during loading and unloading of the Ni _{49.9} Ti _{50.1} at various temperatures. Error bar indicates the instrument resolution.	20
Figure 3.5.—Inverse pole figures (IPFs) from B2 lattice reflections perpendicular to the loading axis at selected strains for each sample. The corresponding maximum and minimum pole intensities (times random) are included at the top left hand corner of each IPF.	21
Figure 3.6.—Austenite peak intensities normalized to 1 at the unstrained condition for the {110} _A , {111} _A , {210} _A and {221} _A reflections perpendicular to the loading axis at (a) 165 °C, (b) 230 °C, (c) 290 °C and (d) 320 °C.	22
Figure 3.7.—Lattice strains associated with {100} _A , {110} _A , {111} _A , {210} _A and {221} _A reflections perpendicular to the loading axis at (a) 165 °C, (b) 230 °C, (c) 290 °C and (d) 320 °C using a single peak fitting technique. Error bars included (Δε~0.02 percent).	23
Figure 3.8.—TEM bright-field (BF) images of the microstructure of Ni _{49.9} Ti _{50.1} at 20, 165 and 320 °C for a virgin sample ((a), (b), and (c), respectively), sample post-deformed to 18 percent strain at 165 °C ((d), (e), and (f), respectively), and sample post-deformed to 18 percent strain at 320 °C ((g), (h), and (i), respectively). (j) BF and (k) SADP of the planar faults observed after deformation.	24
Figure 3.9.—EPSC model predictions for the 320 °C stress-strain response of Ni _{49.9} Ti _{50.1} compared to experimental data. (i) Model 1 with slip systems 1 and 2 active (see Table 3.2 for details), (ii) Model 2 with slip systems 1, 2 and 3 active, (iii) Model 3 with only twin systems 4 and 5 active, and (iv) Model 4 with slip and twin systems 1, 2, 4 and 5 active.	25
Figure 3.10.—Experimental and predicted austenite lattice strains. (a) Experimental data at 320 °C for all reflections, and comparison of the experimental and modeled results for individual reflections (b) {100} _A , (c) {110} _A , (d) {111} _A , (e) {210} _A , and (f) {221} _A	26
Figure 3.11.—Experimental and predicted IPFs at 0 and 18 percent strain. Corresponding slip or twin systems used in each model are included.	27
Figure 3.12.—Strain-temperature response for samples 1 to 4 during unloading from 18 percent strain at their respective deformation temperatures, heating to 500 °C, and cooling back to room temperature.	28
Figure 3.13.—Lattice strain recovery during unloading and heating to 500 °C for (a) 165 °C, (b) 230 °C, (c) 290 °C and (d) 320 °C isothermally deformed samples. Error bars included, but were usually smaller than the symbol size.	29
Figure 3.14.—Austenite pole figures measured at 200 °C for (a) virgin sample, and post deformed and thermally cycled samples (complete history described in Table 3.1): (b) sample 1, (c) sample 2, (d) sample 3, and (e) sample 4.	30
Figure 3.15.—Deformation mechanism map showing the mechanisms responsible for initial inelastic strain behavior in a B2 Ni _{49.9} Ti _{50.1} alloy.	33
Figure 4.1.—General stress-strain response of martensitic NiTi showing the four distinct deformation regimes.	38
Figure 4.2.—Tensile stress-strain-temperature responses of seven Ni _{49.9} Ti _{50.1} samples deformed at room temperature to strains between 6 and 22 percent, unloaded to zero stress, and thermally cycled to 200 °C and back to room temperature.	40
Figure 4.3.—Recovered and unrecovered strains through various regions of the stress-strain-temperature curves for Ni _{49.9} Ti _{50.1} shown in Figure 4.2. (a) Recovered strains after unloading (from the maximum strain to 0 MPa (B→C)) and after the first thermal cycle at 0 MPa (C→D). (b) Total recovered strains including unloading and thermal recovery (B to D) and total unrecovered strains after the first thermal cycle (D to A).	40

Figure 4.4.—Room temperature inverse pole figures (IPFs) for martensitic $\text{Ni}_{49.9}\text{Ti}_{50.1}$ from diffracting planes perpendicular to the loading direction. For a given IPF, the corresponding maximum and minimum pole intensities (times random) are at the top left hand corner and the specific intensity changes for the (230) and (010) poles are indicated below each IPFs. The column letters correspond to the positions identified in Figure 4.2.	41
Figure 4.5.—Transient strain-temperature responses for the very first thermal cycle after load removal. Samples 1 to 7 correspond to the samples identified in Figure 4.2.	43
Figure 4.6.—Lattice strain associated with the a) (011) _M , b) (030) _M , c) (120) _M , and d) (121) _M planes perpendicular to the applied loading direction. Lattice strain data at maximum strain (B), after unloading (C), and after one thermal cycle (D) are shown for samples loaded between 6 and 22 percent strain for each of the planes measured.	45
Figure 4.7.—TWSME strain-temperature responses for all samples pre-strained between 6 and 22 percent. The transient responses due to the very first heating cycle after unloading are also included (dotted lines).	46
Figure 4.8.—TWSME transformation strain plotted as a function of (a) cycle number for all pre-strained conditions, and (b) the pre-applied strain level.	47
Figure 4.9.—Strain reduction during TWSME thermal cycling (measured at room temperature).	48
Figure 4.10.—Transformation temperatures determined during TWSME thermal cycling as a function of increasing cycle number.	48
Figure 5.1.—Tensile stress-strain responses of $\text{Ni}_{49.9}\text{Ti}_{50.1}$ samples deformed at (a) 320 °C austenite and (b) at room temperature martensite to strains between 0 and 18 percent as indicted.	54
Figure 5.2.—Strain-temperature responses for (a) samples deformed and loaded at 320 °C, and (b) samples deformed and loaded at room temperature. The initial cooling (a) and heating (b) are also included. Cycling was performed under a constant 100 MPa stress between room temperature and 230 °C.	54
Figure 5.3.—Transformation strains for (a) and (b) samples deformed and loaded at 320 °C, and (c) and (d) samples deformed and loaded at room temperature. The data is plotted as a function of (a) to (c) cycle number for all pre-strained conditions, and (b) to (d) the pre-applied strain level.	55
Figure 5.4.—Residual strain accumulation during thermomechanical cycling of (a) and (b) samples deformed and loaded at 320 °C, and (c) and (d) samples deformed and loaded at room temperature. These residual strains were measured at (a) to (c) room temperature and (b) to (d) 230 °C.	56
Figure 5.5.—Normalized neutron diffraction spectra acquired at room temperature during cycling of the samples deformed at 320 °C (samples 1 to 4 of Table 5.1). These reflections are from the (100) _M and (010) _M lattice planes (a) to (d) perpendicular and (e) to (h) parallel to the loading axis. The initial no-load cycles and the first cycle after loading to 100 MPa are included. The arrows indicate the intensity increase or decrease when the samples were first loaded (labeled <i>LOAD</i>).	58
Figure 5.6.—Normalized neutron diffraction spectra acquired at room temperature during cycling of the samples deformed at 320 °C (samples 1 to 4 of Table 5.1). These reflections are from the (a-d) (030) _M and (120) _M lattice planes perpendicular to the loading axis, and (e-h) (102) _M lattice planes parallel to the loading axis. The arrows indicate the intensity increase or decrease when the samples were first loaded (labeled <i>LOAD</i>).	59
Figure 5.7.—Room temperature IPFs for martensitic $\text{Ni}_{49.9}\text{Ti}_{50.1}$ from diffracting planes (a) perpendicular and (b) parallel to the loading direction. This data belongs to the samples deformed at 320 °C (samples 1 to 4 of Table 5.1). Cycle numbers C0 to C13 correspond to	

the diffraction spectra shown in Figure 5.5 and Figure 5.6. For clarity in presentation, different scales are used in each direction.	60
Figure 5.8.—The IPFs pole locations for the irreducible (a) monoclinic and (b) cubic stereographs with select crystal orientations.	61
Figure 5.9.—IPFs pole intensities for the selected (a) (030) _M and (150) _M martensite variants perpendicular to the loading axis , and (b) (100) _M and (102) _M martensite variants parallel to the loading axis.	61
Figure 5.10.—Normalized neutron diffraction spectra acquired at the austenite phase during cycling of the samples deformed at 320 °C (samples 1 to 4 of Table 5.1). These reflections are from the {110} _A lattice planes (a) to (d) perpendicular and (e) to (h) parallel to the loading axis. The arrows indicate the intensity decrease when the samples were first loaded to 100 MPa (labeled <i>LOAD</i>). A reference B19' spectrum acquired at RT is also included.	63
Figure 5.11.—B2 IPFs for austenitic Ni _{49.9} Ti _{50.1} from diffracting planes (a) perpendicular and (b) parallel to the loading direction. This data belongs to the samples deformed at 320 °C (samples 1 to 4 of Table 5.1). Cycle numbers C0 to C13 correspond to the diffraction spectra shown in Figure 5.10.	64
Figure 5.12.—IPFs pole intensities for the {110} _A and {111} _A austenite reflections perpendicular to the loading axis.	64
Figure 5.13.—B19' Lattice strains associated with the several reflections (a-d) perpendicular and (e-h) parallel to the loading axis during cycling.	66
Figure 5.14.—B2 Lattice strains associated with the several reflections (a-d) perpendicular and (e-h) parallel to the loading axis during cycling.	66
Figure 5.15.—Evolution of the austenite peak breadth (in the full-width of half-maximum) during cycling.	67
Figure 5.16.—Macroscopic (a) strain-temperature responses, (b) transformation strains and (c) residual strains for two samples loaded to 200 MPa at room temperature (samples 12 and 13 of Table 5.1) and cycled 20 and 50 times between 30 and 230 °C.	68
Figure 5.17.—Martensite pole figures measured at room temperature for a virgin sample, and post cycled samples (samples 11 to 13 of Table 5.1). For clarity in presentation, different scales are used.	68
Figure 5.18.—Austenite pole figures measured at 200 °C for a virgin sample, and post cycled samples (samples 11 to 13 of Table 5.1).	69
Figure 6.1.—Tensile stress-strain response of NiTi at room temperature (from extensometry) during loading and unloading. The symbols indicate the strains at which neutron diffraction spectra were taken.	73
Figure 6.2.—GSAS Rietveld refinement for NiTi with diffracting lattice planes parallel to the loading axis with no applied load. (a) Monoclinic martensite at 27 °C and (b) cubic austenite at 450 °C. The measured data are indicated by cross-marks and the calculated profile is indicated by the solid line. The tick-marks below the profile pattern indicate the reflections. The lower curve is the difference between the measurement and refinement.	74
Figure 6.3.—B19' martensitic NiTi IPFs for diffracting planes (a) parallel and (b) perpendicular to the loading direction. The sample condition (applied strain and associated stress) is indicated above each IPF. The maximum and minimum intensities are indicated at the top left hand corner in multiples of random distribution. Note that the scales used for the IPFs in (a) and (b) are different.	75
Figure 6.4.—Stress-temperature response of NiTi during shape-constrained thermal cycling: (a) and (b) sections of the heating cycle and (c) and (d) sections of the cooling cycle for two successive shape set experiments (from extensometry). The vertical lines represent the	

transformation temperatures obtained from ex situ constant stress thermal cycling tests performed on similar samples.	76
Figure 6.5.—Sections of normalized neutron diffraction spectra acquired during heating and cooling from 30 to 450 °C and back to 30 °C for (a) {100} _A , (011) _M and (100) _M , (b) {110} _A , (002) _M and (111) _M , (c) {111} _A and (102) _M , (d) {210} _A and (013) _M . The reflections are from lattice planes perpendicular to the loading axis. Subscripts ‘A’ and ‘M’ refer to austenite and martensite, respectively. The insets represent the same spectra offset vertically for clarity.	77
Figure 6.6.—Elastic lattice strains associated with austenite reflections measured from planes parallel to the loading axis during: (a) heating and (b) cooling, and from planes perpendicular to the loading axis during: (c) heating and (d) cooling. (Error bars are included but generally not visible as they are often less than the symbol size).	79
Figure 6.7.—IPFs for diffracting planes parallel to the loading direction in B19' martensite and B2 austenite during heating. The temperatures at which data were taken are indicated above and the martensite volume fractions, ξ_M , are indicated at the top right hand corner of each IPF. The maximum and minimum intensities are indicated at the top left hand corner in multiples of random distribution.	81
Figure 6.8.—Axial distribution plots for austenite in NiTi during constrained heating for (a) {100} _A and (b) {111} _A . The initial no-load condition at 450 °C is also plotted for comparison. ϕ is the angle between the plane normal and the loading axis.	82
Figure 6.9.—Sections of the normalized neutron diffraction spectra for NiTi austenite acquired at 450 °C before (as-received condition) and during the first and second shape sets for (a) {100} _A and (b) {110} _A reflections. The reflections are from lattice planes parallel to the loading axis.	83
Figure 6.10.—B2 austenite IPFs for diffracting planes parallel to the loading direction at 450 °C (as-received condition) before and during the first and second shape sets. The maximum and minimum intensities are indicated at the top left hand corner in multiples of random distribution.	83
Figure 6.11.—Strain-temperature response of NiTi under constant stress of (a) 200 MPa and (b) 0 MPa before and after shape setting.	84
Figure 6.12.—B19' IPFs for diffracting planes (a) parallel and (b) perpendicular to the loading direction. From top: (i) as-received material, (ii) after the first shape set cycle, (iii) after the second shape set cycle, (iv) after two thermal cycles at 200 MPa and finally (v) after two thermal cycles at 0 MPa. For clarity in presentation, different scales are used in each direction.	85
Figure 7.1.—Schematic of the SMARTS diffractometer experimental setup showing the incident and diffracted beams and scattering vectors (Q). The irradiated volume is shown in green.	91
Figure 7.2.—GSAS Rietveld refinement output for Ni-29.7Ti-20Hf with diffracting lattice planes parallel to the loading axis with no externally applied load. (a) Monoclinic martensite at 35 °C showing a peak attributed to the precipitate phase and (b) NiTiHf cubic austenite at 300 °C. The measured data are indicated by cross-marks and the calculated profile is indicated by the solid line. The tick-marks below the profile pattern indicate the reflections. The lower curve is the difference between the measurement and refinement.	92
Figure 7.3.—Bright field TEM micrograph showing the microstructure of the NiTiHf alloy, consisting of a B19' monoclinic martensite matrix at room temperature with the inset showing in more detail the homogenous distribution of nanometer sized precipitates.	93
Figure 7.4.—Tensile stress-strain response of Ni-29.7Ti-20Hf at room temperature (from extensometry). a) Initial loading response showing the onset of nonlinearity and the stresses at which neutron diffraction spectra were acquired and (b) complete loading and unloading	

curve to 800 MPa, after isobaric thermal cycling, compared to the initial loading response to 400 MPa.	93
Figure 7.5.—Section of normalized neutron diffraction spectra acquired at various stresses during loading to 400 MPa for (a) (011) and (b) (021) monoclinic crystallographic planes. The reflections are from lattice planes parallel to the loading axis. The insets represent the same spectra offset vertically for clarity.	94
Figure 7.6.—B19' martensitic Ni-29.7Ti-20Hf IPFs for diffracting planes (a) parallel and (b) perpendicular to the loading direction in tension at various stress levels. For a given IPF, the stress state is indicated above the IPF and the corresponding maximum and minimum pole intensities (times random) are at the top left hand corner.	95
Figure 7.7.—Lattice strain associated with the (011), (111), (021) and (030) reflections (a) parallel and (b) perpendicular to the applied loading in tension.	96
Figure 7.8.—Strain-temperature response for Ni-29.7Ti-20Hf for the first three thermal cycles at a stress of 400 MPa.	96
Figure 7.9.—IPFs for martensitic Ni-29.7Ti-20Hf determined at room temperature from diffracting planes (a) parallel and (b) perpendicular to the loading direction. From top to bottom the conditions are (i) as-received material (initial no-load), (ii) after initial load to 400 MPa at room temperature, and after the (iii) first thermal cycle, (iv) second thermal cycle (v) and third thermal cycle between room temperature and 300 °C at a stress of 400 MPa. The last IPF (vi) is after the first no-load thermal cycle, post isobaric thermal cycling.	98
Figure 7.10.—Sections of the normalized neutron diffraction spectra for Ni-29.7Ti-20Hf austenite phase acquired at 300 °C during the first no-load thermal cycle and the first, second, and third isobaric thermal cycles at 400 MPa stress: (a) {100} (b) {110} and (c) {111} crystallographic planes. The reflections are from lattice planes parallel to the loading axis.	99
Figure 8.1.—The complete gripping system design for VULCAN diffractometer.	107
Figure 8.2.—Component 1—Platen.	108
Figure 8.3.—Component 2—Platen collar.	108
Figure 8.4.—Component 3—Sample holder.	108
Figure 8.5.—Component 4-6—Jam nut, hex jam nut torque nut.	109
Figure 8.6.—Modified sample geometry for axial- torsional loading.	109
Figure 8.7.—The complete gripping system including part of the VULCAN load train.	110
Figure 8.8.—Equivalent series thermal resistance model for the simplified platen assembly.	111
Figure 8.9.—Temperature distribution along the INCONEL platen plotted for three different heat transfer coefficients with cooling off.	112
Figure 8.10.—Cooling times from four representative initial temperatures with cooling on.	113
Figure 8.11.—Simplified sample and sample holder geometry for torsional analysis.	114
Figure 8.12.—Shear stress and angle of twist results (note the low stress on the sample holder).	114
Figure 8.13.—Strain-temperature response for the first and second thermal cycles at a stress of 100 MPa. The circles indicate where the neutron diffraction spectra were acquired for 10 min at VULCAN diffractometer.	115
Figure 8.14.—VULCAN normalized neutron diffraction spectra acquired during first cycle (transient cycle) continuous heating and cooling between room temperature and 230 °C at a constant stress of 100 MPa. The reflections are from lattice planes (a) parallel and (b) perpendicular to the loading axis.	116
Figure 8.15.—VULCAN projected neutron diffraction spectra acquired during first cycle (transient cycle) continuous heating and cooling between room temperature and 230 °C at a constant stress of 100 MPa. The reflections are from lattice planes (a) parallel and (b) perpendicular to the loading axis.	117

Deformation and Phase Transformation Processes in Polycrystalline NiTi and NiTiHf High Temperature Shape Memory Alloys

Othmane Benafan
National Aeronautics and Space Administration
Glenn Research Center
Cleveland, Ohio 44135

Abstract

The unique ability of shape memory alloys (SMAs) to remember and recover their original shape after large deformation offers vast potential for their integration in advanced engineering applications. SMAs can generate recoverable shape changes of several percent strain even when opposed by large stresses owing to reversible deformation mechanisms such as twinning and stress-induced martensite. For the most part, these alloys have been largely used in the biomedical industry but with limited application in other fields. This limitation arises from the complexities of prevailing microstructural mechanisms that lead to dimensional instabilities during repeated thermomechanical cycling. Most of these mechanisms are still not fully understood, and for the most part unexplored. The objective of this work was to investigate these deformation and transformation mechanisms that operate within the low temperature martensite and high temperature austenite phases, and changes between these two states during thermomechanical cycling. This was accomplished by combined experimental and modeling efforts aided by an in situ neutron diffraction technique at stress and temperature.

The primary focus was to investigate the thermomechanical response of a polycrystalline $\text{Ni}_{49.9}\text{Ti}_{50.1}$ (in at.%) shape memory alloy under uniaxial deformation conditions. Starting with the deformation of the cubic austenitic phase, the microstructural mechanisms responsible for the macroscopic inelastic strains during isothermal loading were investigated over a broad range of conditions. Stress-induced martensite, retained martensite, deformation twinning and slip processes were observed which helped in constructing a deformation map that contained the limits over which each of the identified mechanisms was dominant. Deformation of the monoclinic martensitic phase was also investigated where the microstructural changes (texture, lattice strains, and phase fractions) during room-temperature deformation and subsequent thermal cycling were captured and compared to the bulk macroscopic response of the alloy. This isothermal deformation was found to be a quick and efficient method for creating a strong and stable two-way shape memory effect.

The evolution of inelastic strains with thermomechanical cycling of the same NiTi alloy, as it relates to the alloy stability, was also studied. The role of pre-loading the material in the austenite phase versus the martensite phase as a function of the active deformation modes (deformation processes as revealed in this work) were investigated from a macroscopic and microstructural perspective. The unique contribution from this work was the optimization of the transformation properties (e.g., actuation strain) as a function of deformation levels and pre-loading temperatures. Finally, the process used to set actuators, referred to as shape setting, was investigated while examining the bulk polycrystalline NiTi and the microstructure simultaneously through in situ neutron diffraction at stress and temperature.

Knowledge gained from the binary NiTi study was extended to the investigation of a ternary Ni-rich $\text{Ni}_{50.3}\text{Ti}_{29.7}\text{Hf}_{20}$ (in at.%) for use in high-temperature, high-force actuator applications. This alloy exhibited excellent dimensional stability and high work output that were attributed to a coherent, nanometer size precipitate phase that resulted from an aging treatment.

Finally, work was initiated as part of this dissertation to develop sample environment equipment with multiaxial capabilities at elevated temperatures for the in situ neutron diffraction measurements of shape memory alloys on the VULCAN Diffractometer at Oak Ridge National Laboratory. The developed capability will immediately aid in making rapid multiaxial measurements on shape memory alloys

wherein the texture, strain and phase fraction evolution are followed with changes in temperature and stress.

Nomenclature

A_f	austenite finish
A_s	austenite start
ADP	axial distribution plot
DSC	Differential Scanning Calorimetry
EDM	Electrical Discharge Machining
GRC	NASA Glenn Research Center
GSAS	General Structure Analysis System
HIPPO	HIgh-Pressure Preferred Orientation
HTSMA	High Temperature Shape Memory Alloy
IPF	inverse pole figure
MAUD	Materials Analysis Using Diffraction
M_d	martensite desist
M_f	martensite finish
M_s	martensite start
NASA	National Aeronautics and Space Administration
SE	superelasticity
SMA	shape memory alloy
SMARTS	Spectrometer for Materials Research at Temperature and Stress
SME	shape memory effect
SPF	single peak fitting
TEM	Transmission Electron Microscopy
TWSME	Two-Way Shape Memory Effect

Chapter 1.—Motivation and Organization

1.1 Motivation

Developing viable shape memory alloy (SMA) actuators for both improved properties and reliable, predictable performance, requires a complete understanding of the deformation and transformation behaviors of the alloy, and the interaction of these two complicated sets of properties. However, given that SMAs change crystal structures as the temperature and/or stress changes, typical ex situ experiments such as macroscopic testing followed by microscopy are of limited utility. A more effective way to accomplish this understanding in any definitive manner is to determine the effect of stress and temperature on the mechanical response of the alloy while simultaneously following changes in the alloys' internal state and microstructure.

The work in this dissertation was initiated with the primary purpose of building such a link between the macroscopic deformation response as a function of stress and temperature and the changes in microstructural evolution, internal strains, texture, and volume fraction of phases that occur in binary and ternary shape memory alloys. This was accomplished by carrying out in situ neutron diffraction measurements during selected combinations of heating/cooling and mechanical loading. Diffraction experiments were conducted on the Spectrometer for MAterials Research at Temperature and Stress (SMARTS) and on the High-Pressure Preferred Orientation neutron diffractometer (HIPPO) at Los Alamos National Laboratory (LANL). Compared to conventional x-ray diffraction techniques, neutron diffraction provides greater penetration depths (sampling volumes up to 1 cm³) representing bulk behavior of polycrystalline samples and avoiding free surface stress effects. Furthermore, in spite of the complicated deformation mechanisms associated with SMAs (e.g., twinning, reorientation, stress induced martensite or slip), it is possible to follow the microstructural changes that occur with stress and temperature, since diffraction patterns are simultaneously recorded.

With the preceding motivation, the following objectives were established:

(1) Deformation mechanisms of the austenite phase in binary NiTi: Motivated by the lack of data and improper formulation of many phenomenological constitutive models, deformation and transformation mechanisms of austenitic NiTi were revealed, which are ultimately responsible for the high ductility (exceeding 30 percent) in this intermetallic alloy.

(2) Deformation of martensitic NiTi and its role on the stability of two-way shape memory effect (TWSME): Martensite deformation is probably the simplest but least understood training scheme for inducing the TWSME behavior. The goal was to perform in situ neutron diffraction and ex situ macroscopic testing to investigate the efficacy and stability of TWSME as a function of martensite deformation.

(3) Microstructural evolution with thermomechanical cycling of NiTi: Instability of the macroscopic response during thermomechanical cycling between martensite and austenite phases, particularly the strain evolution, is often attributed to many different mechanisms. The goal was to investigate the changes in the microstructure during cycling under constant stress and relate them to the proper mechanisms.

(4) Shape setting NiTi with simultaneous neutron spectra acquisition: No experiments have been conducted to mimic the shape setting process while examining the microstructure and the macroscopic behavior simultaneously. The goal was to concurrently investigate the micromechanics of this shape setting process that leads to the final, ready to use SMA actuator [1].

(5) Stability of a ternary NiTiHf high temperature SMA: Alloy design can be targeted to avoid certain deteriorating mechanisms (irreversible mechanisms as revealed in this work). The goal was to investigate the role of precipitates on the microstructure and ensuing stability of a NiTiHf high temperature shape memory alloy [2].

(6) Multiaxial loading capability: While all the goals so far were limited to uniaxial loading of SMAs, a new capability was developed which allows for multiaxial (biaxial, combined torsion and

tension/compression loading) in situ measurements at elevated temperatures. This design was developed for the VULCAN engineering diffractometer at Oak Ridge National Laboratories-Spallation Neutron Source (ORNL-SNS).

Outcomes of this dissertation serve as an important guideline for SMA actuator design, optimization, and material behavior modeling, which will enable the maturation of SMA technologies in engineering applications with optimum thermomechanical performance.

1.2 Organization

The work in this dissertation is organized as follows:

Chapter 2 presents a brief introduction to shape memory alloys, their functional behaviors and advantages in design; followed by a brief introduction to neutron diffraction technique and data analysis.

Chapter 3 describes the deformation and transformation behaviors of a cubic, austenitic, polycrystalline NiTi shape memory alloy. Both experimental (macroscopic and microscopic) and modeling efforts used to reveal the deformation mechanisms are discussed.

Chapter 4 discusses the deformation behavior of a monoclinic, martensitic, polycrystalline NiTi shape memory alloy. Combined macroscopic experiments and neutron diffraction measurements are presented. The role of the martensite deformation on the training behavior of two-way shape memory effect is also outlined.

Chapter 5 addresses the thermomechanical cycling of the same NiTi shape memory alloy investigated using neutron diffraction.

Chapter 6 discusses the shape setting procedures of the NiTi shape memory alloy presented in the previous chapters for actuation application. Simultaneous examination of the microstructure through in situ neutron diffraction and the macroscopic deformation are discussed.

Chapter 7 addresses the micromechanical and microstructural behaviors of a high temperature NiTiHf alloy tested in isothermal and isobaric conditions. Differences between this alloy and the alloy studied in the previous chapters are outlined.

Chapter 8 introduces a newly developed capability that will allow for multiaxial in situ neutron diffraction measurements at elevated temperatures at Oak Ridge National Laboratory.

Chapter 9 presents a summary and conclusions. More detailed conclusions are included at the end of each chapter.

Due to the stand-alone nature of each of these chapters, a more detailed literature review has been done relevant to each topic addressed in the respective chapters.

Chapter 2.—Introduction

This chapter briefly introduces shape memory alloys and their associated behaviors, i.e., shape memory effect and superelasticity, and provides some advantages of designing with shape memory alloys. The second section introduces the neutron diffraction technique, the neutron diffractometers used in this work and tools for data analysis.

2.1 Introduction to Shape Memory Alloys

Shape memory alloys (SMAs) are a unique group of materials that have the ability to change their properties, structures and functions in response to thermal, mechanical and/or magnetic stimuli. This ability is a product of a solid-to-solid, martensitic phase transformation between a high temperature, high symmetry austenite phase (generally cubic) and a lower temperature, low symmetry martensite phase (e.g., monoclinic, tetragonal or orthorhombic). Unlike diffusional solid state transformations which require atomic migration over relatively long distances, this martensitic transformation is diffusionless and occurs in a cooperative movement of atoms (generally less than the interatomic distances) that rearrange into a new crystal structure. Through this cooperative movement, atoms maintain a relationship, called lattice correspondence, between the parent austenite phase and the martensite phase lattices. In a crystallographic context, when SMAs transform from austenite to martensite, they do so through mainly a two-step process consisting of a lattice deformation (Bain strain) and a lattice invariant shear (accommodation mechanism). The Bain strain (after Edgar C. Bain [3]) refers to the lattice-distortive strains resulting from the atomic movements and shuffles needed to transform one Bravais lattice into another. The lattice invariant shear refers to the mechanisms that accommodate the shape change due to atomic shear such as irreversible slip or reversible twinning, where the latter is the dominant process in SMAs.

Consequences of this phase transformation are two useful behaviors known as the shape memory effect (temperature-induced phase transformation) and superelasticity (stress-induced phase transformation). Both behaviors have been widely exploited in a range of applications including aerospace [4, 5], biomedical and industrial applications [6]. A short summary of these two useful behaviors is presented next.

2.1.1 Shape Memory Effect

The shape memory effect (SME) is a phenomenon where large deformation of the martensite phase is recovered when heating the material through the forward martensite-to-austenite transformation. This behavior is illustrated schematically in the stress-strain temperature space of Figure 2.1. In the absence of external loads, the material initially in the austenitic phase transforms to martensite variants when cooled ($0 \rightarrow 1$). These variants, also known as lattice correspondence variants, form with enough orientations as to accommodate the local strains and produce nearly no macroscopic shape change. This transformation process is known as the self-accommodation. When applying a load to what is now a twinned martensitic material ($1 \rightarrow 2$), the deformation is accommodated by rearranging the variants to form a new structure. This occurs through mainly two inelastic deformation-producing recoverable mechanisms, i.e., reorientation and detwinning. Under the effect of the externally applied load, some martensite variants convert to new orientations energetically favored (reorientation), while other favorably oriented variants grow at the expense of less favored ones (detwinning), resulting in a macroscopic shape change. Once unloaded ($2 \rightarrow 3$), the deformed material sustains considerable remnant inelastic strains after some amount of elastic springback. The recovery of the apparent macroscopically permanent deformation is accomplished by heating above a characteristic transformation temperature ($3 \rightarrow 0$) causing any form of martensite variants to regress back to the original unique austenite structure [7]. The essential condition for this complete recovery is the crystallographic reversibility of the martensitic transformation that generally does not include irreversible mechanisms such as slip.

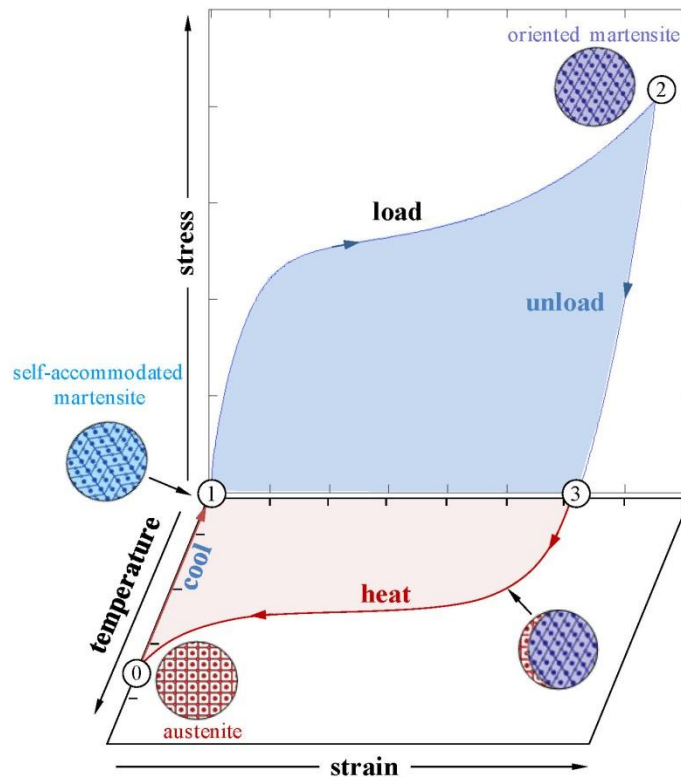


Figure 2.1.—Stress-strain-temperature response of a typical NiTi shape memory alloy. (0→1) Austenite transformation to self-accommodated martensite, (1→2) reorientation and detwinning region, (2→3) nonlinear unloading and finally (3→0) transformation to the austenite phase after heating with the concomitant strain recovery.

In most cases where the SME is employed in actuation applications, a biasing force is used to complete the actuation cycle, since only the original austenitic shape is remembered. In such a case, the SMA can do mechanical work during the phase transformation. A characteristic strain-temperature response during cycling of SMAs under a constant load is shown in Figure 2.2. This constant stress thermal cycling experiments (also known as a load-biased test) are used to determine actuation specific properties including transformation strain, work output, residual strain, transformation temperatures and hysteresis. There are four characteristic temperatures associated with the phase transformation. On the initial heating portion, martensite starts to transform to austenite at the austenite start temperature (A_s) and completes transformation at the austenite finish temperature (A_f). Similarly, during cooling, the forward transformation initiates at the martensitic start temperature (M_s) and finishes at the martensitic finish temperature (M_f). These temperatures are typically measured using the tangent-intercept method as described in the ASTM standard [8]. The transformation strain, a measure of the work output of the material, is calculated as the difference in axial strain measured by the intersection points for the heating portion of the thermal cycle. The residual strain, a measure of the dimensional stability, is determined by measuring the strain difference between the beginning and end of the thermal cycle, either at the low or high temperature side. In an ideal case, this residual strain would be zero, and the actuator would return to the same position in each cycle. Finally, the hysteresis can also be measured by taking the temperature difference between the forward and reverse transformation.

2.1.2 Superelasticity

While the strain recovery in the shape memory effect is thermally induced, in superelasticity (SE), strains are generated and recovered mechanically through a reversible stress-induced transformation. The superelastic behavior occurs when deforming some SMAs at temperatures above A_f as shown in Figure 2.3.

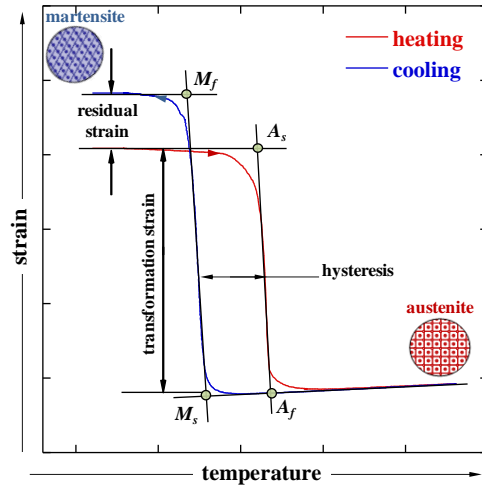


Figure 2.2.—Thermally induced phase transformation curve showing transformation specific properties.

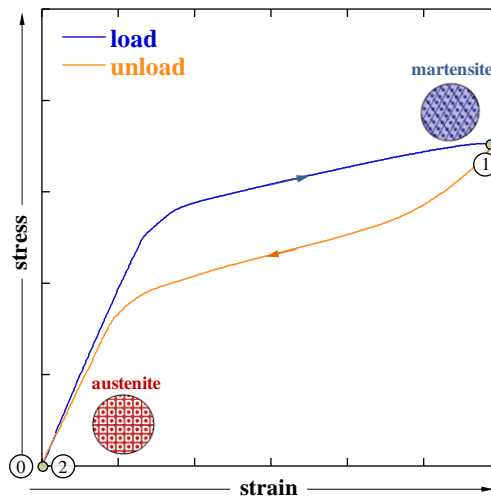


Figure 2.3.—Superelastic effect showing strain recovery at a constant temperature.

In such a case, when the material in the austenitic state is isothermally deformed beyond the elastic limit (0→1), stress-induced martensite variant(s) form to accommodate the deformation. The generated strains, which can exceed 8 percent in some alloys, can be completely recovered upon stress removal (1→2). At a critical stress during unloading, the martensite is no longer thermodynamically stable and reverts back to austenite. This isothermal superelastic response is used in many applications that require large recoverable strains; for example, eyeglass frames, seals, couplings, stents and more [9].

2.1.3 Design With Shape Memory Alloys

Shape memory alloys provide new solutions and alternatives for the development of advanced engineering structures for aeronautic, automotive, bio-medical and other applications. SMA-based technologies can integrate sensing, control and actuation functions in a single entity, which significantly reduces design complexities and most importantly reduces total weight and size of the total system. In addition, SMAs provide many other advantages such as high power/weight and stroke length/weight ratios, smooth movement, and clean, frictionless, spark-free operation. Designing and engineering with SMAs, however, requires a new approach and design paradigm [10]. Testing, modeling and processing methodologies of shape memory alloys need to consider the dynamic responses due to changing external

and internal stimuli. As a result, new design methodologies and standards are needed to engineer high performance and reliable SMA components. To date, only six ASTM standards exist (ASTM F2004-05, F2005-05, F2063-05, F2082-06, F2516-07 and F2633-07) that focus on superelastic behavior. A better understanding of the transformation and deformation mechanisms of SMAs, which is the goal of the present work, may lead to additional standards and methodologies to efficiently and accurately design with SMAs.

2.2 Introduction to Neutron Diffraction

Neutron diffraction is a nondestructive experimental technique used worldwide to study materials and their potentials in diverse fields and applications. Neutrons, discovered by J. Chadwick in 1932, are atomic particles of no net electric charge with a mass of 1.67×10^{-24} g. Since there is no electrostatic interaction with the electron cloud of the atom, neutrons interact with atoms (nuclei) by a very short-range (few fermis= 10^{-15} m) nuclear forces rather than electrical forces such as the case of electrons. Such interaction allows neutrons to penetrate deeper (in the order of ~cm compared to $\sim 10^{-5}$ m in conventional x-rays) into most materials allowing the study of bulk properties. Neutron beams are typically produced in nuclear fission reactors or in high energy particle accelerators (spallation sources). Nuclear reactors produce continuous neutron fluxes by the fissioning of atoms in the reactor with uranium core. These neutrons are normally formed with high energies (e.g., ~MeV) which are then moderated to the required energy and wavelength (~meV range) for use in scattering experiments without damaging the material under test. In this stage, neutrons are brought in thermal equilibrium via a series of collisions with atoms of the moderator material, typically light atoms such as hydrogen, water or graphite, to form what is known as the *thermal neutrons*. The moderated neutrons with a specific wavelength bandwidth are then selected by Bragg scattering from a highly reflective monochromator crystal (e.g., copper, germanium), which results in what is known as a monochromatic beam.

In a spallation source, neutron pulses are produced by the collision of high energy, accelerated protons with a heavy metal target (e.g., tungsten, uranium). Neutrons are moderated in a similar approach, and in contrary to monochromatic beam, all neutrons with a wide energy band can be used in spallation sources to produce a polychromatic, white beam. Neutrons are then guided to the experimental area in tubes or neutron guides. For diffraction measurements in spallation sources, neutron detectors, with fixed diffraction angle, record both the neutron count and arrival time, which is used to determine the precise wavelength. This measurement method is called time-of-flight diffraction. Further details of neutrons and neutron sciences can be found in Refs. [11, 12].

2.1.1 Neutron Diffraction at Los Alamos National Laboratory

In this dissertation, neutron diffraction experiments were performed at the Lujan Neutron Scattering Center at Los Alamos National Laboratory, New Mexico. The Lujan neutron scattering center employs a pulsed spallation neutron source based on time-of-flight diffraction. The instruments used are discussed below.

2.2.1.1 Spectrometer for Materials Research at Temperature and Stress (SMARTS)

The SMARTS (Figure 2.4) is a third-generation neutron diffractometer that employs a polychromatic beam optimized for the study of engineering materials under stress (up to 2 GPa) and extreme temperatures (-183 to 1500 °C) [13]. A schematic of the experimental setup with incident and diffracted neutron beams and scattering vectors is shown in Figure 2.5. The incident neutron beam impinges on a sample with the loading axis positioned at 45° relative to the beam, and scatters in all directions. Two detectors containing ^{196}He tubes are positioned on either side of the incident beam at $\pm 90^\circ$ at a distance of 1.5 m from the sample. These detectors record scattered neutron data simultaneously with diffraction vectors parallel (Q_{\parallel} , -90°) and perpendicular (Q_{\perp} , $+90^\circ$) to the loading axis with an effective d-spacing range of ~ 0.5 to 3.5 Å. This detector setup allows for measurements from lattice planes parallel and perpendicular to the loading axis. Samples are loaded in uniaxial tension or compression using on a servohydraulic load frame with load and position measurement capability. Macroscopic strains are obtained concomitantly while recording neutron data using a high-temperature, 10 mm gauge length extensometer attached to the sample.

Heating is controlled using a 5 kW induction heater and a temperature controller interfaced with LabVIEW (National Instruments Corporation). The induction coils were designed to minimize clipping of the incident and diffracted beams while allowing for a neutron line of sight. Cooling is achieved from natural convection and conduction through the water cooled grips and pull rods.

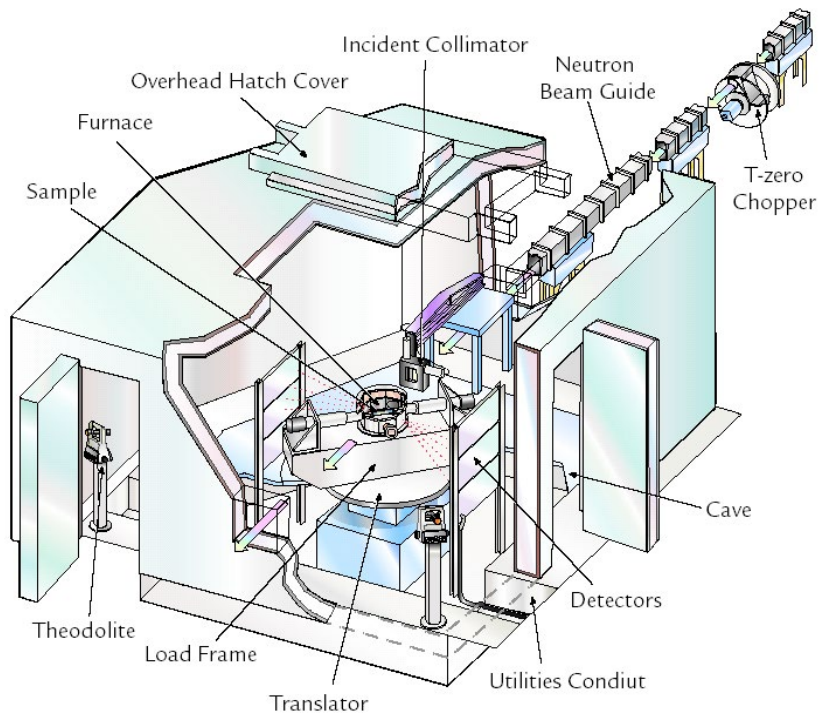


Figure 2.4.—Cutaway schematic of SMARTS diffractometer showing the beam path, sample environment and detector arrangements [13]. (Reproduced with permission from LANL).

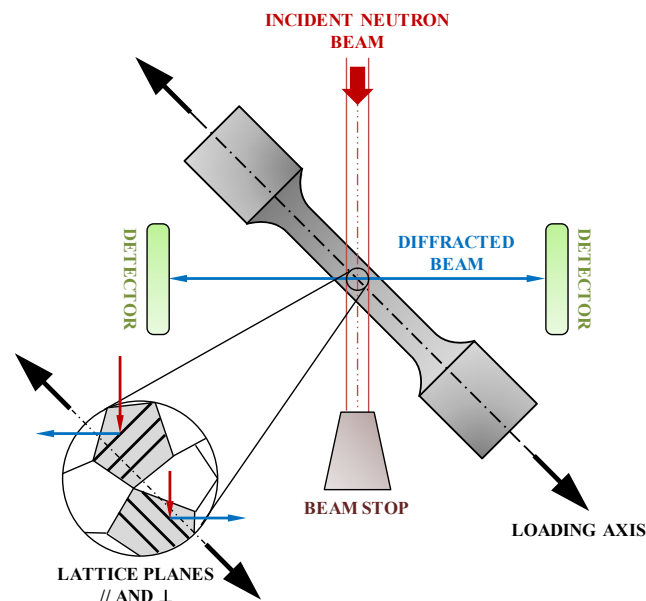


Figure 2.5.—Schematic of the SMARTS diffractometer experimental setup showing the incident and diffracted beams. The perpendicular and parallel lattice planes are shown.

2.2.1.2 High-Pressure-Preferred Orientation (HIPPO)

HIPPO neutron diffractometer, also based on the TOF technique, consists of a sample chamber surrounded by five conical rings of 1360 ^3He detector tubes positioned in panels of 150°, 90°, 40°, 20° and 10° diffraction angles around the incident beam with a d-spacing range of 0.12 to 47.5 Å (Figure 2.6) [14, 15]. This diffractometer attains high neutron count rates due to a short initial flight path of 9 m. The instrument is also equipped with a custom-built 100 kN uniaxial load frame for tension and compression loading, and a 1800 °C furnace for high temperature measurements. For the most part, this instrument was used for bulk texture measurements using a total of 30 detector panels of diffraction angles 150°, 90° and 40°.

2.1.2 Neutron Data Analysis

Neutron diffraction data are analyzed using the Rietveld method implemented in the LANL codes General Structure Analysis System (GSAS) [16, 17] and Materials Analysis Using Diffraction (MAUD) [18, 19]. Both codes are based on a least-squares scheme that minimizes the difference between the observed (measured) diffraction pattern and the calculated pattern [20, 21]. Refinements of the entire spectrum are made by varying the crystal structure, background, lattice shifts, absorption, phase fractions, scale factors, and texture until the difference is minimized to within an acceptable range. The calculated intensity, Y_{ci} , can be determined at every point in the spectrum, and is given by:

$$Y_{ci} = Y_{bi} + s \sum_k L_k |F_k|^2 \phi(2\theta_i - 2\theta_k) P_k A \quad (2.1)$$

where Y_{bi} is background intensity and the second term on the right hand side is the Bragg scattering containing a scale factor s , a Lorentz factor L_k , a structure factor F_k , a reflection profile function ϕ , the observed Bragg peak position $2\theta_i$, the corrected calculated Bragg peak position $2\theta_k$, a preferred orientation P_k , and an absorption factor A . A typical output of the refined spectra is shown in Figure 2.7. From this refined spectra, data such as phase fractions, crystal structure parameters, strains and crystal orientation distribution (texture) are obtained.

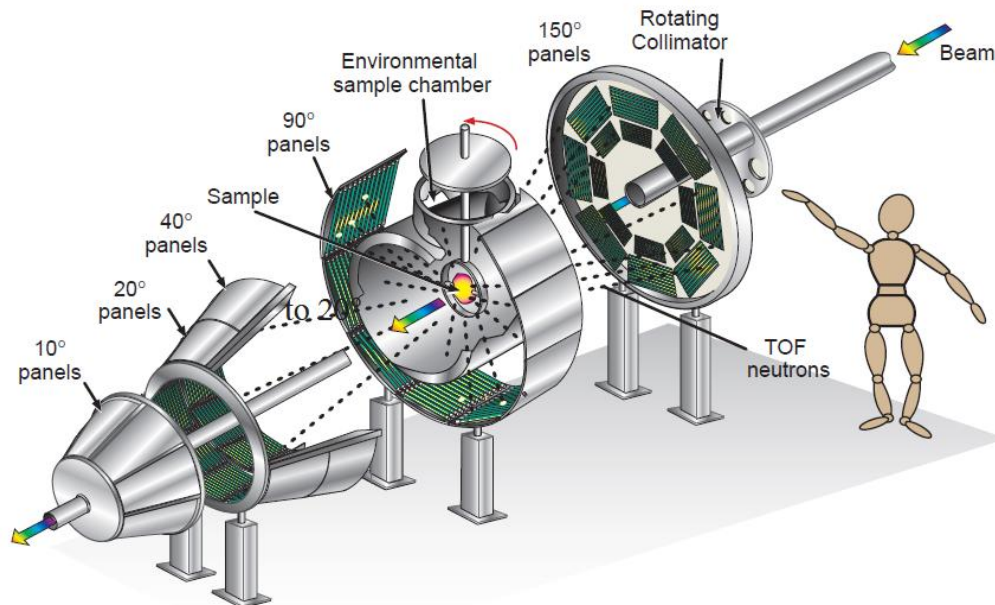


Figure 2.6.—Schematic of HIPPO showing the beam path, sample environment and the arrangement of detector tubes in panels arranged on rings of constant diffraction angle [14]. (Reproduced with permission from LANL.)

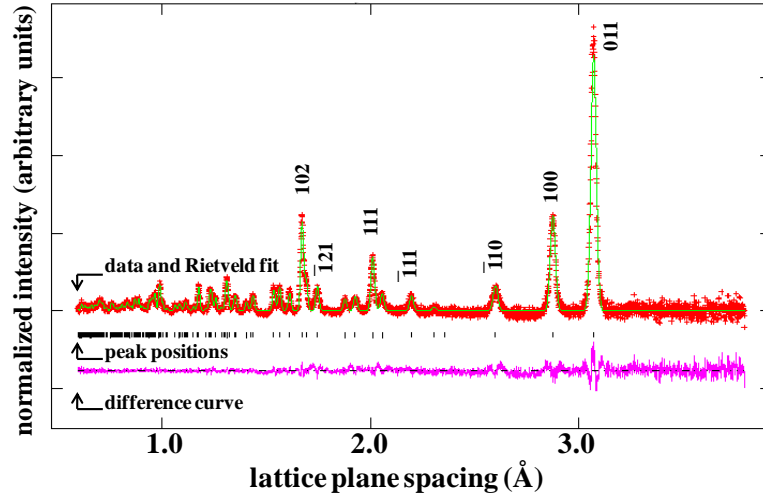


Figure 2.7.—Example of GSAS Rietveld refinement for NiTi. The measured data are indicated by cross-marks and the calculated profile is indicated by the solid line. The tick-marks below the profile pattern indicate the reflections. The lower curve is the difference between the measurement and refinement.

Crystal orientation distribution (crystallographic texture) is analyzed using an 8th order spherical harmonic description implemented in the Rietveld refinement codes. One of the methods used to describe the texture evolution is by evaluating the texture index [22] given by

$$J = \oint [f(g)]^2 dg \quad (2.2)$$

where $f(g)$ is the orientation distribution function that maps the probability of each of the possible grain orientations with respect to the external sample dimensions and the integration is over all orientation space. Alternatively, texture is also captured by the inverse pole figures (IPFs). These IPFs describe the distribution of specific macroscopic directions, e.g., the loading axis, in the coordinate systems of the individual crystallites composing the polycrystal, in multiples of random distribution (one corresponding to a random distribution). IPFs are generated using generic mapping tools after performing a Rietveld refinement from single data histograms. Furthermore, for symmetric cylindrical samples, the actual texture distribution can be obtained from the axial distribution plots (ADPs). These plots represent a radial slice of the pole figure of a specific variant. The angles $\phi=0^\circ$ and $\phi=90^\circ$ of the x-axis represent planes parallel and perpendicular to the loading direction, respectively, whereas the y-axis is a measure of the number of grains that are oriented at an angle ϕ between the normal to the chosen plane and the loading axis. The orientation distribution functions (ODFs) are reconstructed from the measured HIPPO histograms, and the pole figures (PFs) of lattice planes (hkl) are generated. Analogous to the IPFs, the PFs are a graphical representation of the orientation of the crystal coordinate system in the specimen coordinate system.

Lattice strains, integrated intensities and peak breadths are evaluated for specific grain orientations along the corresponding lattice directions. The hkl -specific lattice strains are obtained from the interplanar spacings ($\Delta d_{hkl}/d_{hkl}$) using a single peak fitting method. In general, the lattice strain ϵ_{hkl} is related to the change of interplanar distance d^{hkl} by:

$$\epsilon_{hkl} = \frac{d^{hkl} - d_0^{hkl}}{d_0^{hkl}} \quad (2.3)$$

where d_0^{hkl} is the strain free or reference spacing. Strains from the individual histograms can be evaluated for the most intense peaks identified in Figure 2.7. Plane specific elastic moduli are obtained using Hooke's law from the measured strains. In addition to measurements of shifts in Bragg diffraction peak positions (strains), single peak fits are also used to follow the individual peak shape change or peak broadening. Peak broadening is an indication of the presence of elastic anisotropy, size effects and lattice defects that can originate from particle size, twinning, microstresses, local strain incompatibilities, grain boundaries and instrumental broadening among others [23].

Chapter 3.—Temperature Dependent Deformation of B2 Austenite in a NiTi Shape Memory Alloy

The objective of this chapter was to determine the mechanisms responsible for the macroscopic inelastic strains during isothermal loading of NiTi to 18 percent strain at temperatures above A_f . This study included in situ time-of-flight (TOF) neutron diffraction experiments used to follow the evolution of the lattice strains, texture, and phase fractions during deformation, ex situ macroscopic tensile experiments, hot stage transmission electron microscopy (TEM), and predictions from a self-consistent polycrystalline deformation model based upon grain-level dislocation plasticity. It was found that stress-induced martensite formed at temperatures up to 310 °C, which is well above the stress-free A_f of 105 °C. However, the stress induced martensite formed concurrently with general slip processes and twinning, and did not occur as a separate distinguishable mechanism. Above M_d , the deformation was governed by slip and deformation twinning, in addition to diffusion-assisted deformation processes. The occurrence of $\{114\}_{B2}$ compound deformation twins, confirmed by TEM, along with $\langle 001 \rangle$ slip processes was necessary to explain changes in texture during deformation of the B2 phase as predicted by the self-consistent polycrystalline model. However the model could not explain the observed evolution in internal strains, because of an inability to account for recovery processes. The overall results were combined to generate a deformation map that contains the limits over which each of the identified deformation mechanisms is dominant in this $\text{Ni}_{49.9}\text{Ti}_{50.1}$ alloy.

3.1 Introduction

Shape memory alloys (SMAs) are a unique class of multifunctional materials that exhibit useful behaviors by virtue of a crystallographically reversible martensitic phase transformation between a high symmetry parent austenite phase and a low symmetry martensite phase. Two of these behaviors are the shape memory effect and superelasticity. The former is associated with a thermally-induced phase transformation and refers to the alloy's ability to recover large deformations when heated above the reverse transformation finish temperature (A_f). Superelasticity is a stress-induced phase transformation where deformation and recovery are obtained during loading and unloading, respectively, at temperatures above A_f [24, 25]. Among a long list of alloys exhibiting these behaviors, equiatomic polycrystalline NiTi is of particular interest due to its large transformation strains and commercial availability.

Binary NiTi, with a cubic (B2) to monoclinic (B19') transition, has been shown to exhibit superelastic behavior with complete or partial strain recovery [26-28]. The reversible strains are attributed to elastic deformation and stress-induced martensite (SIM), while the irreversible mechanisms are usually attributed to plastic deformation, the formation of retained martensite, and deformation twinning. At and above the M_d temperature, where no stress-induced martensite can form, binary NiTi still exhibits high ductility (exceeding 30 percent), which is unusual for a B2 intermetallic [29]. Above this M_d , where the martensite formation does not contribute to the generated strain, $\langle 100 \rangle$ type slip is commonly reported in this, as well as in many other B2 intermetallics [30, 31]. This provides only three independent slip systems and therefore cannot accommodate all the strains for generalized polycrystalline plasticity since at least five independent deformation mechanisms are required for compatible plastic deformation [32, 33]. However, additional processes such as twinning [34-36] or climb of $\langle 100 \rangle$ dislocations [37] can provide a sufficient number of independent mechanisms to satisfy generalized plasticity of a polycrystalline material. Thus, identification and understanding of the role of various processes contributing to the overall deformation response of NiTi, along with a complete mapping of the B2 deformation space is imperative to understanding and maturing SMA-enabled technologies.

Over the years, a number of investigations have attempted to clarify the nature and significance of each mechanism to the total strain generation in NiTi alloys. B2 austenite thermal strains were determined for isolated austenite grains through the coefficient of thermal expansion tensor during heating and cooling [38, 39]. The elastic strains were also captured through the elastic stiffness tensor using ultrasonic measurements [40, 41], *ab initio* calculations [42], and in situ neutron diffraction [43]. Investigation of

strains due to stress-induced martensite has been an active area of research for many years [26, 44-54]. Often, the formation of stabilized martensite was observed to be fully reversible. However, in cases where not all the strains are recovered upon unloading, it is unclear as to how much of the accumulated strain is due to the concurrent generation of irreversible deformation processes and how much is due to the stress-induced martensitic transformation not being fully reversed on unloading. Furthermore, it would be expected that both processes are ultimately related in some fashion.

A number of studies have begun to address the issue of inelastic deformation mechanisms in NiTi SMAs. Delville et al. [55] reported observation of $\langle 100 \rangle \{011\}$ dislocations in cold worked and annealed 100 μm diameter NiTi wires. They also showed experimental evidence of $\{114\}_{\text{B2}}$ compound austenite twinning, as previously reported by Li et al. [56]. Goo et al. [57] and Moberly et al. [35] attributed the ductility in B2 austenite to the increase in independent deformation mechanisms due to the addition of $\{112\}_{\text{B2}}$ pseudo and $\{114\}_{\text{B2}}$ mechanical twinning systems. Nishida et al. [36] reported formation of planar defects with a twin relation dominated by $\{114\}_{\text{B2}}$ compound twins. Similar mechanical twins were observed in Ni-47Ti-3Fe by Moberly et al. [58] during deformation by swaging, but the majority of the deformation was attributed to $\langle 100 \rangle$ dislocation motion. Twinning, in addition to dislocation slip, was also reported by Karaman et al. [59] to be a major mode of deformation at high temperatures involving plastic deformation of stress-induced martensite. A recent study by Ezaz et al. [60, 61] established the energetics of (114) and (-211) twinning in B2 NiTi by a coupled shear and shuffle mechanism, which highlighted the contribution of these two mechanisms to the B2 deformation.

Slip dislocations have also been observed in many similar alloys under different loading conditions. Using single crystals, Chumlyakov et al. [62] identified the dominant slip systems in B2 NiTi to be $\langle 100 \rangle \{001\}$ and $\langle 100 \rangle \{011\}$. A STEM study on micro-pillars of solutionized 50.7Ni-Ti by Norfleet et al. [63] revealed $\langle 010 \rangle \{101\}$ dislocation loops in [110] oriented pillars deformed in compression. It was reported in the same study that dislocation slip accompanies the propagation of the austenite/martensite interface on the local level of individual habit planes. Similarly, $\langle 100 \rangle \{011\}$ dislocation loops were observed in [100] oriented 50.4Ni-Ti single crystals that were thermally cycled [40]. During thermomechanical cycling, Pelton [64] reported observations of dislocation bands (parallel to the martensite-austenite interface) and an increase with cycling in the dislocation density of the type a $\langle 100 \rangle$ with $\{011\}$ slip planes. In addition, TEM studies by Gall et al. [65, 66] and Hurley et al. [67] have shown slip dislocations in deformed superelastic NiTi that contribute to the total accumulated strains.

Gall et al. [65] also performed a study on single crystal NiTi where they observed a combination of elastic behavior, plastic deformation, and the formation of stress-induced martensite. They reported that $\langle 100 \rangle \{001\}$ and $\langle 100 \rangle \{011\}$ families of slip systems and the stress-induced martensitic transformation govern the deformation response depending on the crystal orientations. Residual strains during cycling of superelastic NiTi were also attributed to plastic deformation and/or retained martensite by a number of other investigators [68-70]. Although a number of studies have reported on the residual strains and irreversible deformation mechanisms in NiTi alloys, there is still no direct link between microscopic deformation mechanisms and the ensuing macroscopic material response. As a result, the amount and contribution of reversible and irreversible strains to the total deformation response of B2 austenite is still unclear. Likewise, given all of these studies, it is somewhat surprising that the M_d temperature has not been adequately determined for binary NiTi.

One way of providing such quantitative correlation is by using advanced characterization tools such as in situ neutron or synchrotron x-ray diffraction. These techniques are advantageous in that they penetrate several millimeters into most materials, and represent the average microstructural response of the bulk polycrystalline sample. They provide unique means of following the lattice strains, texture, and phase fraction evolution during deformation. Both neutron [26, 28, 71-73] and synchrotron x-ray [49, 73-75] diffraction have been used to study austenitic NiTi. These studies not only serve to provide a link between microscopic and macroscopic behavior, but the much needed experimental data also can supply information pertinent to the proper formulation of internal state variables for phenomenological constitutive models [76-81]. For accurate predictions of the material response, SMA models must consider several key factors such as material history (thermomechanical processing, heat treatments, and previous deformations), evolutionary

parameters (texture, internal stresses, and phase fractions) and rates and temperature dependence of key deformation processes. In many cases, the models need to consider many of these factors at the same time; however, experimental data on most of these factors is scarce or non-existent.

With this in mind, the objective of this work was to examine the temperature dependent deformation of B2 austenitic NiTi using in situ time-of-flight (TOF) neutron diffraction. The goal was to provide insights into the reversible and irreversible strain contributions to the overall macroscopic material deformation response during isothermal loading above A_f . Emphasis was placed on identifying contributions to these strains from reversible stress-induced martensite and irreversible retained martensite, slip, and deformation twinning. Both experimental and computational methods were considered in determining the active mechanisms. Experimental efforts were aimed at capturing changes in diffraction peak intensities, peak breadths, interplanar spacings, and phase volume fractions while loading isothermally at multiple temperatures. In addition, complete preferred orientations were also measured ex situ to capture texture developments. Post-deformed samples were also examined at room and high temperatures using transmission electron microscopy (TEM). Finally, a self-consistent polycrystalline deformation model [82], based upon grain-level dislocation plasticity, was used in an effort to predict both the micromechanical and macroscopic responses as a function of slip or twin systems. Using this tool, internal strains, texture evolution and macroscopic responses were predicted and compared to the measured data in an attempt to determine the active deformation mechanisms.

3.2 Experimental Techniques

3.2.1 Material

Polycrystalline $\text{Ni}_{49.9}\text{Ti}_{50.1}$ (at.%) samples were obtained from a hot-rolled/hot-drawn and hot-straightened 10 mm rod produced by Special Metals, New Hartford, New York. Cylindrical tensile specimens 5.08 mm in diameter and 15.24 mm in gauge length were machined from the hot-rolled stock, and subjected to two no-load thermal cycles between room temperature and 200 °C in a muffle furnace in air. The no-load thermal cycles help relieve any internal stresses generated during sample machining, resulting in a self-accommodated martensite structure. Stress-free transformation temperatures: martensite start (M_s), martensite finish (M_f), austenite start (A_s) and austenite finish (A_f) were measured from the second mechanical no-load thermal cycle using the intercept method [83] and were found to be 71, 55, 92, and 105 ± 2 °C, respectively.

The $\text{Ni}_{49.9}\text{Ti}_{50.1}$ alloy was intentionally selected for this study because it is representative of a “high-temperature” binary alloy and because it does not display a strong, “flag-like” superelastic response (Figure 3.1), so that both reversible and irreversible transformation/deformation mechanisms could be simultaneously investigated.

3.2.2 Neutron Diffraction Experiments

All neutron diffraction experiments were performed at Los Alamos neutron spallation (pulsed) source, Los Alamos National Laboratory, New Mexico.

In situ neutron diffraction experiments were carried out on the Spectrometer for MAterials Research at Temperature and Stress (SMARTS) [13]. A total of four samples were tested in situ, each at a different temperature above the A_f . The temperatures selected were 165, 230, 290 and 320 °C, which were respectively 60, 125, 185 and 215 °C above the A_f . Before heating an individual specimen, neutron spectra were acquired at room temperature and used as a baseline starting martensite microstructure. The specimen was then heated under zero stress to the desired temperature at a rate of 30 °C/min, with neutron data acquired at the test temperature of interest before loading. Heating was controlled using a 5 kW induction system with temperatures measured via type K thermocouples attached to the specimens. Once the test temperature was reached, the specimen was isothermally loaded in uniaxial tension to 18 percent under strain control at a rate of $1 \times 10^{-4} \text{ s}^{-1}$ (using a high-temperature, 10 mm gauge length extensometer). Neutron diffraction spectra were acquired at incremental strains (at least 10 strain data points between 0 and 18 percent) during loading, as

shown in Table 3.1. Once unloaded, additional spectra were collected prior to any subsequent procedures. Post deformation, the specimen was heated to 500 °C and cooled to room temperature (Table 3.1). The specimen was held at various points during this heating and cooling cycle (for 30 min to collect neutron diffraction spectra) to ascertain any changes occurring in the underlying microstructure. This 30 min hold time was necessary to ensure adequate statistical quality of the neutron spectra.

Following the in situ measurements, the samples were analyzed ex situ on the High-Pressure Preferred Orientation neutron diffractometer (HIPPO) [14, 15]. Texture and orientation distribution data were measured for the same four samples used in the SMARTS experiments and for a baseline virgin sample at 200 °C (Table 3.1). Heating was accomplished using a high temperature furnace equipped with niobium heating elements and heat shields.

TABLE 3.1.—EXPERIMENTAL TEST CONDITIONS (TEMPERATURE AND STRAIN) UNDER WHICH NEUTRON DATA WERE ACQUIRED IN SMARTS AND HIPPO FOR SPECIMENS 1 TO 5. THE ‘x’ INDICATES CONDITIONS WHERE NEUTRON DATA WERE OBTAINED.

In situ (SMARTS)																								Ex situ (HIPPO)	
Specimen	Initial temperature, T °C					Loading/unloading, ϵ %													Post heating, T °C						T °C
	30	165	230	290	320	0.5	0.8	1	2	4	6	8	10	12	14	16	18	Unload	300	400	500	T_i	30	T_f	200
1	x	x				x	x	x	x	x	x	x	x	x	x	x	x	x	x	x	x		x	165	x
2	x		x			x	x		x	x		x		x		x	x	x	x	x	x	230	x	230	x
3	x			x		x	x	x	x	x	x	x	x	x	x	x	x	x		x	x	290	x	290	x
4	x				x	x	x		x	x		x		x		x	x	x		x	x	320	x	320	x
5	Undeformed sample																							x	

(T_i and T_f are the initial and final temperatures, respectively, where neutron diffraction data were acquired during post-deformation thermal cycling of the samples.)

3.2.3 Transmission Electron Microscopy

Transmission electron microscopy was accomplished using a FEI CM200 microscope. Samples for TEM were prepared from the baseline virgin sample in the as-received condition, and from samples deformed ex situ to 18 percent strain at 165 and 320 °C to mimic specimens 1 and 4 of Table 3.1. Disks of ~500 µm thickness were sectioned from a 3 mm diameter cylinder that was electro-discharge machined from the gauge section of each of the three samples. These disks were mechanically ground to ~130 µm thickness, and then electro-polished using a solution of 20 percent sulfuric acid and 80 percent methanol cooled to 273 K. A Gatan model 628 single tilt heating sample holder was used for the hot-stage analysis. TEM images were collected at room temperature, 165 and 320 °C for all three samples.

3.2.4 Neutron Diffraction Data Analysis

Neutron diffraction data were analyzed using the Rietveld method implemented in the LANL codes General Structure Analysis System (GSAS) [16, 17] and Materials Analysis Using Diffraction (MAUD) [18, 19]. Strains, phase fractions, and texture changes were then obtained from SMARTS refined data. Complete sample textures were measured on HIPPO using a total of 30 detector panels at diffraction angles of 150°, 90° and 40°. The orientation distribution functions (ODFs) were then reconstructed from the measured histograms, and the pole figures (PFs) of lattice planes (hkl) were plotted. In addition, single peak fitting was used to obtain individual (hkl) lattice strains, integrated intensities, and peak widths for the individual samples.

3.3 Self-Consistent Polycrystalline Deformation Model

Deformation of the polycrystalline $\text{Ni}_{49.9}\text{Ti}_{50.1}$ was modeled using the elastoplastic self-consistent (EPSC) polycrystal model described in detail elsewhere [82, 84, 85]. The EPSC is based upon grain-level deformation mechanisms of dislocation plasticity. Each grain in the specimen is modeled as an elastoplastic ellipsoidal inclusion embedded in an elastoplastic anisotropic homogeneous effective medium. The model inputs include

initial texture, slip and/or twinning systems, material's elastic and thermal properties, macroscopic boundary conditions, loading path, and the appropriate hardening law (Table 3.2). In this work, the initial texture that best represents the grain orientations and weights was obtained from the virgin sample measurements on HIPPO at 200 °C, and is based on 2916 grain orientations. The single crystal stiffness constants [41] and the coefficient of thermal expansion [38] that were used in the model are listed in Table 3.2.

TABLE 3.2.—ELASTOPLASTIC SELF-CONSISTENT (EPSC) MODEL INPUTS FOR AUSTENITIC Ni_{49.9}Ti_{50.1}

	Model inputs	Values	Reference
Material, NiTi	Lattice parameters, Å, °	$a = b = c = 3.03$, $\alpha = \beta = \gamma = 90$	Current study
	Elastic stiffness, GPa	$C_{11}=162$, $C_{12}=129$, $C_{44}=35$	[41]
	Thermal expansion, $10^{-6}/^{\circ}\text{C}$	13.0	[38]
Slip systems	1) $\langle 100 \rangle \{001\}$:	[100]/(010) [100]/(001) [010]/(100) [010]/(001) [001]/(100) [001]/(010)	[63]
	2) $\langle 100 \rangle \{110\}$:	[100]/(011) [100]/(01-1) [010]/(101) [010]/(10-1) [001]/(101) [001]/(-110)	[63]
	3) $\langle 111 \rangle \{110\}$:	[11-1]/(011) [11-1]/(101), [11-1]/(1-10) [1-1-1]/(01-1) [1-1-1]/(101) [1-1-1]/(110) [1-11]/(011) [1-11]/(10-1) [1-11]/(110)	—
Twin systems	4) $\langle 22-1 \rangle \{114\}$:	[22-1](114) [-22-1](-114) [2-12](141) [212](1-41) [-12-2](41-1) [-122](411) $s = 0.7071$	[85]
	5) $\langle -1-11 \rangle \{112\}$:	[-1-11](112) [111] (1-21) [11-1] (2-11) $s = 0.7071$	[57]
Initial texture	HIPPO data	2916 grains	Current study

Both the reported slip systems (6 $\langle 100 \rangle \{110\}$ and 6 $\langle 100 \rangle \{001\}$ [63]) and the dominant twin systems experimentally observed in B2 austenite ($\langle 22-1 \rangle \{114\}$ and $\langle -1-11 \rangle \{112\}$ [34-36, 57, 60, 61, 86]) were initially used for model formulation. However, because of certain observations in texture evolution during deformation of the Ni_{49.9}Ti_{50.1}, $\langle 111 \rangle \{110\}$ slip was also investigated in the modeling scheme to determine its effect on properties and the results are also reported. The activated slip and deformation twinning systems in the EPSC model were described through their critical resolved shear stress (CRSS) using the extended Voce hardening law. This approach accounts for the evolution of resolved shear stress, τ^s , of a system, s , with total accumulated shear strain in the grain, Γ , with the form

$$\tau^s(\Gamma) = \tau_0^s + (\tau_1^s + \theta_1^s \Gamma) \left[1 - \exp\left(-\frac{\theta_0^s \Gamma}{\tau_1^s}\right) \right] \quad (3.1)$$

where τ_0^s is the initial CRSS of the system s , $(\tau_0^s + \tau_1^s)$ is the back-extrapolated stress at the origin, θ_0^s is the initial hardening rate, and θ_1^s is the final linear asymptotic slope in the hardening response [87].

This model was implemented to predict the texture after deformation, global and grain level stress-strain evolution, and the peak intensities of the individual (hkl). The modeling conducted as part of this work was not aimed toward predicting the shape memory effect or superelasticity; instead, it was formulated so as to exclude both the stress-induced transformation and retained martensite, in order to decouple the martensite contributions (both retained and stress-induced) from slip and twinning in the B2 phase. Consequently, only the austenite slip and deformation twinning systems were considered.

3.4 Experimental and Modeling Results

3.4.1 Macroscopic Stress-Strain Response for Ni_{49.9}Ti_{50.1}

The macroscopic stress-strain curves for $\text{Ni}_{49.9}\text{Ti}_{50.1}$, during uniaxial tensile loading at different temperatures, are shown in Figure 3.1. These curves were generated in situ during the neutron diffraction experiments, and the stress relaxations on each experimental curve occurred during the 30 min hold periods for diffraction data acquisition. All samples deformed in a macroscopically linear elastic fashion up to ~ 0.5 percent strain, independent of temperature, with a measured Young's modulus of 74 GPa. At higher strains, inelastic deformation was apparent, quickly transitioning into a region of low or even negative work hardening, depending on temperature, until the load was removed from the sample. Interestingly, this region of low work hardening occurred at a slightly lower stress level in the sample deformed at 165 °C than the sample deformed at 230 °C. At temperatures of 290 and 320 °C, the low work hardening region was shifted to lower stress levels and strain softening behavior was observed, especially in the 320 °C sample. It should be noted that no localized deformation or necking was observed in these samples, so that the strain softening was an actual bulk response of the material. Finally, the unloading curves were nonlinear and the recovered strains were larger than expected from purely elastic deformation, which suggests inelastic mechanisms in addition to the elastic strain recovery.

The effect of temperature on the “yield” behavior of the B2 $\text{Ni}_{49.9}\text{Ti}_{50.1}$ is shown in Figure 3.2. These results are from eight individual samples that were deformed ex situ in tension, similar to the in situ samples, but without the holding periods. The test temperatures were 165, 230, 290 and 320 °C (same as the in situ test temperatures of Figure 3.1), with additional testing done at 340, 360, 400 and 440 °C (Figure 3.2(a)). These curves show similar behavior to those in Figure 3.1, demonstrating that the stress relaxations did not affect the basic stress-strain response of the material. From 165 to 290 °C, the onset of inelastic deformation (referred to here as the “yield” stress) and initial flow behavior were very similar regardless of the level of offset used to describe the stress (Figure 3.2(b)). Above 290 °C, the yield stress decreased with increasing temperature, and a clear demarcation in the yield behavior at each temperature was obtained. For clarity, this is shown in Figure 3.2(b), which represents vertical slices through the curves of Figure 3.2(a) at selected strain values from 0.5 to 8 percent. A change in stress dependence with temperature from independent (or slightly increasing) with temperature to a decreasing trend with temperature was evident after passing 290 °C, indicating a critical change in behavior. It is also important to note that each sample was deformed to 18 percent strain without fracture (Figure 3.2(a)) and without localized necking in the gauge section. Finally, the unloading portion of the stress-strain curves tended to be nonlinear at lower temperatures, consistent with Figure 3.1.

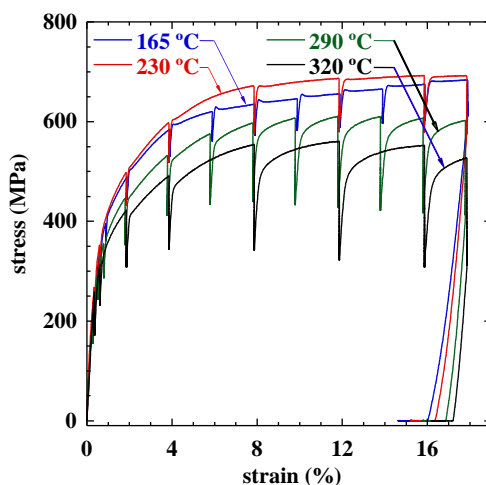


Figure 3.1.—Tensile stress-strain response during in situ neutron diffraction experiments of $\text{Ni}_{49.9}\text{Ti}_{50.1}$ at four different temperatures above A_f . The stress relaxations are due to the 30 min holding periods necessary for neutron data acquisition.

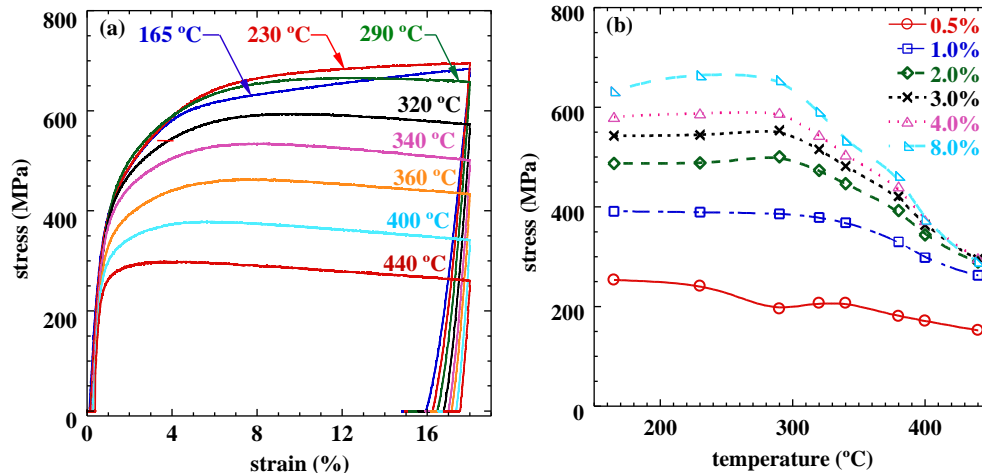


Figure 3.2.—Monotonic tensile data for $\text{Ni}_{49.9}\text{Ti}_{50.1}$ as a function of temperature. (a) Stress-strain curves for samples tested ex situ and (b) stress values at various strain levels as a function of temperature, obtained by taking vertical slices through the stress-strain curves at selected strains.

3.4.1.1 Microstructural Behavior

Assessment of the microstructural evolution during loading at different temperatures was accomplished by in situ neutron diffraction measurements. All spectra were normalized to the same count time and plotted as a function of the macroscopic strain. The reflections from grains with planes perpendicular to the loading direction are shown in Figure 3.3. Surprisingly for the no-load condition, the diffraction patterns obtained at temperatures of 165 and 230 °C indicated the presence of trace amounts (2 to 3 vol.%) of retained martensite ($(121)_M$ at 1.56 Å and $(002)_M$ at 2.06 Å). However, no-load samples analyzed at 290 and 320 °C did not show any detectable retained martensite; hence the structure was assumed to be completely austenitic at these temperatures. Upon straining, the martensite volume fraction increased with increasing strain as indicated by the increase in intensity of the martensite peaks and concomitant decrease in austenite peaks (Figure 3.3(a), (b), and (c)). This was not the case for sample 4 tested at 320 °C (Figure 3.3(d)), as no martensite peaks appear in the diffraction patterns at any strain level (only austenite peak intensity changes were observed).

For a quantitative measure of martensite volume fraction, the Rietveld method was used to refine both histograms (Q_{\parallel} and Q_{\perp}) containing both B2 and B19' phase information. Figure 3.4 summarizes the martensite phase fraction, ξ_M , of all four samples during isothermal loading and unloading. The samples deformed at 165 and 230 °C (samples 1 and 2) initially showed a rapid increase in stress-induced martensite with increasing strain to about 4 percent applied strain, followed by a more gradual increase in martensite to about 8 percent strain, where the phase fraction saturated at $\xi_M \approx 0.25 \pm 0.03$. Sample 3, tested at 290 °C, saturated at 2 percent strain with a phase fraction of $\xi_M \approx 0.1 \pm 0.03$. For sample 4, deformed at 320 °C, no martensite was detected at any strain level and the structure remained fully austenitic during testing. Also included in Figure 3.4 are the retained martensite volume fractions after isothermally unloading to 0 MPa, which show that after deformation at 165, 230 and 290 °C a martensite volume fraction of $\xi_M \approx 0.1 \pm 0.03$ is stabilized in the samples, regardless of test temperature, and does not revert back to austenite, even when the sample is fully unloaded.

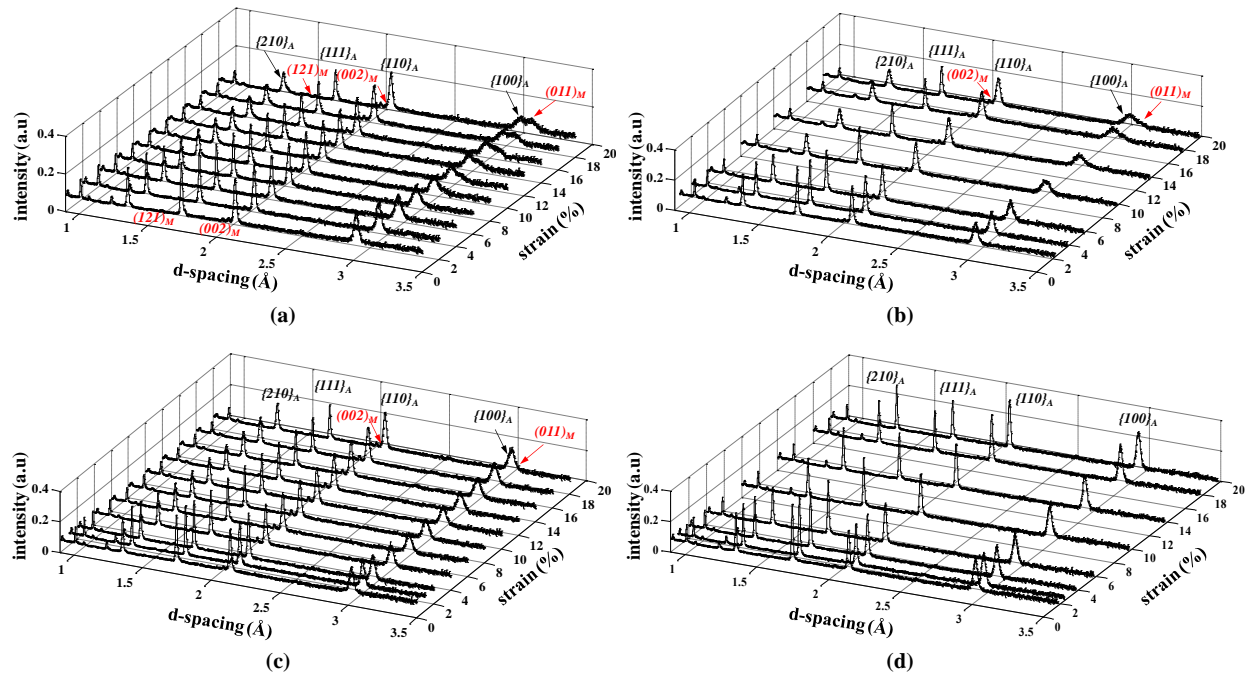


Figure 3.3.—Normalized neutron diffraction spectra acquired at incremental strains up to 18 percent while holding constant temperature at (a) 165 °C, (b) 230 °C, (c) 290 °C and (d) 320 °C. These reflections are from lattice planes perpendicular to the loading axis. Subscripts “A” and “M” denote austenite and martensite, respectively.

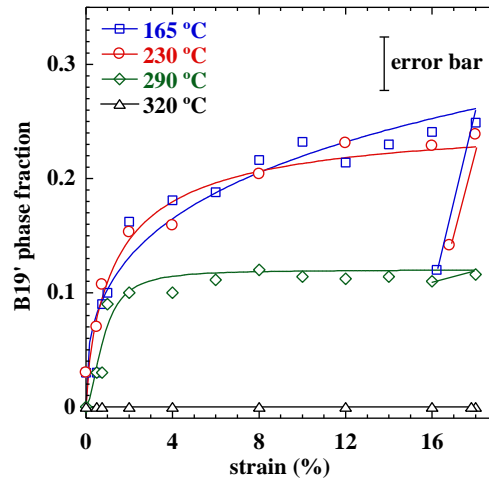


Figure 3.4.—Stress-induced martensite phase fractions during loading and unloading of the $\text{Ni}_{49.9}\text{Ti}_{50.1}$ at various temperatures. Error bar indicates the instrument resolution.

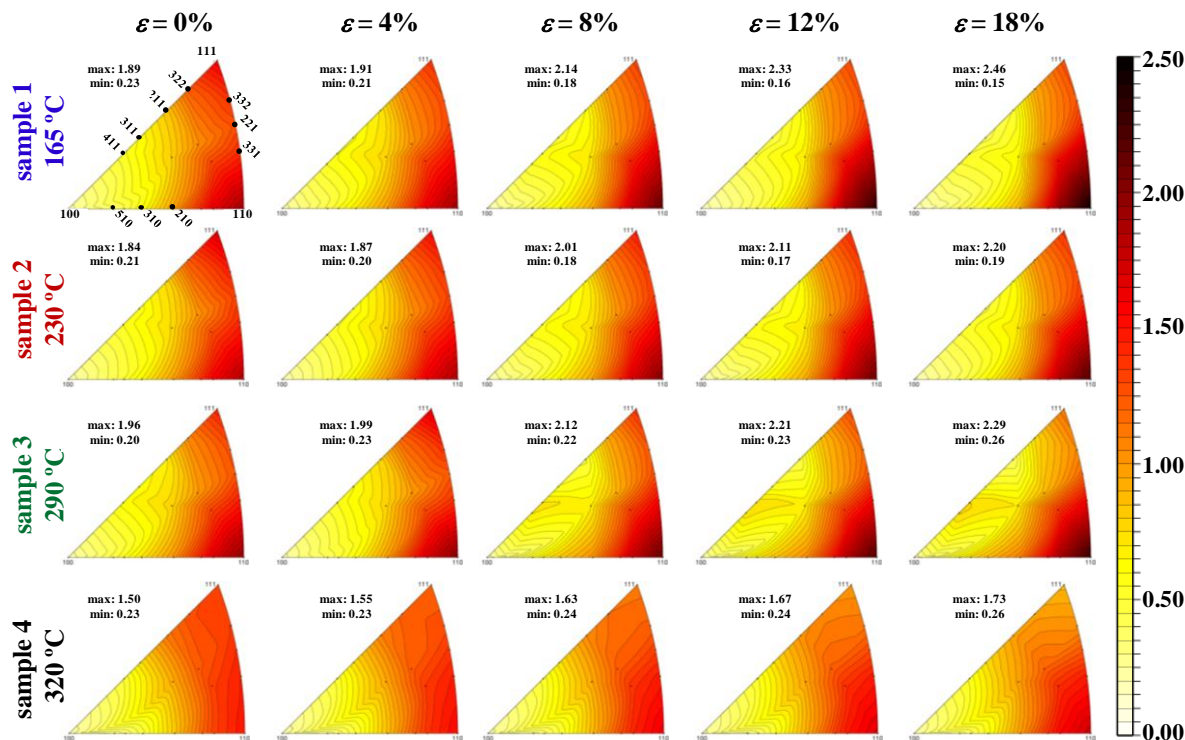


Figure 3.5.—Inverse pole figures (IPFs) from B2 lattice reflections perpendicular to the loading axis at selected strains for each sample. The corresponding maximum and minimum pole intensities (times random) are included at the top left hand corner of each IPF.

The texture evolution depicted in Figure 3.3 is better visualized using the austenite IPFs shown in Figure 3.5. These IPFs are from B2 lattice reflections perpendicular to the loading direction with the minimum unique region for the cubic crystal symmetry in multiples of random distribution (MRD). Texture of all four samples (in rows) at selected strain values of 0, 4, 8, 12 and 18 percent (in columns) are presented. The initial austenite texture shows a higher grain density of $\{110\}_A$ and $\{111\}_A$ and smaller amount of $\{100\}_A$ grains than in a random distribution. Such a texture must have developed during thermomechanical processing of the alloy, but is relatively weak compared to most wrought processed alloys and is indicative of a dynamically recrystallized structure, consistent with the 30 to 40 μm equiaxed grain structure observed in this material.

With increasing strain, a common trend was observed in all samples: the intensity at the $\{110\}_A$ orientation gradually increased as the intensity of the $\{111\}_A$ orientation decreased, with a mostly unchanged $\{100\}_A$ intensity. These diffraction intensities are also shown for the individual lattice planes in Figure 3.6. The variation of the intensities in different samples should also reflect the presence of stress-induced martensite, when present. But the volume fraction of stress-induced martensite was not subtracted from the IPFs in order to examine its effect on the B2 texture results shown in Figure 3.5. However, the accumulation of stress-induced martensite saturates early in samples 1 to 3 (at 2 to 8 percent strain), while the changes in texture continue through deformation to 18 percent strain. Furthermore, the same trend in texture evolution was observed in sample 4, though the trend was much weaker than in the other three samples. Sample 4 was deformed at 320 °C and did not contain any martensite and thus its IPF only reflects changes in texture due to austenite deformation. Therefore, the changes in intensities with strain observed in Figure 3.5 cannot be explained by the presence of retained martensite, but rather are due to deformation processes inherent to the austenite phase.

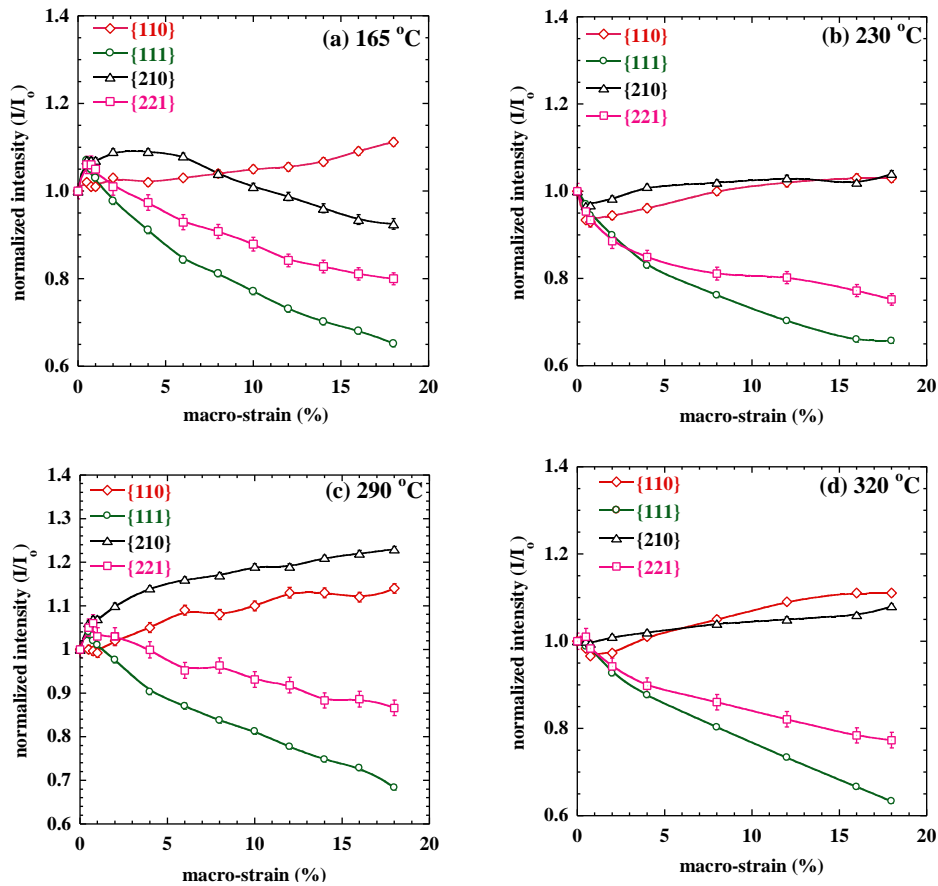


Figure 3.6.—Austenite peak intensities normalized to 1 at the unstrained condition for the $\{110\}_A$, $\{111\}_A$, $\{210\}_A$ and $\{221\}_A$ reflections perpendicular to the loading axis at (a) 165 °C, (b) 230 °C, (c) 290 °C and (d) 320 °C.

For a measure of the internal strain state of the material, the hkl -specific lattice strains were determined. The hkl -specific lattice strains were obtained from the interplanar spacings ($\Delta d_{hkl}/d_{hkl}$) using a single peak fitting method. The measured hkl -specific lattice strains for the $\{100\}_A$, $\{110\}_A$, $\{111\}_A$, $\{210\}_A$ and $\{221\}_A$ crystallographic planes are shown in Figure 3.7(a) to (d). These strains are from lattice planes perpendicular to the loading direction and are plotted as a function of applied macroscopic strain. Below 0.5 percent macro-strain, lattice planes deform in a linear elastic fashion in all samples with average moduli of 69, 78, 87, 78 and 85 GPa, respectively for the above crystallographic planes. Note that the linear elastic region from the macroscopic stress-strain curves in Figure 3.1 also extended to approximately 0.5 percent strain, with a measured Young's modulus of 74 GPa.

For macro-strains above 0.5 percent, the internal strains deviated from linearity and were very dependent on temperature. At all temperatures, the lattice strains in most reflections saturated early during loading and then became nearly constant with increasing strain (Figure 3.7(a) to (d)). Also, the yielding behavior for various lattice planes was similar at all temperatures. The $\{111\}_A$ planes yielded first followed by strain partitioning and yielding by $\{221\}_A$, $\{110\}_A$, and $\{210\}_A$ planes with the $\{100\}_A$ taking on the most strain in all cases.

Finally, TEM analyses were performed on an undeformed and two deformed samples to reveal additional microstructural features. Figure 3.8 contains TEM bright-field images of the $\text{Ni}_{49.9}\text{Ti}_{50.1}$ microstructure of the undeformed sample (Figure 3.8(a) to (c)), and ex situ samples deformed to 18 percent strain at 165 °C (Figure 3.8(d) to (f)) and 320 °C (Figure 3.8(g) to (i)). Stress-strain data for these latter two samples are included in Figure 3.2 All three samples were prepared the same way for TEM examination, and images were taken at room temperature, and at 165 and 320 °C. The baseline

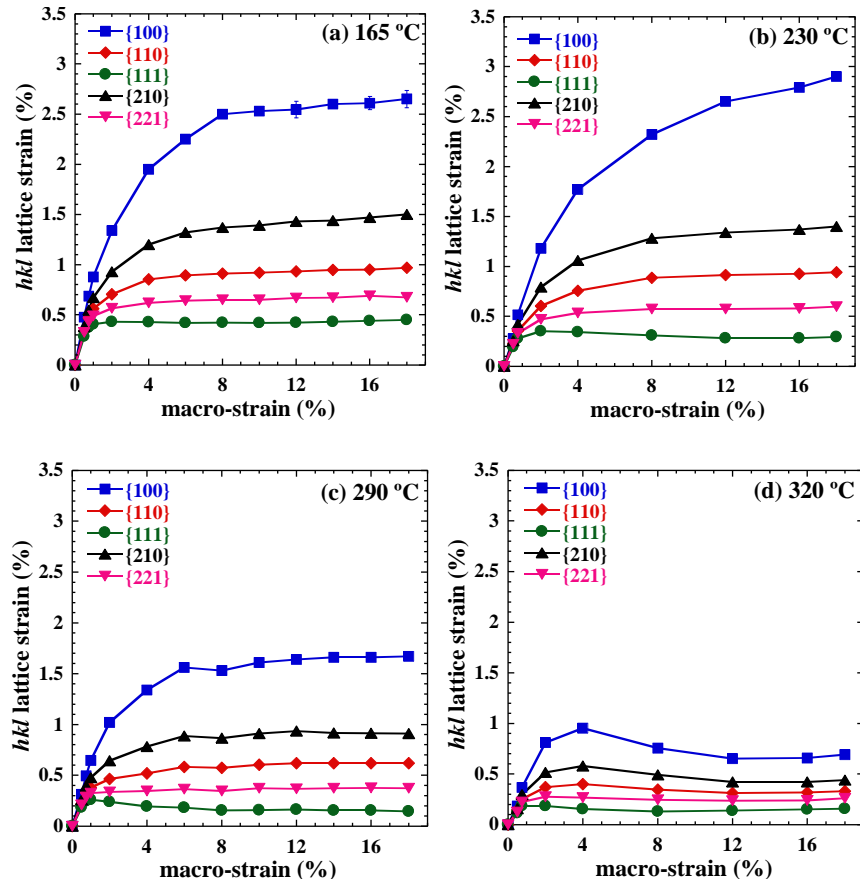


Figure 3.7.—Lattice strains associated with $\{100\}_A$, $\{110\}_A$, $\{111\}_A$, $\{210\}_A$ and $\{221\}_A$ reflections perpendicular to the loading axis at (a) 165 °C, (b) 230 °C, (c) 290 °C and (d) 320 °C using a single peak fitting technique. Error bars included ($\Delta\epsilon \sim 0.02$ percent).

undeformed sample consisted of a single-phase self-accommodated martensite matrix at room temperature (Figure 3.8(a)), which was completely transformed to austenite at 165 and 320 °C (Figure 3.8(b) and (c), respectively). The samples deformed to 18 percent strain at 165 and 320 °C were martensitic at room temperature (Figure 3.8(d) and (g), respectively), but a number of twin related planar defects were still present when the samples were heated to 165 °C (Figure 3.8(e) and (h)). These defects remained in the microstructure even after heating to 320 °C for both the 165 and 320 °C tested samples, as shown in Figure 3.8(f) and (i). In addition to these twins, high densities of dislocations were also observed in the two deformed samples. Selected area diffraction patterns (SADPs) confirmed that the twins in the austenite phase (Figure 3.8(j) and (k)) were compound $\{114\}_{B2}$ deformation twins as reported in Refs. [36, 61].

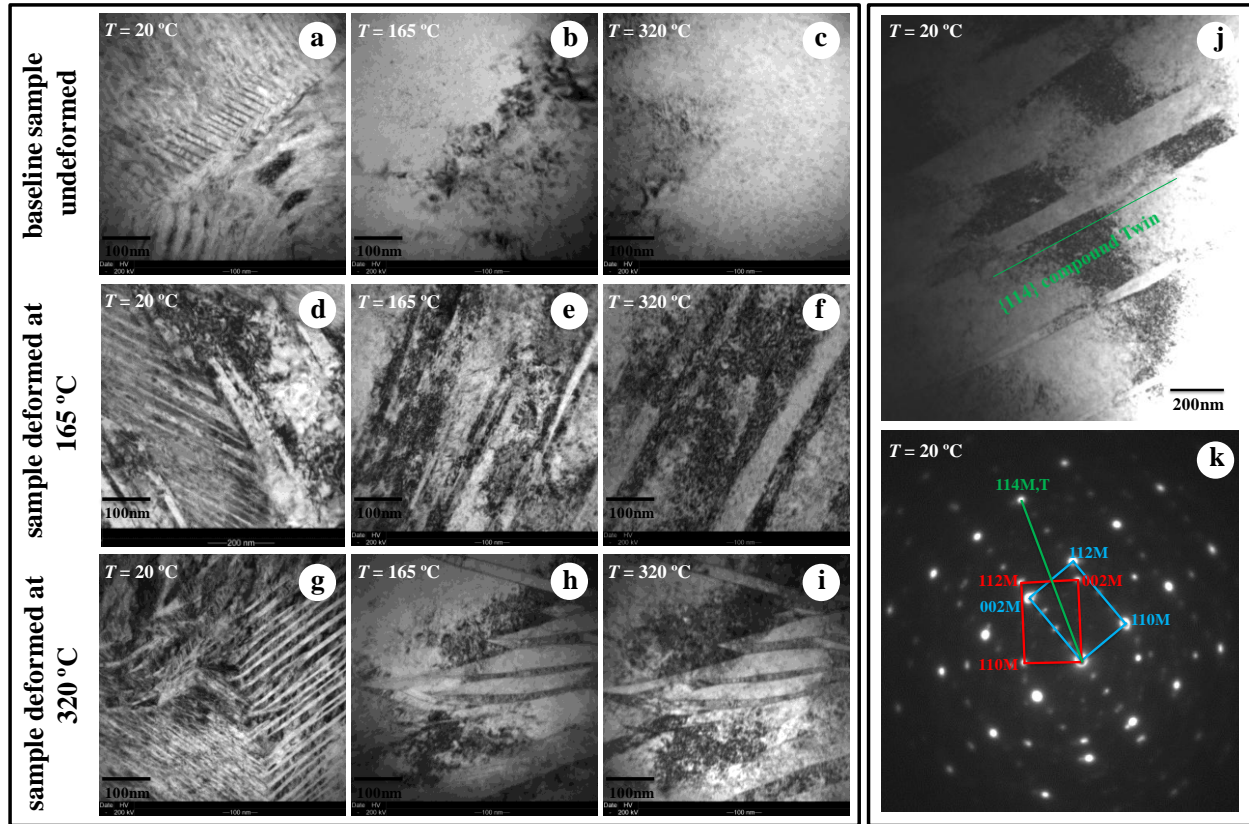


Figure 3.8.—TEM bright-field (BF) images of the microstructure of $\text{Ni}_{49.9}\text{Ti}_{50.1}$ at 20, 165 and 320 °C for a virgin sample ((a), (b), and (c), respectively), sample post-deformed to 18 percent strain at 165 °C ((d), (e), and (f), respectively), and sample post-deformed to 18 percent strain at 320 °C ((g), (h), and (i), respectively). (j) BF and (k) SADP of the planar faults observed after deformation.

3.4.2 Modeling Results

Since no retained or stress-induced martensites were present in the sample deformed at 320 °C (sample 4 in Table 3.1), the EPSC model was formulated for this case with only austenite slip and deformation twin systems considered as possible deformation mechanisms. As $\langle 100 \rangle$ slip processes and $\langle 221 \rangle \{114\}$ and $\langle 111 \rangle \{112\}$ twinning mechanisms are commonly reported to operate in NiTi [32–43], they were obvious choices for incorporation into the model in various combinations. Also, in a non-transforming material, like bcc-steel for example, a texture evolution as observed in Figure 3.5 could result from $\langle 111 \rangle$ type slip processes (see Ref. [88] and references within). While I acknowledge that $\langle 111 \rangle$ slip has never been reported in NiTi, it was also incorporated into the model as a possible deformation mechanism to determine how it might influence the behaviors of the material.

Consequently, a total of 4 modeling runs were examined with the activation of different deformation systems (as defined in Table 3.2): (i) Model 1 with slip systems 1 and 2, (ii) Model 2 with slip systems 1, 2 and 3, (iii) Model 3 with twin systems 4 and 5, and finally (iv) Model 4 with slip and twin systems 1, 2, 4 and 5. The model predictions and experimental data for the macroscopic stress-strain response of $\text{Ni}_{49.9}\text{Ti}_{50.1}$ at 320 °C are compared in Figure 3.9. Model 1 with only $\langle 100 \rangle \{110\}$ and $\langle 100 \rangle \{001\}$ slip accurately depicted the early flow behavior of $\text{Ni}_{49.9}\text{Ti}_{50.1}$ but was not sufficient to capture the hardening behavior of the alloy at larger strains, which was over estimated. This model also did a very poor job at predicting the unloading response. Model 2, with $\langle 100 \rangle \{110\}$, $\langle 100 \rangle \{001\}$ and $\langle 111 \rangle \{110\}$ slip systems activated, was even worse at predicting the stress-strain response. It over predicted the initial yield behavior, under predicted the experimental behavior at early strains, and significantly over predicted the hardening rate at

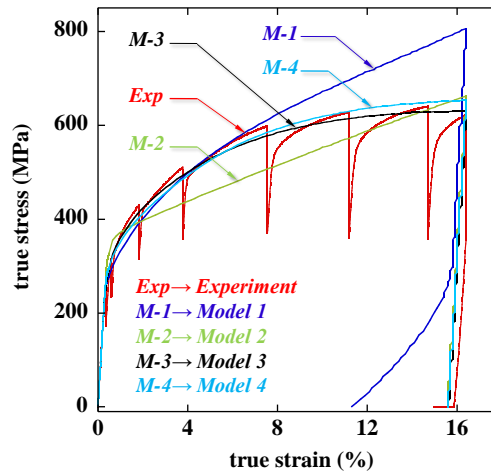


Figure 3.9.—EPSC model predictions for the 320 °C stress-strain response of $\text{Ni}_{49.9}\text{Ti}_{50.1}$ compared to experimental data. (i) Model 1 with slip systems 1 and 2 active (see Table 3.2 for details), (ii) Model 2 with slip systems 1, 2 and 3 active, (iii) Model 3 with only twin systems 4 and 5 active, and (iv) Model 4 with slip and twin systems 1, 2, 4 and 5 active.

larger strains. There was no quantitative or even qualitative agreement between this modeled response and the actual stress-strain behavior of the alloy. Both Models 3 and 4, which contained $\langle 221 \rangle\{114\}$ and $\langle 111 \rangle\{112\}$ twinning systems, best predicted the stress-strain response over the entire strain range, accurately capturing the onset of yield, hardening rates, final stress level, and unloading response.

The microstructural predictions from these models are presented in Figure 3.10 and Figure 3.11. Figure 3.10 compares the experimental and modeled response for the internal strains generated during deformation. Figure 3.10(a) summarizes the experimental lattice strains obtained by neutron diffraction for five austenite reflections in the sample deformed at 320 °C, while Figure 3.10(b) to (f) show the individual experimental and modeled reflections for $\{100\}_A$, $\{110\}$, $\{111\}_A$, $\{210\}_A$, and $\{221\}_A$, respectively. None of the models adequately predicted the experimental results for any reflection. For several reflections, Models 2 and 4 best predicted the final lattice strains, but this was probably more coincidence, since the lattice strain evolution was not captured correctly at all. Conversely, Model 1 best captured the initial lattice strain evolution for several reflections, but not the final states. In the experimental data, there was a relaxation in the lattice strains for all reflections at this temperature (Figure 3.10(a)), which was not predicted in any of the models. This relaxation is due to possible diffusive recovery processes occurring in the material and is confirmed by the stress drops observed in the loading curves while diffraction spectra were being acquired. However, the EPSC model was not formulated to account for diffusive deformation processes and thus cannot adequately predict the internal strain state of the material.

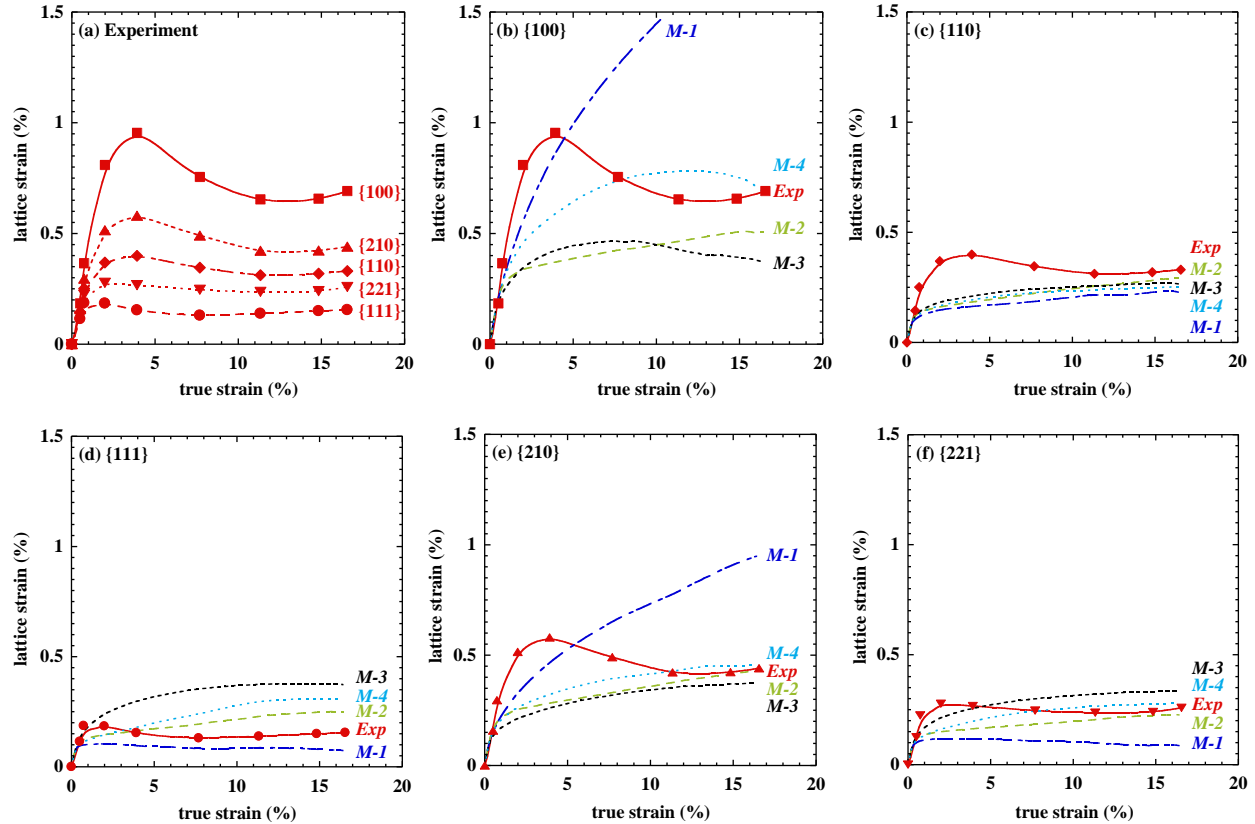


Figure 3.10.—Experimental and predicted austenite lattice strains. (a) Experimental data at 320 °C for all reflections, and comparison of the experimental and modeled results for individual reflections (b) $\{100\}_A$, (c) $\{110\}_A$, (d) $\{111\}_A$, (e) $\{210\}_A$, and (f) $\{221\}_A$.

Texture evolution was also modeled, as shown in Figure 3.11, using IPFs to display the data. The slip and/or twin systems activated in each model are also indicated for reference. An interesting observation is the $\langle 100 \rangle$ slip of Model 1, which produces no texture evolution. When deformation occurs by this mechanism, no crystal rotation is produced resulting in no texture change. Similar observations were reported by Margevicius and Cotton in a study of NiAl [89], where deformation is known to be dominated by $\langle 100 \rangle$ dislocation processes [90]. Alternatively, only Models 2 and 4 were within close agreement with the experimental data. Both of these models predicted an increase in the $\{110\}_A$ orientation intensity with a concomitant decrease in the $\{111\}_A$ intensity as indicated by the circled regions on the IPFs at 18 percent strain in Figure 3.10.

Overall, it is clear that I have not accounted for all the active deformation mechanisms or the correct combination of mechanisms in the modeled responses. An additional mechanism that was not accounted for is localized or bulk climb of $\langle 100 \rangle$ dislocations. However, the EPSC model was not formulated to account for diffusion-assisted deformation processes.

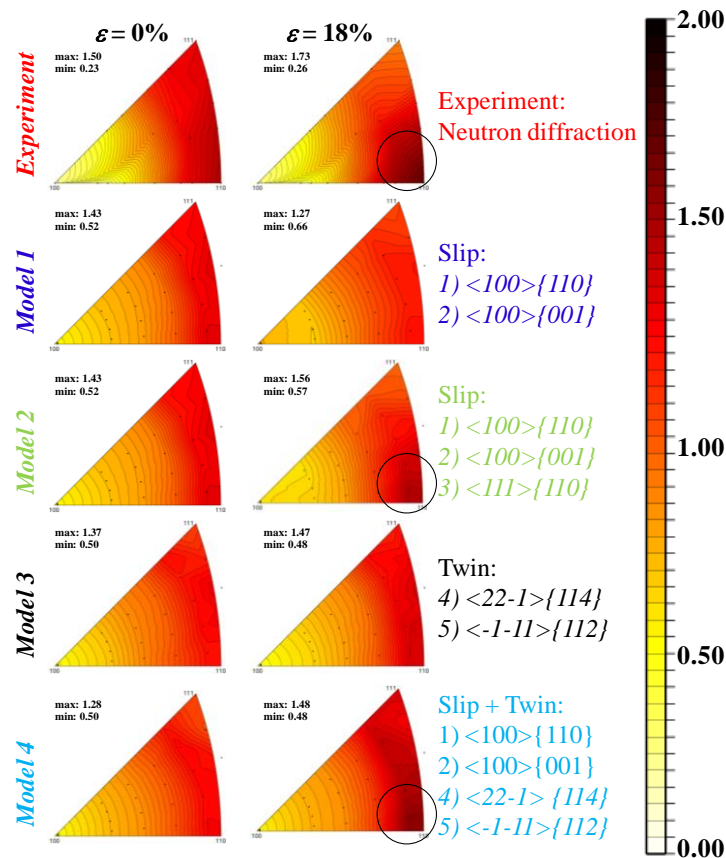


Figure 3.11.—Experimental and predicted IPFs at 0 and 18 percent strain. Corresponding slip or twin systems used in each model are included.

3.4.3 Thermal Recovery of the Isothermally Deformed Samples

On unloading of the four samples in Figure 3.1 to 0 MPa, various amounts of strain were recovered (as summarized in Table 3.3). This is shown in another way in the strain-temperature plot in Figure 3.12 by the vertical lines starting from 18 percent strain. It was shown in Figure 3.4 that at 165, 230, and 290 °C, about 12 vol.% of stress-induced martensite was retained and did not revert back to austenite when the samples were unloaded. In an attempt to fully recover all the strains due to retained martensite, each sample was heated from their respective deformation temperature to 500 °C at 0 MPa in load control mode. During the heating segment shown in Figure 3.12, samples 1, 2, and 3 (deformed at 165, 230, and 290 °C, respectively), which contained retained martensite, continued to recover strain during heating until 450 °C; and beyond this temperature the strain response was dominated by thermal expansion. Sample 4, which was completely austenitic with no measureable retained martensite, also recovered strain until 450 °C. The heating curves not only differ in the amount of strain recovered, but also in their shapes. Up to about 450 °C, the heating curves changed from an exponentially decaying response in samples 1 (165 °C) and 2 (230 °C) to a two-slope curve in samples 3 (290 °C) and 4 (320 °C). In all cases, beyond 450 °C, austenite thermal expansion began to dominate and strains started to increase. Once at 500 °C, the temperature was held constant for 30 min while collecting diffraction spectra, where additional strain (~0.06 percent) was recovered as indicated by the small vertical lines in Figure 3.12 at 500 °C.

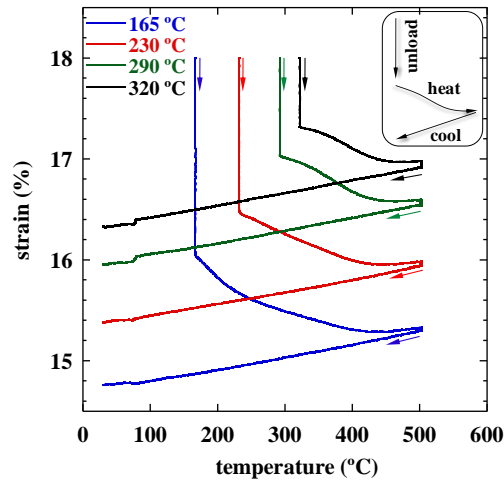


Figure 3.12.—Strain-temperature response for samples 1 to 4 during unloading from 18 percent strain at their respective deformation temperatures, heating to 500 °C, and cooling back to room temperature.

TABLE 3.3.—APPROXIMATE PARTITIONING OF STRAINS DURING THE ISOTHERMAL DEFORMATION OF $\text{Ni}_{49.9}\text{Ti}_{50.1}$

Mechanism	Strain partitioning, %			
	Temperature, °C			
	165	230	290	320
Total deformation	18%	18%	18%	18%
Elastic	0.91	0.92	0.8	0.7
SIM (recovered)	1.05	0.6	0.17	-----
SIM (retained)	0.51	0.2	0.1	-----
Permanent strain	15.53	16.28	16.93	17.3

To help explain the strain-temperature behavior observed in Figure 3.12, the lattice strains of individual austenite reflections were measured by neutron diffraction before and after isothermally unloading the samples and during heating to 500 °C. These lattice strains, for planes perpendicular to the loading direction, are plotted in Figure 3.13. For consistency, the lattice strains reported in Figure 3.13 start at the last value shown in Figure 3.7(a) to (d), which is the lattice strain at 18 percent sample strain. During unloading from this 18 percent macro-strain, some of the lattice planes in the three samples containing retained martensite were driven into compression (hatched regions of Figure 3.13). This was followed during heating by a gradual conversion of all planes in each sample toward the same internal strain value at 500 °C. Quantitatively, heating to 500 °C caused all lattice reflections to go to 0.49, 0.41, 0.28 and 0.31 ± 0.05 percent strain for the 165, 230, 290, and 320 °C deformed samples, respectively. However, all the lattice strains reduced to approximately 0 percent strain when the thermal strains, using a coefficient of thermal expansion of $13 \times 10^{-6}/^\circ\text{C}$ [38], were subtracted. Consequently, at 500 °C all the lattice strains generated during loading to 18 percent macro-strain were recovered, and the internal state of the material was fully relaxed. This was further confirmed by cooling and subsequent heat cycles to the original test temperature (see Table 3.1) without recovering any additional strains macroscopically or microscopically, other than thermal strains.

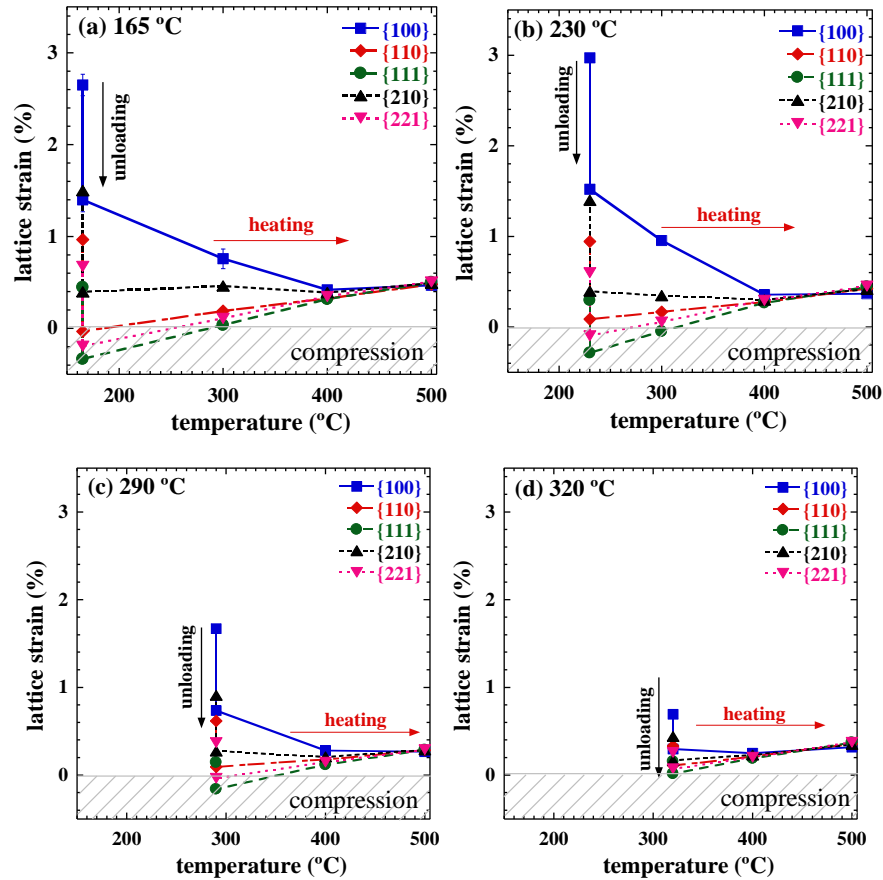


Figure 3.13.—Lattice strain recovery during unloading and heating to 500 °C for (a) 165 °C, (b) 230 °C, (c) 290 °C and (d) 320 °C isothermally deformed samples. Error bars included, but were usually smaller than the symbol size.

For a complete and final measure of texture at the end of the in situ experiments, the four samples (after isothermal deformation and unloading, heating to 500 °C and cooling back to room temperature, followed by another pair of thermal cycles to the original isothermal deformation temperature (as summarized in Table 3.1)) were heated one last time to 200 °C in HIPPO, where neutron diffraction spectra were acquired in the austenite state for 80 min. Figure 3.14 shows the $\{100\}_A$, $\{110\}_A$, $\{111\}_A$ and $\{210\}_A$ pole figures in multiples of random distribution (MRD) reconstructed from the HIPPO data. Each pole figure is a planar stereographic projection that represents the density of diffraction plane normal vectors as a function of their direction within the sample. Thus the middle of the pole figures represents the diffracting vectors parallel to the loading direction while those on the rim represent diffracting vectors normal to the loading direction.

The undeformed sample texture (Figure 3.14(a)) is used as a reference starting texture of the material before testing. The intensity of the $\{110\}_A$ pole in Figure 3.14(a) is the most intense consistent with the IPFs of Figure 3.5 at 0 percent strain. In the deformed samples, slight differences in the $\{110\}_A$ pole density, which are aligned with the loading direction, are evident in samples 1 and 2. But the texture in the $\{110\}_A$ pole figures approached the initial starting texture with increasing testing temperature (samples 3 and 4). The $\{100\}_A$ pole density at $\Theta \approx 45^\circ$ and the $\{111\}_A$ on the rim of the pole figures were very similar in all sample conditions. Also, the random distribution of the $\{210\}_A$ pole density was unchanged in all conditions. Consequently, the final texture ended up being essentially the same or very similar to the original starting texture in each case.

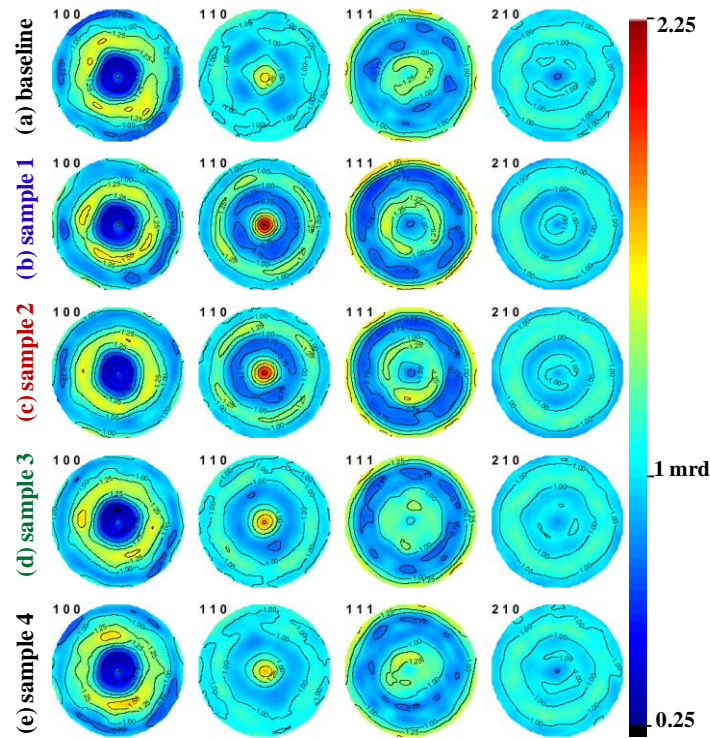


Figure 3.14.—Austenite pole figures measured at 200 °C for (a) virgin sample, and post deformed and thermally cycled samples (complete history described in Table 3.1): (b) sample 1, (c) sample 2, (d) sample 3, and (e) sample 4.

3.5 Discussion

3.5.1 Macroscopic Stress-Strain Behavior

For strains up to 0.5 percent, all samples in Figure 3.1 exhibited similar linear responses independent of testing temperature. From a fit of the macroscopic data, the elastic modulus of polycrystalline $\text{Ni}_{49.9}\text{Ti}_{50.1}$ was 74 GPa, and is consistent with the elastic moduli for individual $\{100\}_A$, $\{110\}_A$, $\{111\}_A$, $\{210\}_A$ and $\{221\}_A$ crystallographic planes, which were 69, 78, 87, 78 and 85 GPa, respectively, measured from Figure 3.7. These values compare well with B2 NiTi elastic moduli reported in the literature [28, 40, 41].

Above 0.5 percent strain, the onset of inelastic deformation and its temperature dependence is evident from Figure 3.1 and Figure 3.2. For samples deformed at 165 and 230 °C the stress-strain curves were parabolic with a quickly decreasing work hardening rate between 0.5 and 6 percent strain, followed by a region of very low and almost constant hardening to the end of test. The microstructural counterpart as revealed by neutron diffraction shows a rapid buildup of stress-induced martensite (B19' phase fraction) for both samples, and saturation at around 6 to 8 percent strain (accounting for the error bars), as shown in Figure 3.4. Stress-induced martensite may occur first, initiating further inelastic deformation mechanisms such as slip and twinning, but it is clear from previous work [52] that plasticity occurs essentially concurrently with the development of the stress-induced martensite. Thus, the rapid work hardening, which is observed over the first ~6 percent strain is due to the concurrent generation of stress-induced martensite and plasticity. If indeed stress-induced martensite was forming without plasticity then the material would be expected to show a stress-plateau, characteristic of other materials where stress-induced martensite is formed (in similar testing conditions). After about 8 percent strain, the amount of

stress-induced martensite has saturated and continued deformation occurs by slip and deformation twinning, but further work hardening is limited.

For sample 3, deformed at 290 °C, martensite was also stress-induced but quickly saturated at about 2 percent strain with $\xi_M \approx 0.1$ volume fraction (Figure 3.4). From Figure 3.1 or Figure 3.2(a), the stress reached at 2 percent strain was approximately 400 MPa. This stress level is apparently high enough to initiate bulk plasticity in the alloy at this temperature, but without significant work hardening, interrupting the formation of any further stress-induced martensite. Also, at 290 °C and above, strain softening was apparent in Figure 3.1 or Figure 3.2(a), which could be due to dynamic recovery, suggesting activation of diffusion controlled mechanisms.

Nonlinear unloading slopes for each sample indicate a combination of elastic strain, the reverse SIM-to-austenite phase transformation, internal back stresses and possible viscoelastic effects. The recovered strains after unloading from 18 percent strain to 0 MPa were $\varepsilon_{rec} = 1.93, 1.5, 0.93,$ and 0.66 percent for samples tested at 165, 230, 290, and 320 °C, respectively (Figure 3.2(a)). Note that the sample tested at 320 °C had no stress-induced martensite, and assuming $E = 74$ GPa and a final stress before unloading of 525 MPa, would have recovered only elastic strain, even though the unloading response looked somewhat nonlinear.

For the three samples deformed at 165, 230, and 290 °C, not all the stress-induced martensite transformed back to austenite while unloading to 0 MPa. This is due to the plastic deformation and its associated strain fields, which act as a barrier for complete retransformation of all the martensite to austenite on unloading. In such a case, the mobility of martensite variants is resisted and an increase in compressive stress or addition of thermal energy is necessary to keep the boundaries moving for complete reversion to austenite. It was also reported that the generation of dislocations and slip can occur in the martensitic phase rather than the parent phase as was reported by Miyazaki et al. [91], which in turn can also trap/stabilize the martensitic variants from reverting to the parent phase. However in this case, plastic deformation of the austenite occurred concurrently with stress-induced martensite formation and then dominated behavior after SIM processes were saturated, trapping the martensite within a heavily deformed austenitic matrix.

3.5.2 Microstructural and Micromechanical Evolution

The dominant stress-induced martensite variants that nucleate and grow during deformation of the austenite were the $(011)_M$ and traces of $(002)_M$ as shown in Figure 3.3. These active variants were the same in each sample, but the volume fractions varied with changes in deformation temperature (Figure 3.4). Besides nucleation of stress-induced martensite, the austenite peak intensities shown in Figure 3.3 exhibited changes above 0.5 percent strain, which indicate texturing of the B2 phase during deformation. This variation in peak intensities, also presented as IPFs in Figure 3.5 and normalized intensities in Figure 3.6, is a direct manifestation of the changes in the lattice plane orientations in the diffraction volume. From Figure 3.5 and Figure 3.6, the gradual shift in intensity from the $\{111\}_A$ orientation to the $\{110\}_A$ orientation suggests that in addition to $\langle 100 \rangle$ slip processes another deformation mechanism must be active. There are two possibilities: (i) the activation of a secondary slip system, specifically $\langle 111 \rangle$ type slip (Model 2) [92, 93], or (ii) deformation twinning, which is manifested as an exchange of $(111)_A$ intensity from the diffraction vectors parallel ($Q_{\parallel}, -90^\circ$) to perpendicular ($Q_{\perp}, +90^\circ$) when deforming the material [94], either acting alone (Model 3) or in combination with $\langle 100 \rangle$ slip (Model 4). All three situations were modeled but only Models 2 and 4 indicated a shift to the $(110)_A$ texture for planes perpendicular to the loading direction (Figure 3.11). However, the results obtained by the models suggest that twinning is more likely the additional mechanism operating with $\langle 100 \rangle$ dislocation processes, since a much better prediction of the macroscopic response was attained (Figure 3.9). Furthermore, $\langle 111 \rangle$ type dislocations have never been observed experimentally in NiTi, nor are they predicted to occur based on energetics [30].

The presence of deformation twinning was further confirmed by the hot stage TEM analysis. The baseline undeformed sample (Figure 3.8(a) to (c)) showed only self-accommodated martensite at room temperature (Figure 3.8(a)), and a clean austenite microstructure with no observable retained martensite at 165 °C (Figure 3.8(b)) and 320 °C (Figure 3.8(c)). On the other hand, samples that were deformed to

18 percent strain in the austenite state at 165 and 320 °C, unloaded and cooled to room temperature, showed a twinned structure at room temperature (Figure 3.8(d) and (g), respectively), and clear evidence of twinning in the B2 austenite at 165 °C (Figure 3.8(e) and (h), respectively) and at 320 °C (Figure 3.8(f) and (i), respectively). The twins in Figure 3.8(i) can be safely assumed to be all deformation twins, since the martensite phase fraction measured by neutron diffraction at 320 °C was zero in this sample (Figure 3.4). These twins were analyzed in the TEM (Figure 3.8(j) and (k)) and were found to be compound $\{114\}_{B2}$ twins, confirming previously reported results [34, 36]. The 165 °C-tested sample when heated in the TEM back to 165 °C (Figure 3.8(e)) and even when heated to 320 °C (Figure 3.8(f)) still contained both the stabilized, stress-induced martensite twins as originally measured by neutron diffraction (Figure 3.4) and the deformation twins.

The onset of inelastic deformation processes in $Ni_{49.9}Ti_{50.1}$ was also revealed by the measured lattice strains. The measured (Figure 3.7) and modeled (Figure 3.10) hkl -specific lattice strains deviate significantly from linearity at macro-strains above 0.5 percent, consistent with all previous results. The lattice strains tend to saturate at lower values with increasing test temperatures and the load partitions to different grains. In all cases, strains along $\{111\}_A$ saturate first at the lowest values, and strain is then shed to the other orientations, with $\{100\}_A$ being a hard orientation, particularly for $\langle 100 \rangle$ slip processes. Also, in samples 1, 2, and 3, lattice strain saturations are associated with both the phase transformation and plastic deformation. But other than lower saturation values for a given hkl strain, the sample deformed at 320 °C is qualitatively similar to the other samples, indicating that slip and twinning are the dominant mechanism controlling internal strains.

At 320 °C (Figure 3.7(d) and Figure 3.10(a)), the maximum in lattice strains at about 4 percent macro strain is not predicted by any of the current deformation models (Figure 3.10). This decrease in lattice strains indicates an internal relaxation of the material. Additional mechanisms not accounted for in the models were diffusion-assisted processes such as thermally activated glide over obstacles and localized or bulk climb. In fact the onset of diffusional processes over this temperature range plays an important role in the deformation behavior of other B2 compounds explaining such observations as the ductile-to-brittle transition, a significant decrease in work hardening, and the strong temperature and rate dependence of yield at intermediate temperatures [95, 96]. However, the EPSC model used was not formulated to account for thermally activated deformation processes. Consequently, none of the models did a very good job at predicting the trend in internal strains as a function of macro-strain measured in the 320 °C deformed sample. But amongst all the models presented, Model 4 did the best job of predicting the final internal lattice strains at 18 percent macro-strain (Figure 3.10), textures (Figure 3.11), and the macroscopic stress-strain response (Figure 3.9).

Further investigation of the diffraction profiles indicated that a relative increase in peak broadening was occurring during loading (Figure 3.3(a) to (c)). The trend in peak shape broadening was very similar in all the three samples tested at 165, 230 and 290 °C. This can be explained by the increase in the density of faults due to stress induced martensite and deformation twinning, and an increase in dislocation density. However, Sample 4 tested at 320 °C exhibited very little broadening. Recalling that there was a significant strain-softening shown in Figure 3.1 and Figure 3.2(a), at this temperature, it is reasonable to assume that in $Ni_{49.9}Ti_{50.1}$, thermally-assisted deformation processes become predominant somewhere between 290 and 320 °C, resulting in dynamic recovery during deformation at these and higher temperatures.

3.5.3 B2 Deformation Map

The polycrystalline B2 $Ni_{49.9}Ti_{50.1}$ studied here does not have a well-defined yield strength as a function of temperature over the range of 169 to 320 °C due to the operation of competing mechanisms with different temperature dependencies. However, based on current mechanical tests, neutron diffraction, TEM, and modeling results, a B2 deformation mechanism map was constructed that highlights the austenite “yield” functions (Figure 3.15). The data points in Figure 3.15 were obtained using a 0.2 percent strain offset applied to the stress-strain curves in Figure 3.2. The yield functions denoted by $\sigma(T)_{SIM}$

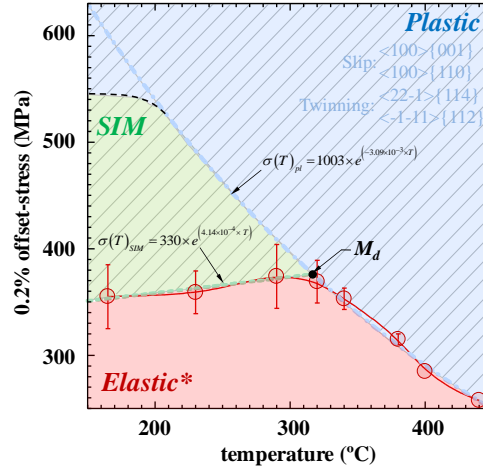


Figure 3.15.—Deformation mechanism map showing the mechanisms responsible for initial inelastic strain behavior in a B2 Ni_{49.9}Ti_{50.1} alloy.

and $\sigma(T)_{pl}$ indicate the limits of where the SIM and plastic deformation start and finish as revealed by the experimental data. The plastic deformation region is comprised of both slip and deformation twinning, since they probably occur somewhat concurrently. The plastic deformation region also extends over the SIM region (hatched region) since the stress-induced martensite formed concurrently with general slip and twinning processes and did not occur as a separate distinguishable mechanism. This map does not consider the rate dependency nor does it distinguish between dislocation glide and coupled glide plus climb, combining these processes in a category known as “plastic” deformation. The stress-induced martensite + plasticity lower boundary and plasticity dominated boundary lines were formulated based on experimental data using exponential functions, given by

$$\sigma(T)_{SIM} = 330 \times e^{(4.14 \times 10^{-4} \times T)} \quad (3.2)$$

$$\sigma(T)_{pl} = 1003 \times e^{(-3.09 \times 10^{-3} \times T)} \quad (3.3)$$

where the subscripts ‘ $_{SIM}$ ’ and ‘ $_{pl}$ ’ stand for stress-induced martensite and plasticity, respectively. The upper SIM limit, at around 550 MPa, was extrapolated from Figure 3.4 where the phase transformation started to saturate due to excessive plastic deformation. Using this map, a demarcation between the operative mechanisms was established and the M_d temperature was determined to be ≈ 310 to 320 °C. It is important to note that this deformation map describes only the initial deformation response at small strains or “yielding” of the austenite. But by utilizing this map, insights into the possible mechanisms that are activated during both isothermal/monotonic and isobaric/thermal cycling conditions can be elucidated.

Even so, thermomechanical cycling in the elastic region of Figure 3.15, for this particular alloy, has been shown to result in large strain evolutions and an unstable cyclic response [97]. This behavior is likely due to dislocations that initially form at the moving austenite/martensite interface during the forward phase transformation as previously reported in NiTi [98] and in a similar fashion to the concurrent generation of stress-induced martensite and plasticity observed in this study. However, the thermomechanical behavior of this alloy is beyond the scope of the current paper, and it will be examined in future work.

3.5.4 Strain Partitioning

The total recovered and unrecovered components of strain that comprise the 18 percent applied strain at each test temperature were estimated and are reported in Table 3.3. When unloading, both elastic strains (determined based on a bulk modulus 74 GPa) and those due to the reversion of SIM were recovered. However, not all the SIM reverts back to austenite when unloading as shown in Figure 3.4. To decouple the strains due to the retained martensite after unloading, from the total strain introduced during deformation, the unloaded samples were heated gradually to 500 °C. Strains were recovered on the heating segment until about 450 °C, at which point thermal expansion began to dominate. The 450 °C temperature is a common shape setting temperature for this alloy and the associated mechanisms that take place during this process are discussed in detail in Chapter 6. From that study, it was shown that the internal state of this $\text{Ni}_{49.9}\text{Ti}_{50.1}$ alloy fully relaxes at 450 °C as is the case in this work (see Figure 3.13).

However, both samples deformed at 165 and 230 °C contained almost the same amount of SIM and the same amount of retained martensite after unloading, but the strains recovered were different (Table 3.3). This could be due to the amount of recovery that occurred in the two samples prior to the heating cycle affecting the internal strains, which were greater in the 165 °C sample (Figure 3.13). During unloading, some internal lattice strains become negative, which gives rise to a compressive internal state. This internal stress arises due to the mismatch that exists between the twinned and slipped austenite grains and the retained martensite. The strains due to this retained martensite in addition to diffusional processes were then recovered as the samples were heated to 500 °C. But more recovery occurred during heating from 165 °C because the internal strains were greater, while more of the strains relaxed during the unloading process and hold at 230 °C while neutron spectrum were acquired, reducing the driving force for strain recovery during the subsequent heating cycle. Note that the sample deformed at 320 °C did not contain any martensite and all the strains recovered during heating of this sample were due to back stresses, recovery processes and to possible low volume fraction (< 3 percent) of martensite that was not detected by the instrument used. It is also possible that some of the deformation twins become unstable after unloading and heating, which result in further strain recovery.

The balance of the deformation induced during testing was permanent deformation and is a result of $\langle 100 \rangle$ slip, $\{114\}_{\text{B2}}$ deformation twinning, and thermally assisted deformation processes and represents the bulk of the deformation imposed on all the samples over the range of temperatures investigated (Table 3.3). An additional no-load thermal cycle was performed to examine the strain evolution; however, no more strain was recovered and all sample shapes remained the same (i.e., no further changes in sample dimensions were observed). Consequently, as previously observed during a study of the shape set behavior of this alloy (Chapter 6), heating to ~450 °C is sufficient to relax all internal strains in this alloy regardless of whether they are due to retained martensite or plasticity. Furthermore, the microstructures of each sample were examined at the end of these experiments using HIPPO, and the observed textures were near-identical to that of the initial virgin sample (Figure 3.14). This further confirms that heating the samples to 500 °C fully recovered all retained martensite and all internal strains and essentially reset the microstructures of each sample back to its as-received condition, similar to what happens in a shape setting procedure (Chapter 6). Note that the $\{110\}$ pole figures for both pre-deformed samples at 165 and 230 °C (samples 1 and 2 of Figure 3.14) show a high grain density aligned with load. This texture may have resulted from some retained austenite deformation twins that did not disappear after heating to 500 °C.

3.6 Conclusions

The deformation behavior of polycrystalline $\text{Ni}_{49.9}\text{Ti}_{50.1}$ (at.%) in the B2 austenite phase was studied over the temperature range of 165 to 320 °C by mechanical testing, in situ neutron diffraction, hot-stage TEM, and elastoplastic deformation modeling. A better understanding of the range of dominance of each of the contributing deformation mechanisms over this temperature range was established supporting the following conclusions:

- a. During isothermal deformation at temperatures between 165 and 290 °C, the total macroscopic strains generated consisted of recoverable strains (elastic and stress-induced martensite) and irrecoverable strains (due retained martensite, slip, and deformation twinning). The same processes, except for those associated with martensite formation, were active during deformation at 320 °C.
- b. The M_d temperature was determined to be between 310 and 320 °C. Above the M_d , no stress-induced martensite was observed and the deformation was governed by deformation twinning and slip, along with thermally assisted deformation processes.
- c. From the elastoplastic self-consistent (EPSC) model, $\langle 100 \rangle$ slip or the $\{114\}_{B2} + \{112\}_{B2}$ deformation twinning alone did not predict the macroscopic or the microstructural responses. On the other hand, when these two mechanisms were coupled, better agreement was obtained, but the prediction of the lattice strains was still far from the measured response, primarily because of the model's inability to account for thermally-assisted deformation processes.
- d. Hot stage TEM confirmed the presence of $\{114\}_{B2}$ compound deformation twins at high temperatures (165 and 320 °C) in addition to a high density of dislocations in the deformed samples.
- e. Heating to 500 °C fully relaxed the internal state of the material, and reset the microstructure to the initial starting texture. Strains were also recovered during this heating process due to completion of the martensite to austenite phase transformation, back stresses, partially unstable deformation twins and enhanced diffusional processes.
- f. A B2 deformation map was generated based on the results presented in this work. This map is divided into regions (elastic, SIM and plastic), which indicate the limits over which each of the identified deformation mechanisms is dominant.

Chapter 4.—Role of B19' Martensite Deformation on the Stability of NiTi Two-Way Shape Memory Effect

Deformation of a B19' martensitic, polycrystalline $\text{Ni}_{49.9}\text{Ti}_{50.1}$ (at.%) shape memory alloy and its role on the magnitude and stability of the ensuing two-way shape memory effect (TWSME) was investigated by combined ex situ mechanical experimentation and in situ neutron diffraction measurements. The microstructural changes (texture, lattice strains, and phase fractions) during room-temperature deformation and subsequent thermal cycling were captured and compared to the bulk macroscopic response of the alloy. With increasing uniaxial strain, it was observed that B19' martensite deformed by reorientation and detwinning towards the $(\bar{1}50)_{\text{M}}$ and $(010)_{\text{M}}$ variants, $(20\bar{1})_{\text{B19'}}$ deformation twinning, and dislocation activity. These mechanisms were indicated by changes in bulk texture through neutron diffraction measurements. Partial reversibility of the reoriented variants and deformation twins was also captured upon load removal and thermal cycling, which after isothermal deformation to strains between 6 and 22 percent resulted in a strong TWSME. Consequently, TWSME functional parameters including transformation strain, strain reduction, and transformation temperatures were characterized and it was found that prior martensite deformation to 14 percent strain provided the optimum condition for the TWSME, resulting in a stable two-way shape memory strain of 2.2 percent. Thus, isothermal deformation of martensite was found to be a quick and efficient method for creating a strong and stable TWSME in $\text{Ni}_{49.9}\text{Ti}_{50.1}$.

4.1 Introduction

Near-equiatomic NiTi shape memory alloys (SMAs) undergo a reversible martensitic phase transformation between a cubic (B2) austenite phase and a monoclinic (B19') martensite phase. This first-order phase transformation gives SMAs their unique shape recovery capabilities, exemplified by two behaviors: the shape memory effect (temperature-induced phase transformation) and superelasticity (stress-induced phase transformation). Both behaviors have been widely exploited in a range of applications in response to aerospace, biomedical and industrial needs, amongst others [6]. NiTi SMAs can produce work (energy densities exceeding 10^7 J/m^3) [99], which allows them to be employed as solid-state actuators. Typically when used in such applications, the SMA elements remember the original austenitic shape and are used in conjunction with a biasing force to complete the actuation cycle. This is known as biased shape memory or one-way shape memory behavior. It is also feasible for these alloys to change and remember shapes on both heating and cooling without an external biasing force, a behavior known as the two-way shape memory effect (TWSME). TWSME is not an inherent behavior of SMAs, but can be obtained after specific thermomechanical training procedures.

Extensive research exists concerning the various methods used for inducing the TWSME [100]. Some of these training procedures consist of: constant load thermal cycling [101-108], martensite deformation and free/constrained recovery [109-116], deformation cycling of austenite to promote the stress-induced martensitic transformation [117-119], or precipitation during constrained aging [120-123]. The principle behind all these training methods involves the formation of internal stress fields that induce the same martensite variants during transformation as was generated during training, but without the need for an external stress. These stresses can be created by mechanisms such as dislocation arrays generated during thermomechanical training [107, 117], stabilized stress-induced martensite [119], retained martensite [116, 117], symmetry and point defects [124], or aligned coherent precipitates [120]. The associated internal stresses that are developed during these training procedures dictate the stability and efficiency of the TWSME. Thus, understanding the role of the adopted training schemes is essential in optimizing the performance of the ensuing two-way shape memory response.

Martensite deformation is probably the simplest but least understood training scheme. B19' martensite deformation proceeds through several mechanisms that operate over distinct strain ranges. Figure 4.1 is a representative stress-strain curve for martensitic NiTi, which for discussion purposes is divided into four main regions. Region I is the initial macroscopic tensile response up to ~1 percent strain, which is

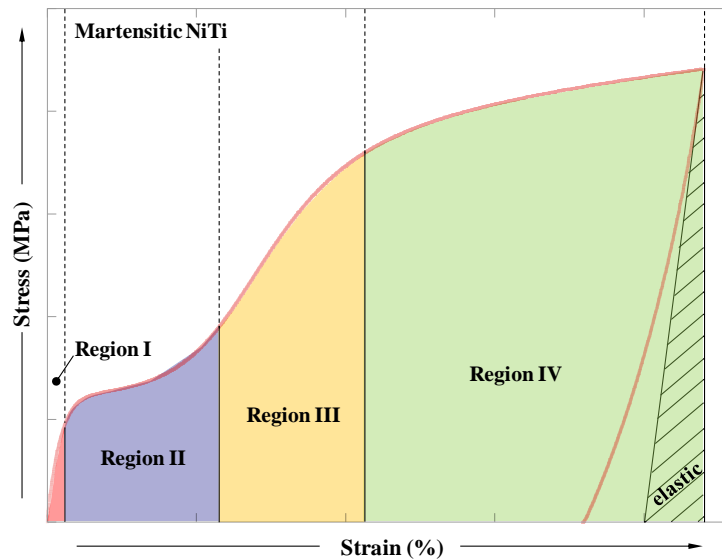


Figure 4.1.—General stress-strain response of martensitic NiTi showing the four distinct deformation regimes.

attributed to the elastic deformation of the self-accommodated B19' martensite coupled with early onset of variant reorientation and detwinning [43]. These latter processes are responsible for the non-linearity observed in the initial loading response of NiTi and the often deflated values of modulus reported based on mechanical test data. With increasing strain (Region II), a broad stress plateau is obtained where the deformation is mainly dominated by variant reorientation and detwinning of the initial [011] type II and ($\bar{1}\bar{1}1$) type I twinning modes [125-127]. In this same region, it has been reported that dislocation networks form in both the martensite twin plates [128] and in the junction plane areas [129] to accommodate the strain mismatch during variant reorientation. Further straining results in a Region III of rapid strain hardening, which is attributed to further reorientation and detwinning, the operation of new ($20\bar{1}$) and (100) deformation twins [126, 127, 130] and plasticity. Finally, Region IV, with a characteristic low work hardening rate, is due to further nucleation and growth of (100) and ($20\bar{1}$) deformation twin systems, possible formation of new (113) twins [126, 127] and dislocation generation [112, 126].

Training via martensite deformation has been shown to be effective in inducing the TWSME [112]. Compared to other methods, training by martensite deformation is relatively easy and quick, requiring little more than a onetime deformation of the material as opposed to aging under some type of constraint or performing multiple thermomechanical cycles. While theories have been proposed to explain this training route, no experimental studies have examined the micromechanical and microstructural changes associated with the martensite deformation that is responsible for development of the TWSME (e.g., texture evolution, internal strain fields, and phase volume fractions). In addition, the underlying martensite deformation mechanisms discussed above have not been linked to TWSME optimization. One way of revealing these microstructural parameters is by in situ neutron diffraction. Neutrons are uniquely suited to study the average microstructural response of bulk polycrystalline samples due to the deep penetration, large sampling volume, and elimination of free-surface effects. Therefore, use of in situ neutron diffraction coupled with ex situ macroscopic testing can provide additional insights into the B19' deformation mechanisms previously discussed and the ensuing TWSME.

Thus, the aim of this work was to investigate the role of martensite deformation on the stability and efficacy of the TWSME by carrying out in situ neutron diffraction measurements during isothermal loading and thermomechanical cycling. TWSME functional parameters and degradation (or lack thereof) were also measured from ex situ macroscopic experiments and correlated to the microstructural observations.

4.2 Experimental Techniques

The material used in this study was a binary NiTi alloy with nominal composition of Ni_{49.9}Ti_{50.1} (at.%) produced by Special Metals, New Hartford, New York. Cylindrical, dog-bone tensile specimens, 5.08 mm in diameter and 15.24 mm in gauge length were machined from a hot-rolled and hot-straightened 10 mm diameter rod. Prior to testing, two no-load thermal cycles were performed on the as-machined samples to relieve any residual stresses resulting from the machining operation. Stress-free transformation temperatures: martensite start (M_s), martensite finish (M_f), austenite start (A_s), and austenite finish (A_f) were measured from the second mechanical no-load thermal cycle using the intercept method [8] and were found to be 71, 55, 92, and 105 ± 2 °C, respectively.

Ex situ thermomechanical tests were performed on an 810 MTS servohydraulic load frame equipped with an MTS FlexTest SE digital controller, a Eurotherm 3504 temperature controller, an Ameritherm NovaStar 7.5 kW induction heater, a set of 646 water cooled hydraulic collet grips, a 22 kN/5 kip load cell, and a high-temperature, 12.7 mm gauge length extensometer. The ex situ experiments consisted of isothermal loading and unloading at room temperature followed by stress-free thermal cycling. Seven samples were strained individually in uniaxial tension to 6, 10, 14, 16, 18, 20, and 22 percent in strain control at a rate of 1×10^{-4} sec⁻¹ (Figure 4.2). The maximum strain imparted to each sample was selected specifically to study the deformation response of martensite in different regions of Figure 4.1. The microstructural response of NiTi during the initial loading up to 6 percent strain has been thoroughly investigated in Ref. [43], and hence omitted in this study. After straining each sample to a predetermined value, it was then unloaded to 0 MPa and thermally cycled 10-times through the phase transformation between room temperature and 200 °C using a heating rate of 30 °C/min (while holding the stress constant at 0 MPa).

In situ neutron diffraction experiments were performed in “time-of-flight” mode using the Spectrometer for Materials Research at Temperature and Stress (SMARTS) at the pulsed neutron source at Los Alamos National Laboratory (LANL). Similar to the ex situ experiments, five samples were individually strained in situ to 6, 10, 14, 18 and 22 percent, unloaded to 0 MPa, heated to 200 °C and cooled to room temperature using the same strain and heating rates listed above. Neutron diffraction spectra were collected at each step, i.e., at room temperature in the initial no-load condition, at the maximum strain achieved after tensile loading, and after unloading at 0 MPa, during heating at 200 °C, and again at room temperature after the cooling cycle. At each condition, neutron spectra were acquired for 30 min for adequate statistical quality.

The Rietveld refinement technique [21] implemented in the LANL code General Structure Analysis System (GSAS) [16] was used to analyze the neutron diffraction spectra. A generalized spherical harmonic description [17] was used in the code to capture the texture evolution during loading and/or heating. The single peak fitting method was also used to compute individual hkl lattice strains from planes perpendicular to the loading direction using the change in the interplanar spacing as described elsewhere [38].

4.3 Results and Discussion

4.3.1 B19' Martensite Deformation

The tensile stress-strain-temperature response of the Ni_{49.9}Ti_{50.1} alloy is shown in Figure 4.2 for seven samples deformed at room temperature to strains between 6 and 22 percent, unloading to zero stress, followed by thermal cycling. For clarity, only the first heating cycle is shown, though each sample was thermally cycled 10-times between room temperature and 200 °C. The first thermal cycle, included in Figure 4.2, will be referred to as the transient response in subsequent discussions.

The effect of martensite deformation on the subsequent strain recovery of the Ni_{49.9}Ti_{50.1} alloy is shown in Figure 4.3. The amount of springback after unloading (from the maximum strain to 0 MPa (B→C)) and the amount of strain recovery after the first thermal cycle at 0 MPa (C→D) are shown in Figure 4.3(a). The letters A-D refer to positions along the stress-strain-temperature curves indicated in Figure 4.2. The data indicate that the strain recovery due to unloading (B to C) increased with increasing

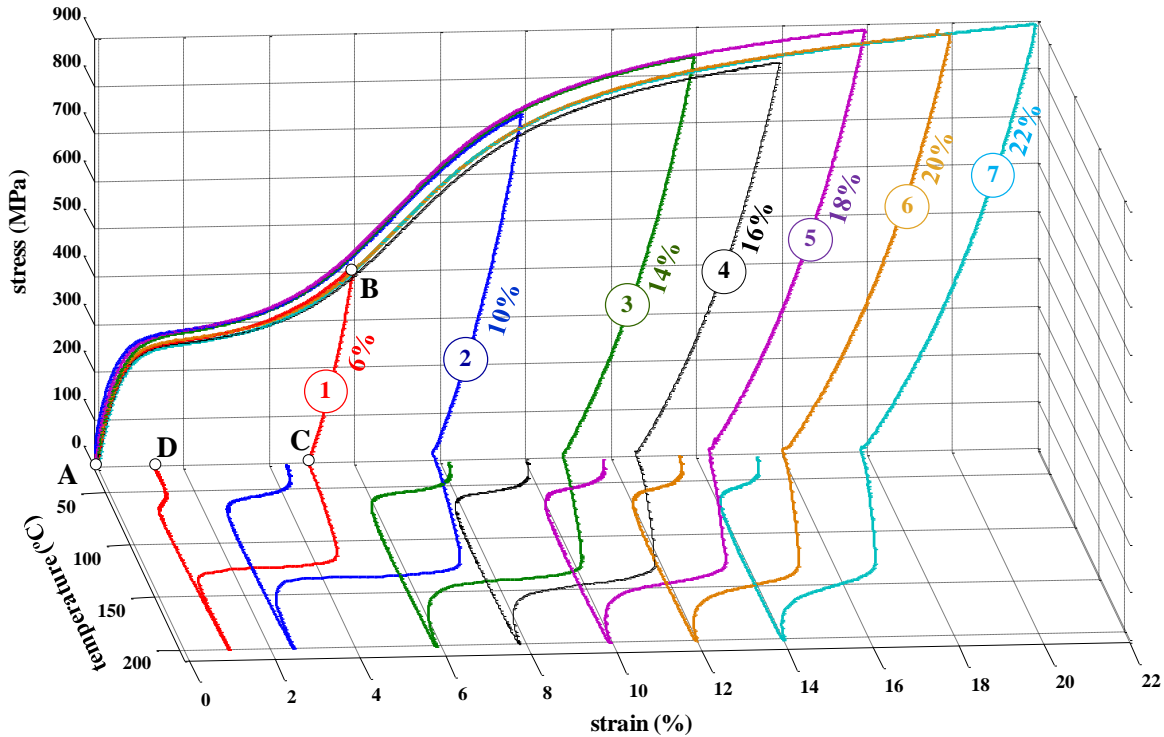


Figure 4.2.—Tensile stress-strain-temperature responses of seven $\text{Ni}_{49.9}\text{Ti}_{50.1}$ samples deformed at room temperature to strains between 6 and 22 percent, unloaded to zero stress, and thermally cycled to 200 °C and back to room temperature.

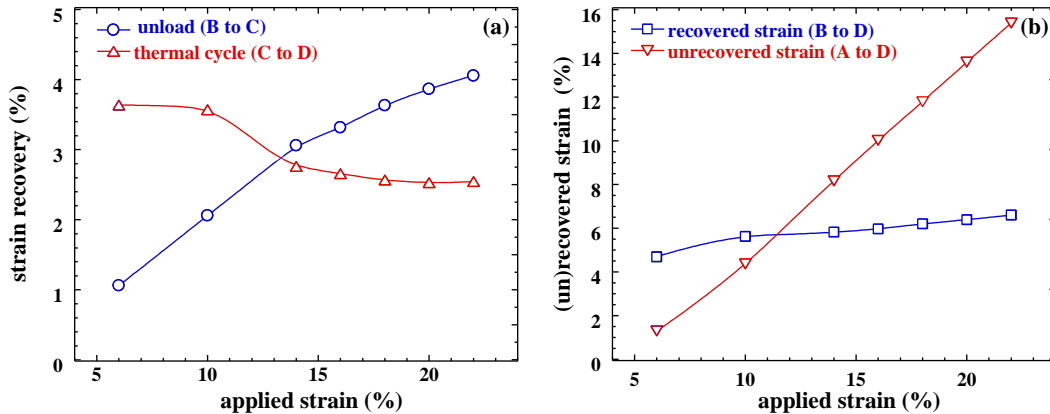


Figure 4.3.—Recovered and unrecovered strains through various regions of the stress-strain-temperature curves for $\text{Ni}_{49.9}\text{Ti}_{50.1}$ shown in Figure 4.2. (a) Recovered strains after unloading (from the maximum strain to 0 MPa (B→C)) and after the first thermal cycle at 0 MPa (C→D). (b) Total recovered strains including unloading and thermal recovery (B to D) and total unrecovered strains after the first thermal cycle (D to A).

applied strain, but was larger than anticipated based solely on elastic recovery. The strain recovery due to the first thermal cycle (C to D) appeared as a step function, decreasing to a lower level between 10 and 14 percent applied strain, as Region IV of Figure 4.1 is reached.

However, if the two strain recovery mechanisms are combined (B to D) the total strain recovery increases with increasing applied strain (Figure 4.3(b)). The unrecoverable component of the strains (D to A) also increased with applied strain, increasing in a nearly linear fashion. These observations are qualitatively consistent with a previous study [112]. The maximum total recoverable strain was 6.6 percent

for sample 7, which was strained to 22 percent. However the maximum thermally recovered strain occurred in the sample deformed only to 6 percent. The unrecovered strains become larger than the recovered strain at about 11.5 percent strain, as indicated by the line crossing in Figure 4.3(b), which is the beginning of Region IV of Figure 4.1. Overall, the linearity in both the total recovered and the unrecovered strains shown in Figure 4.3(b) and the step function in the thermally recovered strain as a function of applied strain implies that martensite deformation from 11 to 22 percent is possibly dominated by the same mechanism(s).

Neutron diffraction data was collected at critical points (i.e., positions A, B, C and D of Figure 4.2) to relate the observed macroscopic behaviors to microstructural mechanism(s). Figure 4.4 shows the IPFs for planes perpendicular to the loading axis in the B19' martensite for samples 1 (6 percent), 2 (10 percent), 3 (14 percent), 5 (18 percent) and 7 (22 percent). The value in parentheses after each sample number is the maximum strain each sample was deformed to initially. The numbers at the top left-hand corner of each IPF in Figure 4.4 indicate the respective maximum and minimum densities of grains with the given pole in the loading direction in multiples of random distribution. For reference, the major B19' variants that contribute to the deformation (i.e., $(\bar{1}50)_M$, $(010)_M$, and $(230)_M$) are indicated on the very first

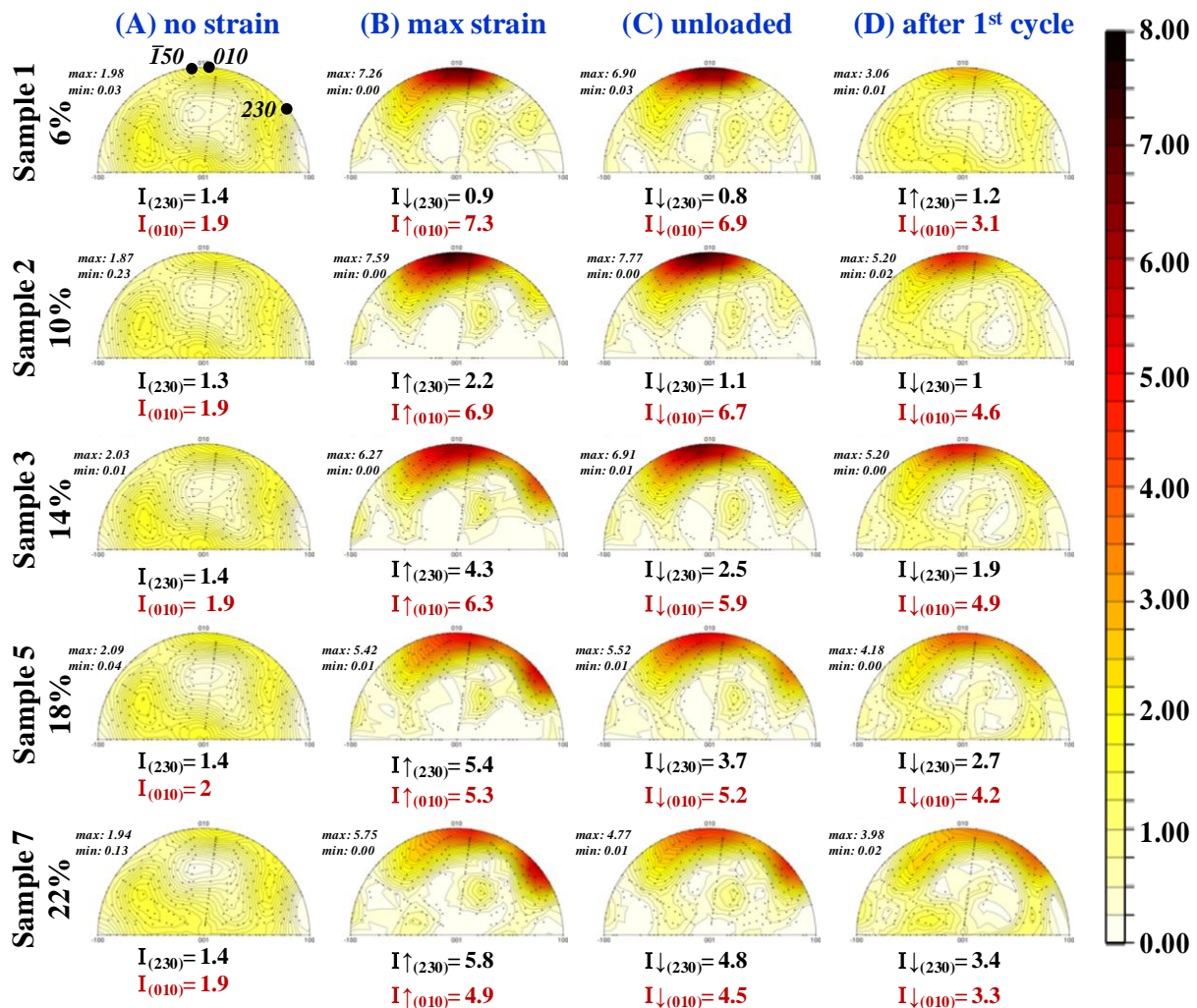


Figure 4.4.—Room temperature inverse pole figures (IPFs) for martensitic $\text{Ni}_{49.9}\text{Ti}_{50.1}$ from diffracting planes perpendicular to the loading direction. For a given IPF, the corresponding maximum and minimum pole intensities (times random) are at the top left hand corner and the specific intensity changes for the (230) and (010) poles are indicated below each IPFs. The column letters correspond to the positions identified in Figure 4.2.

IPF (top left-hand corner). The initial near random texture for the samples prior to testing, shown in column A of Figure 4.4, corresponds to the self-accommodated variants of the martensite phase as they exist in the bulk, polycrystalline aggregate. A similar initial texture was obtained for each sample tested.

On loading to 6 percent strain, direct evidence of variant reorientation/detwinning is presented by the texture shift toward the dominant $(\bar{1}50)_M$ and $(010)_M$ orientations. The initial nucleation and growth of these variants in Regions I and II along the loading direction were captured in detail in Ref. [43]. As observed in Figure 4.2, the 6 percent strain level resides in the initial portion of the rehardening region (Region III of Figure 4.1), where the $(010)_M$ martensite variants were observed to saturate with increasing strain. In fact, continuous texture measurements (not shown here) revealed that $(\bar{1}50)_M/(010)_M$ orientations reach a maximum between 7 and 9 percent strain where the $(230)_M$ orientations start to appear [131]. This is consistent with the IPF results in column B, where by 10 percent strain, which is just beyond the end of Region III, the intensity of $(010)_M$ is just starting to decrease and the intensity of the $(230)_M$ is just starting to develop.

With the saturation of the $(\bar{1}50)_M$ and $(010)_M$ martensite variants, a new texture forms with increasing strain, dominated by $(230)_M$ variant selection as shown by the IPFs in column B of Figure 4.4. This discrete reorientation of the maximum pole density from crystallites whose near $(010)_M$ plane normals were aligned with the loading axis to those whose $(230)_M$ plane normals become aligned with the loading direction starts between 6 and 10 percent strain and dominates the behavior at the higher strain levels. It is also observed that the intermediate area of the IPFs between the $(010)_M$ and $(230)_M$ gets slightly populated during this discrete reorientation. The discrete texture shift was related to the $(20\bar{1})_{B19'}$ deformation twinning, which is the plane normal that bisects the real directions of the $(010)_M$ and $(230)_M$ poles [131].

TEM studies by Zhang et al. [126] indicated that $(20\bar{1})_{B19'}$ deformation twinning was found to start at about 7 percent strain. In addition $(100)_{B19'}$ twinning was also observed by Zhang et al. [126] to take place before and in conjunction with the identified $(20\bar{1})_{B19'}$ twins in Regions III and IV. Consistently, these TEM results show evidence of $(20\bar{1})_{B19'}$ deformation twinning at relatively low strains (~7 percent), and the bulk texture results shown in Figure 4.4, indicate that this deformation mode begin to form at strains between 6 and 10 percent, which corresponds to Region III of the stress-strain response for martensite and that in this region the intensity of the $(230)_M$ continues to increase over the level of strains investigated. Note that the region of the IPFs between the $(010)_M$ and $(230)_M$ poles is not completely unpopulated due to a gradual rotation of the maximum pole density. This is consistent with what is observed when slip mechanisms are activated, although the slip plane and direction were not identified in this work due to the difficulty in studying the dislocation structures within the martensite.

The mechanical unloading sections of the stress-strain curves shown in Figure 4.2 were nonlinear in nature, which was attributed to the reverse reorientation of the martensite. This is captured by the IPFs in column C of Figure 4.4 that show a decrease in the maximum pole density at the $(230)_M$ orientation and a slight decrease in the $(\bar{1}50)_M$ and $(010)_M$ orientations after the samples were unloaded from the applied strain. Clearly, some of the $(20\bar{1})_{B19'}$ twins were partially reverted, contributing to the recovered strains during mechanical unloading (Figure 4.3).

Significantly more of the $(\bar{1}50)_M$ and $(010)_M$ variants were recovered in all samples during the first heating and cooling cycle (column D of Figure 4.4). In addition, $(230)_M$ variants were thermally recovered in samples deformed to 14 to 22 percent strain. In samples deformed to less strain, the $(230)_M$ density was unaffected and very close to randomly distributed in the samples deformed to 6 and 10 percent strain in the unloaded condition and after thermal cycling. This is consistent with the fact that the $(20\bar{1})_{B19'}$ twinning mode, which is presumably responsible for the $(230)_M$ texture changes, only begins to dominate at strain levels corresponding to Region IV. This deformation mechanism results in permanent strain in the martensite phase as shown in Figure 4.3(b). It was also reported [126] that the $(100)_{B19'}$ twins are recoverable upon heating, which could add to the strain recovery of Figure 4.3. However, the self-accommodated texture of the initial martensite (column A compared to column D in Figure 4.4) was not completely restored after one thermal cycle. This is due to preferential nucleation of the martensite variants favored during isothermal straining as the sample cools back to room temperature,

possibly as a result of internal stresses from the $(20\bar{1})_{B19'}$ twins and dislocation activity. This preferred nucleation of certain martensite variants is what is responsible for the TWSME. From the presented IPFs, the large strain recovery in this $\text{Ni}_{49.9}\text{Ti}_{50.1}$ alloy is attributed to the reorientation and detwinning mechanisms (Regions I and II), while the deformation twins along with dislocation generation are for the most part irreversible and lead to the irrecoverable strains (Regions III and IV). These latter mechanisms are responsible for the 70 percent unrecovered deformation in sample 7 deformed to 22 percent as shown in Figure 4.3(b), and the permanent strain in the other samples.

The no-load, transient strain-temperature responses of the first heating and cooling cycle after room-temperature deformation are shown in Figure 4.5(a). These responses were offset to a common starting point for easier comparison between samples as shown in Figure 4.5(b). On heating, strains were already being recovered (negative slopes) before reaching the transition temperatures where the material starts transforming to austenite. The negative slopes for the heating curves, or strain recovery could possibly be attributed to at least three mechanisms: (i) negative thermal expansion (ii) reverse reorientation of the martensite, and (ii) a change in the material compliance. It was recently shown that due to the anisotropy in the monoclinic structure, certain martensite variants exhibit a negative thermal expansion [38]. However, all the variants that formed along the loading direction for this material had a positive CTE and therefore could not contribute to the observed transient response.

That leaves the latter two mechanisms. Additional reverse reorientation with the application of temperature occurs as some variants and deformation twins partially rearrange in the martensite matrix before the phase transformation. Unfortunately, no IPF's were determined at intermediate temperatures, but only after the completed thermal cycle, so that it is not possible to know for certain whether reverse reorientation occurred prior to the transformation to austenite. However, possible strain recovery due to this reverse reorientation mechanism would be significantly aided by the change in the material's compliance during heating. It has been shown that the Young's modulus for NiTi alloys decreases with temperature reaching a significant minimum at about the start of the reverse transformation followed by a steep increase once the reverse transformation is completed [40, 132-134]. The $\text{Ni}_{49.9}\text{Ti}_{50.1}$ alloy studied here exhibits similar compliance characteristics that were measured using a dynamic technique (unpublished work) and would definitely provide a mechanism for reverse reorientation to occur with increasing temperature.

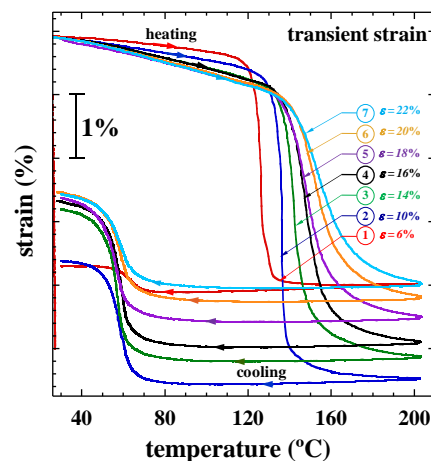


Figure 4.5.—Transient strain-temperature responses for the very first thermal cycle after load removal. Samples 1 to 7 correspond to the samples identified in Figure 4.2.

The initial slopes for the heating curves were also shifted more negative with increasing pre-strain values, which would be due to an increase in twin volume fractions and the internal strain developed in the material (Figure 4.5). This also would be consistent with a relaxation or reverse reorientation mechanism discussed above. Moreover, the transformation temperatures A_s and A_f were shifted to higher temperatures with increasing pre-strain. This is due to the high internal strain developed during reorientation and twinning of the martensite which resists the phase transformation. But on cooling, the forward transformation took place essentially at the same temperature regardless of the pre-strain level, and the final room temperature strain recoveries were grouped in two regions, as demonstrated in Figure 4.5 and by the step function in recovered thermal strain shown in Figure 4.3(a). However, the paths to the final strain level at room temperature were very different in all cases. For example, although samples 1 (6 percent) and 2 (10 percent) exhibited the same final recovered strain at room temperature, the paths for getting to that point were significantly different along every portion of the strain-temperature response. This included major differences in the initial slope during heating, the magnitude of the transformation strain between A_s and A_f , and the amount of TWSM strain developed during the forward transformation. Similar differences were observed for the other five samples deformed to higher strain.

Finally, the transient responses during heating show an incomplete transformation to austenite. Neutron diffraction data was acquired at the upper cycle temperature of 200 °C for each sample, which revealed the presence of untransformed/retained martensite. Through Rietveld refinements, it was estimated that samples 7 (22 percent), 5 (18 percent) and 3 (14 percent) contained ~8, ~5 and ~4 percent volume fraction of retained martensite at 200 °C, even though the stress free A_f temperature for the alloy was 105 °C. No detectable martensite was observed on samples 2 (10 percent) and 1 (6 percent). This retained martensite was mostly of the $(\bar{1}50)_M$, $(010)_M$ and $(230)_M$ orientations that can be both advantageous and disadvantageous to subsequent properties. The retained martensite can affect the internal stress fields aiding the TWSME on cooling, and it can act like dead material that does not transform reducing the transforming volume that contributes to the transformation capability of the material.

For a measure of the local internal state, the hkl -specific lattice strains were determined for the critical points noted in Figure 4.2, specifically at the maximum applied strain, after unloading to zero stress, and after the first thermal cycle. These strains are shown in Figure 4.6 and refer to the average strain in a family of variants with common crystallographic orientation (hkl) relative to the diffraction vector. They were obtained from the interplanar spacings ($\Delta d_{hkl}/d_{hkl}$) using the single peak fitting method. The $(011)_M$, $(030)_M$, $(\bar{1}20)_M$ and $(\bar{1}21)_M$ lattice strains were selected to represent the overall general trend observed in the material and are from diffracting lattice planes perpendicular to the loading direction. The dashed lines connecting the lattice strains during loading are not the actual material response since the strains were not continuously monitored, but only recorded at the discrete points, i.e., 6, 10, 14, 18 and 22 percent.

It is clear from Figure 4.6 that internal strains build up with increasing macroscopic pre-strain, followed by a decrease after unloading. Yet while the macroscopic far-field stress at this point is 0 MPa after unloading, the internal strains, which are related to the average variant-scale stresses, are still finite and in some cases quite significant, imposing local internal stress concentrations at the variant level. Increasing the temperature (before reaching the A_s) combined with a significant reduction in the material compliance relaxes these constraints, and results in further reverse variant reorientation, explaining the negative slopes of the transient responses of Figure 4.5.

After the first thermal cycle, a further decrease in the internal strains occur but they are still not fully relaxed, though in some cases are forced into compression, as observed in Figure 4.6. Consequently, the starting condition for the TWSME cycling (which are the subsequent thermal cycles imposed on the samples) consists of a microstructure that is different from the original microstructure, consisting of some pre-oriented martensite variants, as shown by the IPF's in column D of Figure 4.4, stabilized by a small but finite amount of internal stress/strain as defined in Figure 4.6.

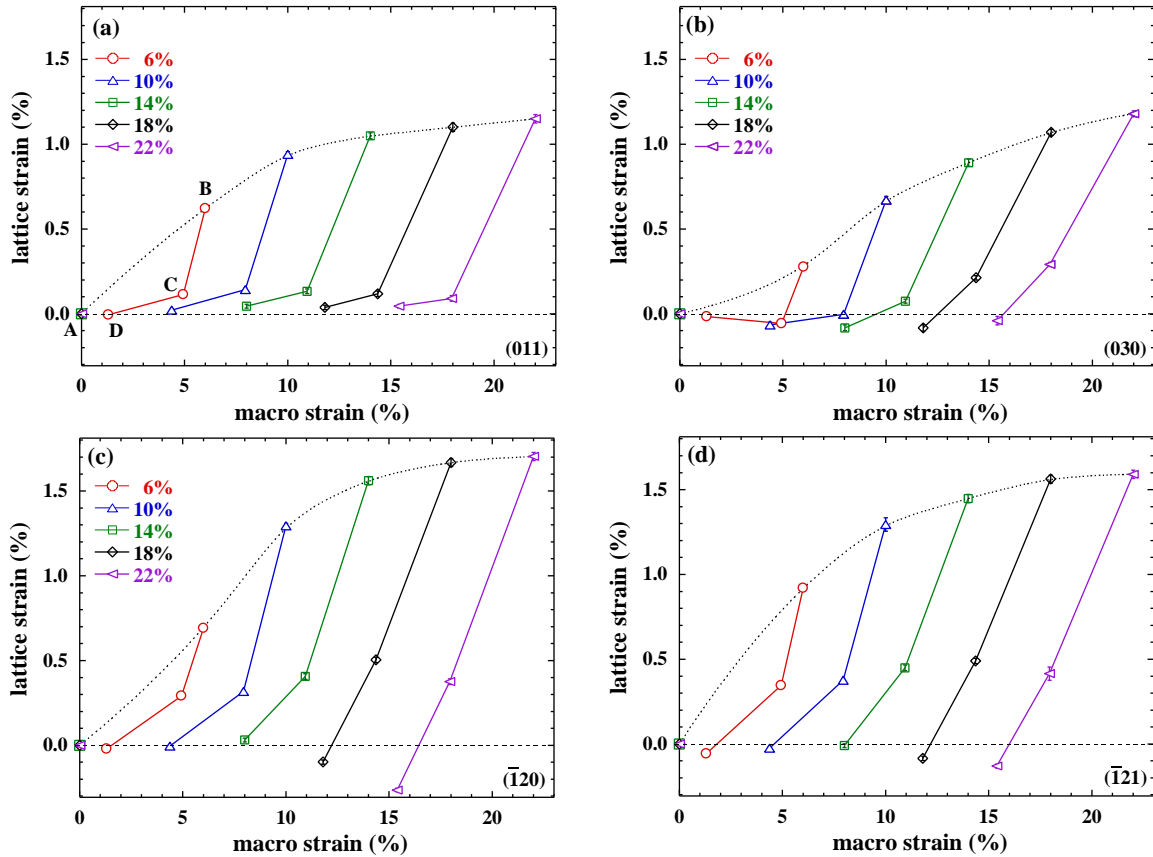


Figure 4.6.—Lattice strain associated with the a) (011)_M, b) (030)_M, c) ($\bar{1}20$)_M, and d) ($\bar{1}21$)_M planes perpendicular to the applied loading direction. Lattice strain data at maximum strain (B), after unloading (C), and after one thermal cycle (D) are shown for samples loaded between 6 and 22 percent strain for each of the planes measured.

4.3.2 TWSME Characterization

TWSME was introduced in this alloy by a onetime loading in the martensite phase to different pre-strain levels. Following this training procedure, the TWSME was characterized by stress-free thermal cycling between room temperature and 200 °C for a maximum of 10 cycles. The choice of the upper cycle temperature was made to ensure complete transformation when cycling under no-load. Figure 4.7 illustrates the strain-temperature responses of the ensuing TWSME as a function of the applied pre-strain levels. The first transient heating curves are also included in Figure 4.7 as indicated by the dotted lines. It was found that the magnitude of the transformation strain (calculated as the difference between the cold and hot-shape strains) was maximized in the samples deformed between 14 to 16 percent strain. This trend is better shown in Figure 4.8(a), which is the TWSME transformation strain plotted versus cycle number for each pre-strain condition, and in Figure 4.8(b) where the transformation strain is plotted as a function of pre-strain level. The TWSME transformation strain started low at 0.5 percent for sample 1 (6 percent), reached a maximum at 2.2 percent for sample 4 (14 percent) and dropped to 1.35 percent for sample 7 (22 percent).

For low pre-strains, the deformation was mainly governed by reorientation and detwinning toward the ($\bar{1}50$)_M and (010)_M variants as shown in Figure 4.4. Most of these variants were reversible upon unloading and thermal cycling, which resulted in a small TWSME as not enough oriented internal stress fields were generated (Figure 4.6) to strongly bias the transformation. At 14 percent strain, a maximum amount of the easily recoverable (010)_M and ($\bar{1}50$)_M variants were retained in the microstructure after unloading and

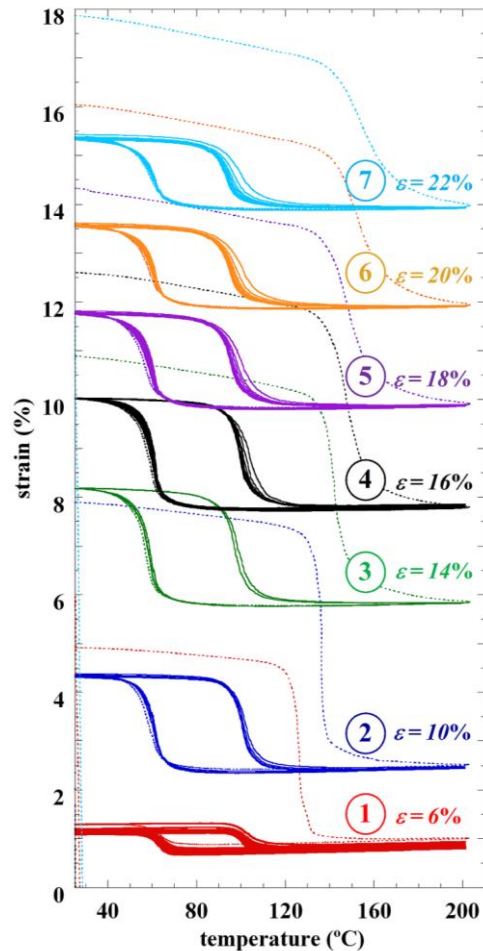


Figure 4.7.—TWSME strain-temperature responses for all samples pre-strained between 6 and 22 percent. The transient responses due to the very first heating cycle after unloading are also included (dotted lines).

even maintained after the first thermal cycle (column D of Figure 4.4). In other words, at this pre-strain level, a maximum volume fraction of these easily recoverable and high-strain capable variants are now reversibly formed in the microstructure. In addition, the $(20\bar{1})_{B19'}$ twin system was activated by this strain level, but a major portion of these twins were recovered primarily during unloading and also during heating (column D of Figure 4.4). Consequently, this pre-strain condition maximized the fraction of retained $(010)_M$ and $(\bar{1}50)_M$ variants, while minimizing processes that are more difficult to recover or carry less strain.

With further straining to higher levels on the second stress plateau (Region IV of Figure 4.1), less of the easily recoverable $(010)_M$ and $(\bar{1}50)_M$ variants and more of the irreversible twins were retained in the material (column D of Figure 4.4), reducing the amount of the transforming volume and strain carrying capability of the material. In addition, over straining can introduce dislocation structures that result in internal strains that do not promote favorable martensite variants and possibly even relax some of the internal constraints that do, resulting in less TWSME. Indirect evidence of this possible slip was presented in the IPFs of Figure 4.4 by the grain rotation between the $(010)_M$ and $(230)_M$ orientations (grains that populate the region between these two orientations). A simple change in twinning mechanism alone would show up in the measurements as a discrete shift in texture without gradual rotation.

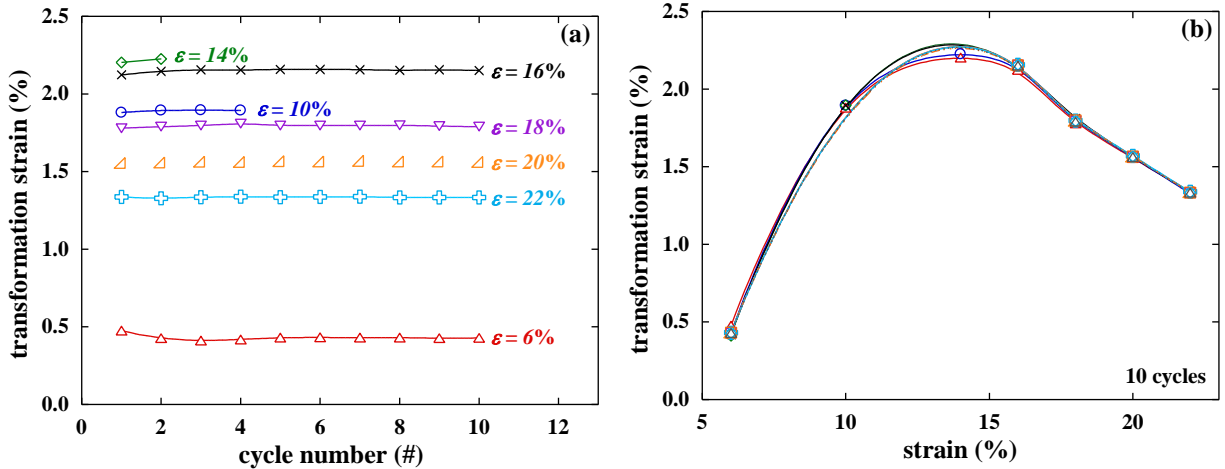


Figure 4.8.—TWSME transformation strain plotted as a function of (a) cycle number for all pre-strained conditions, and (b) the pre-applied strain level.

At every pre-strain value, the transformation strain is shown to be very stable from cycle to cycle (Figure 4.8(a)). However, it is evident from Figure 4.7 that there are some amounts of strain de-evolution (degradation in both the cold and hot-shape strains), particularly in sample 1 (6 percent). As a result, it is more proper to assess the stability of the TWSME by the strain reduction as a function of cycle count. The strain reductions were calculated from the difference in strain from one cycle to the next measured at room temperature. Compared to the other samples in this study, sample 1 (6 percent) exhibited large amounts of strain reduction during cycling (Figure 4.9) even though the transformation strain was relatively constant (Figure 4.8(a)). Samples 3 (14 percent) and 4 (16 percent) had near perfect dimensional stability as negligible strain reduction was obtained (Figure 4.9). At larger pre-strains, strain reduction increased again with increasing pre-strain values as shown by the samples deformed between 18 and 22 percent strain. These results indicate that both the magnitude and stability of the TWSME is maximized by pre-straining to 14 to 16 percent strain. The texture responsible for this optimal behavior includes both maximum contributions from the $(\bar{1}50)/(010)_M$ martensite variants, and minimal contribution, compared to the higher pre-strain levels, of $(20\bar{1})_{B19'}$ twins and dislocation induced plasticity in the material. Consequently, this level of pre-strain is a balancing act between maximizing the amount of high-strain, easily recoverable $(\bar{1}50)/(010)_M$ martensite variants that are biased in the material through internal strain and minimizing the amount of less useful $(20\bar{1})_{B19'}$ twinning and plasticity that occurs during the pre-strain process.

Other TWSME parameters of importance are the transformation temperatures. The data shown in Figure 4.10 illustrate the variation in stability of the transformation temperatures with increasing cycle number. For a given pre-strain level, the M_s , M_f and A_s are all shown to be within 2 °C during cycling, except for the A_f , which shows larger differences. Keeping in mind that these temperatures were measured using the intercept method [8], it is reasonable to associate an experimental error of ± 2 °C to these reported data. Therefore, other than a slight evolution in the A_f temperature with cycling, the transformation temperatures were quite stable regardless of pre-strain level. Also, while there were little differences in the transformation temperatures for samples pre-strained between 18 and 22 percent, there was a general trend. Transformation temperatures were always highest for sample 1 (6 percent) and tended to decrease with increasing pre-strain level. But overall, stability in the transformation temperatures was not an issue when applying this training procedure to $\text{Ni}_{49.9}\text{Ti}_{50.1}$.

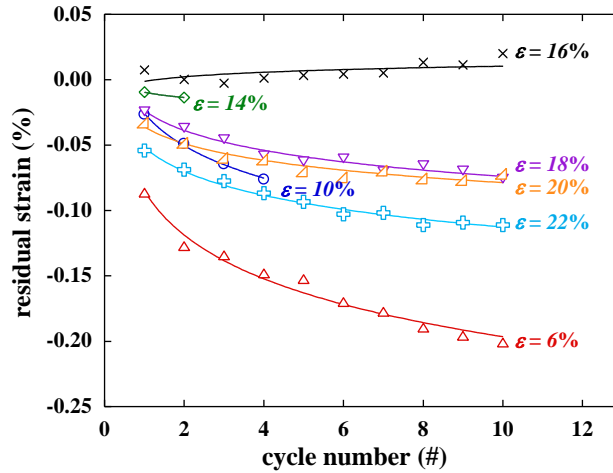


Figure 4.9.—Strain reduction during TWSME thermal cycling (measured at room temperature).

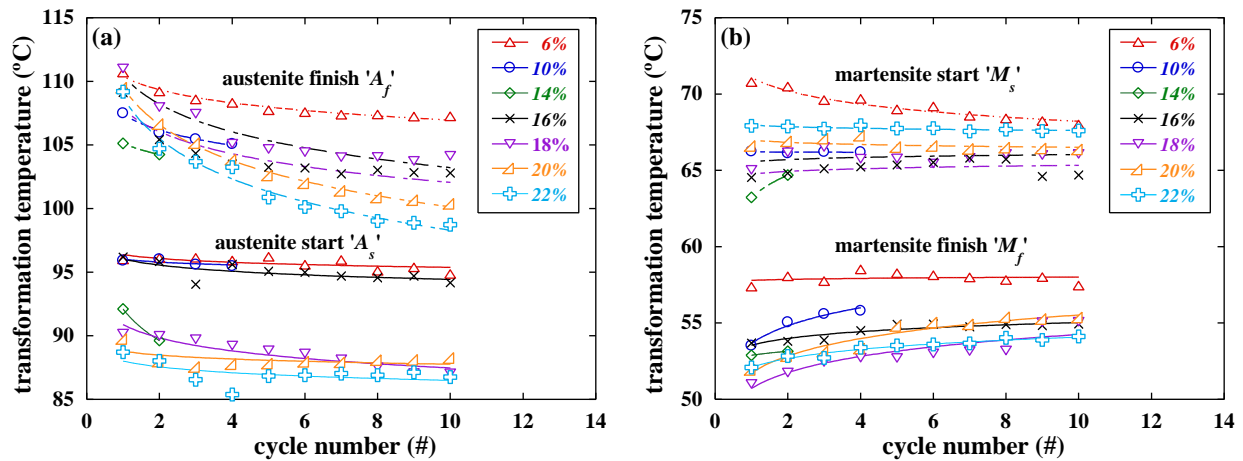


Figure 4.10.—Transformation temperatures determined during TWSME thermal cycling as a function of increasing cycle number.

4.4 Summary

Room-temperature deformation of a martensitic, polycrystalline $\text{Ni}_{49.9}\text{Ti}_{50.1}$ (at.%) shape memory alloy, and its subsequent effect on the TWSME was investigated by combining ex situ thermomechanical experiments and in situ neutron diffraction measurements. The role of the B19' martensite deformation on the magnitude and stability of the TWSME was assessed by examining the transformation strains, strain reduction, and transformation temperatures for a maximum of 10 stress-free thermal cycles. The following conclusions are reached.

- a. The nature of the room-temperature stress-strain response was correlated to the texture change observed at each selected pre-strain value.
 - (1) Deformation to 6 percent strain, which corresponds to the end of Region II deformation behavior (Figure 4.1), was mainly dominated by easy martensite reorientation and detwinning towards $(\bar{1}50)_M$ and $(010)_M$ poles along the loading direction, most of which were easily recovered after thermal cycling.
 - (2) From 6 to 12 percent strain (Region III in Figure 4.1), deformation was still primarily accommodated by martensite reorientation and detwinning towards $(\bar{1}50)_M$ and $(010)_M$ poles

but a secondary deformation mechanism was also observed that produced a strong reflection at the $(230)_M$ pole. This secondary mechanism was related to the $(20\bar{1})_{B19'}$ twin system. While the majority of this twin system was irreversible, fractions were also recovered after thermal cycling.

- (3) Further deformation resulted in a significant change in work hardening (and a transition into Region IV). In this region, at strains from 14 to 22 percent, no new texture components were observed, but deformation seemed to be dominated by processes that were more irreversible in nature. More of the $(20\bar{1})_{B19'}$ twins were retained in the sample after deformation and thermal cycling. Also, indirect evidence of slip mechanisms was also captured by the slight rotation of poles (e.g., $(010)_M$) during deformation.
- b. In general, reversible strains were attributed to the elastic recovery and reverse reorientation during unloading, and additional reverse orientation, and recovery of $(\bar{1}50)_M$ and $(010)_M$ martensite variants during thermal cycling and partial reversibility of the $(20\bar{1})_{B19'}$ twins. Irreversible strains were attributed to the permanent deformation twins and dislocations structures that cause a loss of correspondence to the original parent phase. Irreversible strains exceeded the reversible strains above ~12 percent applied strain (Region IV) as the deformation twins and dislocation generations started to dominate the behavior.
- c. Training via martensite deformation was shown to be a quick and effective way to introduce a stable TWSME.
- d. The pre-straining levels dictated the magnitude and stability of the ensuing TWSME. Pre-straining to 14 to 16 percent strain, or to the end of Region III, was found to be optimum for this material under the current testing conditions. Deformation to these strains maximized the amount of biased $(\bar{1}50)_M$ and $(010)_M$ martensite variants present in the material, while compared to higher strain levels, minimized the amount of $(20\bar{1})_{B19'}$ twinning. Under these conditions, a stable transformation strain of 2.2 percent was obtained with near-zero strain reduction. These strain calculations (transformation and reduction) in addition to the transformation temperature data are relevant to the design of shape memory alloy actuators that employ the two-way effect.
- e. Further work is needed to assess the consequences of changing one or more of the test conditions (tension/compression, strain/stress control, loading/heating rates, and the upper/ lower cycle temperatures) that may result in different behaviors. Moreover the transient response was not fully explored at this point, and more work is needed to explain this behavior.

Chapter 5.—Thermomechanical Cycling Of A Niti Shape Memory Alloy Investigated Using Neutron Diffraction

Thermomechanical cycling of a $\text{Ni}_{49.9}\text{Ti}_{50.1}$ (at.%) shape memory alloy was investigated by time-of-flight neutron diffraction at Los Alamos National Laboratory. Combined ex situ macroscopic experiments and in situ neutron diffraction measurements were performed in order to relate the macroscopic evolution (dimensional instabilities) to the responsible microscopic mechanism(s) through texture, internal strain, and phase evolution. The pre-deformation in the austenite or martensite phases revealed that the macroscopic cyclic properties (e.g., actuation strain) can be tuned to the desired magnitude based on the levels of deformations and associated active microstructural deformation modes. However, the pre-deformation did not stabilize the material response. Subsequent thermomechanical cycling revealed that the martensite and austenite texture did not change with continued thermal cycling, while the macroscopic transformation strains were still increasing. On the other hand, diffraction spectra peak shapes were found to vary with cycling indicative of possible lattice defects that accumulate with thermomechanical cycling. Microstructural evolution observed in texture, lattice strains and peak shapes are reported.

5.1 Introduction

Near-equiatomic NiTi shape memory alloys (SMAs) offer numerous attractive behaviors associated with a thermo-elastic martensitic transformation between a high temperature austenite phase (B2 ordered structure) and a lower temperature martensite phase (B19' monoclinic structure). Of these behaviors, the most commonly used are the shape memory (thermally-induced) and superelastic (stress-induced) behaviors. Both transformations result in large strain recoveries or large stress generation depending on the mode of operation. These unique properties have benefited a large number of applications including aerospace, medical and industrial technologies [6]. Nevertheless, when such applications require repeated thermally based actuation, SMAs have not been the primary material of choice due to their instabilities during thermal/mechanical cycling. As a result, widespread utilization of NiTi SMAs in cyclic actuation applications (particularly when employing the shape memory effect) has not been accomplished.

Cyclic instabilities manifest as changes in the thermomechanical response such as accumulation of irrecoverable strains, changes in transformation temperatures, transformation strains and/or thermal hysteresis. To date, there are several studies that report on the effects cycling has on NiTi functional properties, but a very limited number of studies exist on the microstructural mechanisms that govern these effects. Early work on cycling of NiTi alloys [91, 135-139] and recent work on thermal cycling [8, 76, 98, 137, 140-162] and mechanical cycling [51, 55, 66, 163-170] of SMAs have attributed the evolution of the macroscopic response to defects generation (dislocation and ordering effects), formation of intermediate phases (mostly the R-phase), precipitation, and martensite/austenite texture. Despite all of these studies and others not reported here, the microscopic mechanisms responsible for the instabilities in NiTi SMAs are still not fully understood. Until the underlying mechanisms are better understood, means to properly stabilize, train, and ultimately employ NiTi actuators will remain immature.

Therefore, the objective of this work was to examine the microstructural evolution of NiTi during thermomechanical cycling using combined ex situ macroscopic experiments and in situ neutron diffraction measurements. The high penetration of neutrons, compared to low energy x-rays, is representative of the bulk polycrystalline behavior and is typically free of surface effects. Information from grains and variants of a specific orientation relative to the loading direction are obtained and analyzed. The goal of this investigation was twofold: first, to study the role of pre-deformation in the austenite phase versus pre-deformation in the martensite phase on the subsequent thermomechanical cyclic response, and its role in optimizing transformation properties as they were linked back to the microstructural mechanisms; second, to follow the microstructural evolution including texture, internal strains and phase fraction during pre-deformation and thermomechanical cycling, since the macroscopic behavior of NiTi is related to the underlying changes associated with the martensite and austenite microstructures.

5.2 Material and Experimental Procedures

5.2.1 Material

The material investigated in this work was a binary $\text{Ni}_{49.9}\text{Ti}_{50.1}$ (at.%) alloy produced by Special Metals, New Hartford, New York. The alloy was received in 10 mm diameter rods in the hot-rolled/hot-drawn and hot-straightened condition. Mechanical test samples were machined from the extruded rods into cylindrical, dog-bone tensile specimens with a 5.08 mm diameter and 15.24 mm long gauge section with threaded button ends. Thermomechanical properties of this alloy are available in the literature [38, 43, 76, 171]. To relieve any residual stresses from the machining operation, all samples were subjected to two no-load thermal cycles between room temperature and 200 °C. Stress-free transformation temperatures: martensite start (M_s), martensite finish (M_f), austenite start (A_s), and austenite finish (A_f) were measured from the second no-load thermal cycle using the intercept method [172] and were found to be 71, 55, 92, and 105 ± 2 °C, respectively.

5.2.2 Ex situ Testing

Thermomechanical ex situ experiments were performed on an 810 MTS servohydraulic load frame. Individual samples were deformed isothermally in uniaxial tension to strains between 0 and 18 percent in strain control at a rate of $1 \times 10^{-4} \text{ sec}^{-1}$ (using a high-temperature extensometer), and then unloaded to 0 MPa (Table 5.1). Isothermal deformations in both the austenite phase at 320 °C (samples 1 to 4) and in the martensite phase at room temperature (samples 5 to 10) were carried out. The austenite temperature of 320 °C was selected to be above the M_d to ensure no stress-induced martensite effects (Chapter 3). Once unloaded, the sample was reloaded to 100 MPa at a rate of 10 MPa/s and cycled 10-times through the phase transformation between room temperature and 230 °C using a heating rate of 30 °C/min (while holding load at 100 MPa). This constant stress, thermal cycling tests will be referred to as the load-biased tests.

TABLE 5.1.—EXPERIMENTAL TEST CONDITIONS FOR 13 SPECIMENS
TESTED EX SITU AND/OR IN SITU AS INDICATED BY THE ‘x’

Specimen	Cycle, 0 MPa , 30↔230 °C	Deformation at 320 °C, %	Deformation at 30 °C, %	Unload, MPa	Cycle, 100 MPa , 30↔230 °C	Unload, MPa	Ex situ, Macroscopic	In situ, SMARTS
1	2	0	—	0	10	0	x	x
2	2	5	—	0	10	0	x	x
3	2	10	—	0	10	0	x	x
4	2	15	—	0	10	0	x	x
5	2	—	0	0	10	0	x	x
6	2	—	5	0	10	0	x	—
7	2	—	8	0	10	0	x	—
8	2	—	13	0	10	0	x	—
9	2	—	15	0	10	0	x	—
10	2	—	18	0	10	0	x	—
Specimen	Cycle 0 MPa , 30↔230 °C	Deformation at 320 °C, %	Deformation at 30 °C, %	Unload, MPa	Cycle, 200 MPa , 30↔230 °C	Unload, MPa	Ex situ, Macroscopic	Ex situ, HIPPO
11	2	—	0	—	0	0	x	x
12	2	—	0	—	20	0	x	x
13	2	—	0	—	50	0	x	x

5.2.3 In situ Neutron Diffraction Measurements

In situ neutron diffraction measurements were performed on the Spectrometer for MAterials Research at Temperature and Stress (SMARTS) at the Manuel Lujan Jr. Neutron Scattering Center, LANSCE, at

Los Alamos National Laboratory (LANL). Similar to the ex situ experiments, five tests (samples 1 to 5) were repeated in situ with neutron diffraction spectra collected before and after deformation, and at room temperature and 230 °C on each thermal cycle (Table 5.1). Neutron spectra were acquired for 30 min for adequate statistical quality.

5.2.4 Ex situ Neutron Diffraction Measurements

Additional macroscopic tests were performed ex situ using the same procedure described above. Two more samples were individually cycled 20 and 50 times at a constant stress of 200 MPa between room temperature and 230 °C (Table 5.1). Each sample was then unloaded and analyzed ex situ on the High-Pressure Preferred Orientation neutron diffractometer (HIPPO) [14, 15] for texture measurements at room temperature and at 200 °C (under no-load). In the current study, a total of 30 detector panels of diffraction angles 150°, 90° and 40° were used for texture measurements. For the austenite texture at 200 °C, individual samples were heated using a furnace with Niobium heating elements and heat shields. This furnace was integrated with a motor driven rotation stage to allow automated and accurate bulk texture measurement.

5.1.1 Neutron Diffraction Data Analysis

The Rietveld refinement technique [21] was used to analyze SMARTS and HIPPO neutron diffraction data. Rietveld method was implemented in the LANL codes General Structure Analysis System (GSAS) [16] and Materials Analysis Using Diffraction (MAUD)[18, 19], where both codes are based on minimizing the difference between measured and calculated spectra following a least squares scheme. From SMARTS data, inverse pole figures (IPFs) were constructed from both data with the parallel and perpendicular diffraction vectors using generic mapping tools. A single peak fitting method was also used to compute individual *hkl* lattice strains and peak breadths from the individual reflections. From HIPPO data, pole figures were generated for both the austenite and martensite phases.

5.3 Experimental Results and Discussion

5.3.1 Ex situ Macroscopic Behavior

The macroscopic isothermal stress-strain responses during uniaxial tensile loading of $\text{Ni}_{49.9}\text{Ti}_{50.1}$ are shown in Figure 5.1(a) for samples deformed in the austenite phase and in Figure 5.1(b) for samples deformed in the martensite phase. For samples 1 to 4 deformed at 320 °C (Figure 5.1(a)), the maximum strain imparted to each sample was selected specifically to study the role of austenite deformation on the cyclic behavior of the material (analogous to a hot working process). Particularly, 5 percent strain at the initial work hardening region, 10 percent strain at the low work hardening region, and 15 percent after negative work hardening. Similarly, samples 5 to 10 deformed at room temperature (Figure 5.1(b)) were selected to cover the distinct regions of the martensite phase deformation (analogous to a cold working process). These regions include the initial stress plateau up to 5 percent strain, the rapid rehardening region at 8 and 10 percent, the region of low work hardening at 13 and 15 percent, and finally at low/constant work hardening at 18 percent. The deformation mechanisms associated with each strain level for both the austenite and martensite phases can be found in Ref. [173].

After unloading to 0 MPa, each sample was reloaded to 100 MPa and cycled 10-times under this constant stress as shown in Figure 5.2(a) for the samples reloaded at 320 °C and in Figure 5.2(b) for the samples reloaded at room temperature. Only the samples deformed to 0, 5, 10 and 15 percent at room temperature are shown for clarity. These strain-temperature responses provide important properties for actuator applications such as the transient response, transformation strains, and unrecoverable (residual) strains. The transient response is generally observed on the very first heating cycle under load, and differs from the subsequent cycles. The transformation strain, which is used to compute the work output of the material in actuator form, was determined from the strain change associated with the heating portion of the thermal cycle using the intercept method [174]. The residual strains, a measure of the dimensional stability, were also determined from the difference in strain from one cycle to next at both the lower and upper cycle temperatures.

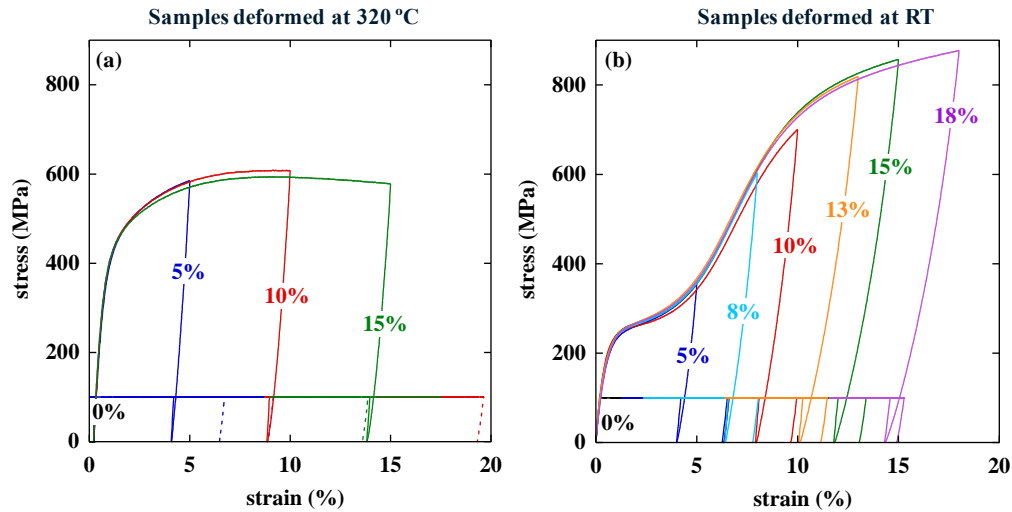


Figure 5.1.—Tensile stress-strain responses of $\text{Ni}_{49.9}\text{Ti}_{50.1}$ samples deformed at (a) 320 °C austenite and (b) at room temperature martensite to strains between 0 and 18 percent as indicated.

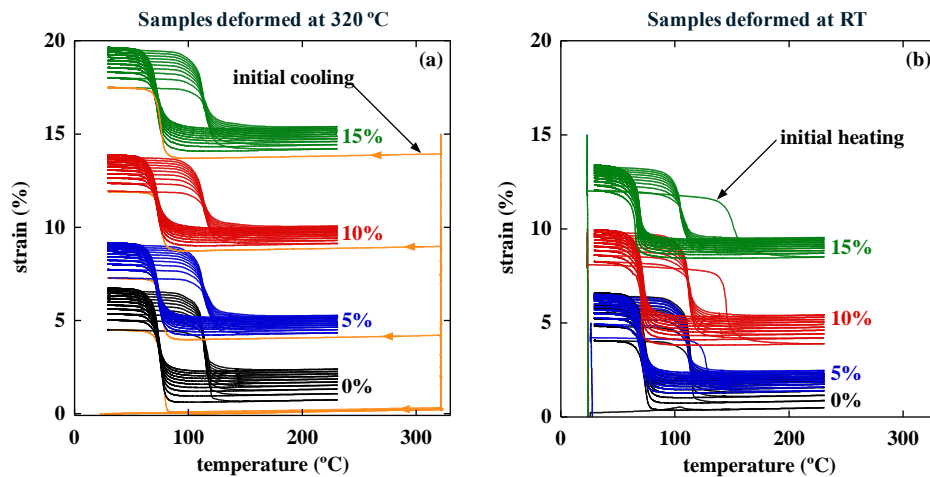


Figure 5.2.—Strain-temperature responses for (a) samples deformed and loaded at 320 °C, and (b) samples deformed and loaded at room temperature. The initial cooling (a) and heating (b) are also included. Cycling was performed under a constant 100 MPa stress between room temperature and 230 °C.

During the initial cooling from 320 °C (Figure 5.2(a)), a large strain was generated as the material transformed from austenite to martensite. The characteristic transient response was not observed in these samples reloaded in the austenite phase. On the other hand, when the samples were reloaded at room temperature and heated for the first time (Figure 5.2(b)), a strain transient was produced. This transient response only appears when twinned martensite variants transform to austenite for the first time (Figure 5.2(b)), and do not emerge when austenite grains transform to martensite (Figure 5.2(a)). The transient response was also dependent on the pre-deformation levels as both the magnitude and transformation temperatures varied. The initial (first cycle) A_s and A_f were shifted to higher temperatures with increasing martensite deformation as the irreversible deformation processes dominate. These permanent processes, mainly activation of irreversible deformation twins and dislocation generation [173], interact with the reoriented/detwinned martensite variants and resist the forward phase transformation, requiring more thermal energy to drive the phase transition.

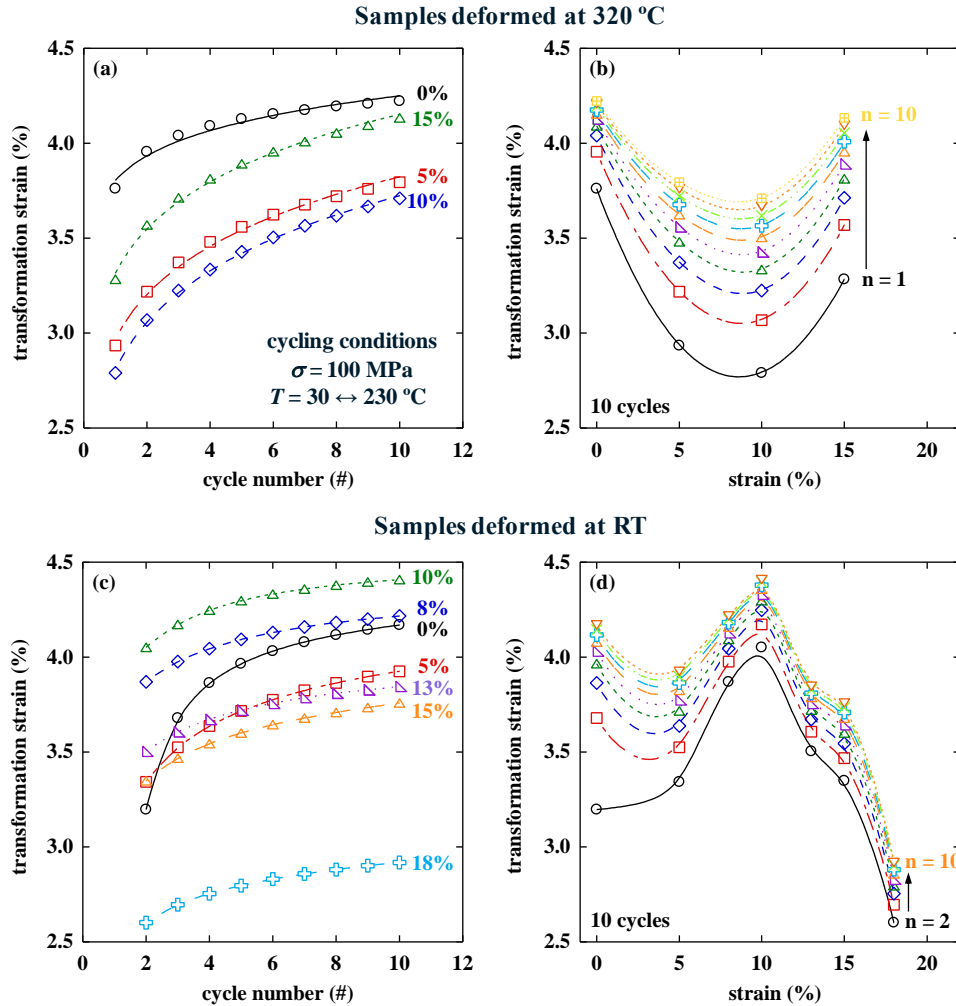


Figure 5.3.—Transformation strains for (a) and (b) samples deformed and loaded at 320 °C, and (c) and (d) samples deformed and loaded at room temperature. The data is plotted as a function of (a) to (c) cycle number for all pre-strained conditions, and (b) to (d) the pre-applied strain level.

Further cycling shows the partial strain recovery and strain evolution with increasing cycle number. The quantitative difference between the transformation strains are shown in Figure 5.3(a) and (b) for the samples deformed and reloaded at 320 °C and in Figure 5.3(c) and (d) for the samples deformed and reloaded at room temperature. At a constant cycle, the transformation strains shown in Figure 5.3(a) and (b) decreased from 0 to 10 percent deformation, and then increased for the sample deformed to 15 percent. It has been shown in Ref. [173] that the B2 austenite deforms by the occurrence of $\{114\}_{B2}$ compound deformation twins along with $\langle 001 \rangle$ slip processes. These irreversible mechanisms significantly reduce the transformation strain. Further loading to 15 percent where strain softening behavior was observed (indication of lower dislocation density), resulted in an increase in transformation strain due to possible activation of diffusion controlled mechanisms. In all cases, the transformation strains increased with increasing cycle number and nearly reached saturation at the 10th cycle as shown in Figure 5.3(b). Note that the maximum transformation strain at the 10th cycle of 4.22 percent was obtained for the undeformed sample (0 percent), while the 15 percent deformed sample showed an increasing trend approaching this value.

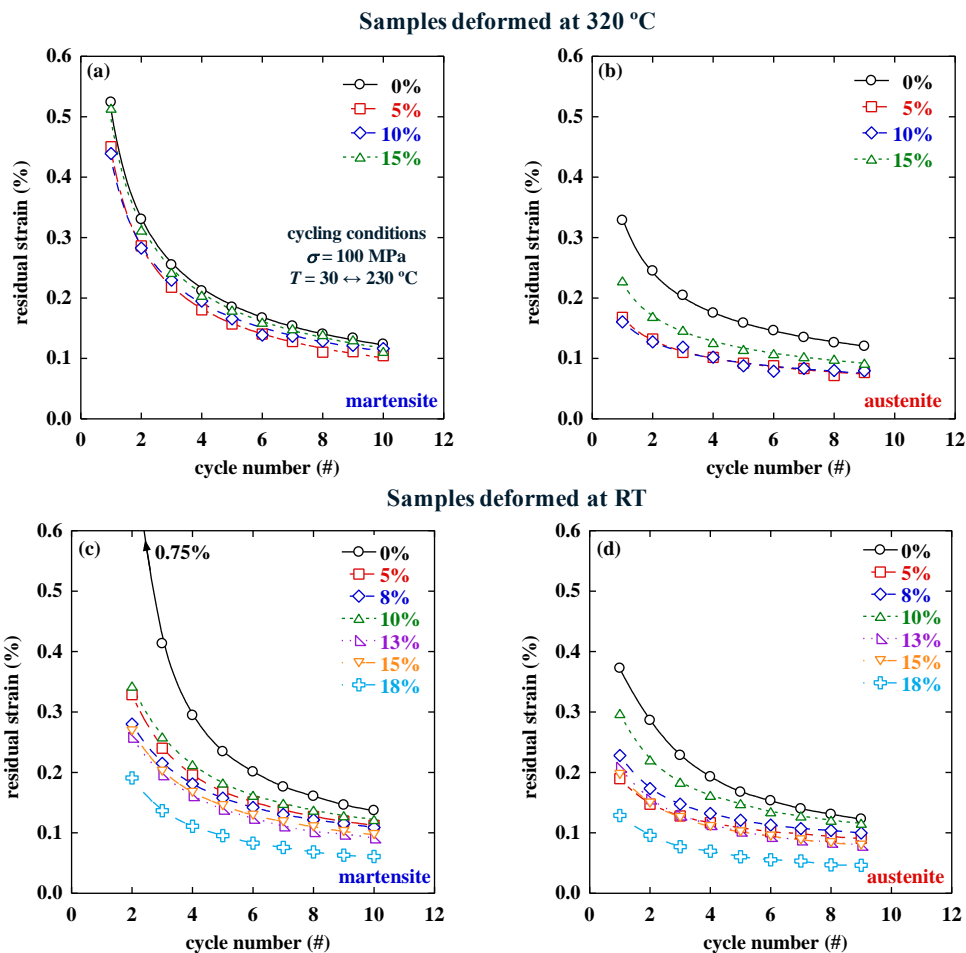


Figure 5.4.—Residual strain accumulation during thermomechanical cycling of (a) and (b) samples deformed and loaded at 320 °C, and (c) and (d) samples deformed and loaded at room temperature. These residual strains were measured at (a) to (c) room temperature and (b) to (d) 230 °C.

The trend of the transformation strains for the samples deformed/reloaded at room temperature was much different as shown in Figure 5.3(c) and (d). The transformation strain was found to be maximum at the sample deformed to 10 percent strain which is opposite to the behavior shown in Figure 5.3(a) and (b). After the 10 percent deformation, higher deformation values resulted in reduced transformation strains which was reduced to 2.2 percent for the sample deformed to 18 percent. The martensite deformation transitions from a region of rapid strain hardening to a region with a characteristic low work hardening rate at about 10 percent strain (Figure 5.1(b)). At this transition point, the unrecovered deformation becomes larger than the recovered deformation due to dominance of $(20\bar{1})$ deformation twins and dislocation generation as was described in Ref. [173]. As result, the transformation strain at the 10th cycle decreased from 4.4 percent at 10 percent pre-deformation to 2.9 percent at 18 percent pre-deformation.

The residual strains measured at both room temperature and at 230 °C are shown in Figure 5.4(a) and (b) for the samples deformed and reloaded at 320 °C and in Figure 5.4(c) to (d) for the samples deformed and reloaded at room temperature. Similar to the transformation strains, at the same cycle, the residual strains decreased for samples deformed to 5 and 10 percent and then increased for the sample deformed to 15 percent (Figure 5.4(a) and (b)). With increasing cycle number, all the samples show an overall decrease in the residual strains, but the rates were different for the residual strains measured at the martensite and austenite phases. At the room temperature side, austenite transforms to martensite with the

applied load in favor, which tends to elongate the sample more resulting in higher rates. On the other hand, at the high temperature side, the martensite transforms to austenite recovering strains against the applied load, resulting in lower evolution rates. These differences in the residual strains (larger at room temperature but smaller at higher temperature) are a result of the deformation/transformation mechanisms that take place during the phase transition, which ultimately dictate the increase/decrease in the transformation strains. For the samples deformed at room temperature shown in Figure 5.4(c) and (d), a similar trend can be observed. However, the difference in the amount of residual strains was larger for samples deformed at room temperature compared to those deformed at 320 °C. In all cases, the residual strains reduced significantly by the end of the 10th cycle, but did not reach saturation as more cycles are needed to stabilize the material.

It is clear from these macroscopic results that both the deformation and loading at different temperatures (i.e., loading at different phases) have an impact on the cyclic thermomechanical response of the material. Moreover, the transformation specific properties are shown to evolve with increasing number of cycles. The underlying microstructural changes as they relate to the observed macroscopic behavior are now presented.

5.3.2 In Situ Neutron Diffraction Results

In situ neutron diffraction experiments were aimed towards capturing the microstructural changes (texture, internal strain and peak breadth) during deformation and subsequent thermomechanical cycling. The microstructure of the Ni_{49.9}Ti_{50.1} alloy consisted of an austenitic, cubic B2 structure best fitted using a *Pm* $\bar{3}$ *m* structure with a no-load lattice parameter of $a=3.0319\text{\AA}$, and a martensitic, monoclinic B19' structure best fitted using a *P112*₁/*m* structure with no-load lattice parameters $a=2.903\text{\AA}$, $b=4.64\text{\AA}$, $c=4.12\text{\AA}$, $\alpha=\beta=90^\circ$ and $\gamma=97.63^\circ$, as determined from the Rietveld refinement method. Both diffraction data from planes perpendicular and planes parallel to the loading direction are reported. Only the results obtained for samples 1 to 4 deformed at 320 °C are presented in the following sections.

5.3.2.1 Texture Evolution

Sections of normalized, room temperature diffraction spectra for samples pre-deformed at 320 °C are shown in Figure 5.5(a) to (d) for diffracting lattice planes perpendicular to the loading axis, and in Figure 5.5(e) to (h) for diffracting planes parallel to the loading axis. These B19' reflections indicate the evolution of the (011)_M and (100)_M planes for the following conditions: (i) the initial two no-load cycles before deformation (cycles 1 to 2), (ii) after deformation, loading to 100 MPa and cooling (labeled *LOAD*), (iii) for the subsequent 10 load-biased thermomechanical cycles (cycles 3 to 12), and (iv) after unloading to 0 MPa (cycle 13). As expected, the initial two no-load cycles were very comparable (both in intensity and breadth) indicative of the self-accommodative nature of the B19' martensite. Once the samples were loaded at 320 °C and cooled back to room temperature, the intensity of the (011)_M increased while the intensity of the (100)_M completely vanished in the perpendicular planes of Figure 5.5(a) to (d). The opposite can be observed for the parallel planes where the (011)_M planes decreased and the (100)_M increased in intensity as shown in Figure 5.5(e) to (h). Continued thermomechanical cycling had little to no effect on the intensities up to the tested 10th load-biased cycle. Similar diffraction spectra for the (030)_M planes perpendicular to the loading axis (Figure 5.6(a) to (d)) and for the (102) planes parallel to the loading direction are also shown in Figure 5.6(a) to (d) and Figure 5.6(e) to (h), respectively. These planes are some of the most favored martensite variants that form in tension as indicated by a large intensity increase after loading, and saturation at the same intensity with cycling.

In addition to the abovementioned planes, analyses of the intensity changes that occur were made by considering the entire spectrum. This is represented by the IPFs acquired at room temperature for the B19' martensite at the same conditions discussed in Figure 5.5. These IPFs, shown in Figure 5.7(a) for planes perpendicular and in Figure 5.7(b) for planes parallel to the loading direction, correspond to the samples deformed to 0, 5, 10 and 15 percent at 320 °C. For clarity, unique multiples of random distribution (MRD) scales were adopted given the differences in the strengths of texture for each data set. The IPFs

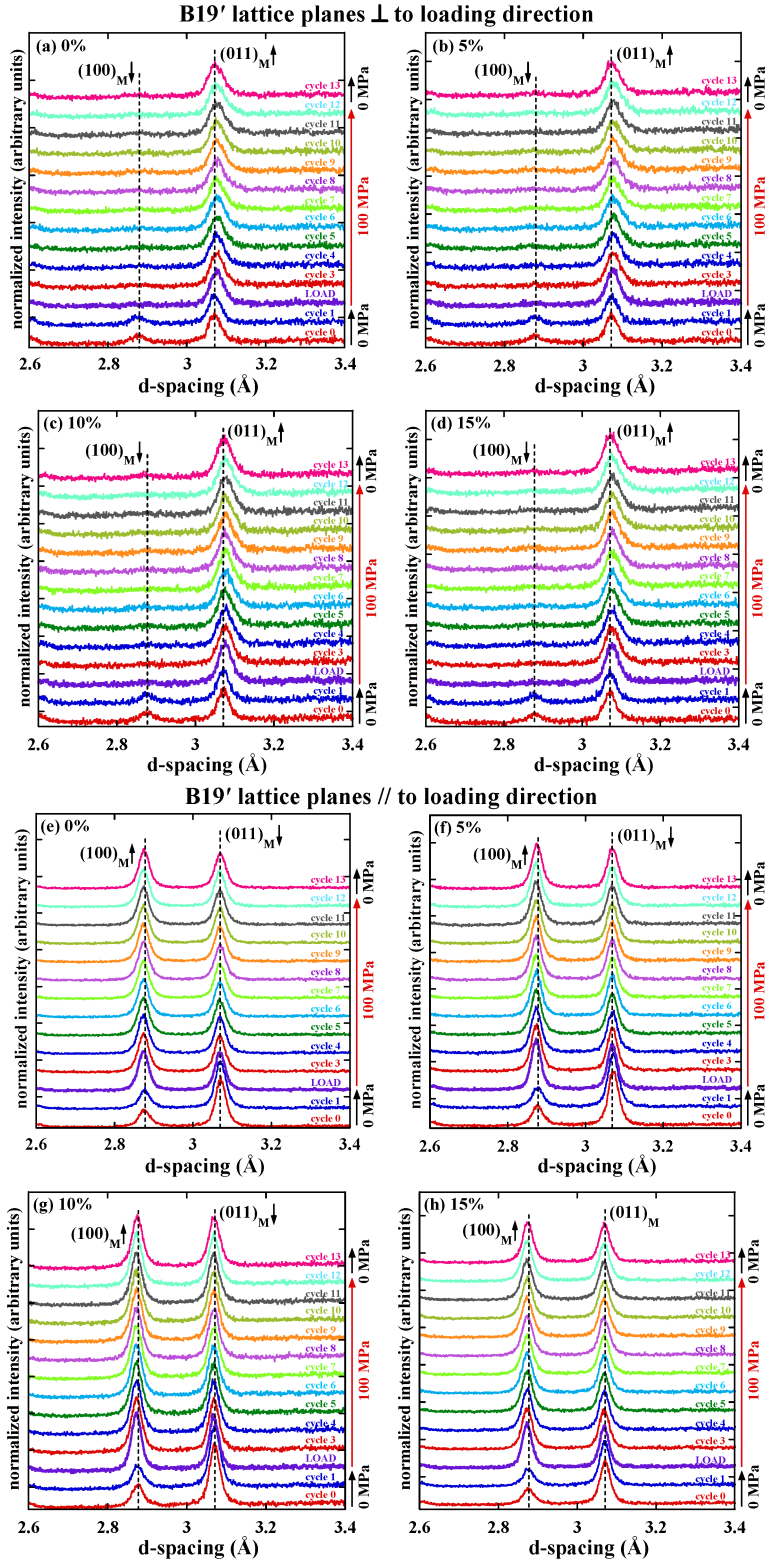


Figure 5.5.—Normalized neutron diffraction spectra acquired at room temperature during cycling of the samples deformed at 320 °C (samples 1 to 4 of Table 5.1). These reflections are from the $(100)_M$ and $(010)_M$ lattice planes (a) to (d) perpendicular and (e) to (h) parallel to the loading axis. The initial no-load cycles and the first cycle after loading to 100 MPa are included. The arrows indicate the intensity increase or decrease when the samples were first loaded (labeled *LOAD*).

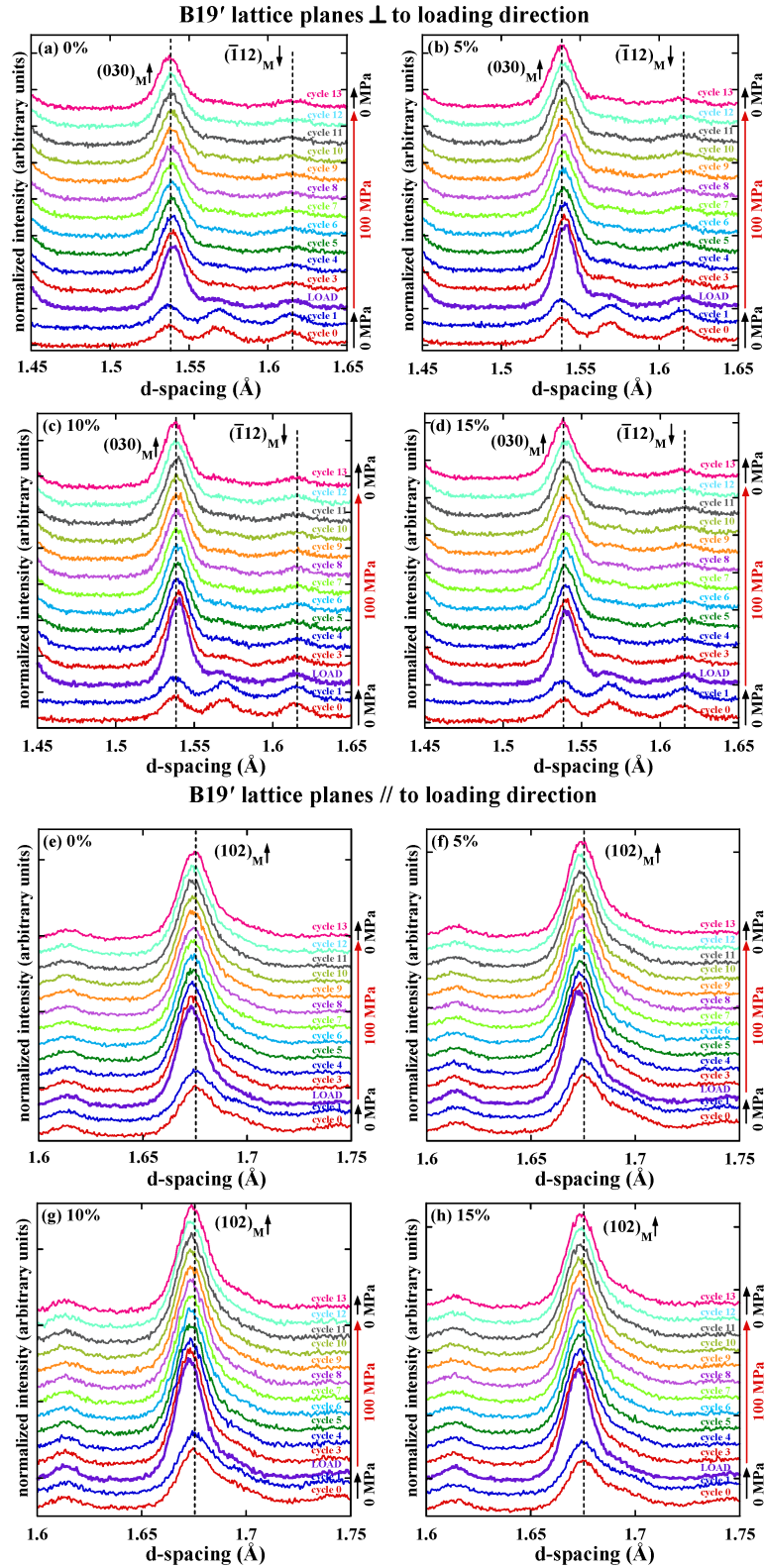


Figure 5.6.—Normalized neutron diffraction spectra acquired at room temperature during cycling of the samples deformed at 320 °C (samples 1 to 4 of Table 5.1). These reflections are from the (a) to (d) $(030)_M$ and $(\bar{1}12)_M$ lattice planes perpendicular to the loading axis, and (e) to (h) $(102)_M$ lattice planes parallel to the loading axis. The arrows indicate the intensity increase or decrease when the samples were first loaded (labeled LOAD).

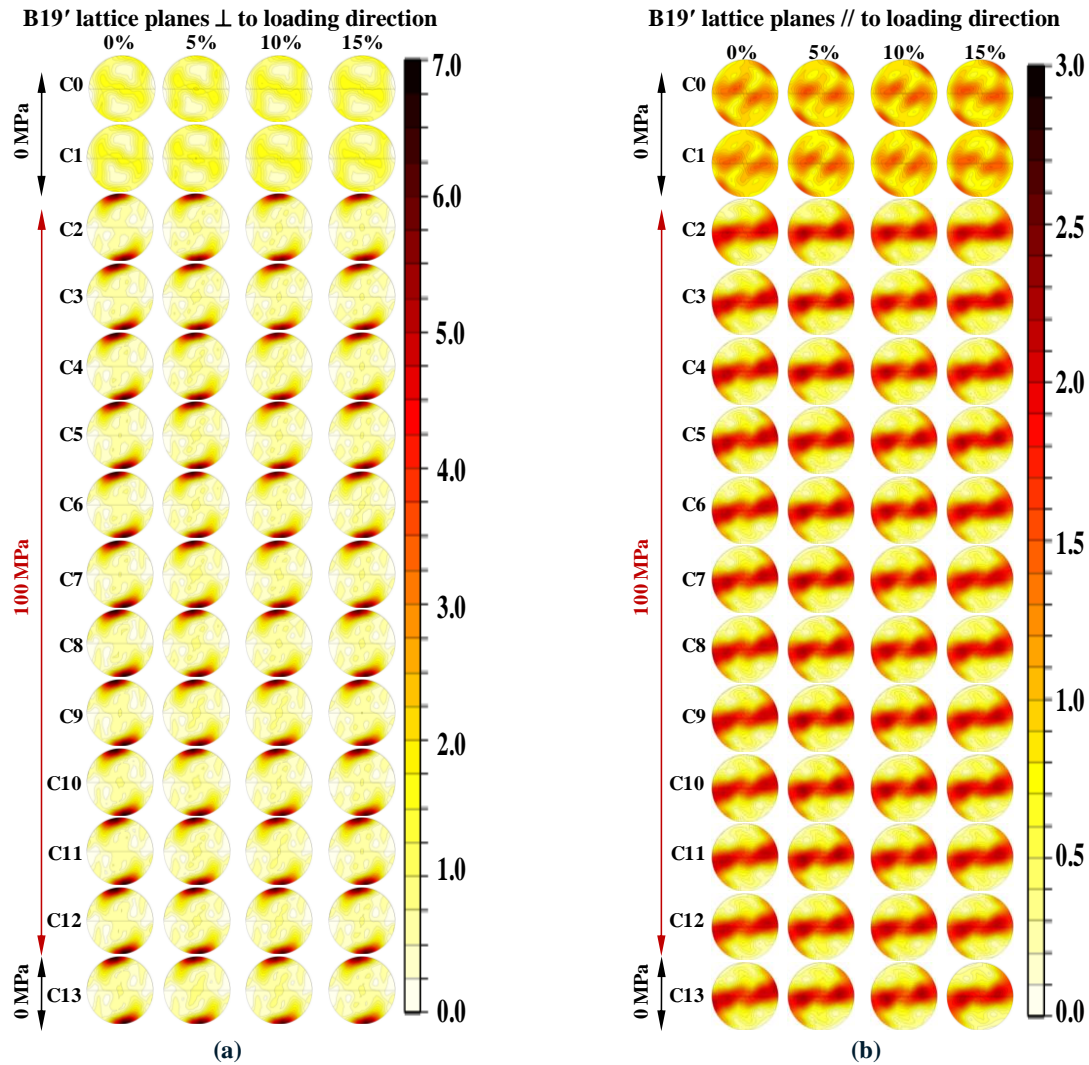


Figure 5.7.—Room temperature IPFs for martensitic $\text{Ni}_{49.9}\text{Ti}_{50.1}$ from diffracting planes (a) perpendicular and (b) parallel to the loading direction. This data belongs to the samples deformed at 320 °C (samples 1 to 4 of Table 5.1). Cycle numbers C0 to C13 correspond to the diffraction spectra shown in Figure 5.5 and Figure 5.6. For clarity in presentation, different scales are used in each direction.

pole locations are shown in Figure 5.8 by the irreducible monoclinic (Figure 5.8(a)) and cubic (Figure 5.8(b)) stereographs with select crystal orientations. The labels C1 to C13 correspond to cycles 1 to 13 shown in Figure 5.5 and Figure 5.6. It is clear from the IPFs in Figure 5.7 that the texture evolved during the first load-biased thermal cycle (indicated by C2) and then remained mostly unchanged for subsequent cycles. In particular, the intensities at the $(030)_{\text{M}}$ and $(\bar{1}50)_{\text{M}}$ orientations (Figure 5.7(a)) increased as the material cycles through the phase transformation for the first time under load, but did not change significantly for succeeding thermal cycles under the same constant load of 100 MPa. Similarly, the intensities at the $(001)_{\text{M}}$, $(102)_{\text{M}}$ and $(100)_{\text{M}}$ orientations (Figure 5.7(b)) increased and remained unchanged after the first load-biased cycle.

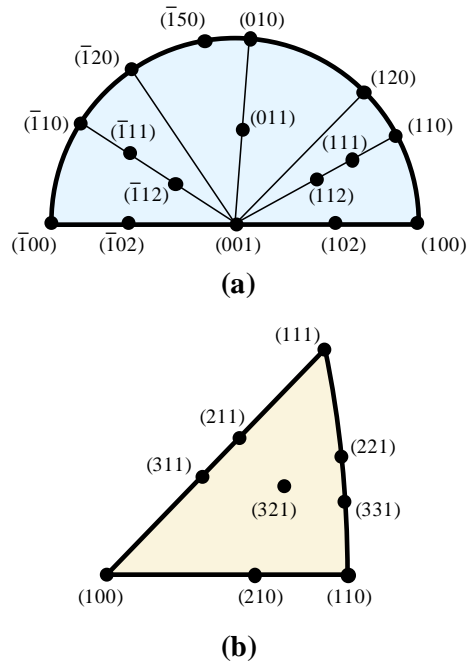


Figure 5.8.—The IPFs pole locations for the irreducible (a) monoclinic and (b) cubic stereographs with select crystal orientations.

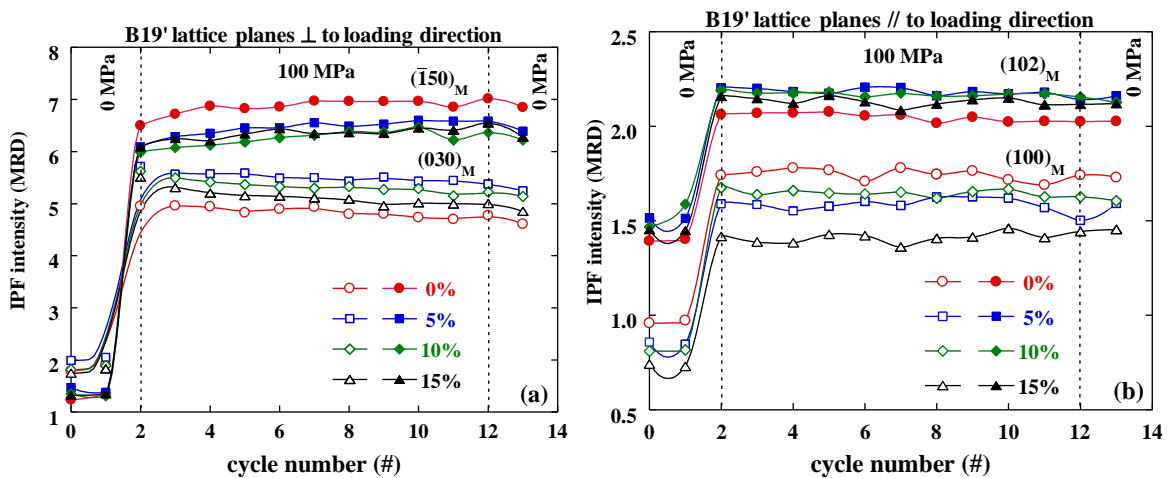


Figure 5.9.—IPFs pole intensities for the selected (a) $(030)_M$ and $(\bar{1}50)_M$ martensite variants perpendicular to the loading axis, and (b) $(100)_M$ and $(102)_M$ martensite variants parallel to the loading axis.

For a quantitative measure of the IPFs magnitude, the pole intensities associated with some of the preferentially oriented variants of Figure 5.7 were plotted in Figure 5.9(a) for planes perpendicular and in Figure 5.9(b) for planes parallel to the loading direction. The intensities of the selected orientations were again observed to increase after loading and cycling for the first time, but remained unchanged in the subsequent cycles, similar to previous observations. However, there were differences in texture between samples that were deformed to 0, 5, 10 and 15 percent strain at 320 °C. The $(\bar{1}50)_M$ intensity decreased in samples 2 and 3 deformed to 5 and 10 percent, respectively, and then increased in sample 4 deformed to

15 percent, consistent with the macroscopic data of Figure 5.3(a) and (b). The opposite behavior can be observed for the $(030)_M$ intensity.

Texture of the B2 phase was also examined in a similar manner by looking at the raw data (Figure 5.10), IPFs (Figure 5.11) and normalized pole intensities (Figure 5.12). Sections of normalized $\{110\}_A$ diffraction spectra acquired at 230 °C for samples initially deformed at 320 °C are shown in Figure 5.10(a) to (d) for diffracting lattice planes perpendicular to the loading axis, and in Figure 5.10(e) to (h) for diffracting planes parallel to the loading axis. The conditions shown here are: (i) B19' spectrum taken at room temperature for reference, (ii) the initial no-load condition taken at 230 °C, (iii) after deformation to the indicated strain level at 320 °C, (iv) after unloading to 0 MPa at 320 °C (cycle 0), (v) after reloading to 100 MPa at 320 °C (indicated by *LOAD*), and (vi) the subsequent 10 load-biased thermomechanical cycles taken at 230 °C (cycles 2 to 11). Changes in intensity were apparent when the samples were deformed and unloaded, but little to no changes were observed as the samples were cycled multiple times. In addition, no new peaks appear that would belong to the retained martensite phase. Considering the entire spectrum, the IPFs were also generated for the B2 phase as shown in Figure 5.11(a) for planes perpendicular and in Figure 5.11(b) for planes parallel to the loading direction. As observed from the raw spectra of Figure 5.10, texture changes can be seen when initially deforming and loading the samples, but the same texture is preserved during the thermomechanical cycling. Note that the texture of the undeformed sample (0 percent) did not change even after loading to 100 MPa, since this load is still in the elastic region of the B2 phase. The deformed samples showed differences in texture as expected since other deformation mechanisms are activated at the 5, 10 and 15 percent strain levels used.

The texture differences between samples during loading and cycling are better visualized in Figure 5.12 for the $\{110\}_A$ and $\{111\}_A$ lattice planes. Similar to the martensite phase, the intensities changed when deforming and loading, but remained relatively constant during thermomechanical cycling. Deformation of the austenite phase to the indicated strain levels resulted in texture differences as shown by the changes in intensities from one sample to another. The intensity of the $\{111\}_A$ decreased in samples 2 and 3 deformed to 5 and 10 percent, respectively, and then increased in sample 4 deformed to 15 percent, again consistent with the macroscopic data of Figure 5.3(a) and (b). The opposite trend can be observed for the $\{110\}_A$ lattice planes.

The texture evolution of the martensite phase (Figure 5.5 to Figure 5.7, and Figure 5.9) and that of the austenite phase (Figure 5.10 to Figure 5.12) did not change significantly during thermomechanical cycling. This is in agreement with previously reported work in Refs. [175, 176], but in disagreement with other work such as the one reported in Ref. [142]. The increase in transformation strain with cycling observed in Figure 5.3 would suggest that the microstructure is evolving towards an attraction state. Such a process would typically require more detwinning and reorientation towards a more favored variant(s) that would be manifested as an increase or change in the peak intensities. However, that data presented in Figure 5.5 to Figure 5.7 indicate that there are no changes in the martensite texture and hence, no detwinning and/or reorientation are taking place. Similar observations can be made about the austenite texture (Figure 5.10 to Figure 5.12) which is unaffected by cycling. Apparently, the texture is not responsible for the macroscopic strain evolution or the increase in the transformation strain available. Keeping in mind that the current measurement resolution is limited to volume fraction detection of 3 percent and higher, it is still unlikely that very low volume fractions (<3 percent) are responsible for the observed macroscopic behavior.

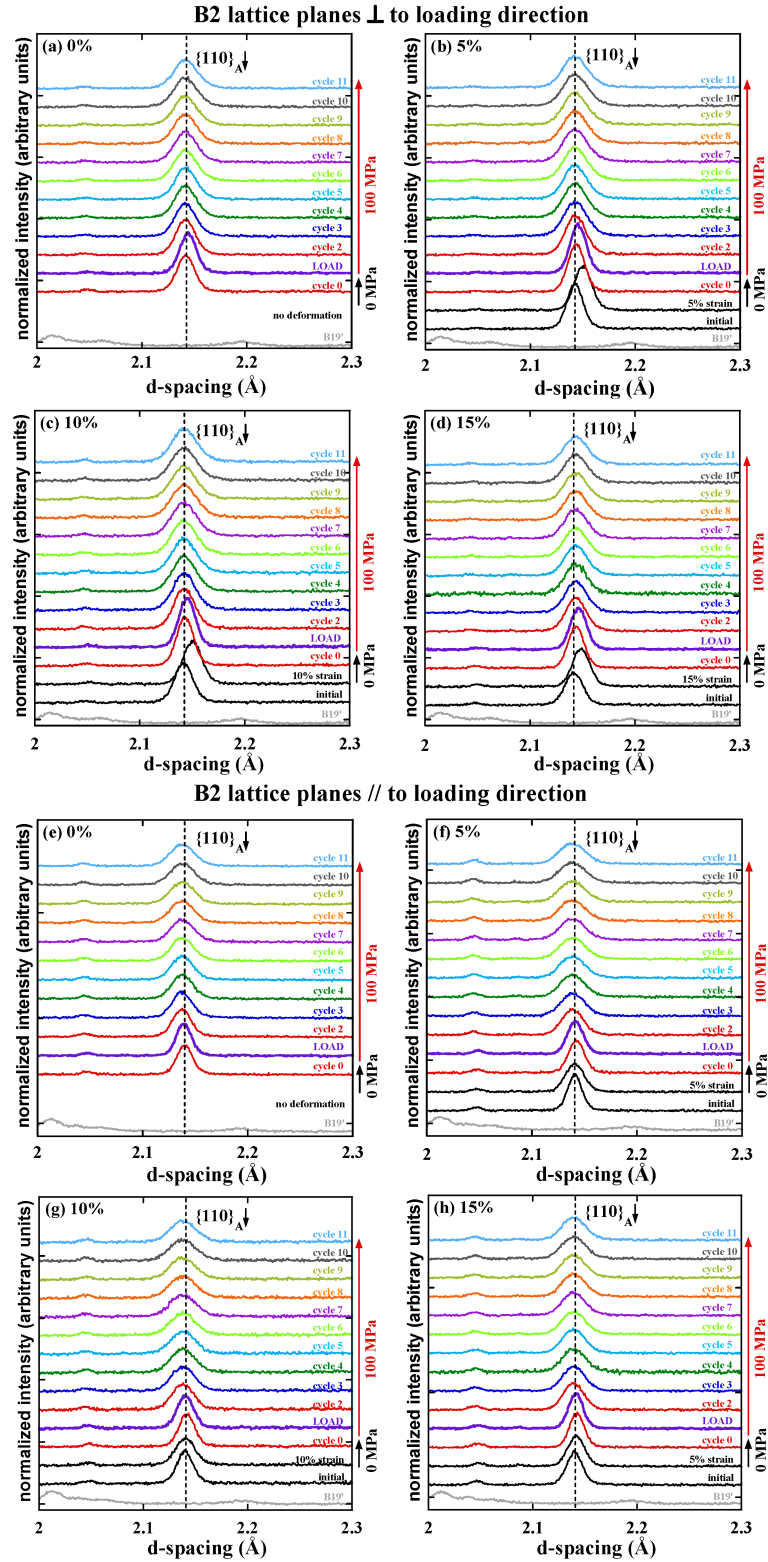


Figure 5.10.—Normalized neutron diffraction spectra acquired at the austenite phase during cycling of the samples deformed at 320 °C (samples 1 to 4 of Table 5.1). These reflections are from the $\{110\}_A$ lattice planes (a) to (d) perpendicular and (e) to (h) parallel to the loading axis. The arrows indicate the intensity decrease when the samples were first loaded to 100 MPa (labeled LOAD). A reference B19' spectrum acquired at RT is also included.

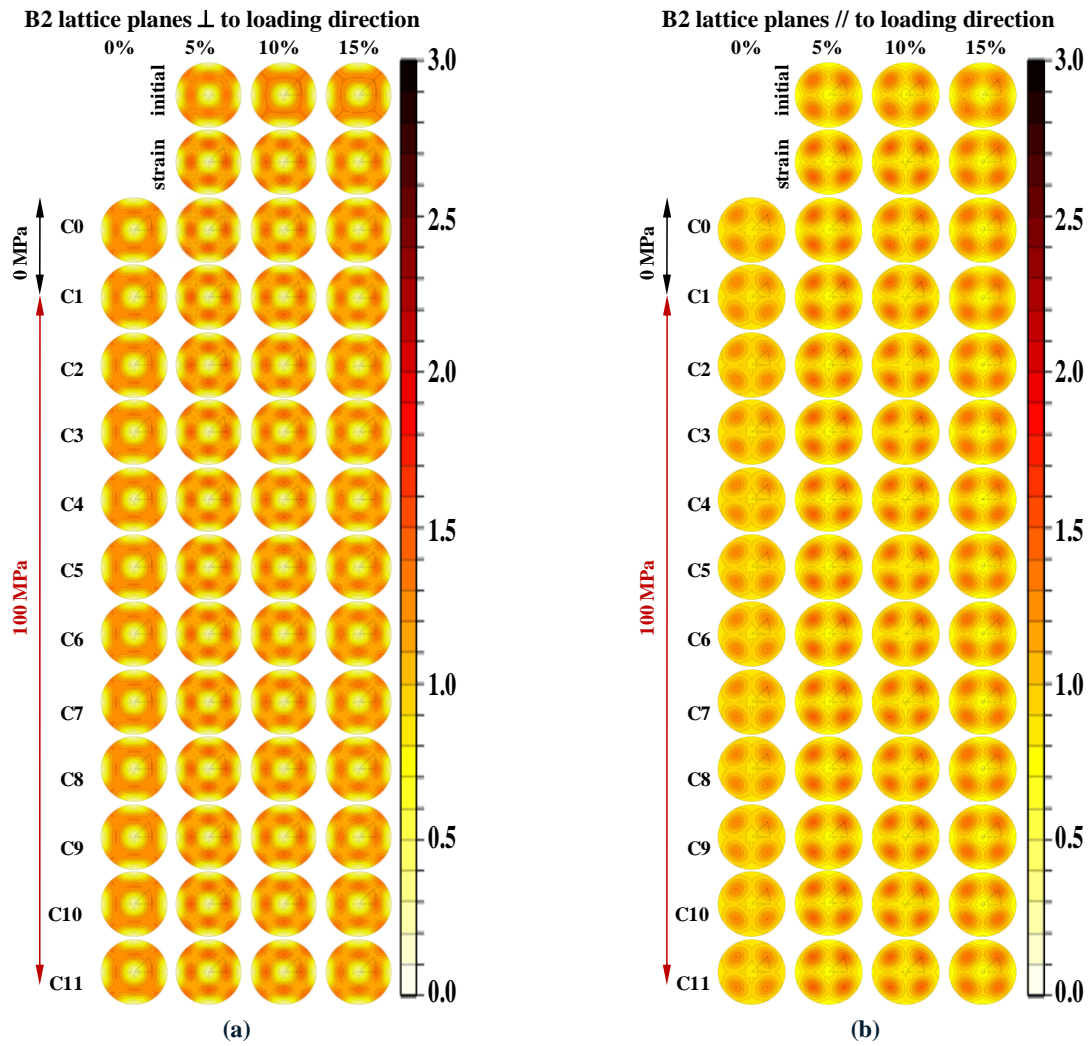


Figure 5.11.—B2 IPFs for austenitic $\text{Ni}_{49.9}\text{Ti}_{50.1}$ from diffracting planes (a) perpendicular and (b) parallel to the loading direction. This data belongs to the samples deformed at 320 °C (samples 1 to 4 of Table 5.1). Cycle numbers C0 to C13 correspond to the diffraction spectra shown in Figure 5.10.

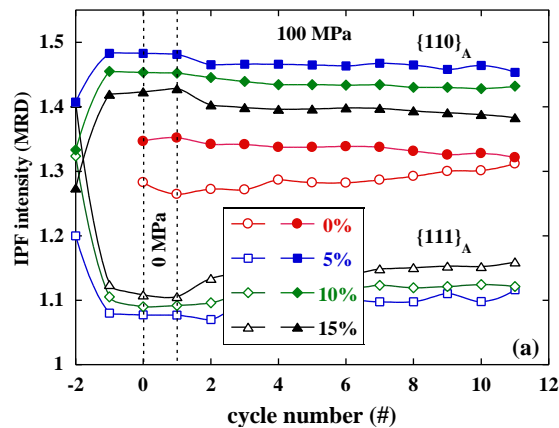


Figure 5.12.—IPFs pole intensities for the $\{110\}_A$ and $\{111\}_A$ austenite reflections perpendicular to the loading axis.

5.3.2.2 Lattice Strain Evolution

The vertical dashed lines included in Figure 5.5 and Figure 5.6 for the martensite phase and in Figure 5.10 for the austenite phase were used to indicate the shifts in the lattice planes with loading and cycling. These interplanar spacings were used to calculate the hkl -specific lattice strains ($\Delta d_{hkl}/d_{hkl}$) using a single peak fitting method. The hkl -specific lattice strain refers to the average strain in the family of crystallites specifically aligned to contribute to that specific diffraction peak. The B19' lattice strains from several reflections are shown in Figure 5.13(a) to (d) for diffracting lattice planes perpendicular to the loading axis, and in Figure 5.13(e) to (h) for diffracting planes parallel to the loading axis. This data belongs to the samples initially deformed to 0, 5, 10 and 15 percent strain at 320 °C. When loading the samples, certain variant orientations went into compression while other exhibited tensile strains, indicative of the large anisotropy of this alloy. The $(111)_M$ variant orientations were found to yield last in all cases, which support an increased portion of the elastic lattice strain. The $(111)_M$ lattice exhibited compressive strain (Figure 5.13(a) to (d)) albeit the applied load is in tension. The opposite can be observed for the $(111)_M$ lattice planes parallel to the loading axis (Figure 5.13(e) to (h)). Moreover, the lattice strain of the $(030)_M$, one of the most favored variant in tension, was observed to yield first in almost all cases of Figure 5.13. During cycling, most of the lattice strains saturated and remained unchanged for succeeding thermal cycles under the same constant load of 100 MPa. For diffracting lattice planes perpendicular to the loading axis (Figure 5.13(a) to (d)), the strains are shown to vary from one sample to another (e.g., the $(111)_M$) with varying magnitude ranging from -1.3 to 0.5 percent. For diffracting planes parallel to the loading axis (Figure 5.13(e) to (h)) similar observations can be made with strains ranging from 0.65 to -0.25 percent. Note that these lattice strains are related tensorially to the average variant-scale stresses, which contribute to the global macroscopic response.

The B2 lattice strains were also determined for the same samples as shown in Figure 5.14(a) to (d) for diffracting lattice planes perpendicular, and in Figure 5.14(e) to (h) for diffracting planes parallel to the loading axis. The initial data point (cycle 0) is the unloaded condition after deforming each sample followed by reloading to 100 MPa (cycle 1), both at 320 °C. The remaining data is taken at 230 °C during thermomechanical cycling. Figure 5.14(a) and (d) start from 0 percent strain since that sample was not initially deformed. On the other hand, Figure 5.14(b) to (c) and (f) to (h) start from different strain values which were reached during deformation. As the samples cycle through the phase transformation for the first time, some reflections from planes perpendicular to the loading direction increased in strain (e.g., $\{100\}_A$), while other decreased (e.g., $\{111\}_A$). However, most of them did not change significantly for succeeding thermal cycles under the same constant load of 100 MPa. For diffracting planes parallel to the loading direction (Figure 5.14(e) to (h)), strains decreased in all reflections after the first thermal cycle, and remained mostly unchanged afterward. For samples deformed to 5, 10 and 15 percent strain, there were no large differences observed, since the lattice strains during deformation of the austenite phase saturate at about 4 percent strain [173].

The rapid saturation of the lattice strains of both the martensite (Figure 5.13) and austenite phases (Figure 5.14) were observed with increasing cycles. The lattice strains increase during the pre-deformation and the initial loading, but did not significantly change after subsequent cycles. It was shown that the microstructure is cycling between a unique austenite texture and a unique martensite correspondence as discussed above; similarly, the internal state required to form the same variant(s) during the forward phase transformation is identically recovered within the measurement errors reported. Having said that, close examination of some of the martensite planes showed lattice strain recovery with increasing cycles as shown for the $(\bar{1}20)_M$ planes. This may contribute to the macroscopic evolution and must be tied back to a microstructural mechanism. Note that there is a large strain partitioning between variants or grains as some exhibit compressive strains (e.g., $(111)_M$ of Figure 5.13(a) to (d)) and others see tensile strains (e.g., $(011)_M$ of Figure 5.13(a) to (d)).

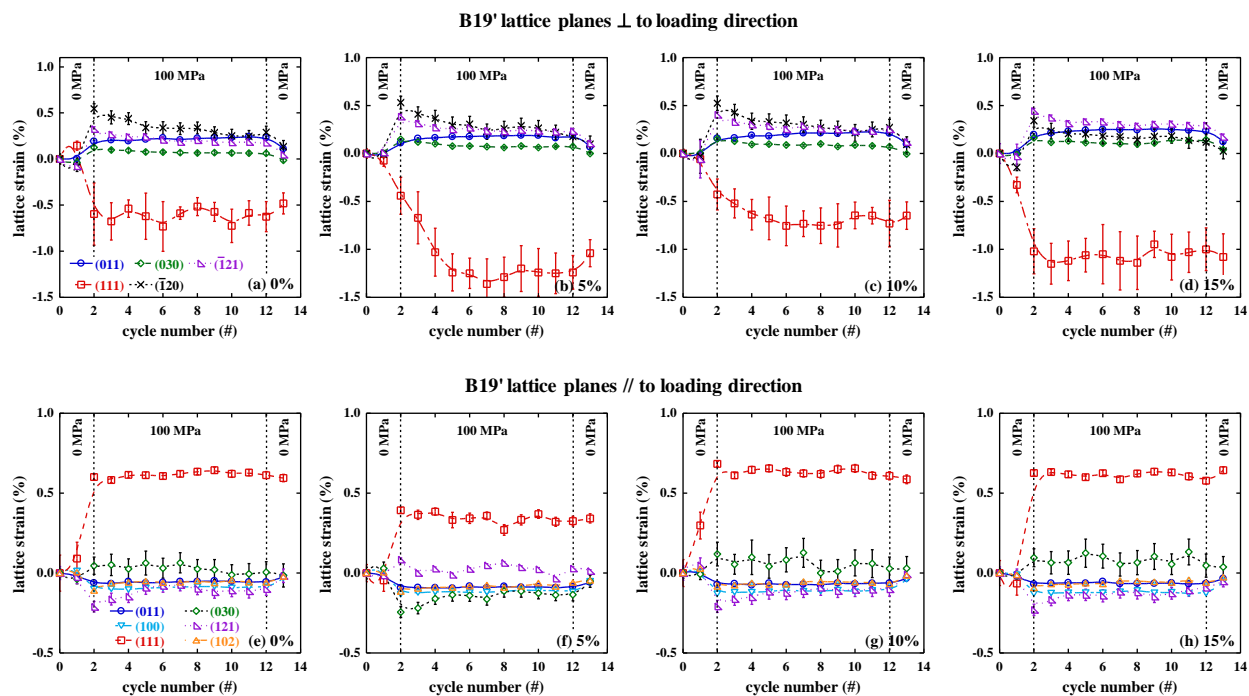


Figure 5.13.—B19' Lattice strains associated with the several reflections (a-d) perpendicular and (e-h) parallel to the loading axis during cycling.

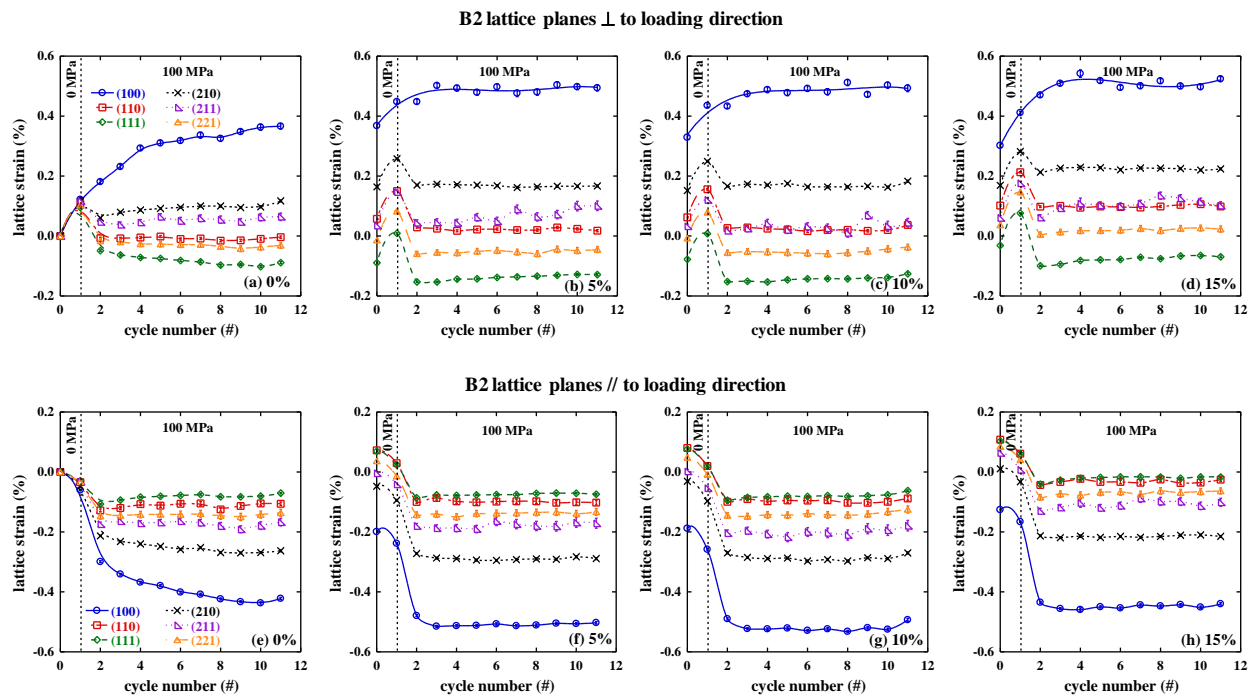


Figure 5.14.—B2 Lattice strains associated with the several reflections (a-d) perpendicular and (e-h) parallel to the loading axis during cycling.

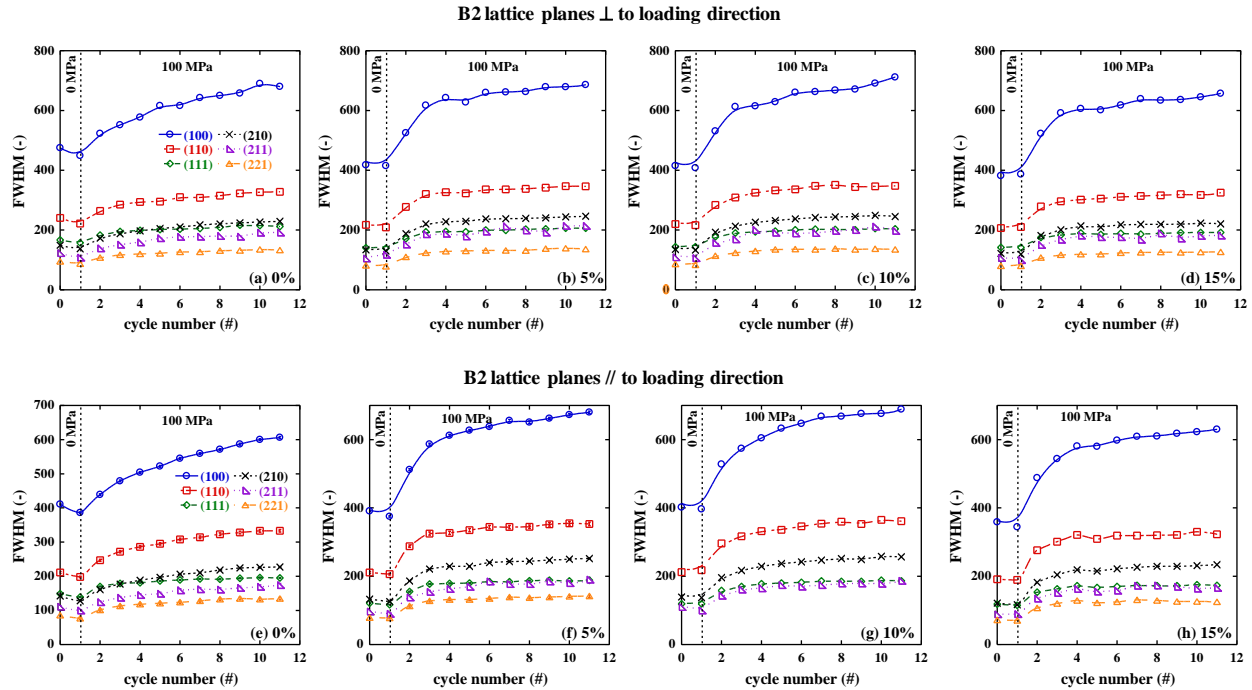


Figure 5.15.—Evolution of the austenite peak breadth (in the full-width of half-maximum) during cycling.

5.3.2.3 Peak Broadening

Another piece of information that can be obtained from the diffraction spectra of Figure 5.10 is the evolution of the austenite peak breadth. Broadening, in general, is useful in quantifying the strain anisotropy and dislocation densities. The peak breadth evolution, represented by full width half maximum (FWHM), is shown in Figure 5.15(a) to (d) for several B2 reflections perpendicular and in Figure 5.15(e) to (h) for reflections parallel to the loading axis. A large increase in the FWHM is observed after loading and cycling through the phase transformation for the first time (from cycle 1 to 2). With increasing number of cycles, an overall increase in the FWHM can be seen in almost all reflections, particularly in the $\{100\}_A$ reflections. This broadening during cycling provides a qualitative measure of lattice defects (size broadening, strain anisotropy due to dislocations, or planar defects). The austenite peak breadth is shown to increase with cycling which may indicate that mechanisms such as retained martensite (undetected using the current method) dislocations or planar defects are generated with cycling. This is clearly shown for the $\{100\}_A$ reflections of Figure 5.15.

5.3.3 Ex situ Neutron Diffraction Results

Additional experiments were conducted to explore both the macroscopic and microstructural changes during further thermomechanical cycling. The macroscopic strain-temperature responses (Figure 5.16(a)), transformation strains (Figure 5.16(b)) and residual strains (Figure 5.16(c)) are shown for the samples loaded to 200 MPa at room temperature (see Table 5.1) and cycled 20 and 50 times between 30 and 230 °C. No previous deformation was applied to these samples. Compared to the 0 percent sample of Figure 5.3(c), the transformation strains were higher in these two samples (under 200 MPa load), and kept increasing with increasing cycles up to 4.7 percent at the end of the 50th cycle. The residual strains were also larger and reached a constant level at ~ 0.3 percent/cycle after the 15th cycle. Following these macroscopic tests, both samples and one additional virgin sample (subjected to only two no-load cycles) were analyzed on HIPPO under no load. The resulting texture, represented by the pole figures, is shown in Figure 5.17 for room temperature martensite and in Figure 5.18 for the austenite measured at 200 °C.

The middle of the pole figures represents the diffracting vectors parallel to the loading direction, while the rim represents diffracting vectors perpendicular to the loading direction. The initial microstructure of the virgin sample shown in Figure 5.17(a) corresponds to the self-accommodated martensite texture as was previously shown in Figure 5.7. Once the samples were loaded and cycled through the phase transformation, preferred variants were selected. Preferred variants were still present in the material even after unloading to 0 MPa before any no-load cycles. Particularly, the $(030)_M$ and $(\bar{1}50)_M$ orientations align with the loading direction, and the $(100)_M$ and $(102)_M$ align parallel to the loading direction. These findings confirm the previous results shown by the IPFs in Figure 5.7. Of importance here are the similarities in texture between the samples cycled 20 and 50 times. Near identical texture is obtained even after 50 cycles which further confirms the lack of texture evolution shown in Figure 5.7.

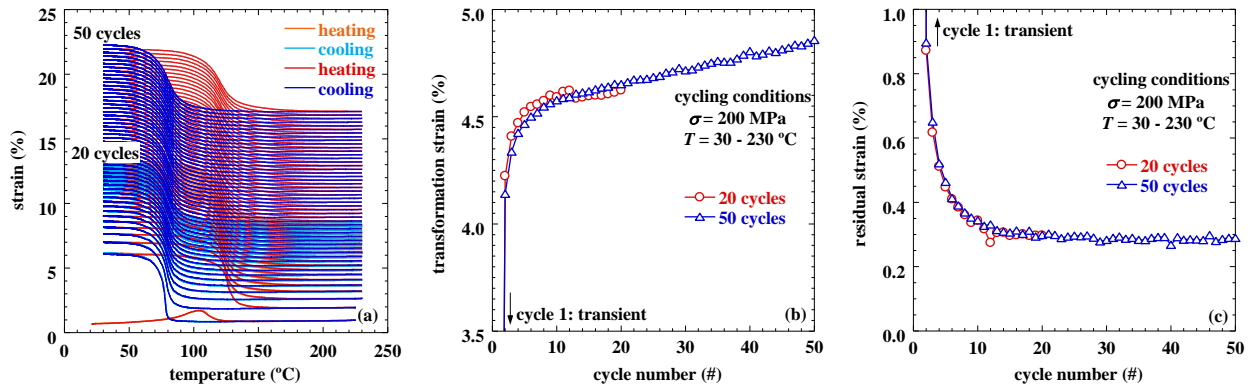


Figure 5.16.—Macroscopic (a) strain-temperature responses, (b) transformation strains and (c) residual strains for two samples loaded to 200 MPa at room temperature (samples 12 and 13 of Table 5.1) and cycled 20 and 50 times between 30 and 230 °C.

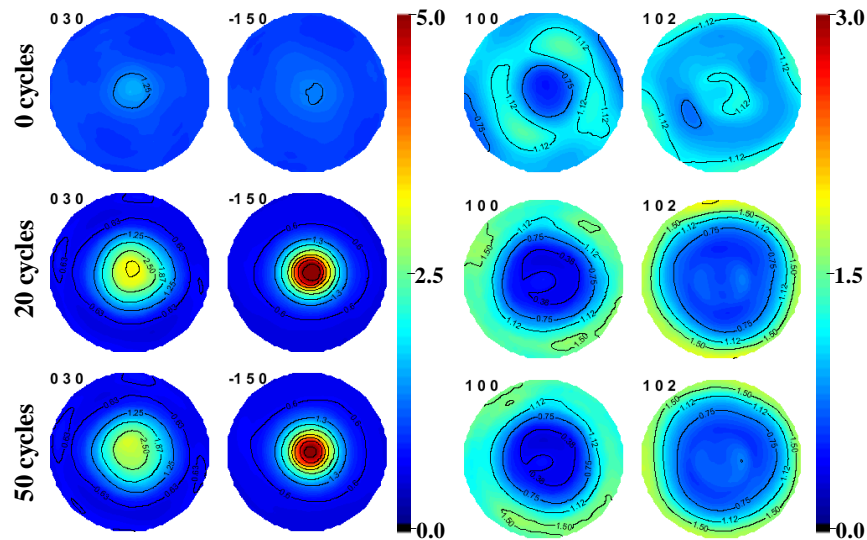


Figure 5.17.—Martensite pole figures measured at room temperature for a virgin sample, and post cycled samples (samples 11 to 13 of Table 5.1). For clarity in presentation, different scales are used.

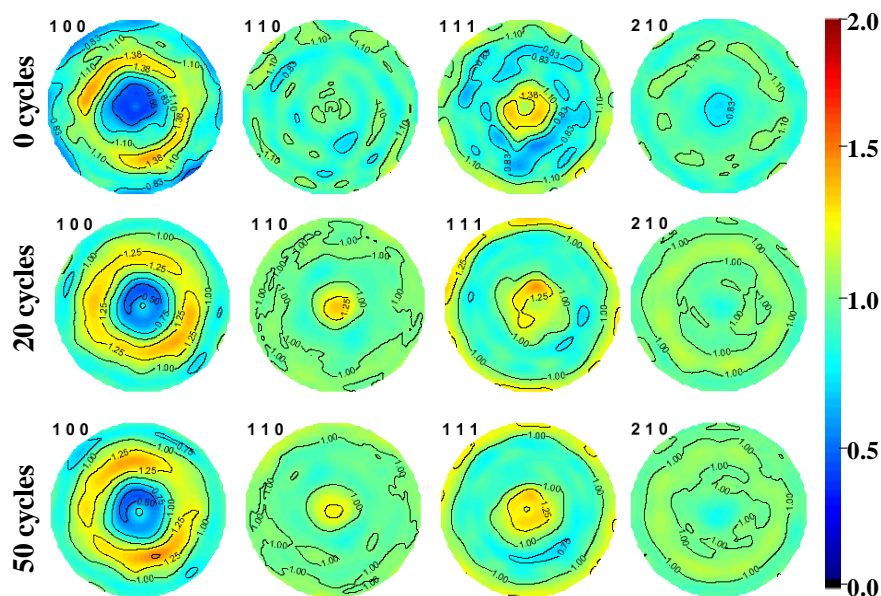


Figure 5.18.—Austenite pole figures measured at 200 °C for a virgin sample, and post cycled samples (samples 11 to 13 of Table 5.1).

The B2 austenite texture is shown in Figure 5.18 for the $\{100\}_A$, $\{110\}_A$, $\{111\}_A$ and $\{210\}_A$ planes as measured at 200 °C after the very first heating under no-load. Note that 200 MPa applied stress is still within the elastic region of the B2 phase. As a result, there were no major differences between the virgin samples and the cycled samples. Thermomechanical cycling seems to have no major effect on the B2 texture which was also observed on the texture measurements of Figure 5.11.

Sample 5 which was loaded at room temperature and cycled 10 times showed near identical microstructure as sample 1 deformed at 320 °C, hence loading in the martensite or austenite had no effect on the ensuing microstructure during cycling. However, deformation in the martensite phase is expected to yield different microstructures, since additional deformation mechanisms are activated. The role of martensite deformation on the no-load thermal cycling (two-way shape memory effect) was investigated in Chapter 4, and its role on the load-biased cycling will be investigated in future work.

5.4 Conclusions

Thermomechanical cycling of a polycrystalline $\text{Ni}_{49.9}\text{Ti}_{50.1}$ was studied by in situ neutron diffraction. Based on the macroscopic data and neutron diffraction measurements presented here, the following conclusions can be made.

- The effect of pre-deformation before cycling on the thermomechanical cyclic response was shown to enhance or degrade the material's performance depending on the deformation temperatures and magnitudes. When deformed at room temperature, the maximum transformation strain (work output) of 4.4 percent was obtained for the sample deformed to 10 percent strain. For the samples tested at 320 °C, the undeformed sample exhibited the highest transformation strain of 4.2 percent, while increasing deformation to 5 and 10 percent resulted in a decreased performance.
- The texture of both the martensite and austenite phases did not evolve with increased cycling, as indicated by the lack of variant evolution observed. Hence, the same martensite variants were selected after each cycle, and these variants transform to the same parent phase texture when heated.

- c. The internal strains partitioned amongst variants and grains during the two initial cycles, and then saturated with further thermomechanical cycling. Some lattice planes were shown to exhibit slight relaxations with cycling.
- d. The peak shapes, particularly peak broadening, was observed in the austenite phase with increasing number of cycles. This broadening can be an indication of lattice defects that could accumulate as the material cycled through the phase transformation.
- e. Cycling to high numbers of cycles resulted in no observable texture evolution.

Chapter 6.—In Situ Neutron Diffraction Study of Shape Setting Niti Shape Memory Alloy

A bulk polycrystalline $\text{Ni}_{49.9}\text{Ti}_{50.1}$ (in at.%) shape memory alloy specimen was shape set while neutron diffraction spectra were simultaneously acquired. The objective was to correlate internal stress, phase volume fraction, and texture measurements (determined from neutron diffraction spectra), with the macroscopic stress and shape changes (from load cell extensometry measurements) during the shape setting procedure and subsequent shape recovery. Experimental results revealed details of the constrained martensitic transformation during both heating and cooling. Constrained heating resulted in stress buildup due to thermal and internal stresses as the B19' to B2 transformation occurred, followed by stress relaxation due to thermal expansion, final conversion of retained martensite, and recovery processes. Constrained cooling also resulted in stress generation due to the thermal contraction and early formation of martensite, followed by relaxation as the austenite fully transforms to martensite. Comparisons were also made between a pre-shape set and the post-shape set specimen conditions, both with and without external constraints. The specimens displayed similar shape memory behavior consistent with the fact that the microstructure of the shape-set sample was mostly unchanged by the shape-setting process and was nearly identical to that of the as-received materials.

6.1 Introduction

Shape memory alloys (SMAs) have the unique ability to recover large inelastic strains (up to 8 percent) or generate high stresses (e.g., greater than 500 MPa) in response to thermal or mechanical loads. This ability has made them a viable option for actuation systems in diverse fields and applications including aerospace [4], medical [177], and automotive [178, 179]. In the case of a thermally-induced transformation, SMA-based actuators can integrate sensing, control and actuation functions in a single entity, which provides new solutions and alternatives for solid-state actuation mechanisms. Since the application of heat is the only essential input, SMA actuators provide high work output while maintaining a small volume and reduced system weight. SMA elements have higher energy densities than pneumatic actuators or D.C motors [180], and have a stroke-to-weight ratio comparable to wax actuators or bimetallics [181].

Nevertheless, while SMA actuators have been developed and used for many years [182], they have only found use in niche applications with limited market growth. Concerns about reliability, stability, and proper use of these materials have precluded the large-scale commercial application of SMA actuators. Some of these concerns arise from the lack of understanding of the micromechanics of the shape setting process that leads to the final, ready to use SMA actuator. Fabrication of SMA actuators requires precise control of the final shape, which is dependent in part on the type of constraint, heat-treatment temperature, and time used to shape set the component.

The primary method of shape setting consists of (i) pre-straining or deforming the raw material (wire, sheet, tube, etc.) in a fixture, die or mandrel with the desired form, (ii) constraining the material in all directions (displacement and rotation), (iii) heat treating at some temperature in the proper environment for a certain time, (iv) cooling the material using a specified cooling procedure, and finally (v) optimizing the final geometry by subsequent shape sets or additional cutting or machining operations. Each step has a micromechanical and microstructural counterpart that must be fully comprehended for optimum thermomechanical performance of the actuator. Yet no comprehensive connection exists between crystallography, microstructure, and macroscopic behavior during and after shape setting of shape memory alloys. Thus, determining the underlying mechanisms contributing to a typical shape set is important to successful development of SMA actuators. A systematic correlation between the martensitic phase transformation and deformation (self-accommodation, reorientation/detwinning, plasticity and thermal recovery) to the measured macroscopic behavior can provide insights into many unresolved matters and lead to improved SMA-enabled technologies.

While many studies have reported on the microstructure of NiTi [38, 43, 183, 184], and independently on the macroscopic behavior of shape setting NiTi [185-192], no experiments have been conducted to mimic the shape setting process while examining the microstructure and the macroscopic behavior simultaneously. A uniquely suited method for obtaining such concurrent analysis is in situ neutron diffraction. Recording neutron spectra during mechanical loading, and constrained heating and cooling reveals phase-specific information about the microstructure representing the bulk polycrystalline specimen as it proceeds through the shape-set process. Deeper penetration of neutrons with sampling volumes up to 1 cm³ allows for more accurate measurements and avoids free surface stress effects as would be the case for other techniques such as conventional x-rays.

In the present chapter, experiments designed to mimic shape setting of a bulk polycrystalline NiTi shape memory alloy while simultaneously examining the microstructure through in situ neutron diffraction are reported. The objective was to correlate the underlying microstructural deformation mechanisms (from neutron diffraction) with the observed and recorded macroscopic response (from load cell and extensometry measurements). Connections were made between the elastic lattice strains, internal stresses, and texture evolution before, during and after the shape setting process. In addition, this work provides insights into the multiple stages of shape setting NiTi with emphasis placed on quantifying the variant-scale intergranular stress mismatch in the polycrystalline bulk response. The role of the external constraints, the evolution of transformation induced blocking (recovery) stresses, and stress-relaxation mechanisms are delineated.

6.2 Material and Experimental Procedures

6.2.1 Material

Cylindrical Ni_{49.9}Ti_{50.1} (in at.%) dog-bone tensile specimens, 5.08 mm in diameter and 15.24 mm in gauge length, were machined from hot-rolled/hot-drawn and hot-straightened 10 mm diameter rod produced by Special Metals, New Hartford, New York. Prior to testing, the cylindrical specimens were subjected to two stress-free thermal cycles in air between room temperature and 200 °C in a muffle furnace to relieve any residual stresses due to machining and processing. Stress-free transformation temperatures: martensite start (M_s), martensite finish (M_f), austenite start (A_s) and austenite finish (A_f) were measured using the intercept method [76] from the second no-load thermal cycle and were found to be 71, 55, 92, and 105 ± 2 °C, respectively.

6.2.2 Test Procedures

In situ neutron diffraction experiments were conducted on the Spectrometer for MAterials Research at Temperature and Stress (SMARTS) at Los Alamos National Laboratory (LANL). For all diffraction experiments presented in this work, a diffraction volume of approximately 100 mm³ was subjected to the neutron beam for a count time of 30 min, which yields acceptable statistics. Prior to performing the shape setting experiments, one no-load thermal cycle between room temperature (RT) and 450 °C at a rate of 15 °C/min was performed with neutron spectra acquired at RT and 450 °C. These measurements provide a reference stress-free condition that is used for the subsequent analyses. After cooling back to room temperature, the sample was uniaxially loaded in tension to 7.5 percent strain in displacement control mode, and subsequently unloaded. The stress-strain response is shown in Figure 6.1. Diffraction data were acquired at three points: the initial no-load condition, the end of loading where a maximum strain of 7.5 percent was obtained, and after unloading to zero stress. These are indicated by the solid points in Figure 6.1. After unloading to zero stress, the sample was constrained in position and heated at a rate of 15 °C/min to 450 °C while neutron spectra were recorded at multiple temperatures (i.e., 100, 200, 300 and 450 °C). During cooling to RT, using the same rate as was used during the heating cycle, scans were performed at temperatures of 300, 200, 100 and 30 °C to determine microstructural differences between the heating and cooling portions of the cycle. The same specimen was subsequently strained an additional 7 percent at room temperature in tension (stress-strain curve shown in Figure 6.1) and subjected to a

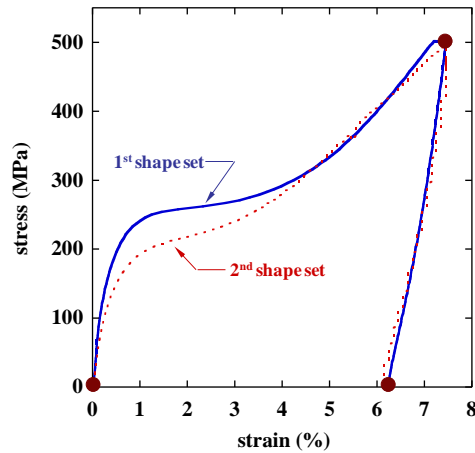


Figure 6.1.—Tensile stress-strain response of NiTi at room temperature (from extensometry) during loading and unloading. The symbols indicate the strains at which neutron diffraction spectra were taken.

second shape set cycle with neutron diffraction acquired at RT, 450 °C and again at RT after cooling. The entire two cycle shape-set experiment was repeated on a second specimen to determine the reproducibility of the results.

Additional experiments were conducted after the second shape set to investigate the shape memory behavior of the resulting shape-set microstructure. Two thermal cycles between RT and 200 °C at a constant stress of 200 MPa were performed while acquiring neutron data at RT and 200 °C for each cycle. Finally, two stress-free thermal cycles between RT and 200 °C were conducted immediately after the 200 MPa cycles to compare the post microstructural effects of shape setting to the original material microstructure, with neutron data acquired at RT and 200 °C.

6.2.3 Neutron Diffraction Data Analysis

Rietveld refinement and single peak fitting methods [16, 20, 21, 193] were used to analyze the neutron data collected on SMARTS. These methods were implemented in the LANL General Structure Analysis System (GSAS) [16] where phase fractions, crystal structure parameters, strains and crystal orientation distribution (texture) were obtained. The output of the refined B19' and B2 neutron spectra under no-load at RT and 450 °C, respectively are shown in Figure 6.2. Peak identification was obtained from the Rietveld refinement and produced best fit lattice parameters $a=2.91$ Å, $b=4.64$ Å, $c=4.12$ Å, $\alpha=\gamma=90^\circ$, $\beta=97.63^\circ$ for monoclinic martensite, and $a=3.032$ Å for cubic austenite.

Crystallographic texture [17, 22] was captured using inverse pole figures (IPFs) and axial distribution plots (ADPs), with the latter representation being constructed assuming cylindrical symmetry of the samples. ADPs represent a radial slice of the pole figure for a specific variant. The angles $\phi=0^\circ$ and $\phi=90^\circ$ of the x-axis represent planes perpendicular and parallel to the loading direction, respectively, whereas the y-axis is a measure of the number of grains that are oriented at an angle ϕ between the normal to the chosen plane and the loading axis.

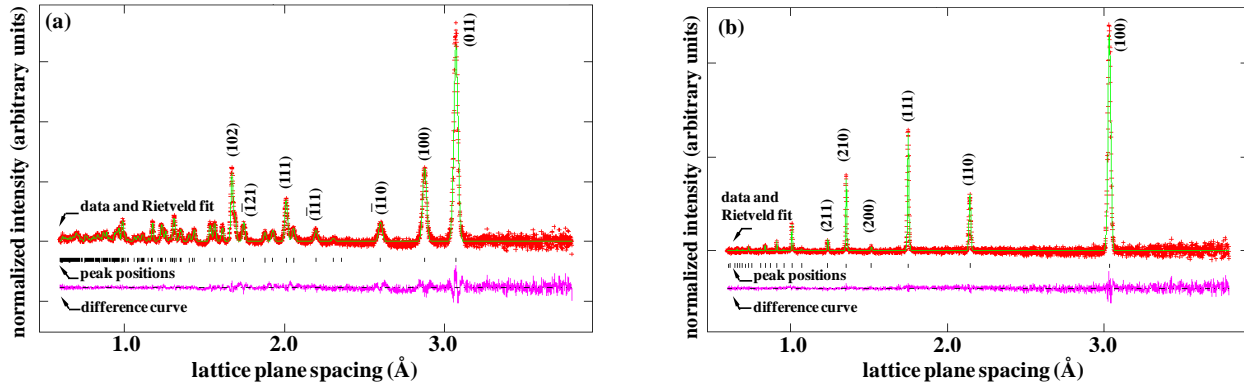


Figure 6.2.—GSAS Rietveld refinement for NiTi with diffracting lattice planes parallel to the loading axis with no applied load. (a) Monoclinic martensite at 27 °C and (b) cubic austenite at 450 °C. The measured data are indicated by cross-marks and the calculated profile is indicated by the solid line. The tick-marks below the profile pattern indicate the reflections. The lower curve is the difference between the measurement and refinement.

6.3 Results

6.3.1 Pre-Straining before Shape Setting

Starting from an initial self-accommodated martensitic texture at room temperature, the NiTi specimen was pre-strained in tension to 7.5 percent strain, which is close to the maximum shape memory strain for NiTi wires [194]. The pre-straining deforms the martensite by means of reorientation and detwinning toward a more favorable variant configuration. The sample was then unloaded to 5 MPa stress (enough stress to keep the sample aligned with the neutron beam) where a pre-strain level of 6.2 percent was achieved after recovering 1.3 percent strain due to elastic springback upon unloading.

The macroscopic no-load, pre-strained, and unloaded conditions (indicated by the solid points in Figure 6.1) were related to their microstructural counterparts by looking at the crystallographic texture and lattice strains. The IPFs for these three conditions are shown in Figure 6.3(a) for planes parallel and in Figure 6.3(b) for planes perpendicular to the loading direction. The initial grain orientations of the polycrystalline NiTi ($\sigma = 0$ MPa, $\varepsilon = 0$ percent) are close to a random distribution as shown by the weak texture with a maximum intensity of 1.77 and 1.93 for diffracting planes parallel and perpendicular to the loading direction, respectively. In this state, the martensite plates are self-accommodated since the variants of martensite have rearranged to accommodate the lattice invariant shear (i.e., no macroscopic shape change).

The growth and conversion of favorably oriented martensite variants is clearly revealed experimentally after loading to 7.5 percent strain. For diffracting planes parallel to the loading axis, the intensity at the $(001)_M$ orientation increases to 2.83. Greater than random distributions are also observed around the $(100)_M$, $(210)_M$ and $(110)_M$ orientations. Similarly, for diffracting planes perpendicular to the loading axis, the intensity at the $(\bar{1}50)_M$ and $(010)_M$ orientations increases to a maximum of 8.02. This texture evolution is a direct indication of reorientation and detwinning due to pre-straining.

Upon unloading, elastic strain (springback) was recovered while the majority of the inelastic strain generated during variant reorientation/detwinning was not. This is not completely obvious in Figure 6.3, but the effect can be observed by looking at the maximum intensity levels in Figure 6.3(b). The observed texture evolution was confirmed using the texture index, J , obtained by refining both spectra (parallel and perpendicular planes) at the same time. The texture indexes were found to be 1.1, 2.9 and 2.6 ± 0.01 for the no-load condition, with application of 7.5 percent strain, and after unloading the sample, respectively (Figure 6.1). This is indicative of the growth and formation of preferred martensite orientations as the material is strained, followed by a slight decrease in texture after springback during stress removal.

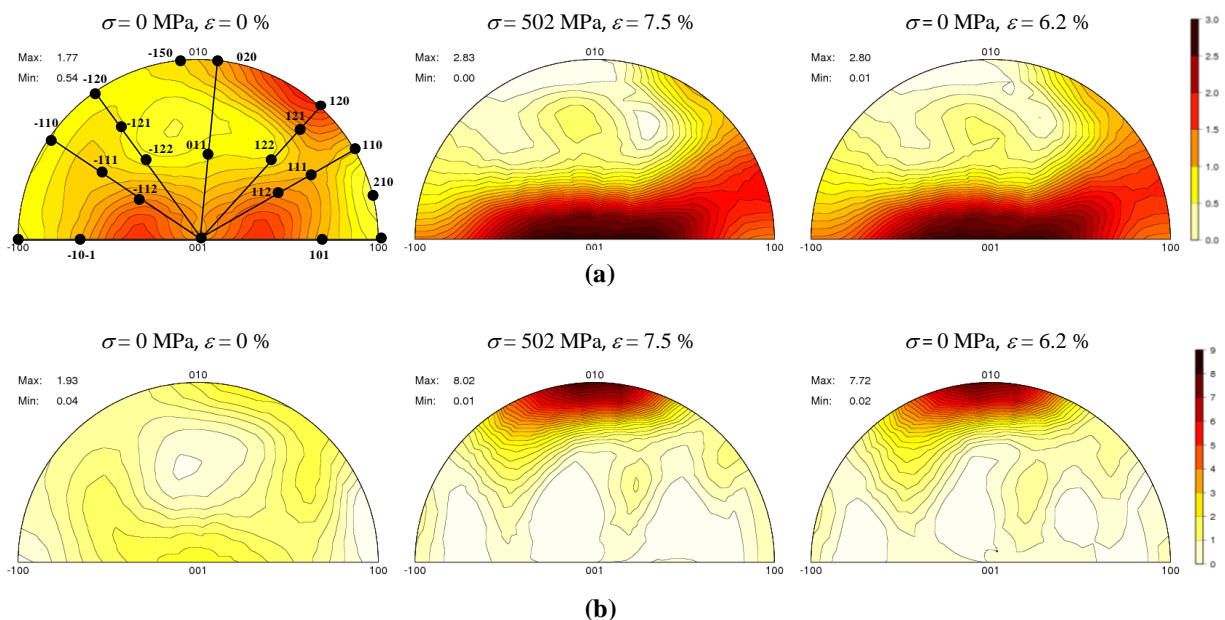


Figure 6.3.—B19' martensitic NiTi IPFs for diffracting planes (a) parallel and (b) perpendicular to the loading direction. The sample condition (applied strain and associated stress) is indicated above each IPF. The maximum and minimum intensities are indicated at the top left hand corner in multiples of random distribution. Note that the scales used for the IPFs in (a) and (b) are different.

To better understand the macroscopic elastic strain recovery after unloading, the elastic lattice strains of planes perpendicular to the loading direction were determined in seven lattice reflections, namely $(\bar{0}11)_M$, $(\bar{1}10)_M$, $(110)_M$, $(\bar{1}11)_M$, $(111)_M$, $(\bar{1}20)_M$ and $(\bar{1}21)_M$. Macroscopically, a strain of 1.3 percent was recovered after unloading the sample. Microscopically, the recovery of the elastic lattice strain varied from ~ 0.4 to ~ 0.6 percent. The difference between the macro and micro strains, i.e., 1.3 percent macro versus 0.5 percent average micro, could be due to reverse reorientation, or what is known as rubber-like behavior [195, 196]. This is consistent with the texture changes from the IPFs in Figure 6.3(b) and the texture index values mentioned above. Finally, once unloaded, the sample was constrained with a remnant 6.2 percent pre-strain and thermally cycled through the phase transformation without further macroscopic shape change.

6.3.2 Shape Setting

6.3.2.1 Macro-Stress and Phase Evolution

Figure 6.4 shows the stress-temperature response of the shape-constrained NiTi for two consecutive shape set cycles. Prior to the first thermal cycle, the sample was deformed to a maximum strain of 7.5 percent at room temperature and then unloaded resulting in a residual strain of 6.2 percent (see Figure 6.1). The sample was then constrained at this 6.2 percent “pre-strain” level and thermally cycled as shown in Figure 6.4. After returning to room temperature the sample was deformed an additional 7 percent, resulting in a residual strain of 5.9 percent. It was then constrained at this level and thermally cycled once again. By the end of the second thermal cycle the sample had been permanently deformed by a total strain of 12.1 percent.

For clarity and succeeding discussions, the middle figure in Figure 6.4 was divided to four subfigures that summarize the different mechanisms that occur at each stage of the shape set process (Figure 6.4(a) to (d)). As the sample was heated, blocking or recovery stresses built up to 380 and 430 MPa for the first and second shape set, respectively (Figure 6.4(a)). Blocking stresses build up as the reoriented/detwinned martensite starts transforming to the parent austenite above the reverse transformation temperature ($A_s=105$ °C), and reach a maximum value at ~ 173 °C, which is slightly above the A_f temperature of

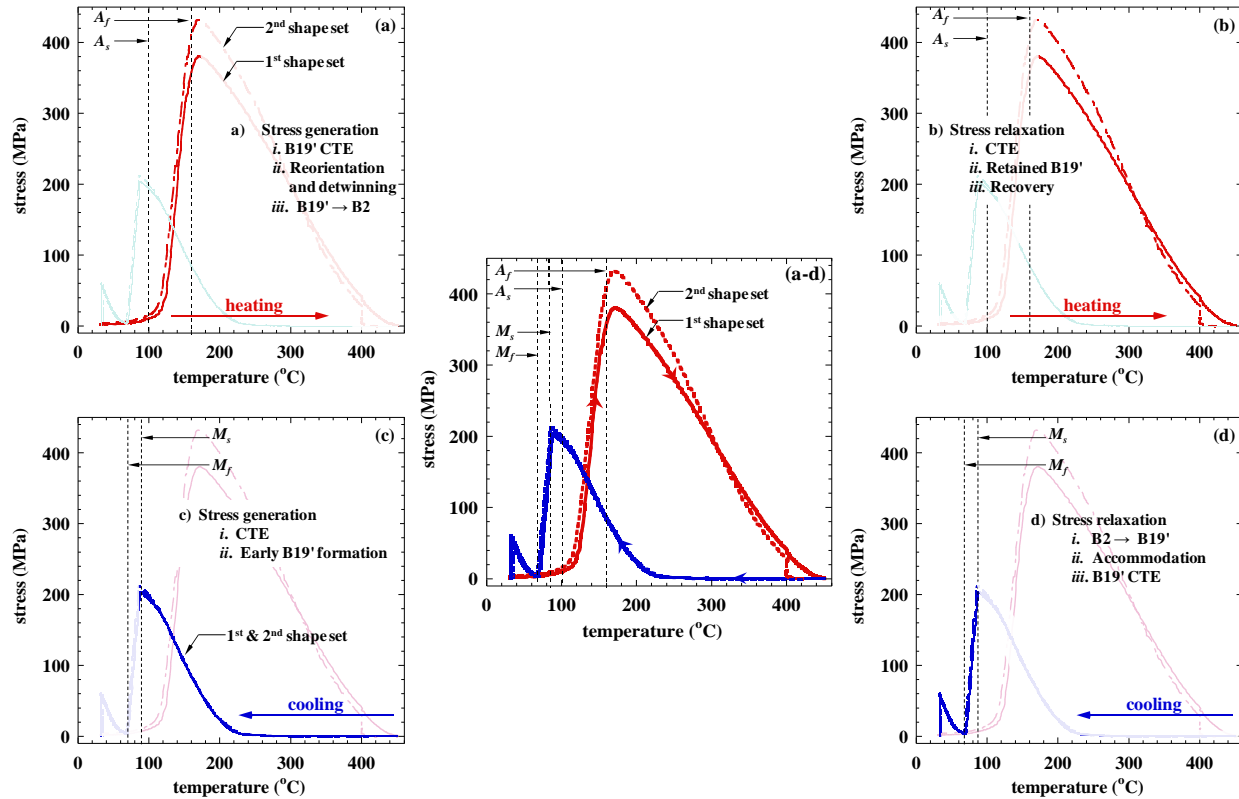


Figure 6.4.—Stress-temperature response of NiTi during shape-constrained thermal cycling: (a) and (b) sections of the heating cycle and (c) and (d) sections of the cooling cycle for two successive shape set experiments (from extensometry). The vertical lines represent the transformation temperatures obtained from ex situ constant stress thermal cycling tests performed on similar samples.

~160 °C. However, it is important to note that these transformation temperatures (as well as M_s and M_f) were obtained from ex situ constant-stress thermal cycling tests performed on different samples from the same lot of material [32], determined simply by the intercept method [76]. Therefore, the temperatures provide a representative (but not exact) depiction of the transformation temperatures for the material in this instance.

In the absence of constraint (free thermal recovery), the sample will fully or partially recover its shape as the martensite transforms to austenite. However, in the presence of a constraint, the phase transformation will still take place but the stresses will evolve as the transformation proceeds while the macroscopic shape remains fixed. During this stress generation, it is possible for mechanisms such as the movement of martensite/austenite interfaces or plastic deformation to occur, which in turn can pin some of the reoriented martensite. Once most of the martensite reverts back to the parent phase, the blocking stresses reach a maximum as there is no more driving force to generate more stress. With further increase in temperature, the stresses relax as observed macroscopically reaching zero stress at 450 °C (Figure 6.4(b)). This gradual decrease in stress is due to relaxation of the austenite phase due to thermal expansion, conversion of any remaining martensite, and recovery processes. Note that heating to temperatures less than 450 °C along the relaxation curve, at the current rate, will not relieve all the pre-strains and will result in an incomplete shape set. However, isothermally holding the sample above A_f for a period of time or thermal cycling may also result in a complete stress relaxation [190].

During cooling, the macroscopic stress state remains constant at zero from 450 to 220 °C, as recovery processes are sufficient to prevent the buildup of any thermal stresses. At temperatures below 220 °C, an increase in the blocking stress is again observed due to thermal expansion of the constrained sample (Figure 6.4(c)). As the sample continues to cool, the stress increases to a maximum of about 200 MPa at

the M_s temperature ($\sim 85^\circ\text{C}$). Once at the M_s temperature, martensite forms, relieving the thermal stresses, with complete stress relaxation (0 MPa stress) at 69°C , (approximately the M_f temperature), due to the accommodative nature of martensite [197] (Figure 6.4(d)). The last stress increase starting at about 67°C corresponds to the thermal stresses generated during the contraction of the martensite phase, which was calculated to be ~ 50 MPa using the B19' coefficient of thermal expansion from Ref. [38], consistent with the bulk measurements shown in Figure 6.4(d). Finally, the sample was unloaded at the end of the experiment as shown by the last stress decrease to 0 MPa. The macroscopic responses of both the heating and cooling cycles of the constrained sample were repeatable as shown by the second shape set in Figure 6.4 and demonstrated in similar ex situ experiments performed on other samples not shown here.

The aforementioned observations are consistent with the microstructural stress evolution and phase volume fractions observed during the in situ neutron diffraction measurements. Sections of normalized neutron spectra from lattice planes perpendicular to the loading direction are shown in Figure 6.5 as the sample undergoes the phase transformation from B19' to B2 during heating and from B2 to B19' during cooling. Since the intensity difference is a relative measurement, all spectra were normalized with respect to the $\{210\}_A$ peak, which therefore have the same maximum intensities (Figure 6.5(d)). For clarity, the same overlay patterns were offset vertically as a function of temperature as shown in the insets of Figure 6.5. Evolution of four austenite peaks $\{100\}_A$, $\{110\}_A$, $\{111\}_A$ and $\{210\}_A$ were followed, along with the neighboring martensite peaks, denoted by the subscripts “A” and “M”, respectively.

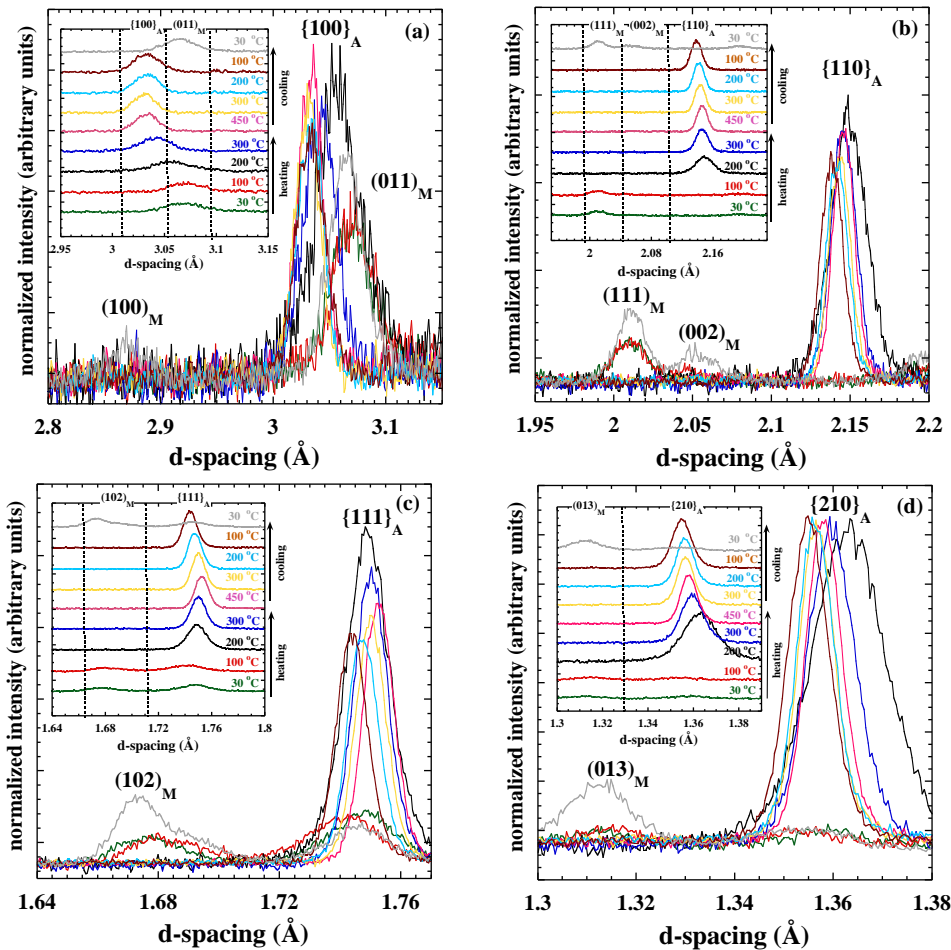


Figure 6.5.—Sections of normalized neutron diffraction spectra acquired during heating and cooling from 30 to 450°C and back to 30°C for (a) $\{100\}_A$, $(011)_M$ and $(100)_M$, (b) $\{110\}_A$, $(002)_M$ and $(111)_M$, (c) $\{111\}_A$ and $(102)_M$, (d) $\{210\}_A$ and $(013)_M$. The reflections are from lattice planes perpendicular to the loading axis. Subscripts ‘A’ and ‘M’ refer to austenite and martensite, respectively. The insets represent the same spectra offset vertically for clarity.

During the constrained heating cycle of the pre-strained martensite, peak evolution develops as nascent B2 forms at the expense of martensite variants. Even after the apparent austenite finish temperature, peak evolution is observed to progress until the maximum temperature of 450 °C is reached. Relating these observations to the macroscopic curve of Figure 6.4, it is clear that phase evolution is taking place not only during the stress generation where the phase change is occurring (Figure 6.4(a)) but also during the stress relaxation (Figure 6.4(b)). One microstructural mechanism responsible for such phase evolution is the continued transformation of martensite to austenite even above the apparent A_f temperature. Neutron data reveals that the volume fraction of martensite is 10 percent at 200 °C, 4 percent at 300 °C and undetectable at 450 °C (therefore less than 3 percent). Thus a considerable amount of retained martensite is detected after the apparent A_f temperature, which can influence the internal stress state and intergranular constraints.

During the cooling cycle, no detectable martensite was found at 200 °C, but a volume fraction of 9 ± 3 percent was detected at 100 °C, and complete transformation occurred below the apparent M_f temperature of 69 °C. The existence of martensite during cooling above the apparent $M_s=85$ °C temperature is not surprising as the transformation temperatures utilized in this study were determined during a previous investigation [171] using the intercept method, which underestimates the actual temperature where martensite begins to form [9]. Phase evolution is not the only change observed in the neutron spectra of Figure 6.5, the peak shifts or lattice strains were also shown to evolve and their influence on the observed response is examined in the following section.

6.1.1.1 Lattice Strain Evolution

The macroscopic stress-temperature behavior is affected by changes in the internal lattice strains of the austenite as the net macro shape is constrained and held constant during thermal cycling. These lattice strains were determined from single peak fits of individual lattice plane reflections in the neutron spectra of Figure 6.5. Austenite strain data taken from grains with diffracting planes parallel and perpendicular to the loading direction are shown in Figure 6.6(a), (c) and (b), (d) during constrained heating and cooling, respectively. The reference lattice spacing, d_0 , is taken at 450 °C of the initial no-load thermal cycle. Also, included in Figure 6.6 is the coefficient of thermal expansion for the austenite, previously determined for this same alloy [38].

Grains of different stiffnesses (different orientations) are not only restricted by their surroundings, but also by the imposed external constraint, which yields different strains between reflections. In addition, it was shown from the phase evolution analysis that residual pockets of martensite continue to transform with increasing temperature, which can also act as an additional intergranular constraint. All these factors contribute to the rise of inhomogeneous intergranular stresses, particularly at lower temperatures where martensite is present and recovery processes are limited. This anisotropy is clearly shown by the strain magnitudes and directions in Figure 6.6(c) where, for example, the $\{111\}_A$ reflection exhibits tensile strains while the $\{100\}_A$ exhibits compressive strains, but which converge to zero as the sample is heated to high enough temperature.

To quantify these intergranular stresses and compare the stress mismatch between a subset of grains, plane specific elastic moduli and thermal strains were considered. Elastic moduli in directions normal to the given (hkl) planes were determined using

$$\frac{1}{E_{hkl}} = S_{11} - 2 \left(S_{11} - S_{12} - \frac{1}{2} S_{44} \right) \left(l_1^2 l_2^2 + l_2^2 l_3^2 + l_3^2 l_1^2 \right) \quad (6.1)$$

where S_{ij} is the single crystal compliance tensor and l_1 , l_2 and l_3 are the direction cosines in the direction normal to the hkl plane [198]. Using single crystal stiffness constants $C_{11} = 137$ GPa, $C_{12} = 103$ GPa and $C_{44} = 34$ GPa [199], the elastic moduli were found to be 49, 76, 93, 63 and 84 GPa for $\{100\}_A$, $\{110\}_A$, $\{111\}_A$ and $\{210\}_A$ and $\{221\}_A$ planes, respectively. The coefficient of thermal expansion, α_{hkl} , was determined previously as $13 \times 10^{-6}/^\circ\text{C}$ [9]. The lattice and thermal strains along with the corresponding elastic moduli were then used to determine the intergranular stresses using the expression

$$\sigma_{hkl} = (\epsilon_{hkl} - \alpha_{hkl} \cdot \Delta T) \cdot E_{hkl} \quad (6.2)$$

where the product of the coefficient of thermal expansion and temperature difference, ΔT , is the thermal strain, ϵ_{ths} , determined from neutron spectra. Table 6.1 summarizes the intergranular stress difference between the $\{111\}_A$ and $\{100\}_A$ planes. These planes have the highest strain in tension and compression, respectively. Therefore, the maximum possible intergranular stress mismatch has to be between this subset of grains. For a given temperature difference, Table 6.1 lists the calculated intergranular stress mismatch along with the measured macroscopic stresses from Figure 6.1.

TABLE 6.1.—CALCULATED INTERGRANULAR STRESS MISMATCH BETWEEN $\{100\}_A$ AND $\{111\}_A$ AUSTENITE REFLECTIONS DURING CONSTRAINED HEATING AND COOLING. THE MACROSCOPIC STRESS DIFFERENCES ARE ALSO SHOWN FOR COMPARISON

ΔT , °C	Intergranular stress mismatch, MPa	Macroscopic stress, MPa
200 to 300 °C	-209 ± 20	-220 ± 20
300 to 450 °C	-142 ± 20	-180 ± 20
200 to 100 °C	185 ± 20	200 ± 20

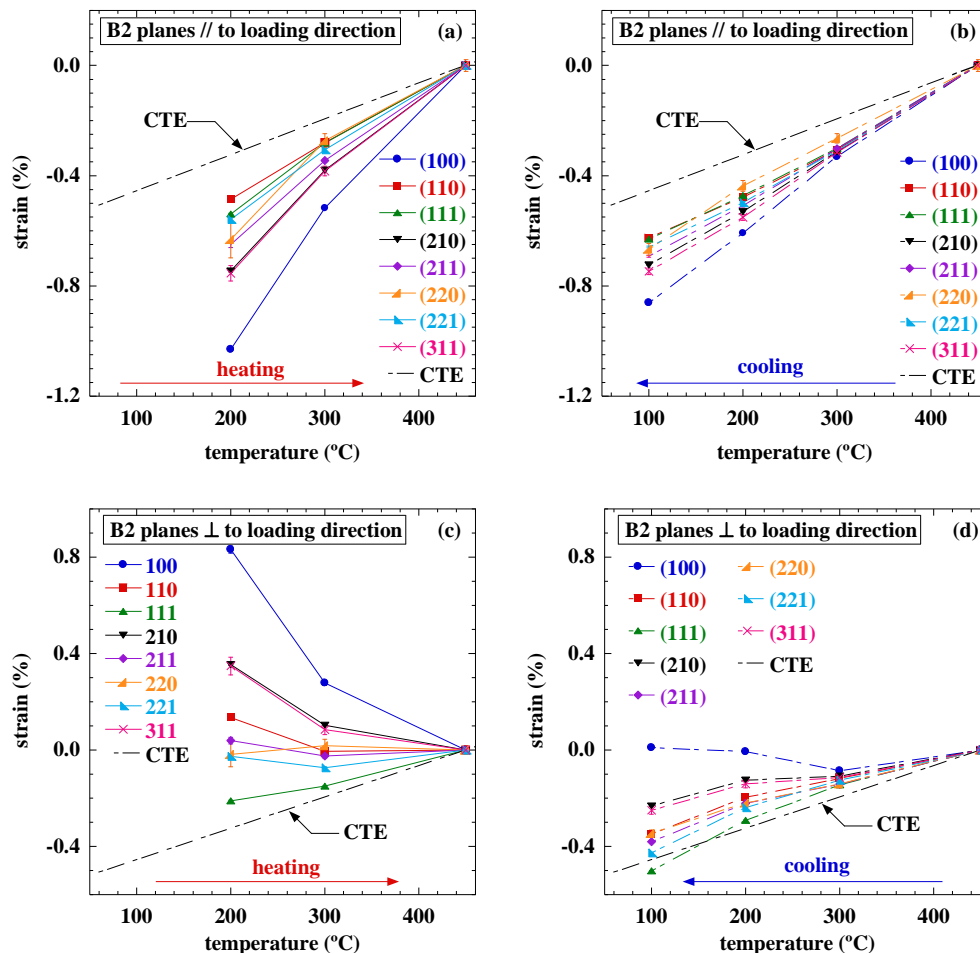


Figure 6.6.—Elastic lattice strains associated with austenite reflections measured from planes parallel to the loading axis during: (a) heating and (b) cooling, and from planes perpendicular to the loading axis during: (c) heating and (d) cooling. (Error bars are included but generally not visible as they are often less than the symbol size).

The close agreement between the microscopic and macroscopic values indicates that the stress relaxation during heating and the initial stress rise during cooling were not exclusively due to thermal expansion effects but also due to the inherent anisotropy and internal stress fields present in the material. For example, heating from 200 to 300 °C gives an intergranular mismatch of –209 MPa, while the recorded macroscopic stress is –220 MPa. In fact, a good agreement was obtained for all temperature differences shown in Table 6.1 both during cooling and heating. Similar computations were performed for other grains (not shown here), which yield lower mismatch stresses as expected since the strains were lower. From these results, the role of the macroscopic 6.2 percent pre-strain and the imposed constraint were linked to the microscopic intergranular stresses and anisotropy induced by the phase and lattice strain evolution.

6.3.2.2 Diffraction Intensity

Detailed diffraction intensity measurements were recorded to determine the extent of the averaged peak evolution during the macroscopic stress generation and relaxation process. Figure 6.7 shows the IPFs from diffracting planes parallel to the loading direction for the B19' during heating. As the temperature increases above the A_s , preferred martensite variants transform to the parent austenite resulting in an observed variation in intensity. The intensity at the $(001)_M$ orientation decreases while the intensities at the $(210)_M$, $(\bar{1}11)_M$ and $(020)_M$ increase as the B19' volume fraction decreases. In other words, $(001)_M$ is lost or transformed to austenite disproportionately at first compared to the other martensite variants. But by 450 °C, no detectable martensite was observed and the IPF shown represents only the austenite texture.

Peak evolution of the austenite phase was also tracked during heating. As observed in Figure 6.5, the peak intensity changes as a function of temperature. Instead of using IPFs, which represent texture in a single direction, intensity distribution was captured using axial distribution plots. These plots represent a slice of the pole figure obtained by refining both complete histograms for planes parallel and perpendicular to the loading axis at the same time. Utilization of this texture representation was possible due to the cylindrical symmetry of the samples. Figure 6.8 shows the orientation of $\{100\}_A$ and $\{111\}_A$ planes during heating along with the initial austenite texture at 450 °C before shape setting. With increasing temperature, the intensities at $\phi=0$ and 90° are shown to evolve toward unity with increasing temperature and, hence toward the initial starting austenite texture that was present before shape setting. This evolution indicates that the actual orientation of the austenite changes very little, but the volume fraction of austenite increases with increasing temperature as more martensite transforms to austenite. At the end of the constrained heating cycle, the sample changes shape, i.e., has grown 6.2 percent in length, but the final austenitic microstructure was mostly unchanged.

Negligible austenite peak evolution was observed in the diffraction spectra during cooling from 450 °C down to 200 °C, consistent with the fact that there was no variation in the phase volume fraction or in the external imposed constraint. Thus the relaxation processes responsible for the lack of macroscopic stress buildup through this temperature range occur without affecting the austenite texture. As it turns out, the typical slip system in B2 NiTi is $\langle 100 \rangle$ [63], and glide and climb of $\langle 100 \rangle$ dislocations in B2 compounds occur without a resulting change in texture, consistent with the current observations [89]. Upon cooling from 200 to 100 °C, stress generation also with negligible texture change was observed, consistent with the generation of essentially elastic thermal strains. However as noted above, if any plastic deformation did occur at these low stresses it would occur without affecting the sample texture. Below 100 °C, the peak intensities again begin to evolve as the phase transformation from austenite to martensite occurs. But these changes in intensity are actually due to changes in phase volume fraction as martensite is formed and not due to any real changes in orientation of the austenite. Finally, by the time the sample was cooled completely to RT, the final martensite texture was found to be very comparable to the starting self-accommodated texture prior to pre-straining.

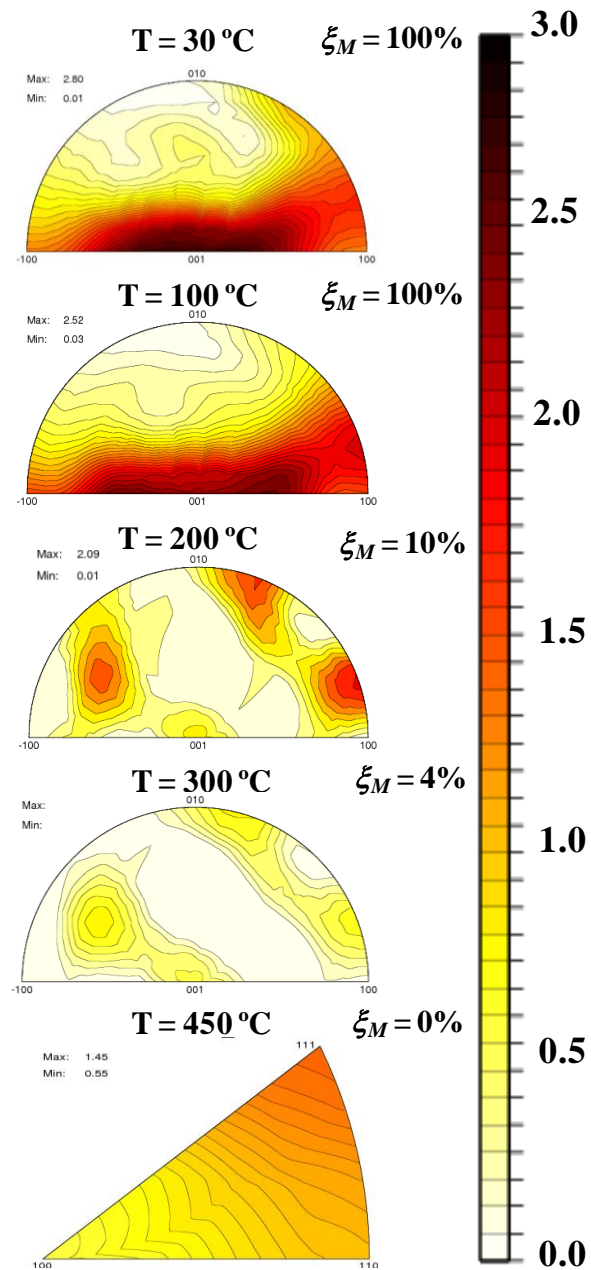


Figure 6.7.—IPFs for diffracting planes parallel to the loading direction in B19' martensite and B2 austenite during heating. The temperatures at which data were taken are indicated above and the martensite volume fractions, ξ_M , are indicated at the top right hand corner of each IPF. The maximum and minimum intensities are indicated at the top left hand corner in multiples of random distribution.

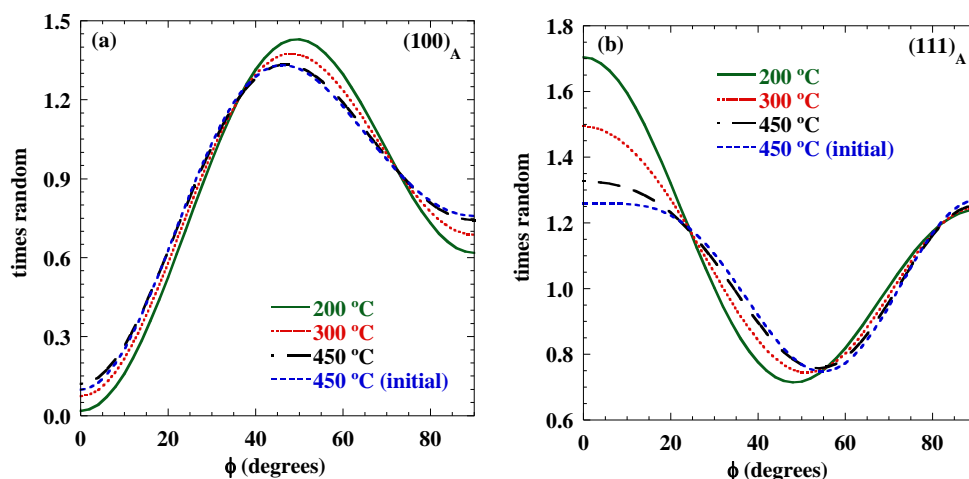


Figure 6.8.—Axial distribution plots for austenite in NiTi during constrained heating for (a) $\{100\}_A$ and (b) $\{111\}_A$. The initial no-load condition at 450 °C is also plotted for comparison. ϕ is the angle between the plane normal and the loading axis.

6.3.3 Second Shape Set

At the end of the first shape set, where the sample was stress-free at room temperature after unloading, the same shape setting procedure was repeated a second time with an additional pre-strain of 7 percent (5.9 percent after unloading). There was some difference in the onset of reorientation/detwinning between the first and second shape sets as indicated in Figure 6.1. However, the stress-strain curves became nearly identical in the rehardening portion of the response (above 4.5 percent strain). The stress-temperature response of the two cycles, depicted in Figure 6.4, shows similar behavior, with the exception that the maximum stress generated during heating was slightly greater during the second shape set cycle. The maximum generated stress reached 380 MPa in the first experiment and 430 MPa during the second shape set. This could be due to small differences in the starting martensitic texture ($J_1=1.1$ versus $J_2=1.3$). But the rest of the stress-temperature response was identical, including the characteristic temperatures where relaxation and stress generation began and ended, as well as the magnitude of the changes.

From a microscopic viewpoint, the measured elastic lattice strains during pre-straining and unloading at room temperature show comparable strains and strain drops due to springback for all B19' hkl reflections. From these results, it is experimentally revealed that shape setting serves to re-zero the material, meaning that the starting and ending internal states of the material after the first thermal cycle were equivalent microscopically, independent of the altered macroscopic shape.

To further confirm these findings, texture evolution in the austenite was examined. Figure 6.9 shows normalized neutron spectra for the austenite phase recorded at 450 °C from diffracting planes parallel to the loading direction both before (as-received material) and during the first and second shape sets. All three conditions exhibit identical texture as indicated by the same peak intensities and peak widths for the $\{100\}_A$ and $\{110\}_A$ planes, as well as other planes not shown here. Furthermore, texture indexes, which consider both parallel and perpendicular plane orientations were evaluated using Rietveld refinement methods and were found to be equal to $J=1.12$ for all three conditions. Figure 6.10 illustrates graphically the texture similarities through the IPFs of planes parallel to the loading direction. All texture representations establish that the austenite texture remains unchanged even after two shape-set cycles, leading to a total change in strain of 12.1 percent. A different sample with similar starting texture was subjected to the same two-cycle test and, as expected, the same macroscopic response and underlying microstructural behaviors were observed.

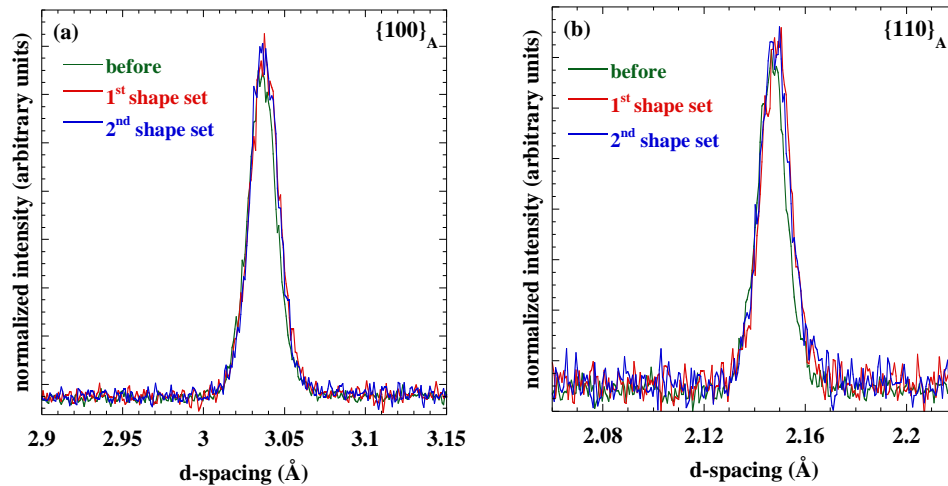


Figure 6.9.—Sections of the normalized neutron diffraction spectra for NiTi austenite acquired at 450 °C before (as-received condition) and during the first and second shape sets for (a) $\{100\}_A$ and (b) $\{110\}_A$ reflections. The reflections are from lattice planes parallel to the loading axis.

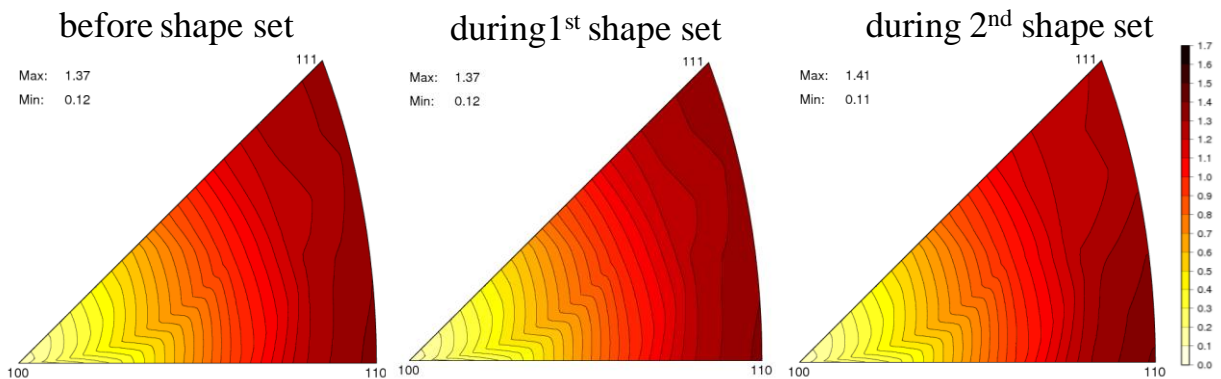


Figure 6.10.—B2 austenite IPFs for diffracting planes parallel to the loading direction at 450 °C (as-received condition) before and during the first and second shape sets. The maximum and minimum intensities are indicated at the top left hand corner in multiples of random distribution.

6.3.4 Pre- and Post-Shape Set Shape Memory Behavior

The effect of the shape setting process on shape memory behavior from both the macroscopic and microstructural perspectives was also investigated. Macroscopically, the shape memory behavior was investigated through stress-free and constant-stress, thermal-cycle testing at 200 MPa. This would be close to the maximum stress that such an alloy would probably be subjected to in a typical application. The microstructural counterpart was studied by looking at the martensite texture before, during, and after thermal cycling.

Consequently, once the second shape set was completed on the original sample, it was loaded to 200 MPa in tension at room temperature and cycled twice from room temperature to an upper cycle temperature of 200 °C. Figure 6.11(a) shows the strain-temperature response under the constant 200 MPa stress for the shape set sample compared to the as-received material. The curves are labeled from 1 to 6 where 1 is the unloaded state at the end of the second shape set, and stage 6 is the end of the 200 MPa load-biased thermal cycling experiment (the as-received material response was labeled in a similar fashion 7-12). Once loaded to 200 MPa (1→2), the stress was fixed and the sample was heated to an upper cycle temperature of 200 °C (2→3) and cooled back to room temperature (3→4). The observed strain evolution as a function of temperature is consistent with typical load-biased thermal cycling

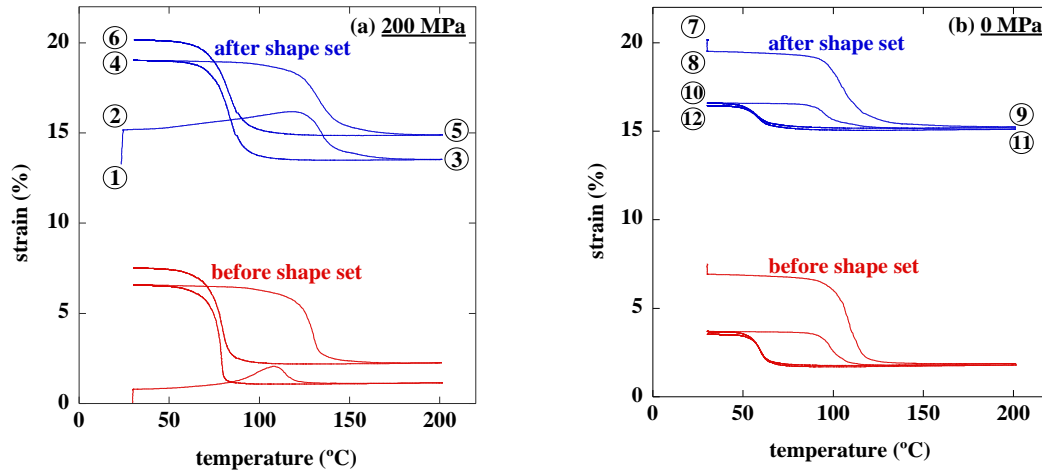


Figure 6.11.—Strain-temperature response of NiTi under constant stress of (a) 200 MPa and (b) 0 MPa before and after shape setting.

experiments on this same material, where an initial transient response was attained on the first cycle [171]. On the second thermal cycle (4→5→6), a characteristic strain-temperature curve was obtained from which transformation strain (from stage 4→5) and unrecovered strain (from stage 4→6) were determined and compared to the properties of the as-received material (Table 6.2).

It is apparent from Figure 6.11(a) and Table 6.2, that there are small differences in the shape memory response between the two materials including the initial transient response, transformation and unrecovered strains, and the work output (work = applied engineering stress×transformation strain). In essence, the shape set material exhibited a slightly larger transient response, marginally larger unrecovered strain, and smaller transformation strain.

TABLE 6.2.—LOAD-BIASED AND STRESS-FREE SHAPE MEMORY BEHAVIOR FOR NiTi IN THE AS-RECEIVED AND SHAPE-SET CONDITIONS

Material	200 MPa		
	Transformation strain, %	Unrecovered strain, %	Work, J cm ⁻³
As-received	4.32	0.95	8.64
After shape set	4.14	1.13	8.28

0 MPa	
Transformation strain, %	Recovered strain, %
1.89	0.16
1.46	0.14

Following the 200 MPa load-biased thermal cycling experiments, the samples were unloaded to 0 MPa stress and thermally cycled to investigate the strain or shape recovery under essentially stress-free conditions to determine the propensity of the material to display two-way shape memory effect (TWSME), after so few “training” cycles. Figure 6.11(b) shows the subsequent strain-temperature response of both the shape set and the as-received material. The data for the two stress-free thermal cycles for the shape materials are labeled from 7 to 12, following the same numbering scheme as in Figure 6.11(a). After completion of the two thermal cycles at 200 MPa, the sample was unloaded at room temperature and the elastic strain was recovered (stage 7→8). A large strain recovery was then observed during the initial heating cycle to stage 9. On cooling and subsequent thermal cycling, the sample was shown to exhibit two-way shape memory effect (stage 10→11) with the residual strains (stage 10→12) reported in Table 6.2. Similar to the trend in the 200 MPa cycling experiments, the magnitude of the TWSME was found to be lower in the shape set material

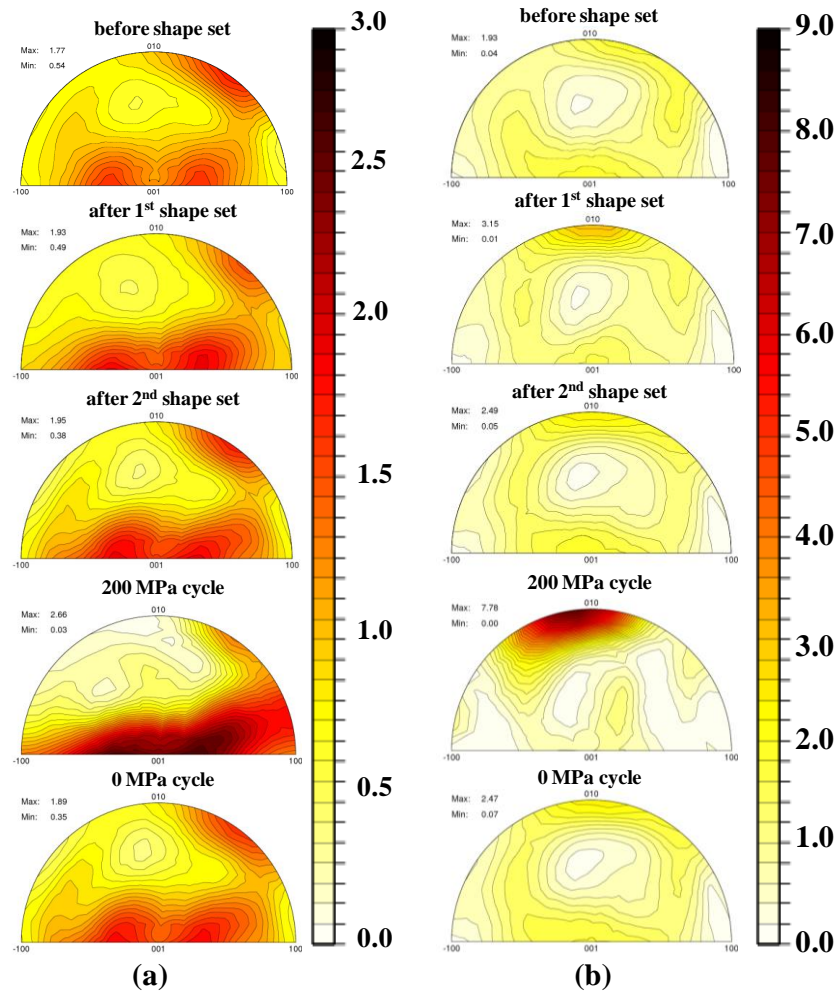


Figure 6.12.—B19' IPFs for diffracting planes (a) parallel and (b) perpendicular to the loading direction. From top: (i) as-received material, (ii) after the first shape set cycle, (iii) after the second shape set cycle, (iv) after two thermal cycles at 200 MPa and finally (v) after two thermal cycles at 0 MPa. For clarity in presentation, different scales are used in each direction.

(1.46 percent compared to 1.89 percent for the as-received material). However, the magnitude of the TWSME was somewhat surprising given that it was developed in only two thermal cycles under a moderate load.

The microstructural counterparts to the abovementioned thermal cycling experiments are shown in the IPFs of Figure 6.12(a) for planes parallel and in Figure 6.12(b) for planes perpendicular to the loading direction. From top to bottom the conditions are (i) as-received material, (ii) after the first shape set cycle that resulted in 6.2 percent permanent strain in the sample, (iii) after second shape set that resulted in an additional 5.9 percent strain (12.1 percent total), (iv) after the two 200 MPa thermal cycles and finally (v) after the two 0 MPa thermal cycles. Texture of the as-received material before shape setting ($J_1=1.1$) and after the first ($J_1=1.3$) and second ($J_1=1.2$) shape set are near-identical. The magnitude differences were attributed to the measured variations in the load-biased and TWSME results presented in Figure 6.11 and Table 6.2, since the starting microstructures of the shape set and as-received material are not exactly identical.

Nucleation and growth of preferred martensite variants that favor the applied stress during thermal cycling were clearly captured on the fourth IPF row (Figure 6.12) when the material was cycled under a constant 200 MPa stress. The transformation strains reported in Table 6.2 are associated with the

orientation of selected martensite variants during transformation indicated by the high intensity at the $(\bar{1}50)_M$ and $(010)_M$ orientations of Figure 6.12(b). On cycling at 0 MPa, the texture relaxes back to a more self-accommodated martensite structure after the two no-load cycles, as it reverts to the original starting texture.

This comparison shows that the material has retained the initial starting texture (self-accommodated state) after shape setting. Hence, shape setting, which consisted of pre-straining, constraining, heating and cooling served to change the macroscopic shape but not the underlying microstructure of the material. Thus, the microstructural changes observed during the shape set procedure occur as a process to alter the net macro shape without significantly impacting the microstructure or properties of the material. Furthermore, after two load-biased thermal cycles, the material also tries to revert back to the original self-accommodated state if given the opportunity, in this case through stress-free thermal cycling.

6.4 Discussion

Based on the macroscopic and neutron diffraction data presented, the micromechanical deformation mechanisms responsible for the stress generation and relaxations shown in Figure 6.4 can be better understood. Before pre-straining, the NiTi sample consisted of self-accommodated martensitic variants with a very weak preferred texture (Figure 6.3). When the sample was isothermally deformed in tension at room temperature, reorientation and detwinning of preferred martensite variants occurred resulting in a macroscopic shape change of 7.5 percent strain. The dominant martensite variants selected in the loading direction were $(\bar{1}50)_M$ and $(010)_M$, as indicated by the IPFs shown in Figure 6.3(b). Unloading resulted in a relatively large strain recovery (1.3 percent strain) due to reverse reorientation (rubberlike behavior [195, 196]) in addition to the elastic strain recovery. This reverse reorientation is demonstrated in Figure 6.3(b) by the intensity decrease at the $(\bar{1}50)_M$ and $(010)_M$ orientations. At this unloaded state, the sample contained reoriented and detwinned martensite capable of accommodating a 6.2 percent change in sample length.

At this point in the experiment, the sample was constrained so that it could no longer undergo any macroscopic change in shape and was then heated. Initially, from room temperature to about 80 to 90 °C, the stress is essentially zero and then starts to increase at the start of the reverse transformation process. Thermally, the stresses that build up in the sample over this temperature range should be negative, but the macro stress that was measured was essentially zero due to accommodation of the thermal stress by additional reorientation/detwinning of the martensite (Figure 6.4(a)).

The martensite then starts converting to austenite at around 90 °C. From the A_s to 173 °C (slightly above $A_f \sim 160$ °C), the reoriented and detwinned martensite transformed to the parent austenite phase, with a significant buildup of stress (Figure 6.4(a)). This stress, also referred to as blocking or recovery stress [185, 192, 200], is attributed to thermal and internal stress buildup due to the constrained phase transformation. The thermal strains were calculated to be 0.0884 percent using a temperature difference of 68 °C and a coefficient of thermal expansion of $13 \times 10^{-6}/^\circ\text{C}$. Assuming the highest elastic modulus of either martensite or austenite (e.g., 134 GPa [43]), the maximum stress that can be generated from the thermal strains is approximated 118 MPa. However, this thermal stress is actually compressive in nature since the sample wants to expand with increasing temperature, which requires a compressive stress to keep the sample length constant. Keeping in mind that this thermal stress component is an estimated upper bound, the macroscopic measured tensile stresses of 380 and 430 MPa from the first and second shape sets, respectively, represent the net macroscopic stress generated by the sample due to the constrained phase transformation and associated volume changes offset by the -118 MPa thermal stresses.

From 173 to 450 °C, the generated stresses relaxed gradually to 0 MPa as observed in Figure 6.4(b). This relaxation can be attributed in large part to thermal stresses due to constrained expansion. Thermal stresses alone would account for ~266 MPa of compressive stress over this temperature range, and would explain the nearly linear decrease in stress with temperature as shown in Figure 6.4. Recovery processes would be needed to keep the stress from driving into compression at the highest temperatures and along

with thermal stresses help accommodate the transformation of retained martensite into austenite. As shown in Figure 6.7, some retained martensite was present even above the apparent A_f temperature, which with the addition of thermal energy converted to austenite. Usually there is no mechanism to accommodate the last of the austenite formation except by plastic deformation, but in this case recovery processes and thermal stresses would also be beneficial in relaxing the internal constraints.

Recovery processes (thermally activated dislocation processes) relax any internal constraints that could have formed during the last martensite conversion, in addition to the bulk thermal stresses. This is even more evident during cooling where stress does not buildup within the sample down to about 200 °C but remain at zero. Here the material is recovering with no change in orientation of the austenite, which as illustrated in Figure 6.5 by the peak intensities and in Figure 6.6(a) and (c) by the lattice strains that evolved toward the starting internal state. Relaxation of the internal state was captured through the stress mismatch calculation presented previously and summarized in Table 6.1. Such a behavior can be explained by a recovery process due to 001 type dislocation glide/climb. The intensity changes during heating from 200 to 450 °C of Figure 6.5 are due the volume fraction changes and not to evolution of a new texture orientation. It is believed that the stress relaxation observed at these low temperatures is the result of short-circuit diffusion-mediated $\langle 100 \rangle$ dislocation processes, as observed in other B2 systems [201]. This behavior is completely consistent with the relaxation that occurs in the material at temperatures greater than ~200 °C, as observed in Figure 6.4(b) and the lack of any change in austenite texture [38].

Cooling from 450 to 220 °C, the microstructure is fully austenitic and essentially all thermal stresses were relaxed through recovery processes that can occur at a rate to maintain zero stress in the material as the sample is cooled under constraint (Figure 6.4(c)). Below 220 °C, thermal stresses were generated and built up to about 200 MPa (as expected from CTE).

Once at the M_s temperature (~100 °C), martensite forms and relieves the thermal stresses to 0 MPa at 69 °C (Figure 6.4(d)). Stresses were relaxed via nucleation and growth of the martensite phase that drive the system toward equilibrium. The orientation of martensite variants relative to the initial austenite crystal, combined with the interaction and combination of different martensite variants offset the 200 MPa stress to zero. The last stress buildup in the martensite phase (below 67 °C) is attributed to the B19' thermal contraction that was calculated to produce ~50 MPa. The final martensite microstructure after shape setting was found to be similar to the starting self-accommodated microstructure, but a small volume fraction of $(010)_M$ oriented variants remained in the system (Figure 6.12(b)).

With a slightly textured starting microstructure compared to the initial starting martensite (presence of $(\bar{1}50)_M$ and $(010)_M$ variants), the second shape set stress-strain curve (Figure 6.1) showed a different reorientation and detwinning response at least initially during loading. However, the general stress-temperature responses of the first and second shape sets were very similar (Figure 6.4), which means that the same mechanisms described in the first shape set process were also active during the second. In contrast to the slight change in martensite texture, the microstructures of the austenite phase during the first and second shape sets at 450 °C were identical as shown in Figure 6.8 and Figure 6.10. This further confirms that the microstructure was fully relaxed at 450 °C through conversion of martensite and recovery processes.

Comparison of the shape memory effect before and after shape setting revealed that the material exhibited similar transient responses, transformation strains, TWSME and unrecoverable deformation strains (Figure 6.11 and Table 6.2). Nevertheless, the magnitudes were slightly different due to the variation in the starting martensitic microstructures (Figure 6.12). From the data presented, it is speculated that this shape set procedure can be repeated many times and the same behavior both macroscopically and microstructurally would be obtained.

6.5 Conclusions

Shape setting of a bulk polycrystalline $\text{Ni}_{49.9}\text{Ti}_{50.1}$ (in at.%) shape memory alloy was investigated using in situ neutron diffraction experiments. By quantitatively linking micromechanical mechanisms with the macroscopic measurements during a shape set experiment the following conclusions can be made.

- a. Room-temperature isothermal deformation of NiTi was accomplished through reorientation/detwinning of preferred martensite variants, which resulted in a microstructure containing $(\bar{1}50)_M$ and $(010)_M$ variants along the loading direction. The same texture was preserved after unloading to 0 MPa, but with reduced intensity due to the reverse reorientation.
- b. Constrained heating from A_s to slightly above A_f resulted in the generation of bulk tensile stresses due to volumetric differences during constrained transformation of martensite to austenite, offset by bulk thermal stresses.
- c. Further heating to 450 °C, resulted in a complete macroscopic and microscopic (intergranular) relaxation of stresses/strains due to constrained thermal expansion and recovery processes, e.g., thermally activated $\langle 001 \rangle$ type dislocation glide/climb processes. The austenite microstructures of both shape sets as well as that of the as-received material were identical at 450 °C as they would not be affected by $\langle 100 \rangle$ glide/climb processes.
- d. Constrained cooling from 450 to 220 °C resulted in no macroscopic changes in stress as the austenite thermal contraction was offset by recovery processes. Stresses generated with further cooling to M_s resulted primarily from thermal contraction and possibly affected by early formation of martensite. These stresses were completely relaxed once all the austenite was converted to martensite, through detwinning/reorientation of the martensite, though the final texture was similar to the as-received material.
- e. A second shape set performed on the same sample showed similar macroscopic response with the observations indicating that the same mechanisms were active during the second shape setting process. This process could be repeated with similar results, since after each cycle the material is reset to a similar starting texture and internal equilibrium.
- f. Comparison of the shape memory effect observations between the as-received and the shape set materials yielded similar characteristics, i.e., transient response, transformation strain, unrecovered strain and TWSME. There were small differences in magnitudes that were attributed to the complete recovery of the as-processed material when cycling through 450 °C during the shape setting procedure.

Chapter 7.—Microstructural Response During Isothermal and Isobaric Loading of a Precipitation Strengthened Ni-29.7Ti-20Hf High-Temperature Shape Memory Alloy

A stable Ni-rich Ni-29.7Ti-20Hf (at.%) shape memory alloy, with relatively high transformation temperatures, was shown to exhibit promising properties at lower raw material cost when compared to typical NiTi-X (X = Pt, Pd, Au) high-temperature shape memory alloys (HTSMA). The excellent dimensional stability and high work output for this alloy were attributed to a coherent, nanometer size precipitate phase observed using transmission electron microscopy. To establish an understanding of the role of these precipitates on the microstructure and ensuing stability of the NiTiHf alloy, a detailed study of the micromechanical and microstructural behaviors was performed. In situ neutron diffraction at stress and temperature was used to obtain quantitative information on phase-specific internal strain, texture, and phase volume fractions during both isothermal and isobaric testing of the alloy. During isothermal testing, the alloy exhibited low isothermal strains due to limited detwinning, consistent with direct measurements of the bulk texture through neutron diffraction. This limited detwinning was attributed to the pinning of twin and variant boundaries by the dispersion of fine precipitates. During isobaric thermal cycling at 400 MPa, the high work output and near-perfect dimensional stability was attributed to the presence of the precipitates that act as homogeneous sources for the nucleation of martensite throughout the material, while providing resistance to irrecoverable processes such as plastic deformation.

7.1 Introduction

The unique property of shape memory alloys (SMAs) to recover their original undeformed shape when heated has made them useful multifunctional materials for the development of adaptive engineering structures. This distinctive ability is a result of a displacive, solid-to-solid martensitic phase transformation between a high temperature, higher symmetry austenite phase (cubic B2) and a lower temperature, lower symmetry martensite phase (e.g., orthorhombic B19 or B33, monoclinic B19', trigonal R-phase, etc.). Through this martensitic transformation, SMAs can generate recoverable shape changes of several percent strain even when opposed by large stresses (e.g., up to 500 MPa), resulting in high work output that is competitive with, or superior to, conventional hydraulic, pneumatic or electromagnetic actuators [180, 202]. In addition, SMAs can function as both the sensor and actuator in a single mechanism, reducing engineering complexities. Hence SMAs are a promising alternative to conventional actuators in aerospace and automotive applications [203-206].

However, broad commercial success of shape memory alloy actuators has been elusive. This is largely attributed to the fact that commercially available SMAs are primarily limited to binary NiTi alloys that generally exhibit phase transformations at temperatures from slightly below room temperature to around 100 °C [9], severely restricting the environment in which they can be used. Furthermore, binary NiTi alloys can be dimensionally unstable, displaying significant irrecoverable strains during repeated thermomechanical cycling [207, 208]. Various methods have been proposed to address both limitations, i.e., the relatively low transformation temperatures and poor dimensional stability often associated with many SMA systems. The addition of Pt, Pd, Zr or Hf to binary NiTi has been shown to increase transformation temperatures [209]. However, none of these systems are without disadvantages, including the rising cost of precious metals, limited transformation strains, and the aforementioned issues associated with dimensional stability. In an attempt to improve the shape memory behavior of these high-temperature systems, various approaches such as solid-solution strengthening [210, 211], thermomechanical cycling/training [9, 212, 213], severe plastic deformation processing [213-216], and precipitation strengthening [217, 218] have been attempted with various degrees of success. In most cases, however, the emphasis has been on mere demonstration of high-temperature shape memory alloy (HTSMA) behavior with little effort to develop HTSMAs with optimal work output and dimensional

stability. Similar techniques have also been applied to ferromagnetic shape memory alloys in an attempt to improve their mechanical and functional properties [219, 220].

Little can be done to address the cost of raw materials other than to focus on systems such as NiTiZr and NiTiHf that do not contain precious metals. Reports on NiTiHf HTSMAs with 8 at.% Hf addition [215, 221, 222], 10 at.% Hf [223, 224], 15 at.% Hf [225-233], and higher Hf additions [234-236] have revealed numerous problems with this system including thermal cyclic response degradation [231], brittleness [236], poor workability [237], low recoverable and transformation strains [231], poor thermal and dimensional stability [209], wide hysteresis [209], generally poor shape memory response [231], and nonexistent superelastic behavior [230]. In all these examples, the materials studied were near stoichiometric or Ni-lean in composition (containing 50 at.% or less Ni). More recently, it has been realized that it is possible to modify the microstructure of Ni-rich NiTiHf alloys through aging, generating submicron precipitate structures and stable transformation temperatures [218]. Preliminary results on a Ni-29.7Ti-20Hf (at.%) alloy indicate that precipitation strengthening also leads to outstanding load-biased shape memory behavior, with little or no irrecoverable strain, and excellent superelastic qualities [238].

Thus, the objective of this chapter was to examine the microstructural mechanisms responsible for the stable high-temperature behavior of a Ni-29.7Ti-20Hf alloy containing coherent nanometer size precipitates. Until now, there have been no experimental investigations on the phase-related micromechanical and microstructural behavior of this Ni-rich NiTiHf alloy. In situ neutron diffraction at stress and temperature is a uniquely suited advanced characterization technique that was used to study this alloy at an atomistic level. Compared to conventional x-ray diffraction techniques, neutron diffraction provides greater penetration depths (sampling volumes up to 1 cm³) representing bulk behavior of polycrystalline samples and avoiding free surface stress effects. Furthermore, in spite of the complicated deformation mechanisms associated with SMAs (e.g., twinning, reorientation or stress induced martensite coupled with the possibility for plasticity) it is possible to follow the microstructural changes that occur with stress and temperature, since diffraction patterns are simultaneously recorded. The role of the precipitates during both isothermal and isobaric testing conditions was explored and the internal strain and texture evolution of martensite and austenite phases were evaluated for this material.

7.2 Experimental Methods

7.2.1 Sample Preparation

A NiTiHf ingot with a nominal composition of 50.3Ni-29.7Ti-20Hf (in at.%) was prepared by vacuum induction melting. The ingot was vacuum homogenized for 72 hr at 1050 °C and furnace cooled followed by hot extrusion (Ext. 124) at 900 °C and an area reduction ratio of 7:1. Cylindrical tensile blanks were removed from the extruded rod and subjected to an aging treatment at 550 °C for 3 hr and furnace cooled. This heat treatment was selected after a previous optimization study of different aging temperatures and times, where it was found that these conditions provided the best thermomechanical properties. The cylindrical blanks were then finish machined into dog-bone tensile specimens with final dimensions of 5.08 mm in diameter and 15.24 mm in gauge length. After machining, the tensile samples were subjected to one stress-free thermal cycle between room temperature and 300 °C in a muffle furnace in air to relieve any residual stresses due to machining and promote a self-accommodated martensite structure. The no-load transformation temperatures: martensite start (M_s), martensite finish (M_f), austenite start (A_s), and austenite finish (A_f) were determined to be 118, 109, 129, and 149 ±2 °C, respectively, using the intercept method as defined in Ref. [148]

7.2.2 Experimental Setup and Test Procedures

In situ neutron diffraction measurements were performed on the Spectrometer for MAterials Research at Temperature and Stress (SMARTS) at the Manuel Lujan Jr. Neutron Scattering Center, LANSCE, at Los Alamos National Laboratory (LANL). A schematic of the experimental setup is shown in Figure 7.1. Similar to the previous experiments, macroscopic strains were obtained concomitantly while recording

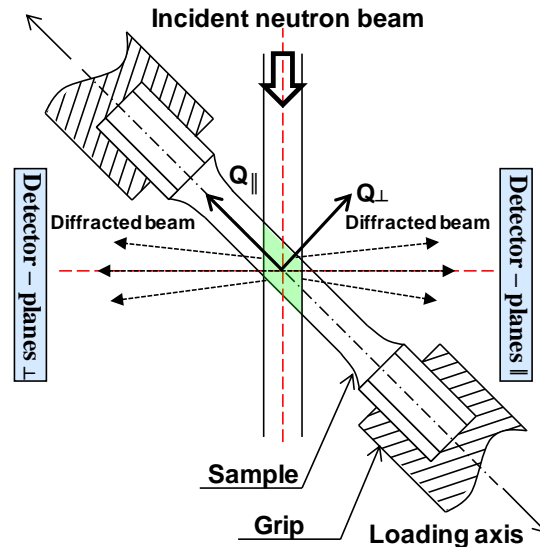


Figure 7.1.—Schematic of the SMARTS diffractometer experimental setup showing the incident and diffracted beams and scattering vectors (Q). The irradiated volume is shown in green.

neutron data using a high-temperature, 10 mm gauge length extensometer attached to the sample. Heating was controlled using a 5 kW induction heater and a temperature controller interfaced with LabVIEW, while cooling was achieved from natural convection and conduction through the water cooled grips and pull rods.

To obtain acceptable diffraction intensities, longer count times of about 50 min (compared to 30 min for binary NiTi) was necessary because of the higher absorption resulting from Hf in the sample. Initially, baseline stress-free diffraction patterns were measured at room temperature and at 300 °C for the purpose of (i) determining the count time and (ii) examining the initial interplanar spacing and starting texture of both the martensite and austenite phases.

Two types of experiments were carried out in this work; the first experiment consisted of isothermal monotonic loading at room temperature. The applied stress was increased in increments of 25 MPa from 0 to 250 MPa, and in increments of 50 MPa from 250 to 400 MPa at a rate of 30 MPa/min, with diffraction patterns being acquired at each stress increment with hold times of 50 min. The second experiment consisted of constant stress (isobaric or load-biased) thermal cycling of the same sample that was used in the first experiment. Without unloading, the 400 MPa stress was held constant and three thermal cycles between room temperature and 300 °C were performed with diffraction patterns recorded for each cycle at the two temperature extremes. Finally, the sample was unloaded to 0 MPa followed by two additional stress-free thermal cycles between the same temperatures while recording neutron spectra at room temperature and 300 °C. The choice of these experimental parameters was based on a condition where this shape memory alloy could likely be employed, particularly for high-temperature, high-force actuator applications. At the end of the experiment, the sample was loaded to 800 MPa at room temperature without acquiring neutron data, but the macroscopic stress-strain response was recorded. This data was used to compare the macroscopic responses of the alloy before and after isobaric thermal cycling. Diffraction data were analyzed using single-peak fitting and Rietveld refinement.

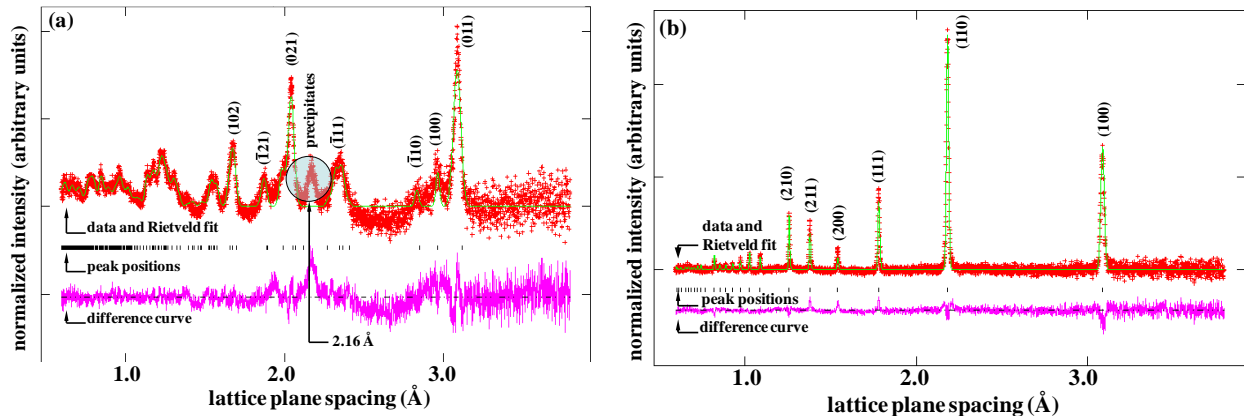


Figure 7.2.—GSAS Rietveld refinement output for Ni-29.7Ti-20Hf with diffracting lattice planes parallel to the loading axis with no externally applied load. (a) Monoclinic martensite at 35 °C showing a peak attributed to the precipitate phase and (b) NiTiHf cubic austenite at 300 °C. The measured data are indicated by cross-marks and the calculated profile is indicated by the solid line. The tick-marks below the profile pattern indicate the reflections. The lower curve is the difference between the measurement and refinement.

7.3 Results

7.3.1 Stress-Free Structure of the Ni-29.7Ti-20Hf Alloy

Figure 7.2 shows the refined neutron spectra for the NiTiHf alloy in the stress-free (unloaded) condition. The spectra confirm that the majority phase is B19' martensite at room temperature and B2 austenite at 300 °C. These refinements are from reflections with lattice planes parallel to the loading axis that were best fitted using a $P112_1/m$ structure for B19' martensite and $Pm\bar{3}m\bar{3}$ for B2 austenite. The best fit lattice parameters as determined from the Rietveld refinement method were $a = 3.041$, $b = 4.136$, $c = 4.886$ Å, $\alpha = \gamma = 90^\circ$, $\beta = 104.35^\circ$ for monoclinic martensite, and $a = 3.086$ Å for cubic austenite.

The profile from the refined martensitic spectrum (Figure 7.2(a)) was still noisy even after a 50 min count time, due to the absorption of neutrons by Hf. Even so, it was possible to capture and identify most of the crystallographic peaks. The difference curve plotted below the peak position tick-marks shows deviations between the raw neutron data and the Rietveld model. B19' martensite was the only phase introduced in the refinement scheme and the observed difference indicates the presence of a secondary phase. This is clearly indicated by the extra peak around a d-spacing of 2.16 Å and in other overlapped reflections with the monoclinic matrix that were not captured with the present single phase refinement. Transmission electron microscopy (Figure 7.3) was used to confirm the presence of a high density of fine precipitates (less than 20 nm) in the current alloy resulting from the original 550 °C, 3 hr aging treatment.

7.3.2 Isothermal Loading in Martensite

Figure 7.4(a) and (b) are the room-temperature tensile stress-strain responses of the NiTiHf alloy obtained from extensometry. Figure 7.4(a) shows the initial loading response, prior to isobaric thermal cycling, and the stresses at which neutron spectra were acquired (indicated by circles). Figure 7.4(b) shows the loading response of the material (superimposed with the response of Figure 7.4(a)) after thermal cycling, which consisted of three thermal cycles at 400 MPa followed by an additional two thermal cycles between room temperature and 300 °C without load. Thermal cycling appeared to have a negligible effect on the observed stress-strain behavior of the material, as the loading curves up to 400 MPa exhibit nearly identical responses. The sample, initially in a self-accommodated martensitic state, starts deforming elastically before reaching a stress where reorientation/detwinning of the martensite is expected to begin. However, no distinct stress plateau was observed even after loading to 800 MPa (Figure 7.4(b)) and it was not readily apparent where the onset of inelastic deformation starts for this alloy. Another significant observation is the limited strain (0.7 percent) attained at 400 MPa during isothermal monotonic loading. This deformation strain is

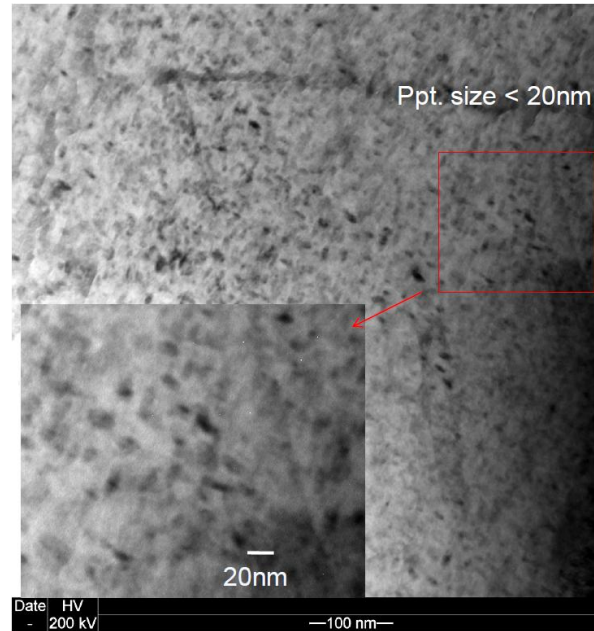


Figure 7.3.—Bright field TEM micrograph showing the microstructure of the NiTiHf alloy, consisting of a B19' monoclinic martensite matrix at room temperature with the inset showing in more detail the homogenous distribution of nanometer sized precipitates.

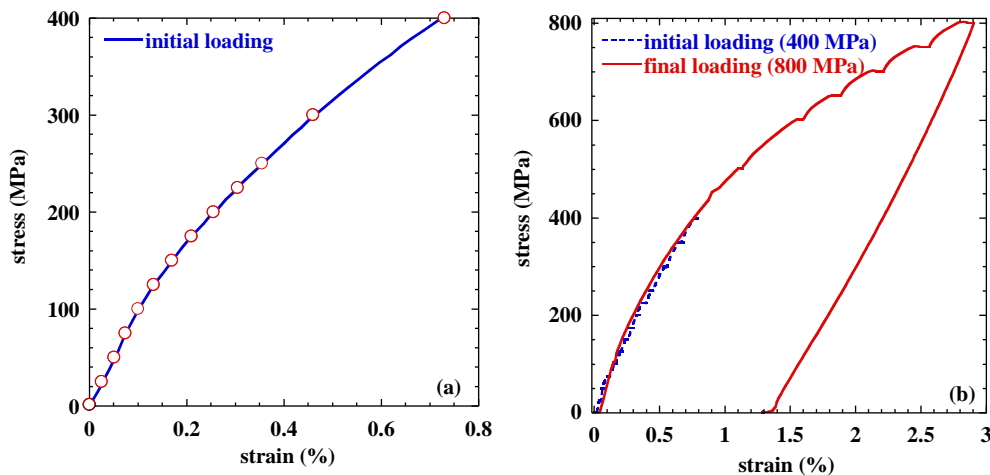


Figure 7.4.—Tensile stress-strain response of Ni-29.7Ti-20Hf at room temperature (from extensometry). (a) Initial loading response showing the onset of nonlinearity and the stresses at which neutron diffraction spectra were acquired and (b) complete loading and unloading curve to 800 MPa, after isobaric thermal cycling, compared to the initial loading response to 400 MPa.

a combination of the elastic strain and inelastic martensite variant reorientation/detwinning that is typically expected to be recovered after unloading and heating to the austenite finish temperature. This total macroscopic strain is nearly an order of magnitude lower than that observed for NiTi at comparable stress levels (e.g., ~6 percent strain), where recoverable strains on the order 5 percent or more are possible through isothermal loading at room temperature followed by thermal recovery [43].

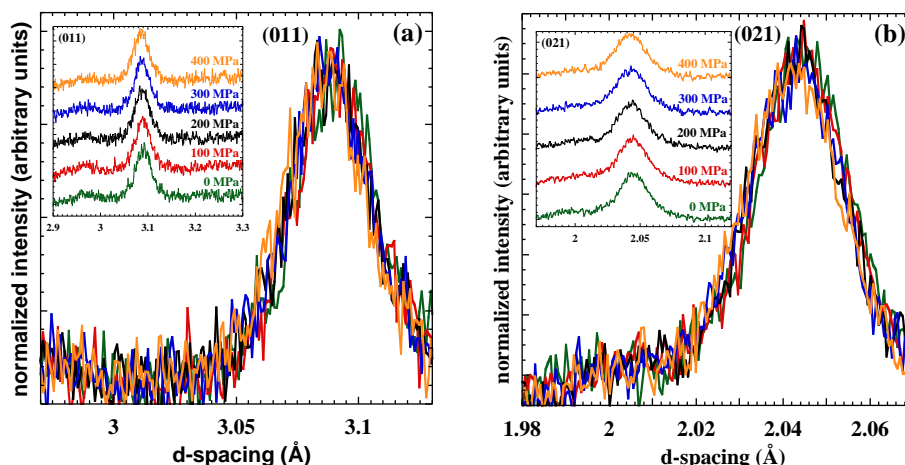


Figure 7.5.—Section of normalized neutron diffraction spectra acquired at various stresses during loading to 400 MPa for (a) (011) and (b) (021) monoclinic crystallographic planes. The reflections are from lattice planes parallel to the loading axis. The insets represent the same spectra offset vertically for clarity.

To investigate the microstructural mechanisms that limit the variant reorientation and detwinning of martensite in this NiTiHf system, neutron diffraction was used. The specimen was loaded under stress control from 0 to 400 MPa with neutron diffraction spectra acquired initially every 25 MPa to capture the start of the stress-strain nonlinearity. Normalized diffraction spectra from lattice planes parallel to the applied stress corresponding to selected stress-strain states are shown in Figure 7.5. All spectra were normalized to the (120) martensite peak so that they have the same area for all stress increments. For clarity, the same overlay patterns were offset vertically with increasing stress as shown in the insets of Figure 7.5. No new peaks and relatively little change in peak intensities were observed as the stress was increased from 0 to 400 MPa. Similar behaviors were apparent using neutron spectra from lattice planes perpendicular to the direction of the applied stress. The absence of a macroscopic stress plateau and limited inelastic strain in Figure 7.4(a) is consistent with the nearly imperceptible changes in both the (011) and (021) diffraction peaks shown in Figure 7.5.

Small changes in texture are better detected when the entire spectrum is considered. Therefore, to differentiate any change in texture that might occur during deformation, inverse pole figures (IPF) were generated utilizing the entire recorded spectra for a given bank of detectors (Figure 7.6). These IPFs were generated for the minimum unique region for the monoclinic crystal symmetry ($P112_1/m$ structure) in multiples of random distribution (MRD). Each IPF is plotted with its corresponding stress at which it was measured and the maximum and minimum pole intensities. Small changes in texture with loading were observed in Figure 7.6(a) at the (110) and (012) orientations and in Figure 7.6(b) at the (130) orientation.

Figure 7.7 shows the elastic lattice strains in the martensite as a function of applied stress obtained from single peak fits for the (011), $(\bar{1}11)$, (021) and (030) crystallographic planes. Lattice strains develop in compression or tension depending on whether the diffracting lattice planes are parallel (Poisson strain) or perpendicular to the loading direction. These strains were obtained from shifts in diffraction peaks to lower d-spacing for lattice planes parallel to the loading axis due to Poisson contraction, and due to tensile stresses to higher d-spacing for lattice planes perpendicular to the loading direction. The strains are the average strain in a subset of all variants with the same crystallographic orientation that contribute to the peak reflection (i.e., all variants with diffracting lattice planes perpendicular to the loading direction). Plane specific elastic moduli in directions normal to given hkl planes, E_{hkl} , for stresses up to 100 MPa were determined based on linear fits through the data and were found to be 93, 87, 84 and 64 ± 10 GPa for the (011), $(\bar{1}11)$, (021) and (030) lattice planes, respectively. From extensometry, the elastic modulus was measured for the linear region up to 100 MPa (onset of nonlinearity in lattice strains) and was found to be 87 ± 10 GPa (error from sample to sample variation). Therefore in this isothermal testing condition,

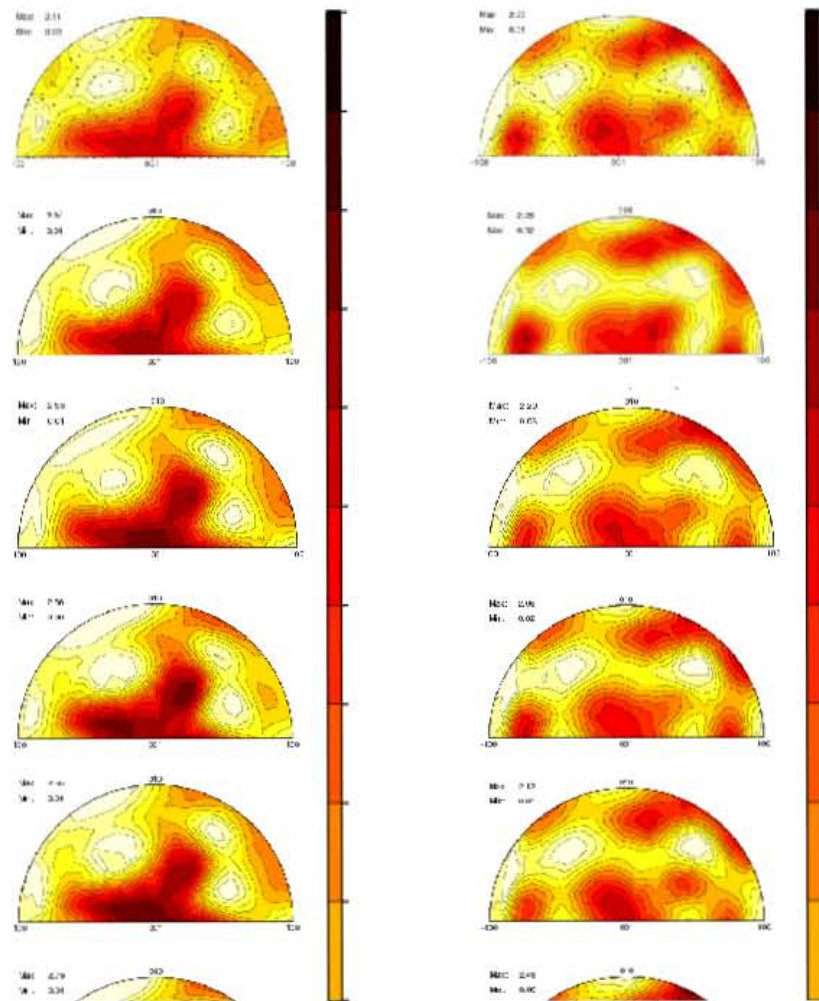


Figure 7.6.—B19' martensitic Ni-29.7Ti-20Hf IPFs for diffracting planes (a) parallel and (b) perpendicular to the loading direction in tension at various stress levels. For a given IPF, the stress state is indicated above the IPF and the corresponding maximum and minimum pole intensities (times random) are at the top left hand corner.

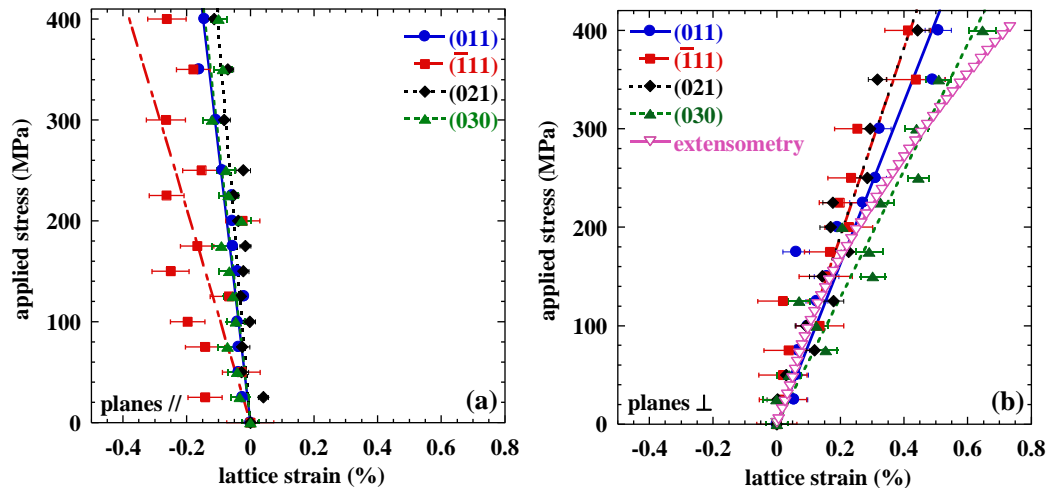


Figure 7.7.—Lattice strain associated with the (011), $(\bar{1}11)$, (021) and (030) reflections (a) parallel and (b) perpendicular to the applied loading in tension.

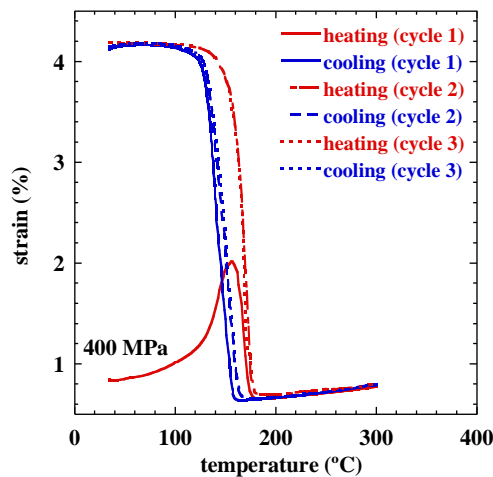


Figure 7.8.—Strain-temperature response for Ni-29.7Ti-20Hf for the first three thermal cycles at a stress of 400 MPa.

the elastic strain contributions to the overall mechanical response at 400 MPa is about 0.4 percent, where only the remaining 0.3 percent is attributed to the inelastic strains from variant reorientation and detwinning. Plane specific elastic moduli were also observed to exhibit comparatively lower elastic anisotropy than binary NiTi [43].

7.3.3 Isobaric Strain-Temperature Behavior

The isobaric strain-temperature response for the NiTiHf alloy is shown in Figure 7.8. Three thermal cycles are shown, including the first cycle, at a constant stress of 400 MPa between room temperature and 300 °C. The first heating cycle starts from a strain of 0.8 percent, which was generated from loading to 400 MPa at room temperature (0.1 percent strain higher than the original isothermal loading due to a longer hold time at 400 MPa, while acquiring neutron spectra). As the sample is heated during the first thermal cycle, strain in the uniaxial direction continues to build to about 2 percent and then recovers

completely as the sample transforms to B2 austenite. This initial cycle response will be referred to as the transient response in subsequent sections, as this behavior was only observed during the heating portion of the first thermal cycle.

Two important observations can be made from the successive thermal cycles; first, the transformation strains, determined from intercepts of the heating portion of the second and third thermal cycles, were constant at 3.5 percent. This is the available amount of actuation strain associated with a bias stress of 400 MPa. Second, no residual strains (i.e., strain difference between the start and finish of one thermal cycle at room temperature) were observed. No prior training was done to this alloy, and the observed behavior in strain-temperature space was obtained from the three initial cycles of a hot worked and aged material under stress, demonstrating the inherent dimensional stability of this alloy.

Figure 7.9 is a compilation of IPFs, acquired at room temperature for the B19' martensite at the initial no-load condition, the initial isothermal loading to 400 MPa, after the first three load-biased thermal cycles between room temperature and 300 °C at 400 MPa, and after the first no-load thermal cycle for both planes parallel and perpendicular to the loading direction. It is clear from the IPFs that the texture evolves during the first thermal cycle and then remains mostly unchanged for subsequent cycles. In particular, the intensities at the (020) orientation (Figure 7.9(b)) and at the (001) and (120) orientations (Figure 7.9(a)) increase as the material cycles through the phase transformation for the first time, but do not change significantly for succeeding thermal cycles under the same constant load of 400 MPa. Another important observation is the similarity in texture between the initial IPF and the IPF after the first no-load thermal cycle between room temperature and 300 °C (top and bottom IPFs). The material is shown to readily revert to the initial self-accommodating texture after the very first no-load thermal cycle. Both sets of data (Figure 7.6(a) and (b)) show this unique aspect, which further attest to the alloy's inherent stability by demonstrating an insensitivity of the response of the material to prior history.

The observed macroscopic dimensional stability was further investigated from a microstructural perspective by looking at sections of normalized diffraction spectra at 300 °C, shown in Figure 7.10. These spectra correspond to the austenite phase and are from lattice planes parallel to the loading direction. The overlay diffraction patterns were offset vertically with increasing cycle count and shown in the insets in Figure 7.10. A significant shift in peak positions to lower d-spacing from the no-load condition to the subsequent isobaric cycles was observed, which is due to Poisson strains in planes parallel to the loading direction. The lattice strains from the initial no-load condition to the 400 MPa first cycle were measured for the {100}, {110}, {111} and {210} crystallographic planes and found to be equal to -0.19 percent and 0.48 percent for planes parallel and perpendicular (not shown) to the loading axis, respectively. Similar to the isothermal loading in martensite, a sample (not shown here) was loaded in the austenite phase where the plane specific elastic moduli in directions normal to given *hkl* planes were measured. These moduli were found to be 85, 83, 77 and 80 GPa for the {100}, {110}, {111} and {210} lattice planes, respectively. From extensometry, the elastic modulus was measured to be 81 GPa. Poisson's ratio was also measured for this austenite phase to be 0.39. From Figure 7.10, no further shift in d-spacing (lattice strain) was seen after the second and third cycles. Note that all lattice planes exhibit nearly the same strain value, which is an indication that the austenite phase is essentially isotropic within experimental error. Texture and peak intensities were also unchanged, both after the initial loading and after thermal cycling. The intensity ratio of {100}/{110} and {100}/{111} planes were found to be 0.62 and 1.38, respectively for all three cycles. Another important parameter of value from Figure 7.10 is the peak breadth. Broadening is useful in quantifying the strain anisotropy and dislocation densities. All diffraction patterns for a specific plane were shown to exhibit the same breadth within error. Consequently, the neutron diffraction analyses indicated no evolution or change in the austenite phase with thermal cycling, which is yet another indication of the excellent stability of this alloy.

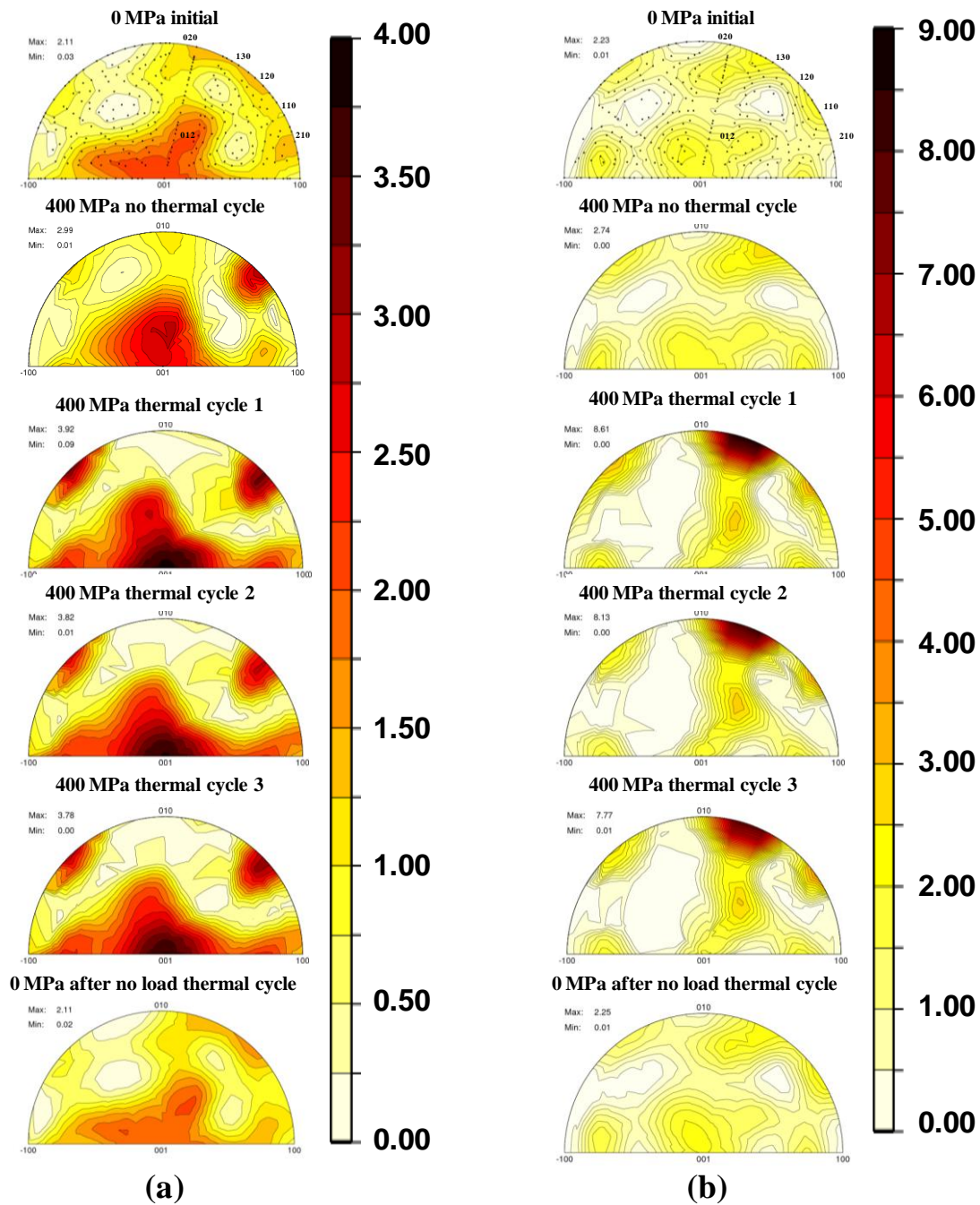


Figure 7.9.—IPFs for martensitic Ni-29.7Ti-20Hf determined at room temperature from diffracting planes (a) parallel and (b) perpendicular to the loading direction. From top to bottom the conditions are (i) as-received material (initial no-load), (ii) after initial load to 400 MPa at room temperature, and after the (iii) first thermal cycle, (iv) second thermal cycle (v) and third thermal cycle between room temperature and 300 °C at a stress of 400 MPa. The last IPF (vi) is after the first no-load thermal cycle, post isobaric thermal cycling.

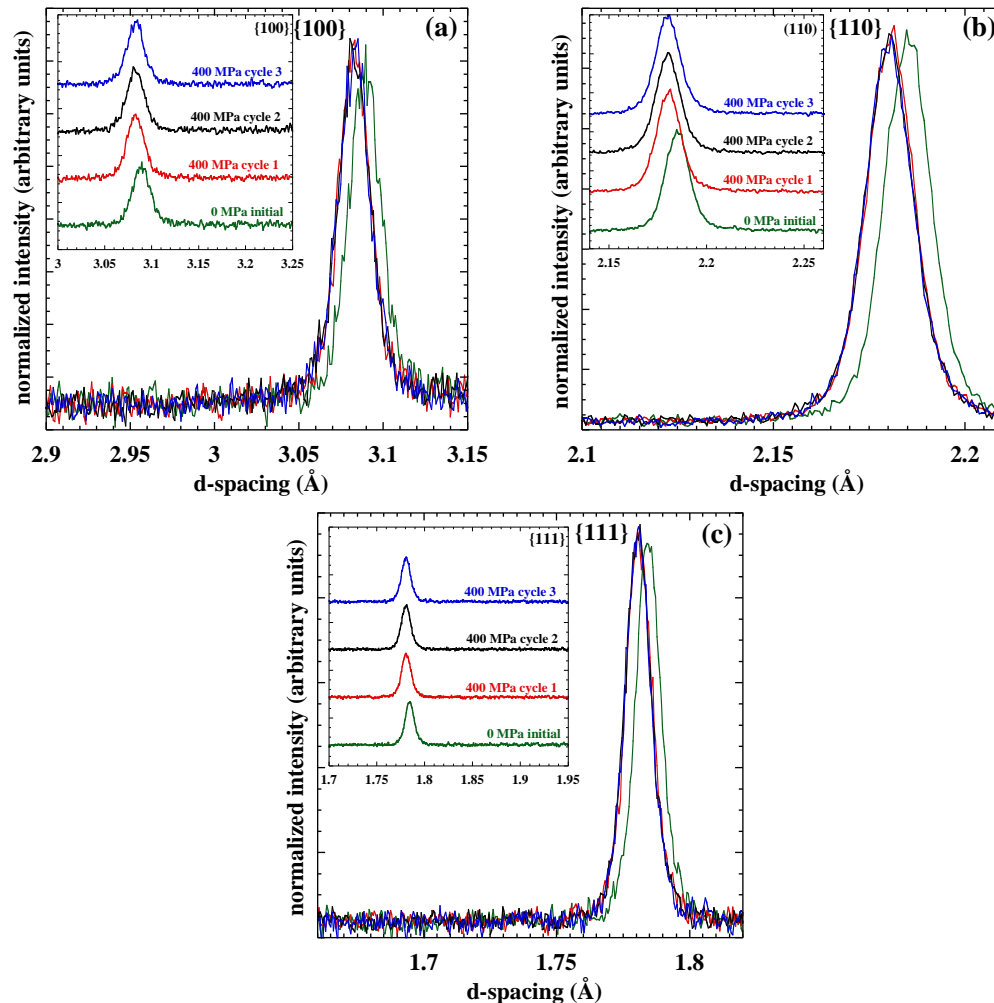


Figure 7.10.—Sections of the normalized neutron diffraction spectra for Ni-29.7Ti-20Hf austenite phase acquired at 300 °C during the first no-load thermal cycle and the first, second, and third isobaric thermal cycles at 400 MPa stress: (a) {100} (b) {110} and (c) {111} crystallographic planes. The reflections are from lattice planes parallel to the loading axis.

7.4 Discussion

In the following sections, the isothermal and isobaric responses of the precipitation strengthened Ni-29.7Ti-20Hf alloy are discussed with respect to the microstructural observations and micromechanical plane specific strains obtained from the in situ neutron diffraction results.

7.4.1 Initial Ni-29.7Ti-20Hf Microstructure

The refined B19' diffraction pattern adequately captures the crystallographic planes that belong to the martensitic phase, but does not include those related to the fine precipitate phase (Figure 7.2(a)). The presence of a fine precipitate phase was confirmed using transmission electron microscopy (Figure 7.3), but to date its structure has not been conclusively identified. It is believed that these fine precipitates are the secondary phase present in the neutron diffraction pattern unaccounted for in the refinement. One of the precipitate phase peaks is clearly shown at a d-spacing of 2.16 Å. It is probable that other precipitate peaks are present, but they were not detectable due to convolution with the B19' monoclinic matrix.

The austenitic diffraction spectrum, taken at 300 °C, is shown in Figure 7.2(b). No additional peaks that could be attributed solely to the precipitate phase were observed. This could be due to a close crystallographic relationship and similar crystal orientation as the parent B2 phase, since strains and thermal effects that take place during the martensitic transformation are not large enough to mask the appearance of the precipitate phase in the 300 °C diffraction spectrum. This situation would be similar to the case for the fine P_L -phase $Ti_{11}Ni_9Pt_4$ precipitates in Ni-rich NiTiPt [239, 240]. In this case, the precipitate has a close relationship to the B2 parent phase due to ordering of Pt on the Ni-sublattice. In fact, preliminary results indicate that the fine precipitate phase in the NiTiHf alloy has many similarities to the P_L -phase, including a very fine, coherent morphology and a complicated structure with strong relationship to the B2 parent phase [241]. While efforts are continuing to identify the detailed structure of these NiTiHf precipitates, several types of precipitate structures have been ruled out for this phase including the P_L -phase, the Ni_4Ti_3 phase, and the NiTiHf precipitate phase identified by Han et al. [227].

7.4.2 Isothermal Response

The monotonic room-temperature tension test (Figure 7.4) served to highlight several characteristics of the stress-strain response of the NiTiHf alloy. The macroscopic B19' elastic modulus, the onset of detwinning/reorientation, and the elastic and inelastic components of the total isothermal strain were examined. The initial linear elastic portion of the loading curve up to 100 MPa yielded an elastic modulus of 87 ± 10 GPa. The corresponding macroscopic elastic strain (up to 100 MPa) is approximately 0.1 percent. From a macroscopic standpoint, some nonlinearity is noticeable at stresses above 100 MPa, which is considered to be the onset of martensite variant reorientation/detwinning. However, in contrast to other SMA systems (e.g., NiTi [43]), there is no perceptible stress plateau indicative of easy reorientation/detwinning and the inelastic strains generated during deformation were relatively small. A total strain of 0.7 percent at 400 MPa and 2.85 percent at 800 MPa were recorded. This would be the maximum expected strain that could be recovered upon heating to above the austenite finish temperature under stress-free conditions. However, given the fairly large component of elastic strain in these values, the recovered transformation strain would be even smaller. As inelastic deformation starts in the NiTiHf alloy, detwinning of favorably oriented twins does not continue without increasing the externally applied stress. This could be attributed to the interaction of precipitates with the twin and variant boundaries [242]. The mobility of twin and variant boundaries is resisted by the dispersion of fine, coherent precipitates and their associated strain fields, requiring an increasing level of externally applied stress in the system to keep boundaries moving. While these precipitates may pin boundaries, they also act as very efficient obstacles to irreversible plastic deformation. This type of behavior was also observed in Ti-rich NiTiPd alloys containing Ti_2Ni type precipitates [217] and in NiTiPt alloys containing $Ti_{11}Ni_9Pt_4$ type precipitates [239], where the precipitate phase increased the critical stress for slip in both the low temperature and high temperature phases. Evidence for the effectiveness of the precipitate phase in the NiTiHf alloy to resist deformation processes of all kinds can be found in the microstructural observations.

The normalized diffraction intensities (Figure 7.5) remain mostly unaffected by increasing stress, which is a direct manifestation of limited variant reorientation and detwinning. Consequently, Figure 7.5 provides indirect microstructural evidence that the martensite variants are pinned by the surrounding precipitates and the associated internal stress fields, resulting in only a small evolution in texture.

For a more sensitive measure of texture, pole intensity changes, which indicate texture evolution, were tracked using IPFs (Figure 7.6) through appropriate refinement schemes. From the IPFs of diffracting planes parallel to the loading direction (Figure 7.6(a)), the intensity at the (110) and (012) orientations increase modestly with increasing applied stress at the expense of the (020) and (210) orientations. Likewise for diffracting planes perpendicular to the loading direction, the intensity at the (130) orientation increases while the intensity at the (110) orientation decreases. Thus, evidence of martensite reorientation or detwinning was apparent from the IPFs but was not very pronounced, especially compared to other alloy systems such as binary NiTi [43]. However, the fact that the texture is

changing a small amount provides direct experimental evidence of limited variant reorientation and detwinning, leading to the small inelastic strains observed during loading at room temperature.

Elastic strains along various crystallographic planes were assessed for two reasons: (i) to provide insight into the hkl elastic moduli and compare them with the macroscopic Young's modulus and (ii) to examine the strain anisotropy that arises from the symmetry (or lack of symmetry) of the monoclinic martensite and intergranular interactions. Elastic lattice strains reported here are the average strains measured in all variants homogeneously distributed throughout the diffracting volume with their planes oriented perpendicular (plane normals parallel) to the loading direction. Direction-dependent elastic moduli for directions normal to (011), ($\bar{1}11$), (021) and (030) lattice planes (Figure 7.7) were determined to be 93, 87, 84 and 64 ± 10 GPa, respectively. Moduli were obtained for stresses up to 100 MPa since nonlinearities were observed at higher stresses. The anisotropy in these moduli is relatively small (between 64 and 93 GPa) compared to the anisotropy in NiTi where moduli for the same four planes were found to vary from 82.3 to 174.5 GPa [42, 43]. Macroscopically, the elastic modulus was found to be 87 ± 10 GPa as determined by extensometry. In contrast to the NiTi alloy where the macroscopic elastic modulus is deflated due to early variant reorientation and detwinning at low stresses, the macroscopic measurement on this alloy can be considered the actual Young's modulus of this material, since variant reorientation and detwinning processes were very limited. Therefore, the measured B19' Young's modulus can be used for modeling purposes or design without considerable error.

7.4.3 Isobaric Response

The macroscopic strain-temperature response of the Ni-29.7Ti-20Hf alloy under a constant stress of 400 MPa, shown in Figure 7.8, provides information on the transient response, transformation temperatures, hysteresis, transformation strains, and unrecoverable (residual) strains. As the sample is heated for the first time at a constant load of 400 MPa, a relatively large (compared to binary NiTi [171]) strain transient develops. Apparently, the additional thermal energy introduced during the initial heating cycle causes further detwinning/reorientation of the martensite phase, which leads to additional inelastic strain in the material. Then once the austenite start temperature is reached, the original inelastic deformation plus the additional strain that developed during heating start to recover as the material transforms to austenite until all the strain is recovered at the austenite finish temperature. Another possible mechanism that could contribute slightly to this transient response is the change in the material's compliance during heating. This change in compliance was measured for several HTSMA alloys (Figure 20 of Ref. [132]) using a dynamic technique, where a drop in the Young's modulus was observed with increasing temperatures around the transformation range of each alloy.

During the initial cooling cycle, a relatively large strain (up to 4.1 percent) is generated and this level of strain is reproducibly obtained on the second and third cycles. The enhanced strain during cooling under load is due to the nucleation and growth of preferred martensite variants that favor the applied stress. Evidence for this preferred variant selection under the effect of the applied load was clearly captured by the measured IPFs (Figure 7.9). During the subsequent heating cycle all the strain generated during cooling is recovered. The remarkably reproducible strain that is generated each and every cycle (after the initial heating cycle) can be attributed to the presence of the precipitate phase and its effect on this dynamic system. First of all, the precipitate phase effectively resists slip in both the martensite and austenite phases so that plastic deformation, which is an irrecoverable process, does not occur at any point during the transformation process. Also, the strain fields associated with the precipitates act as multiple nucleation sites for martensite. During the forward transformation, martensite nucleates from homogeneously distributed sources throughout the material, essentially in a single burst driven by the strain fields around all the precipitates. Therefore, the transformation is completed over a much narrower temperature range than would be required if only a few fronts were nucleated and had to propagate through a larger volume of material, storing additional elastic strain energy. The disadvantage to nucleation of martensite in this manner is that transformation strains will tend to be smaller than in precipitate-free material because of fewer variant interactions. However in practice, the advantage of

enhanced strain expected of single-phase material is usually offset by the early onset of plastic deformation and a lack of dimensional stability.

The transformation temperatures at this selected load were also assessed. At 400 MPa the martensite start, martensite finish, austenite start, and austenite finish temperatures were determined to be 163, 131, 158 and 178 ± 2 °C, respectively. These temperatures were found to be different from what is reported in Ref. [238] where the corresponding transformation temperatures were determined to be 179, 159, 183 and 200 °C, respectively. This approximately 22 °C difference in transformation temperatures is likely due to the manner in which temperature was measured. In Ref. [238], temperature was measured using a thermocouple spot welded directly to the specimen gauge section, while in this study, temperature was measured using a thermocouple tied to the specimen, which would tend to underestimate the actual temperature of the material. Heat-to-heat compositional variation could also play a role in the observed discrepancy.

Hysteresis is another important parameter, particularly for active control and high frequency response applications. Large hysteresis on the order of 40 to 80 °C were observed in Ti-rich or near stoichiometric NiTiHf alloys containing 15 to 20 percent Hf [243-245]. In this work, a relatively small hysteresis in the order of 20 to 25 °C was obtained, which is comparable to that reported previously [238]. The decreased hysteresis is attributed to the effect of the precipitates to nucleate the transformation from sources homogeneously distributed throughout the material resulting in reduced overall movement of transformation fronts rather than having to pass a few transformation fronts through larger volumes in the material. The consequence of this reduced movement of the fronts and/or interfaces is reduced frictional resistance, energy dissipation and hysteresis.

Transformation strains during 400 MPa load-biased thermal cycling were determined to be 3.5 percent and are repeatable from cycle to cycle through the third cycle shown in Figure 7.8. This strain is associated with the orientation of selected martensite variants. Preferred variant selection under load, indicated by the high intensity at the (020) orientation in Figure 7.9(b), is identically promoted in each cycle by the applied load and magnified by the stress concentration due to the presence of the precipitates that in turn act as homogeneous sources for the nucleation of martensite throughout the material. This is in contrast to inhomogeneous nucleation of martensite and the subsequent growth of a few phase fronts, as occurs in single phase alloys. As a result, cycling under load leads to a near identical transformation strain of 3.5 percent for each cycle. This transformation strain value was used to calculate the work output of the SMA, an important property in actuator applications, which was determined to be 14 J cm^{-3} . It was shown in Ref. [238] that the work output in this alloy is at least 18.7 J cm^{-3} at a stress level of 500 MPa. Hence this precipitation strengthened alloy is a promising replacement for conventional actuation systems.

Stability was also examined by measuring the amount of irrecoverable strain that developed during thermal cycling by looking at the difference in strain at room temperature after each thermal cycle. At the end of the second cycle, the unrecoverable strain was about 10^{-3} percent and was negligibly changed in the subsequent third cycle. This is an indication of nearly perfect dimensional stability without any prior training of the material. This improved stability is promoted by the existence of the precipitates, which has at least two major effects on the overall microstructure. The first is providing resistance to permanent deformation mechanisms such as slip, as was discussed in preceding sections. For instance, the applied 400 MPa stress is below the stress at which slip would be activated over twinning. The second effect is the prevention of retained martensite above the austenite finish temperature, which was shown to be responsible for a major component of total accumulated strain after cycling of a NiTiPd HTSMA [246]. This latter effect is demonstrated in Figure 7.10, which shows that there is no texture evolution in the austenite phase and no martensite peaks appear in the spectra recorded at 300 °C during thermal cycling.

This unchanging austenitic texture is also an indication that no new or additional deformation mechanisms ensue from thermal cycling under a 400 MPa bias stress. The initial shift in position in all three peaks is due to the elastic lattice strains found to be -0.19 percent as a result of the 400 MPa stress. For the subsequent cycles, no additional shift is observed in the recorded reflections. These equivalent

lattice strains for the subsequent cycles are consistent with the lack of macroscopic residual strain development during load-biased thermal cycling, Figure 7.8. Moreover, all diffraction patterns are shown to exhibit the same breadth. Hence the transformation to the parent austenite phase is identically recovered after each cycle with no change in texture, no retained martensite, and no evidence of any plastic or other inelastic deformation mechanisms, consistent with the thermomechanical test results and the lack of any residual strain after load-biased thermal cycling.

From the no-load thermal cycles performed after the load-biased tests, the measured texture was found to be nearly identical to the initial starting texture. This ability to revert back to the initial self-accommodated state after only one no-load thermal cycle demonstrates essentially history independent behavior for this alloy, which is quite rare in any SMA system. This complete reversion to its original self-accommodated state after thermomechanical testing is also demonstrated by reloading the sample at room temperature, where its tensile behavior after all these thermomechanical cycles is identical to its original state (Figure 7.4(b)). Since the material easily reverts back to a self-accommodated texture when the load is released, it can be optimized or trained under new conditions without being affected by loading path history. For other alloys with no precipitates, for example 55NiTi or NiTiPd alloys, training using this same isobaric cycling method, will require a large number of cycles as the material tends to evolve or de-evolve to its saturated state [8, 63]. The current NiTiHf SMA only requires a few thermal cycles under a particular (stress-temperature) condition for it to be fully trained. Therefore, training to optimum behavior is actually much easier without costly and time consuming training procedures.

7.5 Conclusions

The study of uniaxial tension experiments, both in isothermal and isobaric testing modes, were presented for a Ni-rich NiTiHf alloy. The stability of this high-temperature shape memory alloy was investigated macroscopically through extensometry measurements and concurrently at the microscopic level with in situ neutron diffraction at stress and temperature. The stability of the alloy in terms of the observed strain characteristics were elucidated by examining the crystal structure, micromechanics, and microstructure evolution resulting in the following conclusions:

- a. Neutron and electron diffraction confirmed the formation of fine, nanometer size, coherent precipitates through careful stoichiometry control and aging. This precipitate phase is believed to be the stabilizing factor in this NiTiHf alloy.
- b. During isothermal deformation, restricted detwinning and low isothermal strains were consistent with limited martensite texture changes, as observed in diffraction spectra and IPFs. Limited detwinning was attributed to the pinning of twin and variant boundaries by the dispersion of fine precipitates.
- c. Average monoclinic lattice elastic strain limits were found to be of the order of 0.1 percent strain and the corresponding plane specific elastic moduli for directions normal to (011), ($\bar{1}11$), (021) and (030) lattice planes were 93, 87, 84 and 64 ± 10 GPa, respectively, and exhibited relatively small anisotropy compared to binary NiTi.
- d. The observed transient strain response during the first load-biased thermal cycle was relatively large compared to binary NiTi. This behavior is believed to result from (i) additional detwinning and reorientation as the mobility of twin/variant boundaries increases with temperature and (ii) changes in the material's compliance with the additional thermal energy.
- e. Relatively narrow hysteresis, on the order of 20 to 25 °C, bodes well for use of this alloy in active and precise control applications. This reduced hysteresis, when compared to other shape memory alloys, is a result of the role of the precipitates to nucleate the transformation homogeneously throughout the material over a very narrow temperature window.
- f. Repeatable high transformation strains (3.5 percent at 400 MPa, 14 J cm⁻³ work output) and insignificant unrecoverable strains ($<10^{-3}$ percent) during isobaric thermal cycling make this alloy a good candidate for actuator applications at high temperatures (above 100 °C).

- g. Excellent shape memory behavior with nearly 100 percent shape recovery in the initial cycles eliminates the need for costly and time consuming training.
- h. Ability of this alloy to revert readily to the initial self-accommodating structure after only one no-load thermal cycle indicates history independent behavior and further explains the excellent stability in this Ni-rich NiTiHf HTSMA.

Chapter 8.—Design of a Multiaxial Loading Capability on an Engineering Neutron Diffractometer

A novel capability was designed for in situ neutron diffraction measurements during multiaxial loading on the VULCAN engineering materials diffractometer at the spallation neutron source at Oak Ridge National Laboratory. This capability would allow for the acquisition of neutron spectra during tension, compression and/or torsional loading at elevated temperatures, while simultaneously permitting the measurement of texture, internal strain, and phase fraction evolution. The design and analysis stages of this axial/torsional gripping system are described in this chapter.

8.1 Introduction

Neutron diffraction technique offers unique capabilities to study the microstructure of bulk materials in a non-destructive approach. This technique is ideally suited to measure the micromechanical response (internal stresses, strains), microstructural evolutions (texture, defects) and transformation properties (phases, chemistry) of most engineering materials under stress, temperature or other severe environments. Due to the high penetration of neutrons compared to conventional x-rays, such measurements can be done at depth on the bulk materials, or essentially on engineering components and large structures [11, 12].

Neutron diffraction has been successfully applied to the investigation of shape memory alloys for many years (e.g., [43, 247]). Deformation and transformation behaviors have been revealed in a suite of alloys under many different testing conditions. However, when these measurements were performed in situ under load, most if not all of the diffraction experiments were done under a uniaxial tensile or compressive load. In situ neutron diffraction in a multiaxial loading configuration has not been done due to the limited loading capabilities of most engineering diffractometers.

Recently, a new engineering diffractometer, named VULCAN, was built at the Spallation Neutron Source (SNS), Oak Ridge National Laboratory [248, 249]. This new instrument is equipped with a unique multiaxial tension-torsion load frame for in situ neutron diffraction measurements. Although ex situ multiaxial experiments have been conducted in the past, a challenge is encountered when trying to do these experiments while simultaneously accounting for the neutron beam path, instrumentation, and acquisition time. Performing such in situ experiments efficiently and accurately requires special gripping capabilities. The objective of this chapter is to report on the design and analysis of an axial/torsional gripping system for implementation on the VULCAN diffractometer. The immediate motivation for developing this capability was to initiate the investigation of shape memory alloys under complex loading paths. One of the more promising aspects of these materials is the ability to use them in rotary actuation processes (torque) for applications in aerospace (e.g., flaps and variable geometry inlets and nozzles). This capability will help determine both functional and mechanical behaviors of SMAs during multiaxial deformation in order to explore their full potentials other than just uniaxial functions. This design would allow for the acquisition of neutron spectra during tension, compression and/or torsional loading at elevated temperatures, while simultaneously allowing the measurement of texture, internal strain, and phase fraction evolution. These measurements are particularly relevant given that the constitutive behavior of SMAs is still not completely known, especially under multiaxial conditions. Furthermore, fundamental deformation mechanisms in these alloys (detwinning, stress-induced and temperature-induced transformation) have still not been probed under multiaxial conditions. A second motivation is the need for more comprehensive and accurate SMA models. Calibration, verification and validation of existing models to predict polycrystalline NiTi responses have been limited due to a lack of experimental data that ties together crystallographic evolution with macroscopic responses (stress-strain-temperature). Implementation of this gripping system is critical in developing a more complete understanding of SMA deformation and will enable the development of new high temperature shape memory alloys. This capability is not only limited to the investigation of SMAs, but it will be made available for future investigations of other engineering materials.

8.2 Engineering Materials Diffractometer—VULCAN

The neutron diffractometer VULCAN at SNS, the world's most intense pulsed accelerator-based neutron source, is designed to tackle a broad range of challenges in materials science and engineering under a variety of conditions [248, 249]. VULCAN has an extensive array of sample environments and equipment including a unique axial-torsional load frame, a high temperature vacuum furnace, a portable friction stir-welding machine, and other auxiliary equipment. Currently, VULCAN has two position-sensitive detectors positioned on either side of the incident beam at $\pm 90^\circ$ at a distance of 2 m from the sample. The incident neutron beam impinges on the sample with the loading axis positioned at 45° relative to the beam, with diffraction data collected simultaneously by the two detectors. Due to high intensities (high neutron count rates), VULCAN provides rapid volumetric mapping with a measurement time of minutes for most materials. This added benefit allows for in situ and time-resolved measurements of the phase transformation kinetics and dynamic mechanical deformation responses of materials.

8.3 Design Requirements

The gripping system, designed in this work, will expand VULCAN's capabilities to perform in situ neutron diffraction measurements at multiaxial stress and elevated temperatures with the following requirements:

- (i) Samples to be tested, particularly SMAs, had to be properly gripped from both ends to allow for proportional and non-proportional axial and torsional loading paths. Simple clamping (e.g., wedge grips) was not suitable due to the transformation characteristics of SMAs.
- (ii) The grip design needed to sustain high stresses (limit of the 250 kN load cell) at high temperatures (e.g., $\sim 600^\circ\text{C}$) without any damage or yielding. Material selection and heat treatments to the required hardness had to be selected accordingly.
- (iii) The incident, diffracted and transmitted neutron beams were not to be obstructed by any of the gripping components. A free beam path was to be maintained at all time during the in situ measurements. Altering the beam path would result in flawed measurements (e.g., additional peaks, misrepresented intensities and peak shapes).
- (iv) Cooling from high temperatures to room temperature had to be fast enough or ultimately controlled for efficient usage of neutron beam time (since neutron acquisition is achieved in a matter of minutes on VULCAN).
- (v) The sample had to be mounted and removed from the grips in a reasonably quick and simple manner for any general user. Additionally, mounting or removing the sample had to be done without introducing any unwanted loads (e.g., bending or twisting).

8.4 Grip Components

The complete grip assembly with a mounted sample is shown in Figure 8.1 with a cut-out at one end to show the internal details. The gripping system is composed of six components made of INCONEL 718 alloy (properties shown in Table 8.1) to withstand the required mechanical and thermal loads. The platen shown in Figure 8.2 was designed with the proper threads at one end (M68 \times 2 mm left hand thread) to fit with the existing VULCAN load frame. Internal cooling passages (~ 5 mm deep into the platen) were designed for rapid cooling by circulating chilled water during thermomechanical cycling experiments. The other end of the platen was tapered to allow for a free neutron beam path during in situ measurements. The collar of Figure 8.3 was designed to fit over the platen with two holes for fluid inlet and outlet in line with the cooling channels. This collar is intended to be welded over the platen using INCONEL 625 filler material that will fill the inner and outer 45° chamfers. The sample holder shown in Figure 8.4 will allow for rapid sample mounting/dismounting through the cylindrical and hexagonal surfaces designed to fit within close tolerances with the platen and the other components. The sample will

be threaded for axial loading constraint, and the hexagonal cuts will be used in conjunction with the jam nuts shown in Figure 8.5 for rotational constraints (to allow for torsional loading). The last component, torque nut, was designed to lock the sample holder in place as a last step before starting the experiment. After initial machining, each component will be subjected to an ageing treatment at 850 °C for 24 hr, air cooled, followed by a final ageing at 760 °C for 16 hr and air cooled to achieve the desired hardness.

The sample geometry was also redesigned as shown in Figure 8.6 with the proper length and aspect ratio to allow for tension, compression and/or torsion loading with enough spacing for the incident and diffracted beams to enter and exit without interruption. The final completed assembly including part of the VULCAN load train is shown in Figure 8.7.

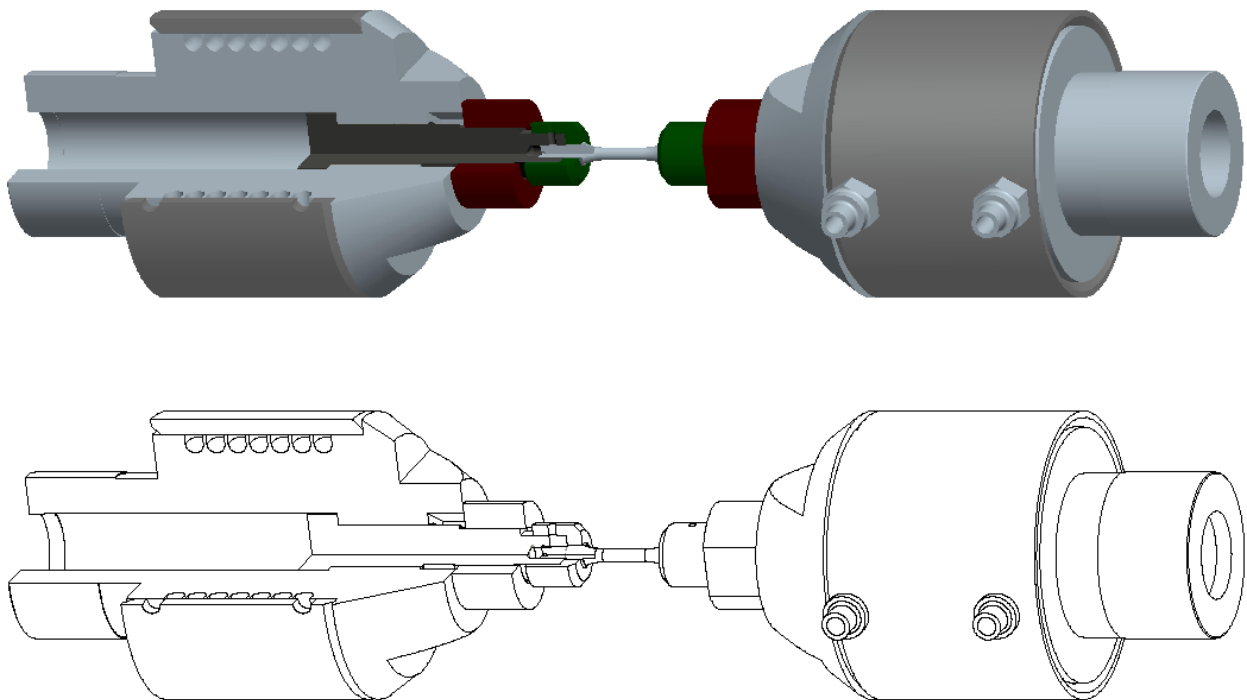


Figure 8.1.—The complete gripping system design for VULCAN diffractometer.

TABLE 8.1.—PROPERTIES OF INCONEL 718 USED IN THE ANALYSES

INCONEL 718 Properties		
Property	Symbol	Value
Young's modulus	E	200 GPa
Shear modulus	G	80 GPa
Poisson's ratio	ν	0.29
Yield strength	σ_y	1034 MPa
Mass density	ρ	8190 kg/m ³
Thermal conductivity	k	11.4 W/m°C
Specific heat capacity	c_p	435 J/kg °C
Coefficient of thermal expansion	α	13×10 ⁻⁶ /°C
Melting point	T_M	1260 to 1336°C

<http://asm.matweb.com>

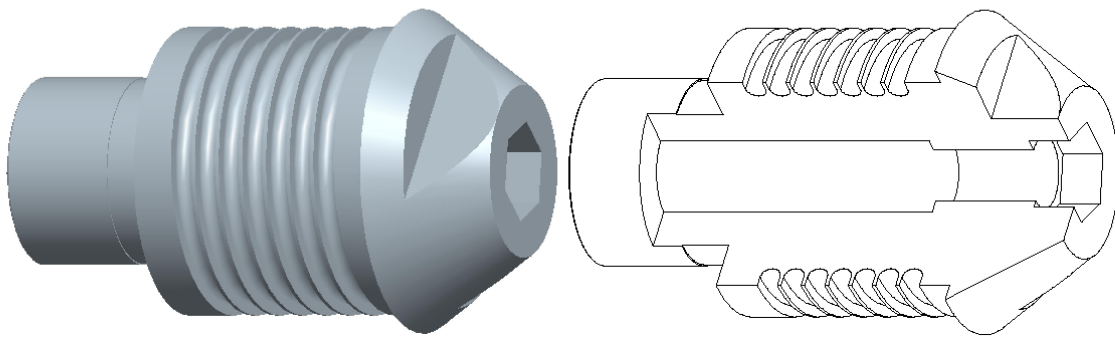


Figure 8.2.—Component 1—Platen.

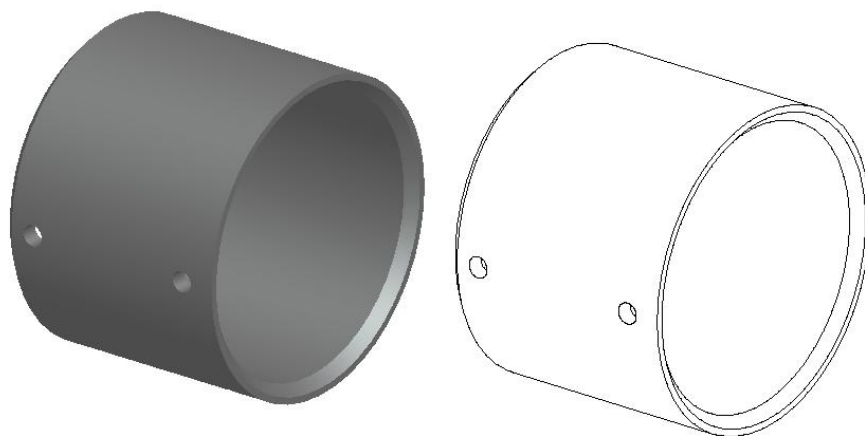


Figure 8.3.—Component 2—Platen collar.

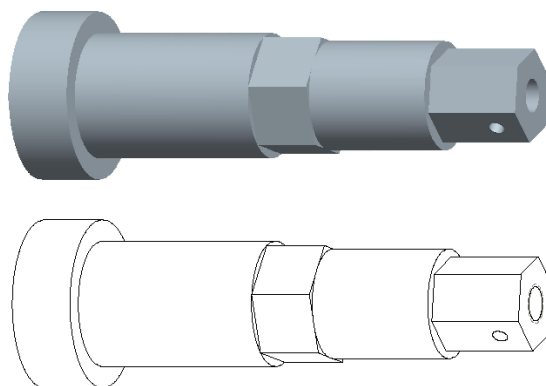


Figure 8.4.—Component 3—Sample holder.

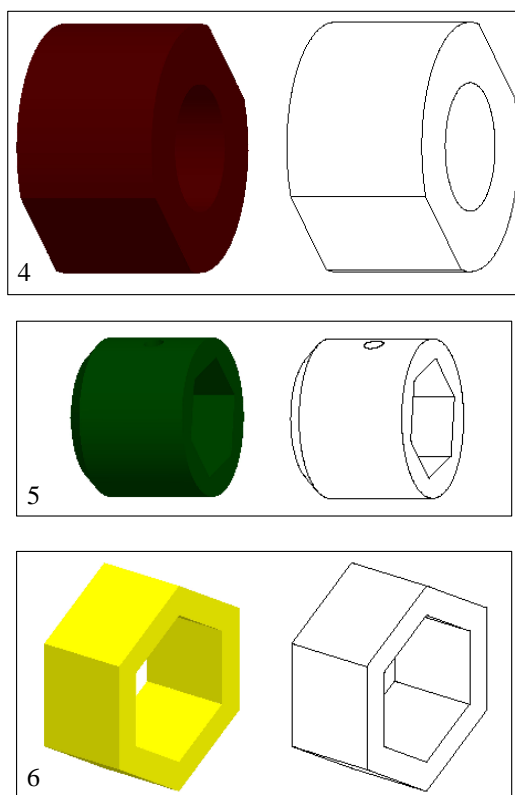


Figure 8.5.—Component 4-6—Jam nut, hex jam nut torque nut.

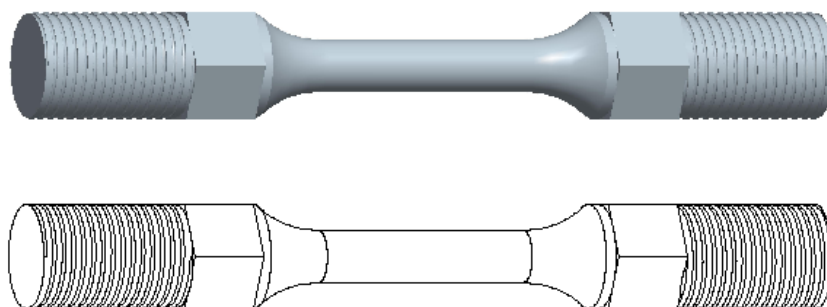


Figure 8.6.—Modified sample geometry for axial- torsional loading.

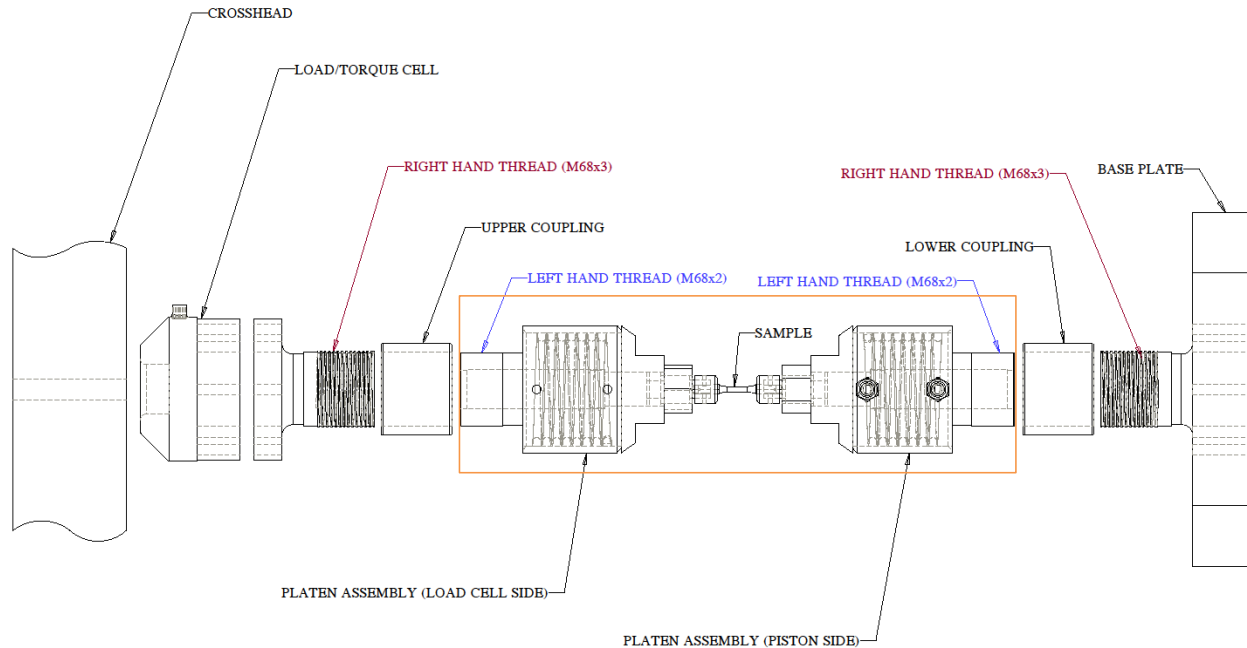


Figure 8.7.—The complete gripping system including part of the VULCAN load train.

8.5 Heat Transfer and Torsional Analyses

The presented analyses were intended to obtain a first order approximation of the grip performance during the design phase. Parameters such as dimensions and environments were iterated based on these simplified analyses to meet the desired requirements. A complete 3D-model with more detailed structural and thermal analyses is underway

8.5.1 Heat Transfer Analysis

The sample under test will be heated using an induction heater with two coils centered on the gauge section. Cooling will be simultaneously supplied to the grips to protect the load train from overheating and to provide rapid cooling when needed. The goal of this analysis was twofold: to (i) estimate the conduction heat transfer from the grips to the sample in order to determine the cooling efficacy and the temperature gradients along the grip extension; and (ii) to determine the cooling time once the induction heater is turned off. The heat transfer problem was simplified to one dimensional, steady state conduction with the boundary conditions shown in Figure 8.8. The temperature distribution at the critical points was obtained using the thermal resistance model in series where the heat transfer rate was obtained by the expression:

$$q_x = \frac{T_{\infty,0} - T_{\infty,4}}{\sum R_t} = \frac{T_{\infty,0} - T_{\infty,4}}{\left[\left(\frac{1}{h_0 A_1} \right) + \left(\frac{L_1}{k_m A_1} \right) + \left(\frac{L_2}{k_m A_2} \right) + \left(\frac{L_3}{k_m A_3} \right) + \left(\frac{1}{h_4 A_3} \right) \right]} \quad (8.1)$$

where h is the heat transfer coefficient, k is the thermal conductivity, L is the platen length, A is the cross section area and $(T_{\infty,0} - T_{\infty,4})$ is the temperature difference as indicated in Figure 8.8. Using the parameters and properties reported in Table 8.1, Table 8.2, and Table 8.3, the temperature distribution along the platen with the cooling turned off is shown in Figure 8.9 for three different heat transfer coefficients at the induction side (sample side) taken from literature [250, 251]. The temperature at the piston side was

considerably high (80 to 100 °C lower than the induction side) which would overheat the system. The other important outcome of this analysis is the temperature gradient along the sample. SMAs undergo a phase transformation with changing temperatures, and any gradient will affect the thermomechanical response. The cooling passages of Figure 8.2 were designed to address both problems, i.e., overheating and temperature gradients. When cooling is supplied to the grips, the temperature at the end of the grip (piston side) remains relatively cold, significantly reducing the overheating potential. Moreover, the cooling passages were modified to span for only 7.6 mm (3 in) along the platen to reduce the gradients on the sample.

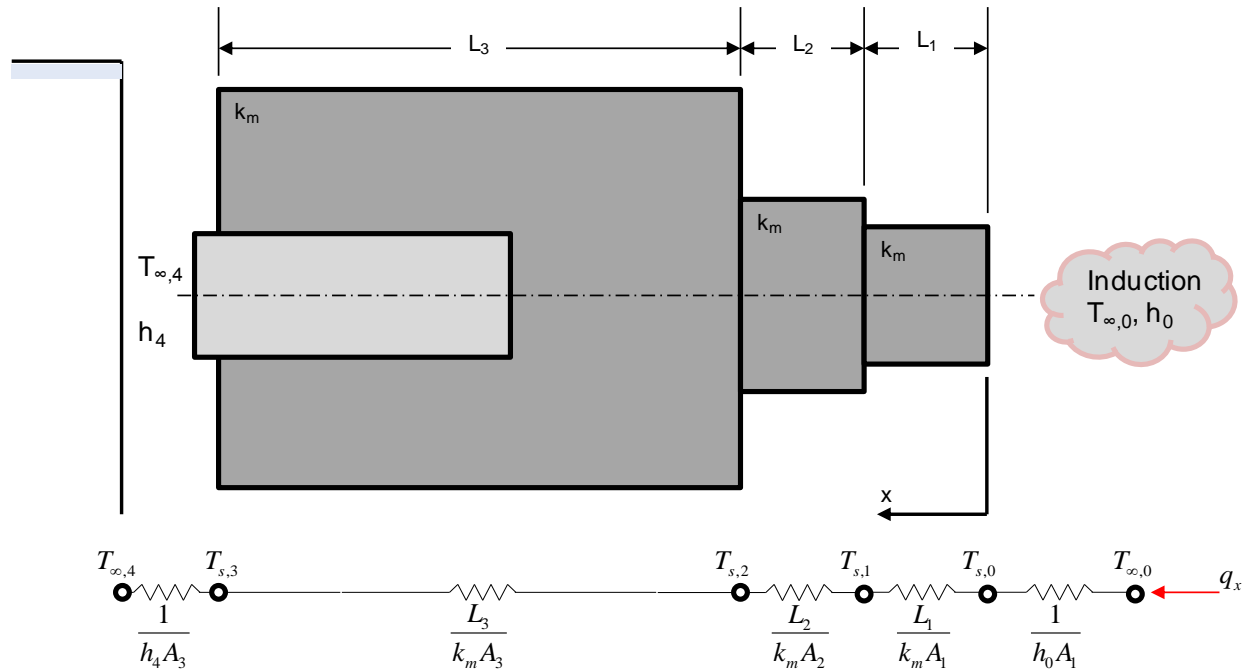


Figure 8.8.—Equivalent series thermal resistance model for the simplified platen assembly.

TABLE 8.2.—PROPERTIES OF BINARY NiTi USED IN THE ANALYSES

NiTi Properties at room temperature		
Property	Symbol	Value
Young's modulus	E_{SMA}	40 GPa
Shear modulus	G_{SMA}	20 GPa
Poisson's ratio	ν_{SMA}	0.33
Yield strength	σ_{y-SMA}	140 MPa
Mass density	ρ_{SMA}	6450 kg/m ³
Thermal conductivity	k_{SMA}	8.6 W/m °C
Specific heat capacity	c_{p-SMA}	837 J/kg °C
Coefficient of thermal expansion	α_{SMA}	$6.6 \times 10^{-6}/^{\circ}\text{C}$
Melting point	T_{M-SMA}	1300 °C

<http://jmmedical.com>

TABLE 8.3.—GEOMETRIC PARAMETERS AND
FLUID PROPERTIES USED IN THE ANALYSES

Cooling channels parameters		
Parameter	Symbol	Value
Cross section area	A_c	0.52 cm^2
Surface area	A_s	346 cm^2
Coil turns	N_c	7
Coil span	L_c	7.6 cm

Grip parameters		
Parameter	Symbol	Value
Platen diameter	D_p	8.9 cm
Wall thickness	x	0.635 cm
Jam nut	L_1/A_1	$2.54/7.94 \text{ cm/cm}^2$
Jam nut 2	L_2/A_2	$2.54/14.65 \text{ cm/cm}^2$
Platen	L_3/A_3	$11.43/81.03 \text{ cm/cm}^2$

Fluid properties (water at 30 °C)		
Parameter	Symbol	Value
Water temperature	$T_{w,c}$	30 °C
Specific heat	$c_{p,w}$	4.18 kJ/kg-°C
Viscosity	μ^f	$959 \times 10^{-6} \text{ N-s/m}^2$
Thermal conductivity	k_w	606 W/m-°C
Prandtl number	Pr	6.62

Fluid properties (air)		
Parameter	Symbol	Value
Air temperature (induction side)	$T_{\infty,0}$	300 °C
Air temperature (piston side)	$T_{\infty,0}$	300 °C
Heat transfer coefficient	h_0	1 to 10 W/m ² -K
Heat transfer coefficient	h_4	100 to 300 W/m ² -K

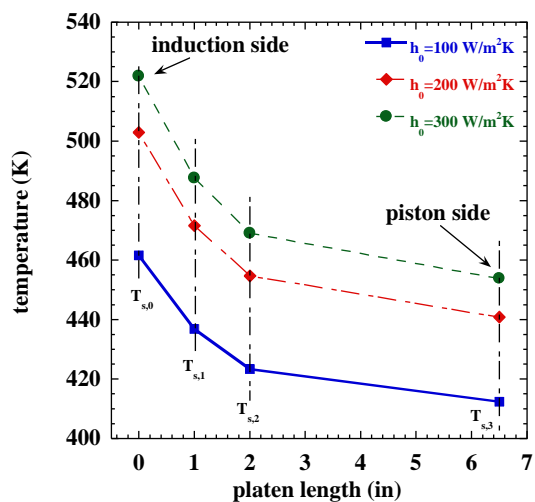


Figure 8.9.—Temperature distribution along the
INCONEL platen plotted for three different heat
transfer coefficients with cooling off.

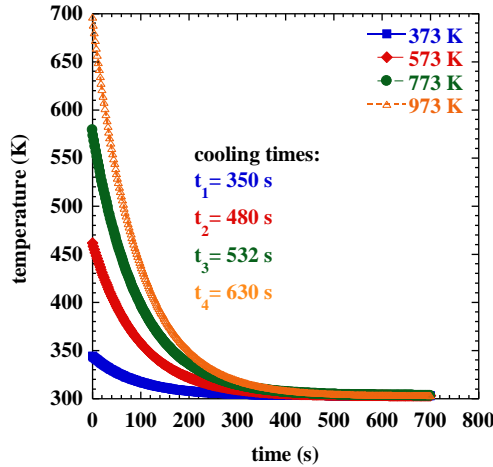


Figure 8.10.—Cooling times from four representative initial temperatures with cooling on.

Once the induction heater stops, $T_{\infty,0}$ decreases exponentially until equilibrium is reached with the surrounding air $T_{\infty,\text{far}}=30^\circ\text{C}$. The heat removed by the cold water circulating in the cooling channels can be calculated using

$$Q_w = m_w c_{p,w} (T_{w,\text{out}} - T_{w,\text{in}}) \quad (8.2)$$

where m_w is the mass flow rate of water, $c_{p,w}$ is the specific heat at constant pressure, $T_{w,\text{in}}$ and $T_{w,\text{out}}$ are the water inlet and outlet temperatures, respectively. Applying conservation of energy and ignoring radiation effects, the cooling time was estimated using

$$\frac{T(t) - T_{\infty}}{T_i - T_{\infty}} = \exp \left[- \left(\frac{h_w A}{\rho V c_{p,m}} \right) t \right] \quad (8.3)$$

where ρ is the mass density, V is the volume and t is time required to cool the grip and sample to room temperature. This study was done assuming the sample was initially heated to 100, 300, 500 and 700 °C (possible testing temperatures). Moreover, the water temperature flowing in the cooling passages was set to 30 °C. The achieved cooling times (Figure 8.10) were not fast enough and further modification was needed. The cooling channels depth was increased to 8 mm to increase the surface area, and the water temperature will need to be decreased (using a water chiller) in order to meet the design requirements.

8.1.1 Torsional Analysis

This torsional analysis was carried out to estimate the grip compliance when testing. The maximum shear stress in the sample and the corresponding angle of twist transmitted from the holder (Figure 8.4) was calculated using a simplified model shown in Figure 8.11. The maximum shear stress and angle of twist were determined for a typical NiTi material (Table 8.1 to Table 8.3), and INCONEL 718 sample holder using

$$\tau_{\text{max}} = \frac{Tc}{J}, \quad J = \frac{1}{2} \pi c^4 \quad (8.4)$$

$$\phi = \frac{TL}{JG} \quad (8.5)$$

where T is the applied torque, c is the radius of the sample section, J is the polar moment of inertia, L is the section length and G is the shear modulus [252]. The result (Figure 8.12) based on the current design indicated that the torque exhibited by the grip assembly is very small (within the elastic limit), and the torque is transmitted efficiently to the sample gauge section.

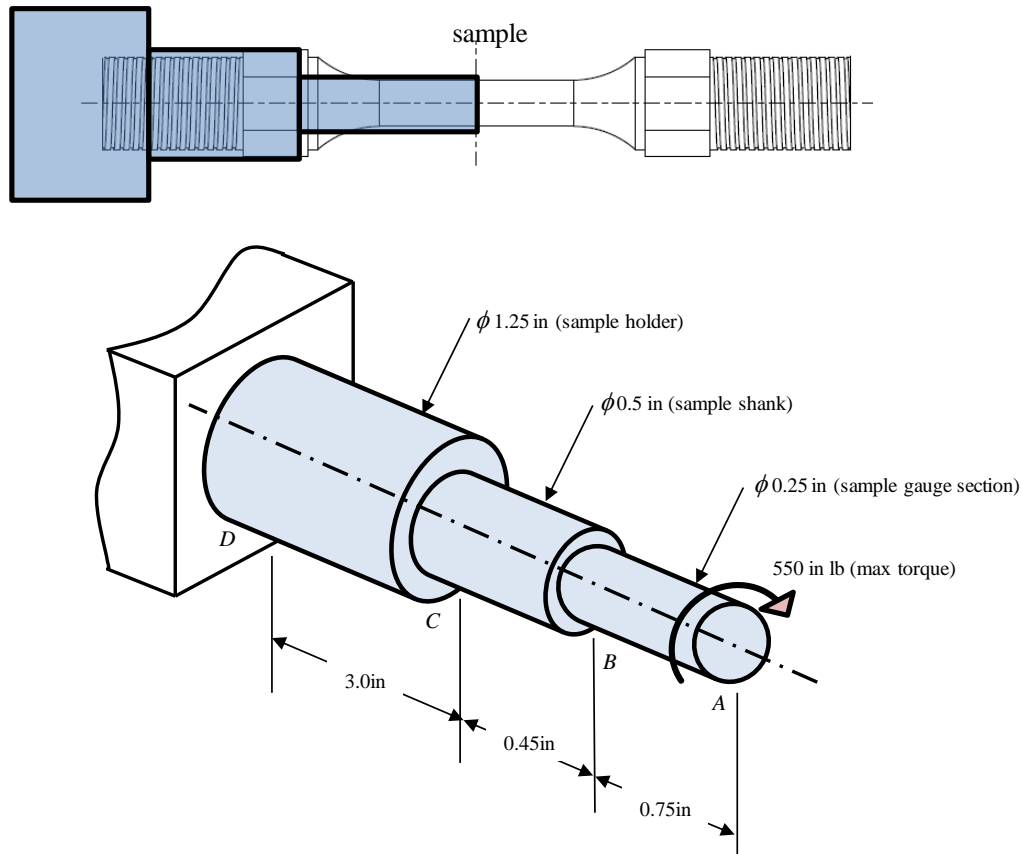


Figure 8.11.—Simplified sample and sample holder geometry for torsional analysis.

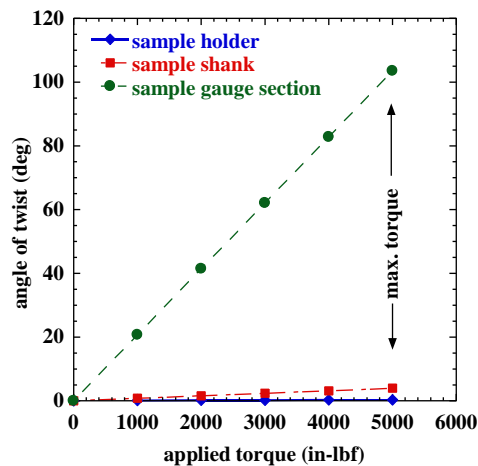


Figure 8.12.—Shear stress and angle of twist results (note the low stress on the sample holder).

8.6 Preliminary VULCAN Diffraction Spectra

The neutron diffractometer VULCAN was used to study the microstructural evolution and deformation mechanisms during thermomechanical cycling of NiTi shape memory alloy in uniaxial testing mode. VULCAN offered the possibility of performing measurements in a continuous scanning mode which provided valuable information in establishing correlations between microstructure, macroscopic transformation strain and irrecoverable strain evolution. In Chapter 5, the microstructural evolution during thermomechanical cycling experiments was not continuously captured due to flux limitations on SMARTS and critical data between 1 and 10 cycles was not acquired. The high flux of the VULCAN diffractometer to obtain continuous scans helped to capture this evolution that provided insight into the observed macroscopic behavior and the possible mechanisms behind irrecoverable strain. Thus the objective was to examine the phase fraction, texture and strain evolution during thermomechanical cycling of shape memory alloys (building on knowledge gained from Chapter 5) to elucidate the mechanisms that lead to irrecoverable strain.

Experiments were performed in situ on NiTi shape memory alloys under isobaric conditions of constant 100 MPa. They consisted of loading the sample to 100 MPa, followed by thermally cycling 10 times under stress between room temperature and 230 °C with neutron spectra collected continuously and at discrete points. Heating and cooling rates were controlled at 2 °C/min in order to obtain adequate statistical quality during the continuous neutron scanning. In this section, only some examples of VULCAN diffraction spectra are presented and not the complete analyses. Additional details of the experimental setup along with all the analyses will be published soon.

The macroscopic strain-temperature response from extensometry is shown in Figure 8.13 for the first cycle under 100 MPa (transient response), and for the heating portion of the second cycle. The solid symbols indicate the temperatures at which the neutron diffraction spectra were obtained while holding at temperature for 10 min. In addition to the indicated discrete points, neutron data was also acquired continuously during heating and cooling. The corresponding normalized diffraction spectra are shown in Figure 8.14 and Figure 8.15. These spectra show the microstructural evolution as the material, initially martensitic at room temperature, transforms to austenite during heating and back to martensite during

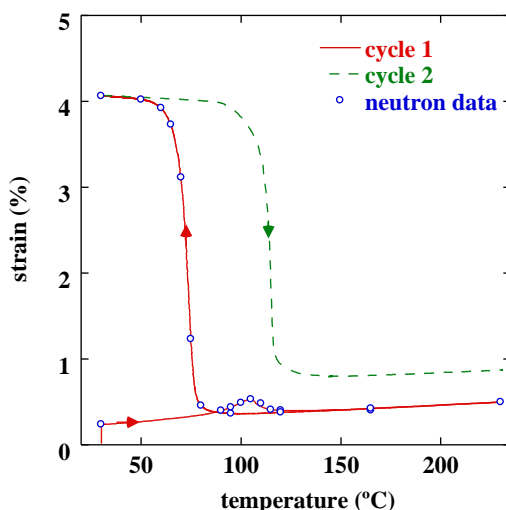


Figure 8.13.—Strain-temperature response for the first and second thermal cycles at a stress of 100 MPa. The circles indicate where the neutron diffraction spectra were acquired for 10 min at VULCAN diffractometer.

cooling. The peak identifications are labeled for austenite and martensite by the subscripts “A” and “M”, respectively. The data shown here provides direct and accurate measurements of the phase transition temperatures. This current measurements along with complete texture, lattice and peak shape evolution is an example of how VULCAN can be used to understand the underlying deformation mechanisms that govern the material response. The proposed gripping system will help conduct similar experiments under multiaxial loading configuration.

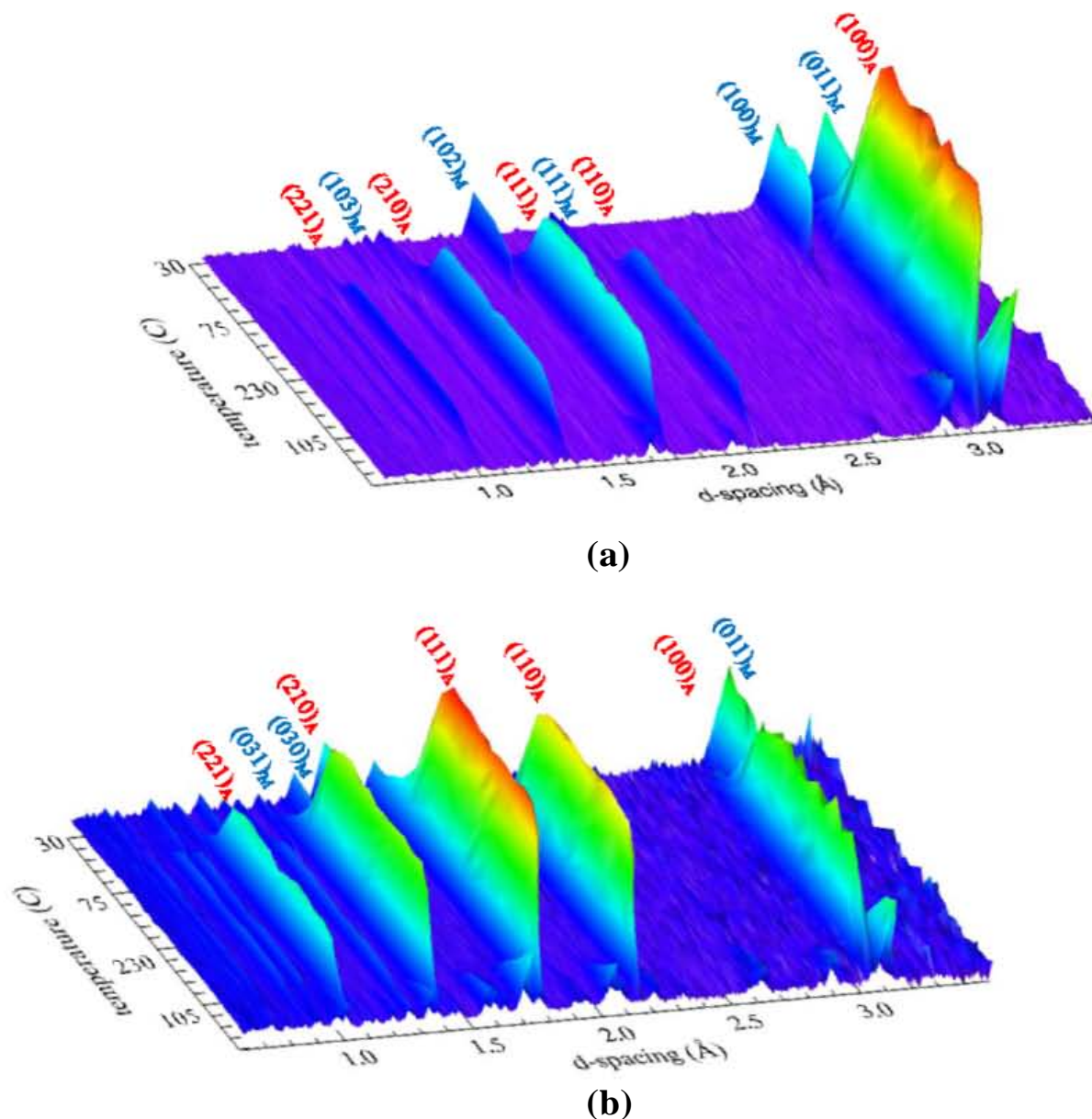


Figure 8.14.—VULCAN normalized neutron diffraction spectra acquired during first cycle (transient cycle) continuous heating and cooling between room temperature and 230 °C at a constant stress of 100 MPa. The reflections are from lattice planes (a) parallel and (b) perpendicular to the loading axis.

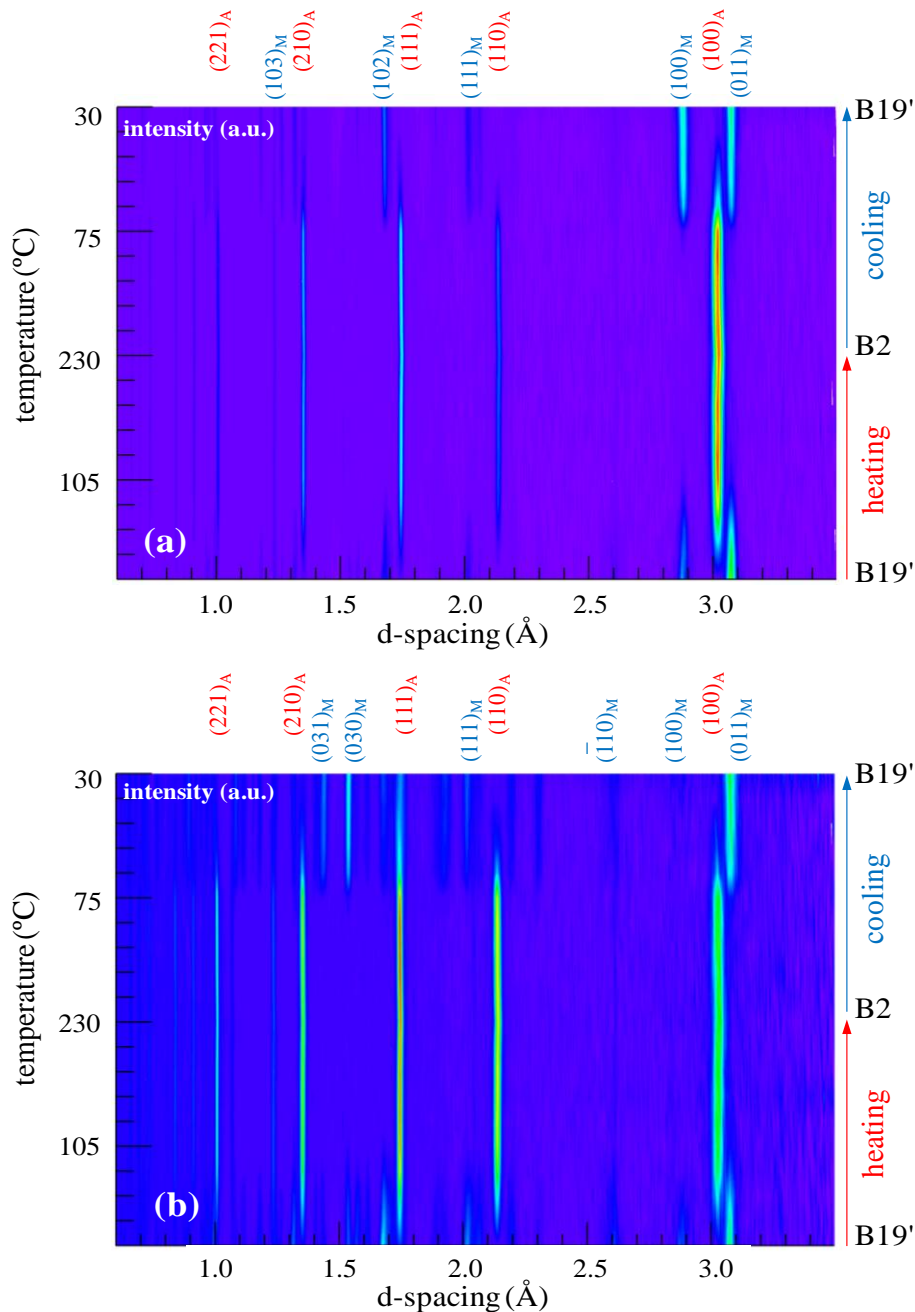


Figure 8.15.—VULCAN projected neutron diffraction spectra acquired during first cycle (transient cycle) continuous heating and cooling between room temperature and 230 °C at a constant stress of 100 MPa. The reflections are from lattice planes (a) parallel and (b) perpendicular to the loading axis.

8.7 Concluding Remarks

The gripping capability designed in this work will be installed and tested on the VULCAN diffractometer this year. The design has been finalized and machining of the components is partially completed. Performance parameters such as mechanical integrity, cooling rates, and beam clearance) will be evaluated once the grips are installed. Detailed engineering drawings are included in Appendix A.

Chapter 9.—Conclusions

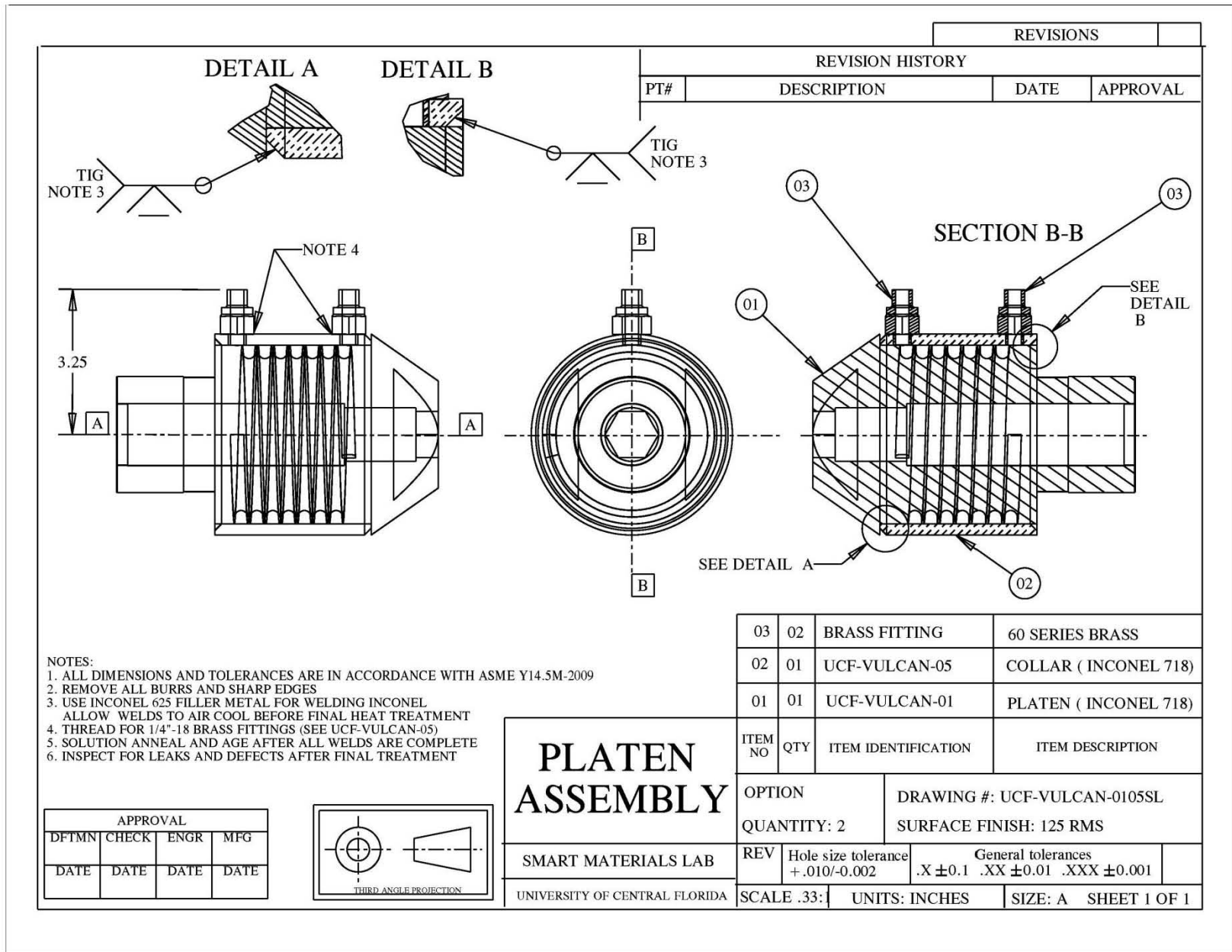
Due to the stand-alone nature of each chapter in this dissertation, appropriate conclusions have already been included at the end of each chapter. This final chapter provides a summary of the unique contributions of this dissertation.

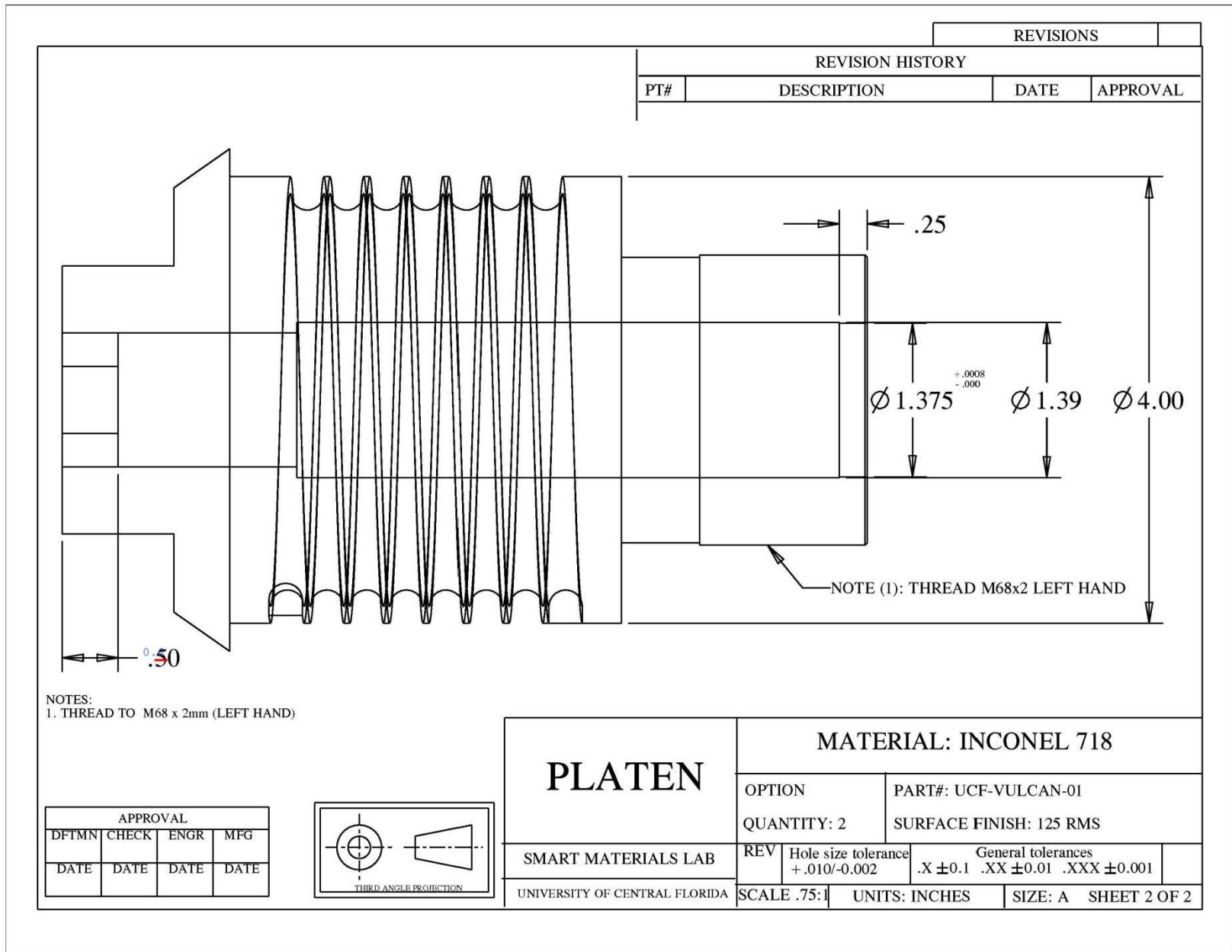
1. Temperature dependent deformation behavior of polycrystalline $\text{Ni}_{49.9}\text{Ti}_{50.1}$ (at.%) in the B2 austenite phase was examined over the temperature range of 165 to 440 °C by mechanical testing, in situ neutron diffraction, hot-stage transmission electron microscopy (TEM), and elastoplastic deformation modeling. The macroscopic inelastic strains were attributed to the formation of stress-induced martensite up to the M_d temperature of 310 °C, which was previously unidentified. Concurrently, below and above the M_d , the deformation was governed by the occurrence of $\{114\}_{\text{B2}}$ compound deformation twins, confirmed by TEM, along with $\langle 001 \rangle$ slip processes and possible recovery processes at higher temperatures. A better understanding of the range of dominance of each of the contributing deformation mechanisms over this temperature range was established which aided in generating a B2 austenite deformation map in $\text{Ni}_{49.9}\text{Ti}_{50.1}$ alloy (Chapter 3).
2. Room temperature deformation behavior of polycrystalline $\text{Ni}_{49.9}\text{Ti}_{50.1}$ in the B19' martensite phase was investigated by combining ex situ thermomechanical experiments and in situ neutron diffraction measurements. Strain generation in the material was attributed to reorientation and detwinning mechanisms, $(20\bar{1})_{\text{B19'}}$ deformation twinning, and dislocation activity as revealed by the bulk texture measurements. The role of this deformation on subsequent no-load thermal cycles (TWSME), on both magnitude and dimensional stability, was evaluated by optimizing the transformation strains (up to 2.2 percent), residual strains (~ 0 percent), and transformation temperatures (± 2 °C). It was found that the room temperature deformation of martensite prior to cycling is a quick and efficient method for creating a strong and stable TWSME in $\text{Ni}_{49.9}\text{Ti}_{50.1}$ (Chapter 4).
3. Thermomechanical cycling of polycrystalline $\text{Ni}_{49.9}\text{Ti}_{50.1}$ between the B2 austenite phase and the B19' martensite phase was investigated by time-of-flight neutron diffraction experiments. The macroscopic dimensional instabilities were related to the microstructural evolution through texture, internal strain, and phase evolution. The transformation strain magnitude during cycling was examined as a function of pre-deformation at the austenite or martensite phase. This pre-deformation was found to enhance or degrade the thermomechanical cyclic response depending on the deformation temperatures and magnitudes, and was used to optimize the cyclic performance of the material. In situ thermomechanical cycling revealed no texture evolution in the martensite and austenite phases, and a saturation of internal strains at early cycles (cycle 2). The microstructural changes in the peak shapes (broadening) indicated possible lattice defects that could accumulate as the material cycled through the phase transformation (Chapter 5).
4. Shape setting of the bulk polycrystalline $\text{Ni}_{49.9}\text{Ti}_{50.1}$ specimen was done while neutron diffraction spectra were simultaneously acquired. The temperature and shape of the specimen were controlled in a load frame while the stress exerted by the specimen on the grips was monitored during these in situ neutron diffraction experiments. Correlations were made between the internal stress, phase volume fraction, and texture measurements (determined from neutron diffraction spectra), and the macroscopic stress and shape changes (from a load cell and extensometry) during the shape setting procedure and subsequent shape recovery. Experimental results revealed details of the stress build up and relaxation during both the heating and cooling cycles of the constrained martensitic transformation. Comparisons were made between the pre-shape set specimen and the post-shape set specimen, both with and without external constraints. The specimens displayed similar shape memory behavior consistent with the fact that the microstructure of the shape-set sample was mostly unchanged by the shape-setting process and was nearly identical to that of the as-received materials (Chapter 6).
5. Isothermal and isobaric deformation of a Ni-rich $\text{Ni}_{50.3}\text{Ti}_{29.7}\text{Hf}_{20}$ high temperature SMA was investigated macroscopically through extensometry measurements and concurrently at the

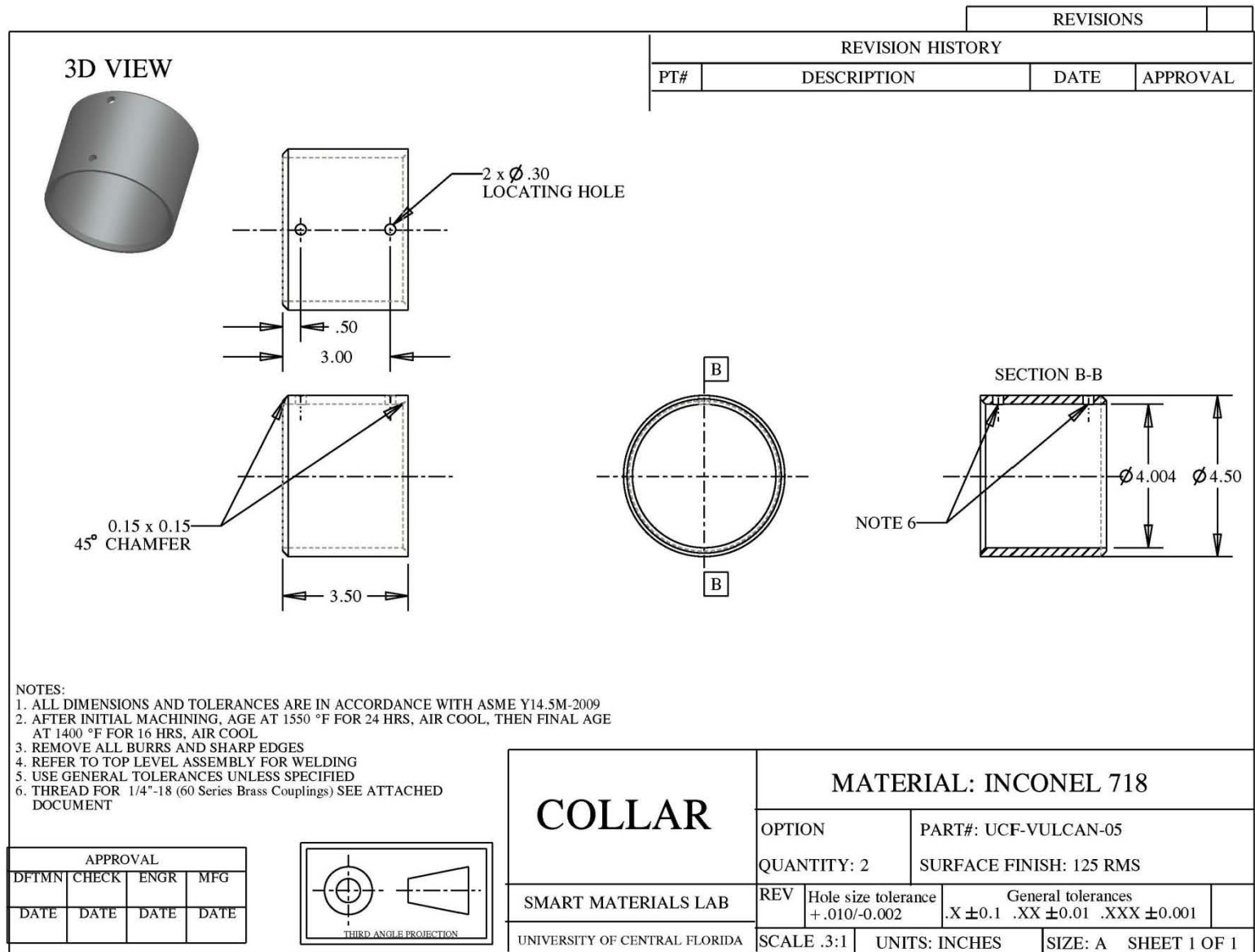
microscopic level with in situ neutron diffraction at stress and temperature. The excellent dimensional stability and high work output for this alloy were attributed to a coherent, nanometer size precipitate phase as confirmed by neutron and electron diffraction. This alloy exhibited low isothermal strains due to limited detwinning resulting from the pinning of twin and variant boundaries by the dispersion of fine precipitates. When deformed and cycled at a constant load, the high work output and near-perfect dimensional stability was attributed to the presence of the precipitates that act as homogeneous sources for the nucleation of martensite throughout the material, while providing resistance to irrecoverable processes such as plastic deformation (Chapter 7).

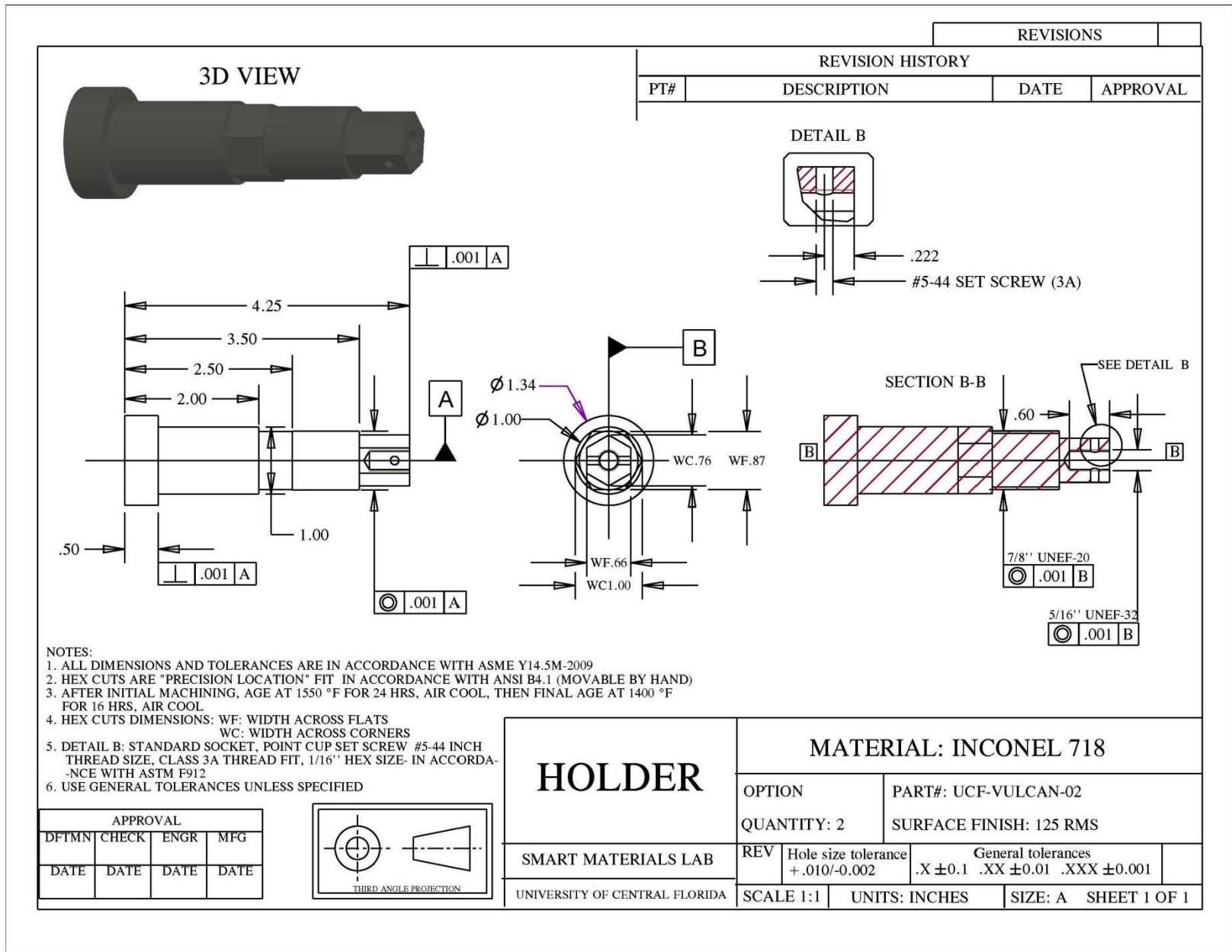
6. A multiaxial loading capability was designed for the VULCAN engineering materials diffractometer at the spallation neutron source at Oak Ridge National Laboratory. This design will allow for in situ neutron diffraction measurements on shape memory alloys and other engineering materials during selected combinations of heating, cooling and multiaxial loading. The gripping system can accommodate in situ experiments that require tension, compression and/or torsion in proportional or non-proportional loading configuration (Chapter 8).

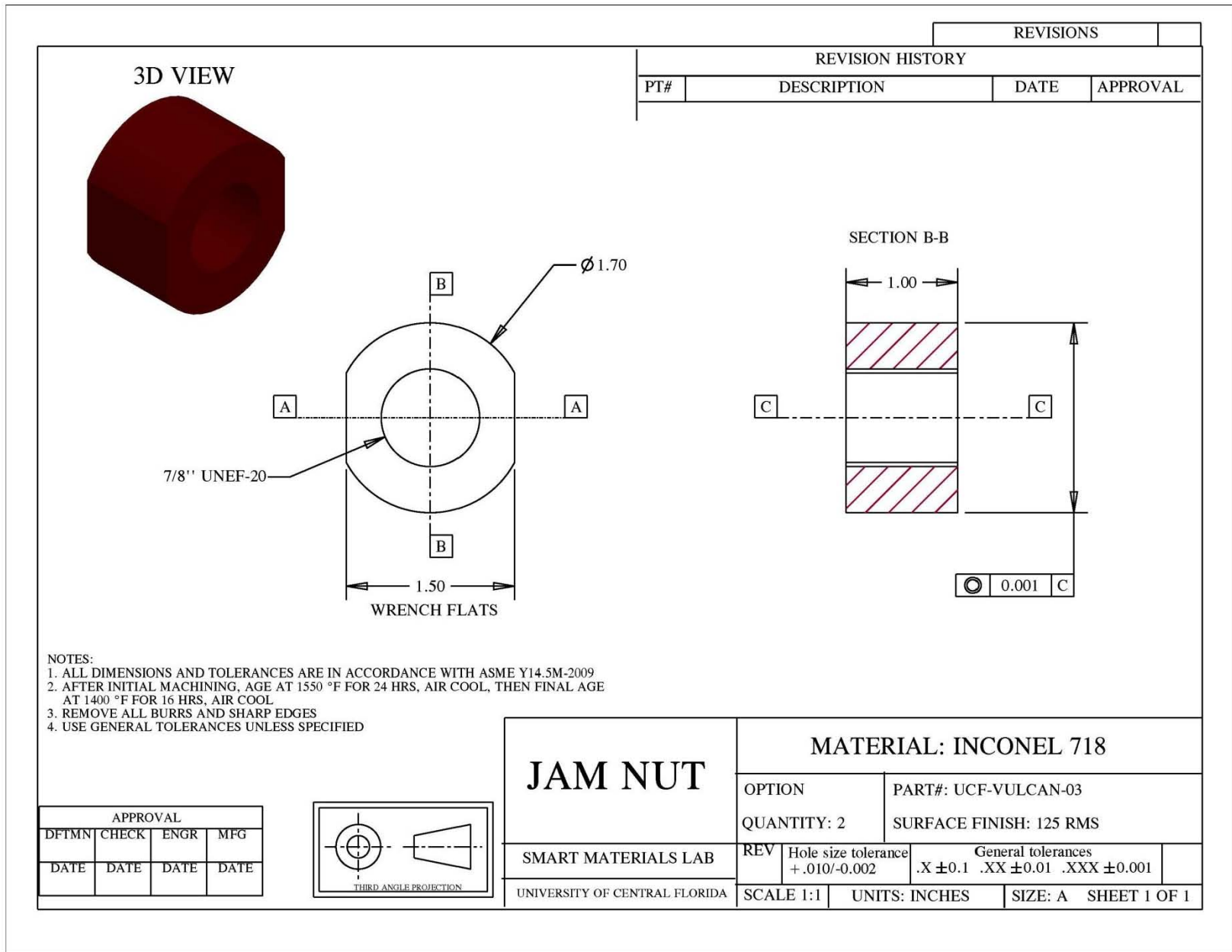
Appendix A.—Grip Design Machine Drawings

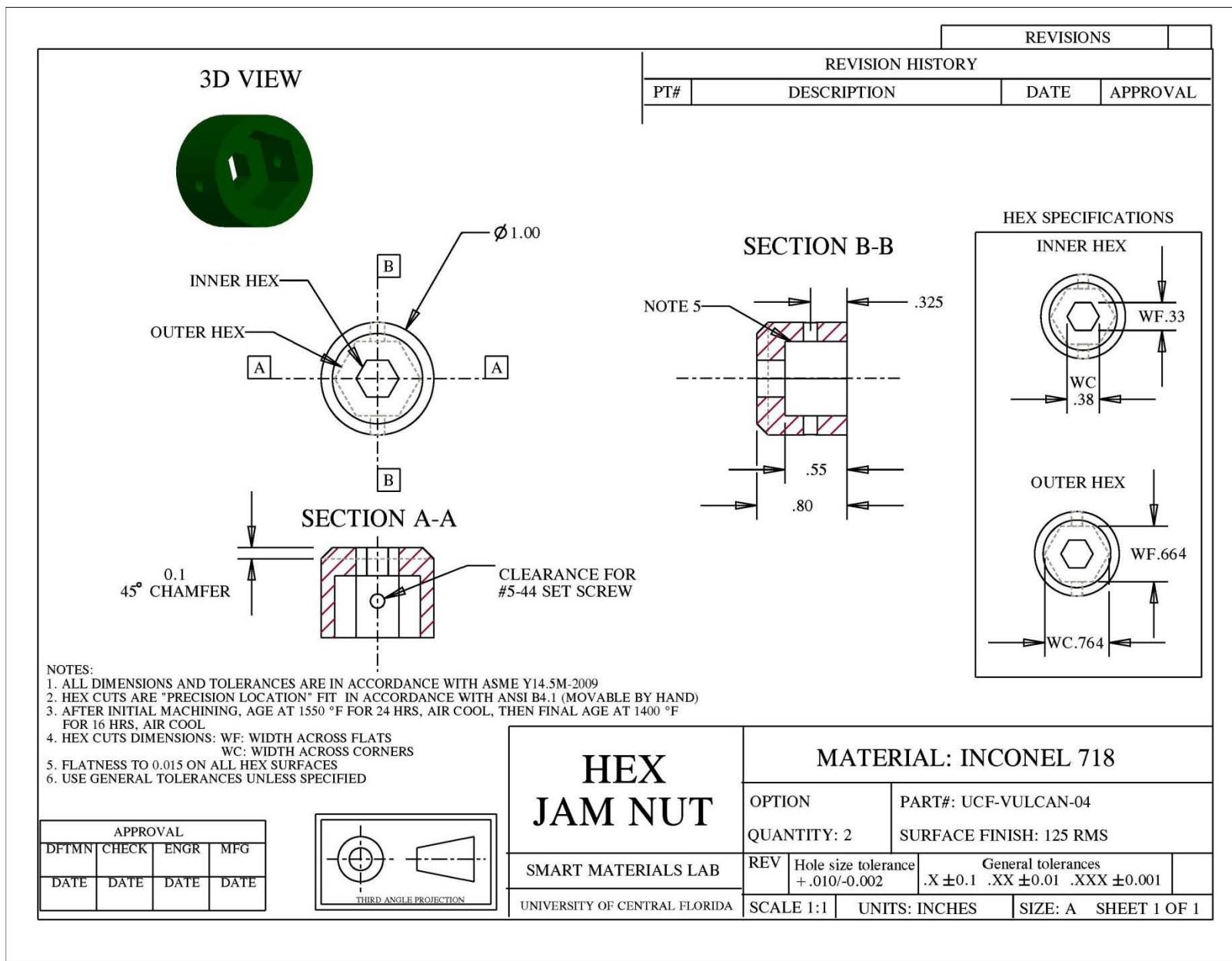


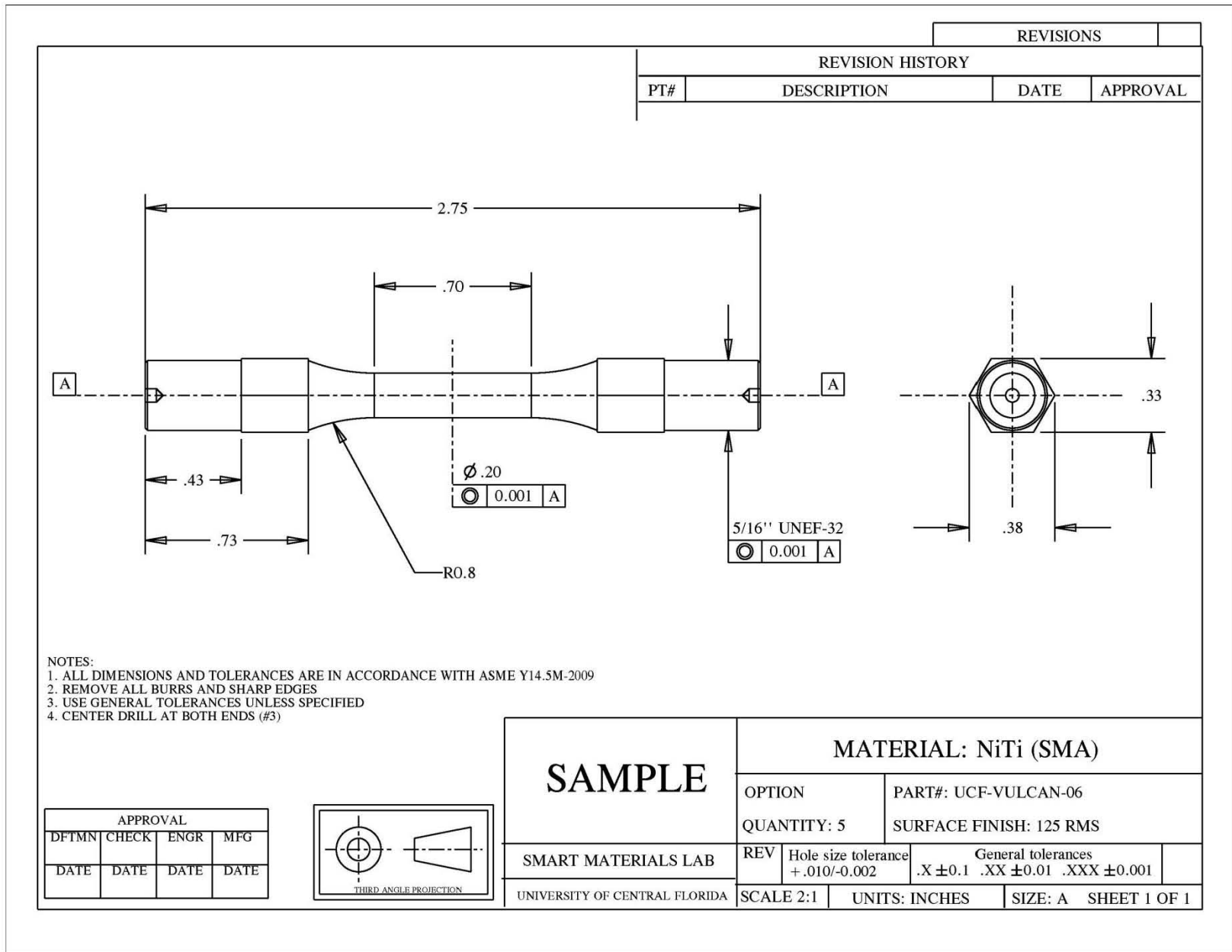







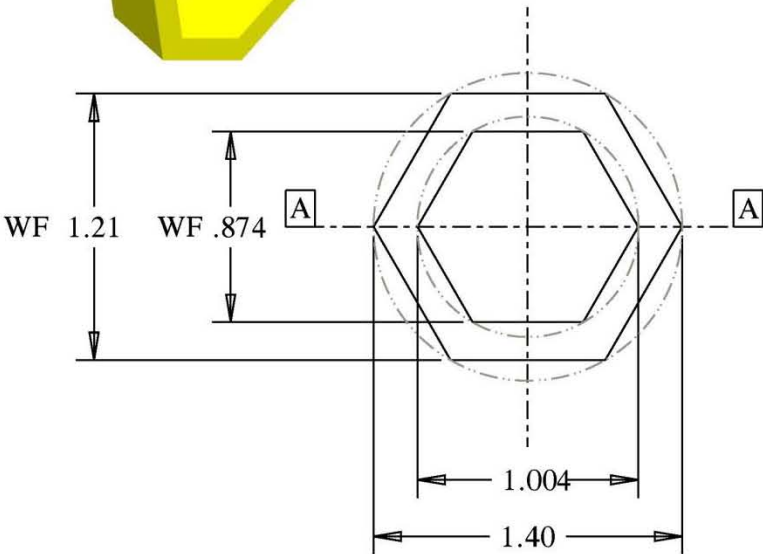


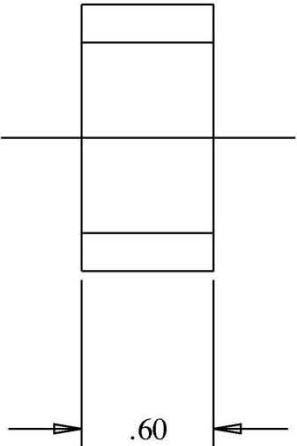




REVISIONS	
REVISION HISTORY	
PT#	DESCRIPTION
DATE	APPROVAL
<p>DRILL 4 SMALL THRU-HOLES ON THE FACE (WILL BE USED TO REMOVE NUT FROM PLATEN)</p>	

3D VIEW

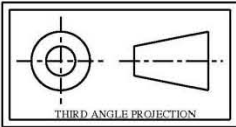





NOTES:

1. ALL DIMENSIONS AND TOLERANCES ARE IN ACCORDANCE WITH ASME Y14.5M-2009
2. HEX CUTS ARE "PRECISION LOCATION" FIT IN ACCORDANCE WITH ANSI B4.1 (MOVABLE BY HAND)
3. AFTER INITIAL MACHINING, AGE AT 1550 °F FOR 24 HRS, AIR COOL, THEN FINAL AGE AT 1400 °F FOR 16 HRS, AIR COOL
4. HEX CUTS DIMENSIONS: WF: WIDTH ACROSS FLATS
WC: WIDTH ACROSS CORNERS
5. FLATNESS TO 0.015 ON ALL HEX SURFACES
6. USE GENERAL TOLERANCES UNLESS SPECIFIED

APPROVAL			
DFTMN	CHECK	ENGR	MFG
DATE	DATE	DATE	DATE



THIRD ANGLE PROJECTION

TORQUE NUT

SMART MATERIALS LAB

UNIVERSITY OF CENTRAL FLORIDA

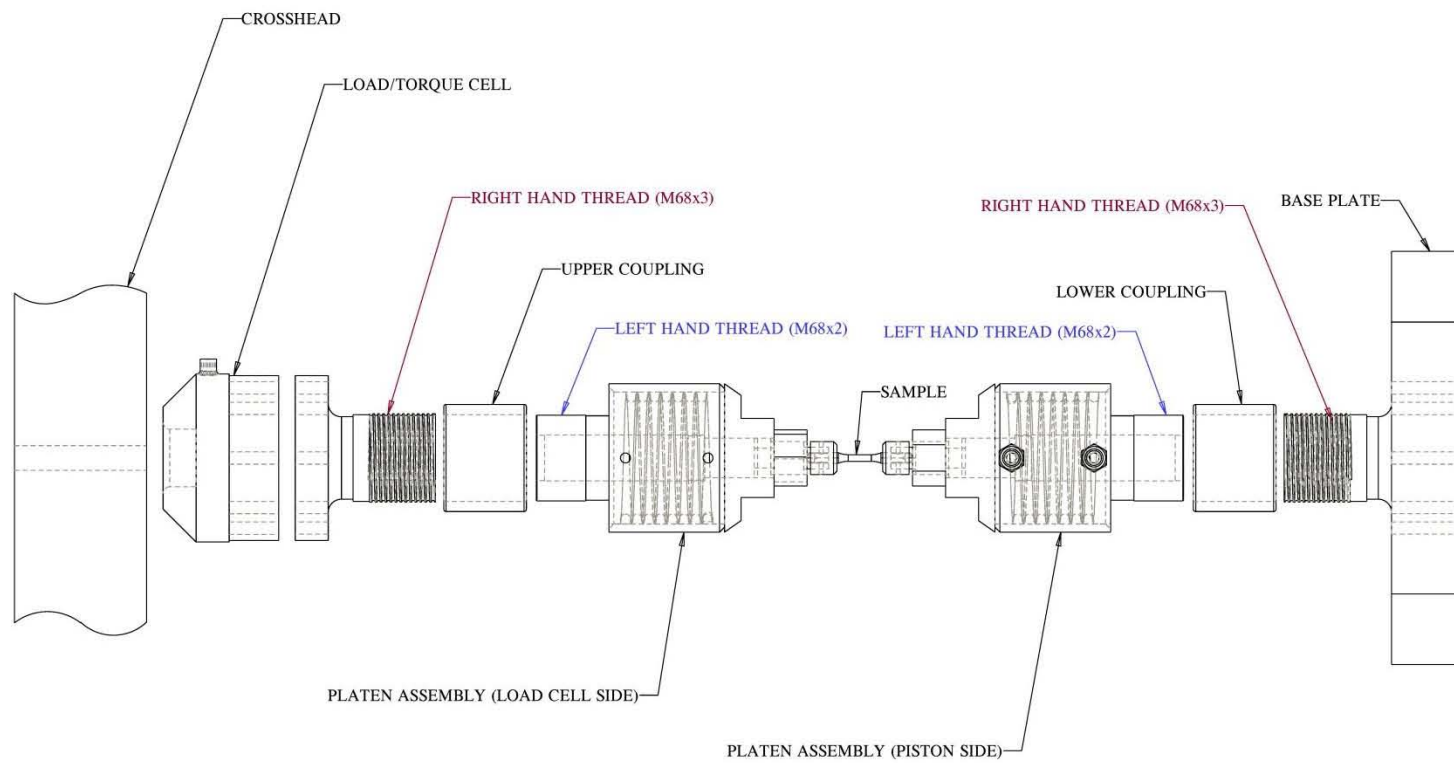
MATERIAL: INCONEL 718

OPTION: PART#: UCF-VULCAN-07

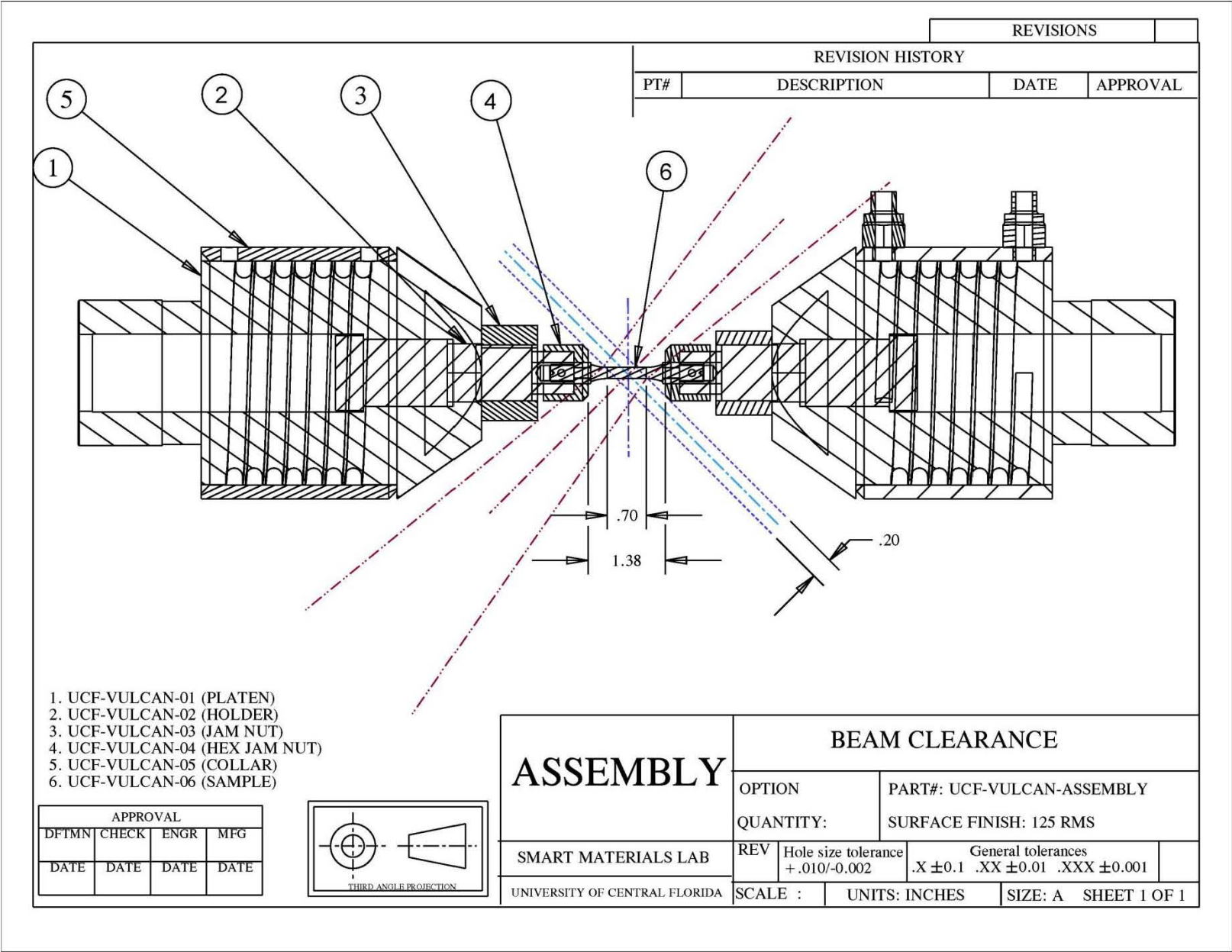
QUANTITY: 2 SURFACE FINISH: 125 RMS

REV	Hole size tolerance +.010/-0.002	General tolerances .X ±0.1 .XX ±0.01 .XXX ±0.001
-----	-------------------------------------	---

SCALE 1:1 UNITS: INCHES SIZE: A SHEET 1 OF 1



AXIAL TORSIONAL GRIP COMPONENTS



References

- [1] O. Benafan, S.A. Padula II, R.D. Noebe, D.W. Brown, B. Clausen and R. Vaidyanathan, *Acta Mater.* Submitted.
- [2] O. Benafan, R. Noebe, S.A. Padula II and R. Vaidyanathan, *Metall. Mater. Trans. A* Accepted.
- [3] E.C. Bain, *Trans. AIME Steel Div.* 70 (1924) 25.
- [4] O. Benafan and R. Vaidyanathan, in *Proc. ASME International Mechanical Engineering Congress and Exposition* (Lake Buena Vista, FL, 2009) p. 107.
- [5] O. Benafan, R. Vaidyanathan, W.U. Notardonato and B.J. Meneghelli, in *International Conference on Shape Memory & Superelastic Technologies* (Pacific Grove, CA, 2010).
- [6] K. Yamauchi, I. Ohkata, K. Tsuchiya and S. Miyazaki, *Shape memory and superelastic alloys: technologies and applications* (Woodhead Pub., 2011).
- [7] C.M. Wayman and T.W. Duerig, in "Engineering Aspects of Shape Memory Alloys", edited by T.W. Duerig, K.N. Melton, D. Stockel and C.M. Wayman (Butterworth-Heinemann, London, 1990) p. 3.
- [8] L.J. Chiang, C.H. Li, Y.F. Hsu and W.H. Wang, *J. Alloys Compd.* 462 (2008) 47.
- [9] K. Otsuka and C.M. Wayman, *Shape Memory Materials* (Cambridge University Press, Cambridge, 1999).
- [10] O. Benafan, J. Brown, F.T. Calkins, P. Kumar, A. Stebner, T. Turner, R. Vaidyanathan, J. Webster and M.L. Young, in *The ASME 2011 Conference on Smart Materials, Adaptive Structures and Intelligent Systems-SMASIS* (Phoenix, AZ, 2011).
- [11] M.E. Fitzpatrick and A. Lodini, *Analysis of Residual Stress by Diffraction using Neutron and Synchrotron Radiation* (Taylor & Francis, New York, 2003).
- [12] A.D. Krawitz, *Introduction to Diffraction in Materials Science and Engineering* (Wiley-Interscience, New York, 2001).
- [13] M.A.M. Bourke, D.C. Dunand and E. Ustundag, *Appl. Phys. A* 74 (2002) s1707.
- [14] S.C. Vogel, C. Hartig, L. Lutterotti, R.B. Von Dreele, H.-R. Wenk and D.J. Williams, *Powder Diffr.* 19 (2004) 64.
- [15] H.-R. Wenk, L. Lutterotti, S. Grigull and S.C. Vogel, *Nucl. Instrum. Methods A* 515 (2003) 575.
- [16] A.C. Larson and R.B. Von Dreele, *General Structure Analysis System (GSAS)*, Los Alamos National Laboratory Report LAUR 86-748, 2004.
- [17] R. B. Von Dreele, *J. Appl. Cryst.* 30 (1997) 517.
- [18] L. Lutterotti, S. Matthies, H.-R. Wenk, A.J. Schultz and J.W. Richardson, *J. Appl. Phys.*, 81 (1997) 594.
- [19] H.-R. Wenk, L. Lutterotti and S. C. Vogel, *Powder Diffr.* 25 (2010) 283.
- [20] M.R. Daymond, M.A.M. Bourke, R.B. Von Dreele, B. Clausen and T. Lorentzen, *J. Appl. Phys.* 82 (1997) 1554.
- [21] H. Rietveld, *J. Appl. Crystallogr.* 2 (1969) 65.
- [22] E.F. Sturcken and J.W. Croach, *Trans. Metall. Soc. AIME* 227 (1963) 934.
- [23] M.T. Hutchings, P.J. Withers, T.M. Holden and T. Lorentzen, *Introduction to the Characterization of Residual Stress by Neutron Diffraction* (Taylor & Francis, Boca Raton, FL, 2005).
- [24] H. Funakubo, *Shape Memory Alloys* (Gordon and Breach Science Publishers, New York, 1987).
- [25] K. Bhattacharya, *Microstructure of martensite: why it forms and how it gives rise to the shape-memory effect* (Oxford University Press, New York, 2003).
- [26] R. Vaidyanathan, M.A.M. Bourke and D.C. Dunand, *Mater. Sci. Eng., A* 273-275 (1999) 404.
- [27] K. Otsuka and X. Ren, *Prog. Mater Sci.* 50 (2005) 511.
- [28] R.M. Manjeri, S. Qiu, N. Mara, A. Misra and R. Vaidyanathan, *J. Appl. Phys.* 108 (2010) 023501.
- [29] T.W. Duerig, *Mater. Sci. Eng., A* 438-440 (2006) 69.
- [30] Y.-S. Lin, M. Cak, V. Paidar and V. Vitek, *Acta Mater.* 60 (2012) 881.
- [31] M.H. Yoo, T. Takasugi, S. Hanada and O. Izumi, *Mater. Trans., JIM* 31 (1990) 435.
- [32] G.I. Taylor, *J. Inst. Met.* 62 (1938) 307.

- [33] R. Von Mises, *Z. Angew. Math. Mech.*, 8 (1928) 161.
- [34] E. Goo, *Scr. Metall.* 22 (1988) 1079.
- [35] W.J. Moberly, J.L. Proft, T.W. Duerig and R. Sinclair, *Acta Metall. Mater.* 38 (1990) 2601.
- [36] M. Nishida, M. Matsuda, T. Fujimoto, K. Tanka, A. Kakisaka and H. Nakashima, *Mater. Sci. Eng., A* 438-440 (2006) 495.
- [37] G.W. Groves and A. Kelly, *Phil. Mag.* 8 (1963) 1437.
- [38] S. Qiu, V.B. Krishnan, S.A. Padula II, R.D. Noebe, D.W. Brown, B. Clausen and R. Vaidyanathan, *Appl. Phys. Lett.* 95 (2009) 141906.
- [39] K. Fukami-Ushiro, D. Mari and D. Dunand, *Metall. Mater. Trans. A* 27 (1996) 183.
- [40] T.M. Brill, S. Mittelbach, W. Assmus, M. Mullner and B. Luthi, *J. Phys.:Condens. Matter.* 3 (1991) 9621.
- [41] O. Mercier, K.N. Melton, G. Gremaud and J. Hagi, *J. Appl. Phys.* 51 (1980) 1833
- [42] M.F.-X. Wagner and W. Windl, *Acta Mater.* 56 (2008) 6232.
- [43] S. Qiu, B. Clausen, S.A. Padula II, R.D. Noebe and R. Vaidyanathan, *Acta Mater.* 59 (2011) 5055.
- [44] S. Miyazaki, K. Otsuka and Y. Suzuki, *Scr. Metall.* 15 (1981) 287.
- [45] R. Vaidyanathan, M.A.M. Bourke and D.C. Dunand, *Acta Mater.* 47 (1999) 3353.
- [46] C.R. Rathod, B. Clausen, M.A.M. Bourke and R. Vaidyanathan, *Appl. Phys. Lett.* 88 (2006) 201919.
- [47] R.S. Elliott, N. Triantafyllidis and J.A. Shaw, *J. Mech. Phys. Solids* 59 (2011) 216.
- [48] G. Airoidi, A. Corsi and G. Riva, *Mater. Sci. Eng., A* 241 (1998) 233.
- [49] M. Hasan, W.W. Schmahl, K. Hackl, R. Heinen, J. Frenzel, S. Gollerthan, G. Eggeler, M.F.-X. Wagner, J. Khalil-Allafi and A. Baruj, *Mater. Sci. Eng., A* 481-482 (2008) 414.
- [50] Y. Liu and H. Yang, *Mater. Sci. Eng., A* 260 (1999) 240.
- [51] X.M. Wang, Y.F. Wang, Z.Z. Lu, C.H. Deng and Z.F. Yue, *Mech. Mater.* 42 (2010) 365.
- [52] P. Thamburaja and L. Anand, *Int. J. Plast.* 18 (2002) 1607.
- [53] B. Strnadel, S. Ohashi, H. Ohtsuka, S. Miyazaki and T. Ishihara, *Mater. Sci. Eng., A* 203 (1995) 187.
- [54] V. Abbasi-Chianeh and J. Khalil-Allafi, *Mater. Sci. Eng., A* 528 (2011) 5060.
- [55] R. Delville, B. Malard, J. Pilch, P. Sittner and D. Schryvers, *Int. J. Plast.* 27 (2011) 282.
- [56] S. Li, K. Yamauchi, Y. Maruhashi and M. Nishida, *Scripta Mater.* 49 (2003) 723.
- [57] E. Goo, T. Duerig, K. Melton and R. Sinclair, *Acta Metall.* 33 (1985) 1725.
- [58] W.J. Moberly, T. Duerig, J.L. Proft and R. Sinclair, *Mater. Sci. Forum* 56-58 (1990) 759.
- [59] I. Karaman, G.G. Yapici, Y.I. Chumlyakov and I.V. Kireeva, *Mater. Sci. Eng., A* 410-411 (2005) 243.
- [60] T. Ezaz and H. Sehitoglu, *appl. Phys. Lett.* 98 (2011) 241906.
- [61] T. Ezaz, H. Sehitoglu and H.J. Maier, *Acta Mater.* 60 (2011) 339.
- [62] Y.I. Chumlyakov, A.S. Surikova and A.D. Korotaev, *Phys. Met. Metall.* 82 (1996) 102.
- [63] D.M. Norfleet, P.M. Sarosi, S. Manthiraju, M.F.-X. Wagner, M.D. Uchic, P.M. Anderson and M.J. Mills, *Acta Mater.* 57 (2009) 3549.
- [64] A.R. Pelton, *J. Mater. Eng. Perform.* 20 (2011) 613.
- [65] K. Gall, M.L. Dunn, Y. Liu, P. Labossiere, H. Sehitoglu and Y.I. Chumlyakov, *J. Eng. Mater. Technol.* 124 (2002) 238.
- [66] K. Gall and H.J. Maier, *Acta Mater.* 50 (2002) 4643.
- [67] J. Hurley, A. Ortega, J. Lechniak, K. Gall and H. Maier, *Z. Metallkd.* 94 (2003) 547.
- [68] G. Kang, Q. Kan, L. Qian and Y. Liu, *Mech. Mater.* 41 (2009) 139.
- [69] H. Sehitoglu, R. Anderson, I. Karaman, K. Gall and Y.I. Chumlyakov, *Mater. Sci. Eng., A* 314 (2001) 67.
- [70] X. Wang, B. Xu and Z. Yue, *J. Alloys Compd.* 463 (2008) 417.
- [71] M.A.M. Bourke, R. Vaidyanathan and D.C. Dunand, *Appl. Phys. Lett.* 69 (1996) 2477.
- [72] P. Sittner, P. Lukás, D. Neov, M.R. Daymond, V. Novák and G.M. Swallowe, *Mater. Sci. Eng., A* 324 (2002) 225.

- [73] J. Khalil-Allafi, B. Hasse, M. Kloenne M, M.F.-X. Wagner, T. Pirling, W. Predki and S. W.W. Schmahl, *Materialwiss. Werkstofftech.* 35 (2004) 280.
- [74] A. Mehta, X.-Y. Gong, V. Imbeni, A. Pelton and R.O. Ritchie, *Adv. Mater.* (2007) 19.
- [75] M.L. Young, M.F.-X. Wagner, J. Frenzel, W.W. Schmahl and G. Eggeler, *Acta Mater.* 58 (2010) 2344.
- [76] S. Manchiraju, D.J. Gaydosch, O. Benafan, R.D. Noebe, R. Vaidyanathan and P.M. Anderson, *Acta Mater.* 59 (2011) 5238.
- [77] A.F. Saleeb, S.A. Padula II and A. Kumar, *Int. J. Plast.* 27 (2011) 655.
- [78] Y. Chemisky, A. Duval, E. Patoor and T. Ben Zineb, *Mech. Mater.* 43 (2011) 361.
- [79] V. Novák and P. Sittner, *Mater. Sci. Eng., A* 378 (2004) 490.
- [80] D.J. Hartl, G. Chatzigeorgiou and D.C. Lagoudas, *Int. J. Plast.* 26 (2010) 1485.
- [81] M. Panico and L.C. Brinson, *J. Mech. Phys. Solids* 55 (2007) 2491.
- [82] P.A. Turner and C.N. Tomé, *Acta Metall. Mater.* 42 (1994) 4143.
- [83] ASTM, Standard Test Method for Determination of Transformation Temperature of Nickel-Titanium Shape Memory Alloys by Bend and Free Recovery. 2010, ASTM International: West Conshohocken, PA.
- [84] B. Clausen, T. Lorentzen and T. Leffers, *Acta Mater.* 46 (1998) 3087.
- [85] B. Clausen, C.N. Tome, D.W. Brown and S.R. Agnew, *Acta Mater.* 56 (2008) 2456.
- [86] E. Goo and K. T. Park, *Scr. Metall.* 23 (1989) 1053.
- [87] C. Tomé, G.R. Canova, U. F. Kocks, N. Christodoulou and J. J. Jonas, *Acta Metall.* 32 (1984) 1637.
- [88] R. Dakhlaoui, V. Klosek, M.H. Mathon and B. Marini, *Acta Mater.* 58 (2010) 499.
- [89] R.W. Margevicius and J.D. Cotton, *Acta Metall. Mater.* 43 (1995) 645.
- [90] R.D. Noebe, R.R. Bowman and M.V. Nathal, *Inter. Mater. Rev.* 38 (1993) 193.
- [91] S. Miyazaki, T. Imai, Y. Igo and K. Otsuka, *Metall. Mater. Trans. A* 17 (1986) 115.
- [92] H.-R. Wenk and P. Van Houtte, *Rep. Prog. Phys.* 67 (2004) 1367.
- [93] U.F. Kocks, C.N. Tomé and W.H.-R., *Texture and anisotropy: preferred orientations in polycrystals and their effect on materials properties* (Cambridge University Press, Cambridge, 1998).
- [94] D.W. Brown, S.R. Agnew, M.A.M. Bourke, T.M. Holden, S.C. Vogel and C.N. Tomas, *Mater. Sci. Eng., A* 399 (2005) 1.
- [95] R.R. Bowman, R.D. Noebe, S.V. Raj and I.E. Locci, *Metall. Mater. Trans. A* 23 (1992) 1493.
- [96] R.D. Noebe, C.L. Cullers and R.R. Bowman, *J. Mater. Res.* 7 (1992) 605.
- [97] K.C. Atli, (Ph.D. dissertation, Texas A&M University, College Station, TX, August 2011).
- [98] A.R. Pelton, G.H. Huang, P. Moine and R. Sinclair, *Mater. Sci. Eng., A* 532 (2012) 130.
- [99] D.S. Grummon, *JOM* 55 (2003) 24.
- [100] X.M. Zhang, J. Fernandez and J. M. Guilemany, *Mater. Sci. Eng., A* 438-440 (2006) 431.
- [101] K.C. Atli, I. Karaman and R.D. Noebe, *Scr. Mater.* 65 (2011) 903.
- [102] L. Wang, X. Meng, W. Cai and L. Zhao, *J. Mater. Sci. Technol.* 17 (2001) 13.
- [103] L. Contardo and G. Guenin, *Acta Metall. Mater.* 38 (1990) 1267.
- [104] Y. Liu and P.G. McCormick, *Acta Metall. Mater.* 38 (1990) 1321.
- [105] H. Scherngell and A.C. Kneissl, *Scr. Mater.* 39 (1998) 205.
- [106] R. Lahoz and J. A. Puertolas, *J. Alloys Compd.* 381 (2004) 130.
- [107] R. Stalmans, J. Van Humbeeck and L. Delaey, *Acta Metall. Mater.* 40 (1992) 501.
- [108] K.C. Atli, (Ph.D. dissertation, Texas A&M University, College Station, TX, August 2011).
- [109] Z. Balak and S.M. Abbasi, *Mater. Des.* 32 (2011) 3992.
- [110] Y.I. Yoo and J.J. Lee, *Physics Procedia* 22 (2011) 449.
- [111] R. Lahoz, L. Gracia-Villa and J. A. Puertolas, *J. Eng. Mater. Technol.* 124 (2002) 397.
- [112] Y. Liu, Y. Liu and J. Van Humbeeck, *Acta Mater.* 47 (1998) 199.
- [113] X.L. Meng, W. Cai, Y.F. Zheng, Y.B. Rao and L.C. Zhao, *Mater. Lett.* 57 (2003) 4206.
- [114] X.L. Meng, Y.F. Zheng, W. Cai and L.C. Zhao, *J. Alloys Compd.* 372 (2004) 180.
- [115] D.A. Hebda and S.R. White, *Smart Mater. Struct.* 4 (1995) 298.
- [116] K. Wada and Y. Liu, *J. Alloys Compd.* 449 (2008) 125.

- [117] J. Perkins and R. Sponholz, *Metall. Mater. Trans. A* 15 (1984) 313.
- [118] S. Eucken and T.W. Duerig, *Acta Metall.* 37 (1989) 2245.
- [119] J.M. Guilemany, B.G. Mellor and J. Fernandez, *Mater. Lett.* 13 (1992) 105.
- [120] M. Nishida and T. Honma, *Scr. Metall.* 18 (1984) 1293.
- [121] C.-Y. Chang, D. Vokoun and C.-T. Hu, *Metall. Mater. Trans. A* 32 (2001) 1629.
- [122] J. Pons, M. Sade, F.C. Lovey and E. Cesari, *Mater. Trans., JIM* 34 (1993) 888.
- [123] M.S. Shakeri, J. Khalil-Allafi, V. Abbasi-Chianeh and A. Ghabchi, *J. Alloys Compd.* 485 (2009) 320.
- [124] K. Otsuka and X. Ren, *Mater. Sci. Eng., A* 312 (2001) 207.
- [125] K. Madangopal and R. Banerjee, *Scr. Metall. Mater.* 27 (1992) 1627.
- [126] J.X. Zhang, M. Sato and A. Ishida, *Acta Mater.* 54 (2006) 1185.
- [127] T. Ezaz, H. Sehitoglu and H. J. Maier, *Acta Mater.* 59 (2011) 5893.
- [128] Z. Xie, Y. Liu and J. Van Humbeeck, *Acta Mater.* 46 (1998) 1989.
- [129] Y. Liu, Z. Xie, J. Van Humbeeck and L. Delaey, *Acta Mater.* 46 (1998) 4325.
- [130] M. Nishida, S. Ii, K. Kitamura, T. Furukawa, A. Chiba, T. Hara and K. Hiraga, *Scr. Mater.* 39 (1998) 1749.
- [131] A.P. Stebner, (Ph.D. dissertation, Northwestern University, 2012).
- [132] A. Stebner, S.A. Padula II, R.D. Noebe, B. Lerch and D. Quinn, *J. Intell. Mater. Syst. Struct.* 20 (2009) 2107.
- [133] X. Ren and K. Otsuka, *Scr. Mater.* 38 (1998) 1669.
- [134] X. Huang, G. J. Ackland and K. M. Rabe, *Nat. Mater.* 2 (2003) 307.
- [135] K. N. Melton and O. Mercier, *Acta Metall.* 27 (1979) 137.
- [136] S. Miyazaki, Y. Igo and K. Otsuka, *Acta Metall.* 34 (1986) 2045.
- [137] H. Matsumoto, *Mater. Lett.* 11 (1991) 40.
- [138] J. Van Humbeeck, *J. Phys IV* 1 (1991) 189.
- [139] R.J. Wasilewski, *Scr. Metall.* 5 (1971) 207.
- [140] A. Baruj, A. Fernandez Guillermet and M. Sade, *Mater. Sci. Eng., A* 273-275 (1999) 507.
- [141] X.-M. He, L.-Z. Zhao, X.-M. Wang, R.-F. Zhang and M.-S. Li, *Mater. Sci. Eng., A* 427 (2006) 327.
- [142] N.G. Jones and D. Dye, *Intermetallics* 19 (2011) 1348.
- [143] L. Jordan, M. Masse, J.Y. Collier and G. Bouquet, *J. Alloys Compd.* 211-212 (1994) 204.
- [144] B. Kockar, I. Karaman, J.I. Kim, Y.I. Chumlyakov, J. Sharp and C.J. Yu, *Acta Mater.* 56 (2008) 3630.
- [145] Y. Li, X. Mi, B. Gao and J. Tan, *Rare Metals* 27 (2008) 522.
- [146] Y. F. Li, X. J. Mi, J. Tan and B. D. Gao, *Mater. Sci. Eng., A* 509 (2009) 8.
- [147] Y. Liu, J. Laeng, T.V. Chin and T.-H. Nam, *Mater. Sci. Eng., A* 435-436 (2006) 251.
- [148] Y. Liu, J. Laeng, T.V. Chin and T.-H. Nam, *J. Alloys Compd.* 449 (2008) 144.
- [149] H. Matsumoto, *J. Alloys Compd.* 350 (2003) 213.
- [150] M. Morin and F. Trivero, *Mater. Sci. Eng., A* 196 (1995) 177.
- [151] Y. Motemani, P.J. McCluskey, C. Zhao, M.J. Tan and J.J. Vlassak, *Acta Mater.* 59 (2011) 7602.
- [152] M. Pattabi, K. Ramakrishna and K. K. Mahesh, *Mater. Sci. Eng., A* 448 (2007) 33.
- [153] A.S. Paula, J.P.H.G. Canejo, R.M.S. Martins and F.M. Braz Fernandes, *Mater. Sci. Eng., A* 378 (2004) 92.
- [154] V. Pelosin and A. Riviere, *Metall. Mater. Trans. A* 29 (1998) 1175.
- [155] C.N. Saikrishna, K.V. Ramaiah and S. K. Bhaumik, *Mater. Sci. Eng., A* 428 (2006) 217.
- [156] T. Tadaki, Y. Nakata and K. Shimizu, *Trans. Jpn. Inst. Met.* 28 (1987) 883.
- [157] J. Uchil, K. Ganesh Kumara and K.K. Mahesh, *J. Alloys Compd.* 325 (2001) 210.
- [158] J. Uchil, K.K. Mahesh and K. G. Kumara, *Physica B: Condensed Matter* 324 (2002) 419.
- [159] C. Urbina, S. De la Flor and F. Ferrando, *Mater. Sci. Eng., A* 501 (2009) 197.
- [160] M.F.-X. Wagner, S.R. Dey, H. Gudel, J. Frenzel, C. Somsen and G. Eggeler, *Intermetallics* 18 (2010) 1172.
- [161] P. Filip and K. Mazanec, *Scr. Metall. Mater.* 30 (1994) 67.

- [162] P.G. McCormick and Y. Liu, *Acta Metall. Mater.* 42 (1994) 2407.
- [163] S. De la Flor, C. Urbina and F. Ferrando, *J. Alloys Compd.* 469 (2009) 343.
- [164] S. Nemat-Nasser and W.-G. Guo, *Mech. Mater.* 38 (2006) 463.
- [165] H. Sakamoto, *Trans. Jpn. Inst. Met.* 24 (1983) 665.
- [166] B. Strnadel, S. Ohashi, H. Ohtsuka, T. Ishihara and S. Miyazaki, *Mater. Sci. Eng., A* 202 (1995) 148.
- [167] B. Strnadel, S. Ohashi, H. Ohtsuka, S. Miyazaki and T. Ishihara, *Mater. Sci. Eng., A* 203 (1995) 187.
- [168] M.F.-X. Wagner, N. Nayan and U. Ramamurty, *J. Phys. D: Appl. Phys.* 41 (2008) 185408.
- [169] R.M. Tabanli, N.K. Simha and B.T. Berg, *Mater. Sci. Eng., A* 273-275 (1999) 644.
- [170] W. Tang and R. Sandstrom, *Mater. Des.* 14 (1993) 103.
- [171] S.A. Padula II, S. Qiu, D.J. Gaydosh, R.D. Noebe, G.S. Bigelow, A. Garg and R. Vaidyanathan, NASA/TM-2011-217408. (2011).
- [172] ASTM Standard F2082-06, "Standard Test Method for Determination of Transformation Temperature of Nickel-Titanium Shape Memory Alloys by Bend and Free Recovery," 2010, ASTM International: West Conshohocken, PA, DOI: 10.1520/F2082-06, www.astm.org.
- [173] O. Benafan, unpublished work.
- [174] S.A. Padula II, R.D. Noebe, G.S. Bigelow, D.J. Gaydosh, A. Garg, D. Lagoudas, I. Karaman and K.C. Atli, in *Proc. SPIE* (2008) p. 692912.
- [175] B. Ye, B.S. Majumdar and I. Dutta, *Applied Physics Letters* 91 (2007) 061918.
- [176] B. Ye, B.S. Majumdar and I. Dutta, *Acta Mater.* 57 (2009) 2403.
- [177] T. W. Duerig, A. Pelton and D. Stockel, *Mater. Sci. Eng. A* 273 (1999) 149.
- [178] A. Bellini, M. Colli and E. Dragoni, *IEEE Trans. Ind. Electron.* 56 (2009) 2644.
- [179] K. Yamauchi, I. Ohkata, K. Tsuchiya and S. Miyazaki, eds., *Shape memory and superelastic alloys: Technologies and applications* (Woodhead Publishing Philadelphia, 2011).
- [180] C. Mavroidis, *Res. Nondestr. Eval.* 14 (2002) 1.
- [181] J. Van Humbeeck, *J. Alloys Compd.* 355 (2003) 58.
- [182] S. Seelecke and I. Muller, *Appl. Mech. Rev.* 57 (2004) 23.
- [183] V.B. Krishnan, R.M. Manjeri, B. Clausen, D.W. Brown and R. Vaidyanathan, *Mater. Sci. Eng., A* 481-482 (2008) 3.
- [184] S. Rajagopalan, A.L. Little, M.A.M. Bourke and R. Vaidyanathan, *Appl. Phys. Lett.* 86 (2005) 081901.
- [185] D. Jiang, L. Cui, Y. Zheng, X. Zhao and Y. Li, *Mater. Sci. Eng. A* 515 (2009) 131.
- [186] H.C. Lin, T.P. Wang, K.M. Lin, C.Y. Chung, P.C. Wang and W.H. Ho, *J. Alloys Compd.* 466 (2008) 119.
- [187] P. Pappas, D. Bolas, J. Parthenios, V. Dracopoulos and C. Galiotis, *Smart Mater. Struct.* 16 (2007) 2560.
- [188] Y. Zheng, L. Cui, D. Zhu and D. Yang, *Mater. Lett.* 43 (2000) 91.
- [189] K.A. Tsoi, R. Stalmans and J. Schrooten, *Acta Mater.* 50 (2002) 3535.
- [190] X. Yan and J. Van Humbeeck, *J. Alloys Compd.* 509 (2011) 1001.
- [191] P. Sittner, D. Vokoun, G.N. Dayananda and R. Stalmans, *Mater. Sci. Eng. A* 286 (2000) 298.
- [192] Y. Li, L.S. Cui, H.B. Xu and D.Z. Yang, *Metall. Mater. Trans. A* 34 (2003) 219.
- [193] R.A. Young, *The Rietveld Method* (Oxford University Press, 1995).
- [194] T.W. Duerig, K.N. Melton, D. Stockel and C.M. Wayman, in "Engineering Aspects of Shape Memory Alloys" (Butterworth-Heinemann, London, 1990).
- [195] K. Otsuka, X. Ren, Y. Murakami, T. Kawano, T. Ishii and T. Ohba, *Mater. Sci. Eng. A* 273-275 (1999) 558.
- [196] O. Takao, *Mater. Sci. Eng. A* 312 (2001) 57.
- [197] V. Plotnikov and Y. Paskal, *Russ. Phys. J.* 40 (1997) 448.
- [198] J.F. Nye, *Physical Properties of Crystals* (Clarendon Press, Oxford, 1985).

- [199] T.M. Brill, S. Mittelbach, W. Assmus, M. Mullner and B. Luthi, *J. Phys. Condens. Matter* 3 (1991) 9621.
- [200] Y. Zheng, J. Schrooten, L. Cui and J. Van Humbeeck, *Acta Mater.* 51 (2003) 5467.
- [201] R. Bowman, R. Noebe, S. Raj and I. Locci, *Metall. Mater. Trans. A* 23 (1992) 1493.
- [202] S. Hirose, K. Ikuta and Y. Umetani, *Adv. Robot.* 3 (1989) 3.
- [203] D.J. Hartl, D.C. Lagoudas, F.T. Calkins and J.H. Mabe, *Smart Mater. Struct.* 19 (2010) 015020.
- [204] D.J. Hartl, D.C. Lagoudas, F.T. Calkins and J.H. Mabe, *Smart Mater. Struct.* 19 (2010) 015021.
- [205] D. Stoeckel, *Mater. Des.* 11 (1990) 302.
- [206] R. Vaidyanathan, H. J. Chiel and R. D. Quinn, *Rob. Autom. Syst.* 30 (2000) 103.
- [207] G.S. Bigelow, S.A. Padula II, A. Garg, D.J. Gaydosch and R.D. Noebe, *Metall. Mater. Trans. A* 41A (2010) 3065.
- [208] C. Grossmann, J. Frenzel, V. Sampath., T. Depka and G. Eggeler, *Metall. Mater. Trans.* A 40 (2010) 2530.
- [209] J. Ma, I. Karaman and R.D. Noebe, *Inter. Mater. Rev.* 55 (2010) 257.
- [210] G.S. Bigelow, S.A. Padula II, A. Garg and R.D. Noebe, Correlation between mechanical behavior and actuator-type performance of Ni-Ti-Pd high-temperature shape memory alloys, (SPIE, 2007) p. 65262B.
- [211] K.C. Atli, I. Karaman, R.D. Noebe, A. Garg, Y.I. Chumlyakov and I.V. Kireeva, *Metall. Mater. Trans. A* 41 (2010) 2485.
- [212] G.S. Firstov, J. Van Humbeeck and Y.N. Koval, *Mater. Sci. Eng., A* 378 (2004) 2.
- [213] K.C. Atli, I. Karaman, R.D. Noebe and H.J. Maier, *Scripta Mater.* 64 (2011) 315.
- [214] B. Kockar, K.C. Atli, J. Ma, M. Haouaoui, I. Karaman, M. Nagasako and R. Kainuma, *Acta Mater.* 58 (2010) 6411.
- [215] B. Kockar, I. Karaman, J. I. Kim and Y. Chumlyakov, *Scr. Mater.* 54 (2006) 2203.
- [216] J. Ma, I. Karaman, B. Kockar, H.J. Maier and Y.I. Chumlyakov, *Mater. Sci. Eng., A* 528 (2011) 7628.
- [217] S. Shimizu, Y. Xu, E. Okunishi, S. Tanaka, K. Otsuka and K. Mitose, *Mater. Lett.* 34 (1998) 23.
- [218] X.L. Meng, W. Cai, Y.D. Fu, Q.F. Li, J. X. Zhang and L.C. Zhao, *Intermetallics* 16 (2008) 698.
- [219] D.Y. Cong, S. Wang, Y.D. Wang, Y. Ren, L. Zuo and C. Esling, *Mater. Sci. Eng., A* 473 (2008) 213.
- [220] E. Panchenko, Y.I. Chumlyakov, H.J. Maier, E. Timofeeva and I. Karaman, *Intermetallics* 18 (2010) 2458.
- [221] F. Dalle, E. Perrin, P. Vermaut, M. Masse and R. Portier, *Acta Mater.* 50 (2002) 3557.
- [222] P.L. Potapov, A.V. Shelyakov, A.A. Gulyaev, E.L. Svistunov, N.M. Matveeva and D. Hodgson, *Mater. Lett.* 32 (1997) 247.
- [223] P.E. Thoma and J.J. Boehm, *Mater. Sci. Eng., A* 273-275 (1999) 385.
- [224] S. Besseghini, E. Villa and A. Tuissi, *Mater. Sci. Eng., A* 273-275 (1999) 390.
- [225] S. Han, W. Zou, S. Jin, Z. Zhang and D. Yang, *Scr. Metall. Mater.* 32 (1995) 1441.
- [226] X.D. Han, R. Wang, Z. Zhang and D.Z. Yang, *Mater. Lett.* 30 (1997) 23.
- [227] X.D. Han, R. Wang, Z. Zhang and D.Z. Yang, *Acta Mater.* 46 (1998) 273.
- [228] X.D. Han, W.H. Zou, R. Wang, Z. Zhang and D.Z. Yang, *Acta Mater.* 44 (1996) 3711.
- [229] X.L. Meng, W. Cai, Y.F. Zheng, Y.B. Rao and L.C. Zhao, *Mater. Lett.* 57 (2003) 4206.
- [230] X.L. Meng, W. Cai, Y.F. Zheng, Y.X. Tong, L.C. Zhao and L.M. Zhou, *Mater. Lett.* 55 (2002) 111.
- [231] X.L. Meng, Y.F. Zheng, Z. Wang and L.C. Zhao, *Mater. Lett.* 45 (2000) 128.
- [232] Y.Q. Wang, Y.F. Zheng, W. Cai and L.C. Zhao, *Scr. Mater.* 40 (1999) 1327.
- [233] Y. Tong, F. Chen, B. Tian, L. Li and Y. Zheng, *Mater. Lett.* 63 (2009) 1869.
- [234] R. Santamarta, C. Seguí, J. Pons and E. Cesari, *Scr. Mater.* 41 (1999) 867.
- [235] M. Zarinejad, Y. Liu and T.J. White, *Intermetallics* 16 (2008) 876.
- [236] M. Liu, X.M. Zhang, Y.Y. Li, J.Z. Chen and M.J. Tu, *J. Alloys Compd.* 334 (2002) 147.
- [237] C.C. Wojcik, *J. Mater. Eng. Perf.* 18 (2009) 511.

- [238] G.S. Bigelow, A. Garg, S.A. Padula II, D.J. Gaydosch and R.D. Noebe, *Scripta Mater.* 64 (2011) 725.
- [239] L. Kovarik, F. Yang, R.D. Noebe and M.J. Mills, *Microscopy and Microanalysis* 15 (2009) 1402.
- [240] L. Kovarik, F. Yang, A. Garg, D. Diercks, M. Kaufman, R.D. Noebe and M.J. Mills, *Acta Mater.* 58 (2010) 4660.
- [241] T. Sasaki, (University of Alabama, personal communication, 2010).
- [242] S. Banerjee and J. Mukhopadhyay, *Phase Transformations-Examples from Titanium and Zirconium Alloys* (Pergamon, Oxford, 2007).
- [243] D.R. Angst, P.E. Thoma and M.Y. Kao, *J. Phys. IV* 5 (1995) C8.
- [244] X.L. Meng, Y.F. Zheng, Z. Wang and L.C. Zhao, *Scripta Mater.* 42 (2000) 341.
- [245] P. Olier, J.C. Brachet, J.L. Bechade, C. Foucher and G. Guenin, *J. Phys. IV* 5 (1995) C8.
- [246] J. A. Monroe, I. Karaman, D.C. Lagoudas, G. Bigelow, R.D. Noebe and S.A. Padula II, *Scripta Mater.* 65 (2011) 123.
- [247] R. Vaidyanathan, M.A.M. Bourke and D. Dunand, *Metall. Mater. Trans. A* 32 (2001) 777.
- [248] X.L. Wang, T.M. Holden, G.Q. Rennich, A.D. Stoica, P.K. Liaw, H. Choo and C.R. Hubbard, *Phys. Rev. B* 385 (2006) 673.
- [249] X.-L. Wang, T.M. Holden, A.D. Stoica, K. An, H.D. Skorpenske, G.Q. Rennich, E.B. Iverson and A.B. Jones, *Mater. Sci. Forum* 652 (2012) 105.
- [250] A. Bejan, *Heat Transfer* (John Wiley and Sons, New York, NY., 1993).
- [251] F.P. Incropera, DeWitt D.P., T.L. Bergman and A.S. Lavine, *Fundamentals of Heat and Mass Transfer* (John Wiley and Sons, 2007).
- [252] F.P. Beer, *Mechanics of Materials* (McGraw-Hill, Inc., New York, NY, 2001).

REPORT DOCUMENTATION PAGE				Form Approved OMB No. 0704-0188	
<p>The public reporting burden for this collection of information is estimated to average 1 hour per response, including the time for reviewing instructions, searching existing data sources, gathering and maintaining the data needed, and completing and reviewing the collection of information. Send comments regarding this burden estimate or any other aspect of this collection of information, including suggestions for reducing this burden, to Department of Defense, Washington Headquarters Services, Directorate for Information Operations and Reports (0704-0188), 1215 Jefferson Davis Highway, Suite 1204, Arlington, VA 22202-4302. Respondents should be aware that notwithstanding any other provision of law, no person shall be subject to any penalty for failing to comply with a collection of information if it does not display a currently valid OMB control number.</p> <p>PLEASE DO NOT RETURN YOUR FORM TO THE ABOVE ADDRESS.</p>					
1. REPORT DATE (DD-MM-YYYY) 01-12-2012		2. REPORT TYPE Technical Memorandum		3. DATES COVERED (From - To)	
4. TITLE AND SUBTITLE Deformation and Phase Transformation Processes in Polycrystalline NiTi and NiTiHf High Temperature Shape Memory Alloys				5a. CONTRACT NUMBER	
				5b. GRANT NUMBER	
				5c. PROGRAM ELEMENT NUMBER	
6. AUTHOR(S) Benafan, Othmane				5d. PROJECT NUMBER	
				5e. TASK NUMBER	
				5f. WORK UNIT NUMBER WBS 984754.02.07.03.16.04.02	
7. PERFORMING ORGANIZATION NAME(S) AND ADDRESS(ES) National Aeronautics and Space Administration John H. Glenn Research Center at Lewis Field Cleveland, Ohio 44135-3191				8. PERFORMING ORGANIZATION REPORT NUMBER E-18486	
9. SPONSORING/MONITORING AGENCY NAME(S) AND ADDRESS(ES) National Aeronautics and Space Administration Washington, DC 20546-0001				10. SPONSORING/MONITOR'S ACRONYM(S) NASA	
				11. SPONSORING/MONITORING REPORT NUMBER NASA/TM-2012-217741	
12. DISTRIBUTION/AVAILABILITY STATEMENT Unclassified-Unlimited Subject Categories: 37 and 32 Available electronically at http://www.sti.nasa.gov This publication is available from the NASA Center for AeroSpace Information, 443-757-5802					
13. SUPPLEMENTARY NOTES					
14. ABSTRACT The deformation and transformation mechanisms of polycrystalline Ni _{49.9} Ti _{50.1} and Ni _{50.3} Ti _{29.7} Hf ₂₀ (in at.%) shape memory alloys were investigated by combined experimental and modeling efforts aided by an in situ neutron diffraction technique at stress and temperature. The thermomechanical response of the low temperature martensite, the high temperature austenite phases, and changes between these two states during thermomechanical cycling were probed and reported. In the cubic austenite phase, stress-induced martensite, deformation twinning and slip processes were observed which helped in constructing a deformation map that contained the limits over which each of the identified mechanisms was dominant. Deformation of the monoclinic martensitic phase was also investigated where the microstructural changes (texture, lattice strains, and phase fractions) during room-temperature deformation and subsequent thermal cycling were compared to the bulk macroscopic response. When cycling between these two phases, the evolution of inelastic strains, along with the shape setting procedures were examined and used for the optimization of the transformation properties as a function of deformation levels and temperatures. Finally, this work was extended to the development of multiaxial capabilities at elevated temperatures for the in situ neutron diffraction measurements of shape memory alloys on the VULCAN Diffractometer at Oak Ridge National Laboratory.					
15. SUBJECT TERMS Mechanical engineering; Metals and metallic materials					
16. SECURITY CLASSIFICATION OF:			17. LIMITATION OF ABSTRACT	18. NUMBER OF PAGES 176	19a. NAME OF RESPONSIBLE PERSON
a. REPORT U	b. ABSTRACT U	c. THIS PAGE U			STI Help Desk (email: help@sti.nasa.gov)
					19b. TELEPHONE NUMBER (include area code) 443-757-5802

